

Study of Ternary Transition Metal Oxides as Conversion Anodes in Li-Ion Batteries

Zur Erlangung des akademischen Grades eines
DOKTORS DER NATURWISSENSCHAFTEN
(Dr. rer. nat.)

von der KIT-Fakultät für Chemie und Biowissenschaften
des Karlsruher Instituts für Technologie (KIT)
genehmigte

DISSERTATION

von
Master-Material Science and Engineering

Zijian Zhao
aus Tianjin (China)

KIT-Dekan: Prof. Dr. Reinhard Fischer

Referent: Prof. Dr. Helmut Ehrenberg

Korreferent: Prof. Dr. Stefano Passerini

Tag der mündlichen Prüfung: 15.10.2019

Acknowledgements

First of all, I would like to appreciate my supervisor Prof. Dr. Helmut Ehrenberg, and group leader Dr. Sonia Dsoke, for giving me the chance to study in conversion-type anodes for lithium-ion batteries. With their kind help and smart advices in these three years, I feel happy and satisfied to work in our group (IAM-ESS) in KIT. Here I was allowed to research what I found interesting, and for believing me to solve problems with an independent approach. I appreciate the freedom and opportunities they offered. I am grateful that they challenged me to meet standards for PhD graduation and their high scientific level.

It is a great pleasure to acknowledge the financial supports by the China Scholarship Council (No. 201506880038).

I would like to thank my thesis committee members: Prof. Dr. Stefano Passerini, Prof. Dr. Jan-Dierk Grunwaldt, Prof. Dr. Rolf Schuster and Prof. Dr. Patrick Théato, for all of their guidance and valuable discussion.

I would like to express my appreciation and gratitude to all the people for their helpful scientific support and fruitful discussions with my colleagues. This work is impossible to be finished without the support and contribution from my nice colleagues in IAM-ESS, I would like to thanks again to the group, and especially to: Dr. Angelina Sarapulova (*in situ* XRD and XAS), Liuda Mereacre (TGA, FT-IR, Raman), Udo Geckle (SEM), Vanessa Trouillet (XPS), Dr. Qiang Fu (*in situ* XRD), Lihua Zhu (Raman), Dr. Julia Maibach (XPS), Lydia Gehrlein (XPS), Dr. Michael Knapp (XRD refinement), Georg Bosch (German correction), Mayer Marcus (equipment support), Almut Kriese (administrative support), Bettina Hunzinger (safety training), Heinz-Robert Goebel (equipment support), and Richard Hans Schneider (IT support).

I am grateful to the technical support from Dr. Martin Etter (*in situ* SRD) and Dr. Jozef Bednarcik (HT-SRD) of the beamline P02.1, as well as from Dr. Edmund Welter (*ex situ* XAS) of the beamline P65, PETRA III, DESY.

I would like to express my gratitude to Dr. Aleksandr Missiul (*in situ* SRD) of the beamline BL04-MSPD, ALBA.

Also, many thanks to Dr. Georgian Melinte, Dr. Cristian Kübel and Suya Liu from the Institute of Nanotechnology (INT, KIT) for the TEM measurements.

I would also thank Prof. Dr. Andrea Balducci from the Friedrich-Schiller-University Jena for the preparation of the CPAME electrolyte.

I greatly appreciate to Dr. Daniel Carriazo, Dr. Jon Ajuria, Dr. M. Angeles Moreno and Juan Luis Gómez Urbano for the many helps during my exchange study in CIC energiGUNE.

I would like to thank Prof. Dr. Maximilian Fichtner, Dr. Anji Reddy Munnangi, Dr. Alexander Pohl, Dr. Ping Gao, Dr. Le Zhang, Dr. Xiumei Lin and other group members who gave me great support when I studied at the Helmholtz Institute Ulm (HIU).

Finally, I would like to especially thank my family members and my husband Dr. Guiying Tian for their endless support, encouragement and love during my life. Thank you all again.

Abstract

Nowadays, severe environmental and energy issues, such as excessive consumption of fossil sources, oil crisis and air pollution, inevitably lead to increasing demand for renewable energy sources and development of energy storage systems. As power sources for consumable electronics and electric vehicles, secondary batteries are expected to possess excellent electrochemical properties including high energy/power density, long cycling life, low cost and superior safety. Currently, Li-ion batteries using graphite anode have achieved great commercial success. However, graphite anode suffers from the relatively low specific capacity (theoretical capacity of 372 mAh g⁻¹, and practical capacity of 330~350 mAh g⁻¹). Considering this, the development of novel anode materials with high capacity is urgently needed. Given their high gravimetric/volumetric capacity and abundant resources, conversion-type transition metal oxides have attracted much attention as the next generation of anode materials for Li-ion batteries.

Ideal anode materials should display high electronic/ionic conductivity, high specific capacity, long cycling stability, as well as low and stable working potential. However, as the most typical category of conversion-type anode materials, transition metal oxides undergo huge volume change and severe electrode pulverization during the cycling process. This is because of the massive Li insertion/extraction and repeated phase transformation. In addition, the low electronic conductivity of the oxides also represses the kinetics of electrochemical reactions, and the high reactivity of the lithiated products (Li₂O and metal) can induce excessive electrolyte decomposition and thick solid electrolyte interphase formation. Moreover, large voltage hysteresis of the conversion-type anodes leads to unwanted low energy efficiency. Figuring out a solution to these issues relies on the understanding of the underlying electrochemical mechanism during the charge/discharge processes. In order to in-depth understand the Li storage mechanism occurring in the initial cycle and during long-term cycling, the zinc-manganese(cobalt) oxides are selected as typical conversion/alloying anode materials. In this thesis, the synthesis of nanoscaled ternary transition metal oxides is based on green and facile co-precipitation or hydrothermal methods. The chemical and physical properties of the materials are comprehensively studied with the help of complementary techniques. Their electrochemical properties as anode materials for Li-ion batteries are evaluated, and the energy storage mechanisms are also discussed in terms of the initial cycle and long-term cycles.

In this thesis, Chapter 1 introduces the current status and developing trend of Li-ion batteries with special focus on anode materials. The employed characterization methods and their operating principle are introduced in Chapter 2. The result and discussion is divided in three main parts: Chapter 3, 4 and 5. Chapter 3 explores the energy storage mechanism of spinel ZnCo_2O_4 during the 1st cycle and how carbon cloth compositing can improve its electrochemical performance. In Chapter 4, the phase transformation during the 1st cycle of the more environmental friendly ZnMn_2O_4 is explored, and the benefits of carbon coating on cycling stability and rate performance in LIB anodes is discussed. In Chapter 5, the factors that affect cycling stability of zinc/manganese-contained oxide anodes are comprehensively studied; and moreover, an ester-based electrolyte (1 M LiPF_6 in cyanopropionic acid methyl ester / vinylene carbonate) is used and discovered to be useful to stabilize capacity variations. Finally, conclusions and outlooks are summarized in Chapter 6. The experimental part, synthesis and characterization of the samples, is presented in Chapter 7.

In sum, the study carried out in this thesis clearly demonstrates that ternary transition metal oxides are promising candidates for next generation anode materials of Li ion batteries. The phase evolution of the zinc-manganese(cobalt) oxides during the 1st cycle, the effect of carbon compositing on improving cycling stability, and the application of a promising ester-based electrolyte, in-depth elucidate the electrode working mechanism and degradation process, and help to optimize the conversion/alloy anode materials.

Zusammenfassung

Heutzutage führen wichtige Umwelt- und Energieaspekte wie übermäßiger Verbrauch fossiler Vorkommen, Ölkrisen und Luftverschmutzung zwangsläufig zu einer steigenden Nachfrage nach erneuerbaren Energiequellen und zur Entwicklung von Energiespeichersystemen. Es wird erwartet, dass Sekundärbatterien als Energieversorgung für Verbrauchselektronik und Elektrofahrzeuge hervorragende elektrochemische Eigenschaften wie eine hohe Energie-/ Leistungsdichte, eine lange Lebensdauer, niedrige Kosten und höchste Sicherheit aufweisen. Derzeit sind Li-Ionen-Batterien mit Graphitanode am erfolgreichsten. Graphitanoden leiden jedoch unter einer relativ geringen spezifischen Kapazität (theoretische Kapazität von 372 mAh g^{-1} und praktische Kapazität von $330\text{--}350 \text{ mAh g}^{-1}$). In Anbetracht dessen ist die Entwicklung neuartiger Anodenmaterialien mit hoher Kapazität dringend erforderlich. Aufgrund ihrer hohen gravimetrischen/ volumetrischen Kapazität und ihres reichlichen Vorkommens als Ressource, haben Übergangsmetalloxide vom Konversionstyp als Anodenmaterialien der nächsten Generation für Li-Ionen-Batterien viel Aufmerksamkeit auf sich gezogen.

Ideale Anodenmaterialien sollten eine hohe elektronische/ ionische Leitfähigkeit, eine hohe spezifische Kapazität, eine lange Zyklenstabilität, sowie ein niedriges und stabiles Arbeitspotential aufweisen. Jedoch unterliegen Übergangsmetalloxide, als eine der typischsten Konversionsmaterialien für Anoden, einer großen Volumenänderung und einer starken Pulverisierung der Elektroden während des Zyklusprozesses. Dies liegt an der massiven Li-Insertion / Extraktion und von sich wiederholten Phasenumwandlungen. Darüber hinaus unterdrückt die geringe elektronische Leitfähigkeit der Oxide die Kinetik elektrochemischer Reaktionen, was, durch die hohe Reaktivität der lithiierten Produkte (Li_2O und Metall) zu einer übermäßigen Zersetzung des Elektrolyten und zur Bildung einer dicken Solid Electrolyte Interphase führen kann. Darüber hinaus führt eine große Spannungshysterese der Anoden vom Konversionstyp zu einer unerwünscht niedrigen Energieeffizienz. Um eine Lösung für diese Probleme zu finden, muss der zugrunde liegende elektrochemische Mechanismus während der Lade-/ Entladevorgänge verstanden werden. Um die im Anfangszyklus und in den Langzeitzyklen auftretenden Li-Speichermechanismen besser verstehen zu können, werden die Zink-Mangan (Cobalt) -oxide als typische Konversions-/ Legierungsanodenmaterialien ausgewählt. In dieser Arbeit basiert die Synthese nanoskaliger ternärer Übergangsmetalloxide auf nachhaltigen und

einfachen Co-Präzipitations- oder hydrothermalen Methoden. Die chemischen und physikalischen Eigenschaften der Materialien werden mit Hilfe komplementärer Techniken umfassend untersucht. Ihre elektrochemischen Eigenschaften als Anodenmaterialien für Li-Ionen-Batterien werden bewertet, und die Energiespeichermechanismen auch im Hinblick auf den Anfangszyklus und die Langzeitzyklen diskutiert.

In dieser Arbeit wird in Kapitel 1 der aktuelle Status und der Entwicklungstrend von Li-Ionen-Batterien vorgestellt, wobei der Schwerpunkt auf Anodenmaterialien liegt. Die verwendeten Charakterisierungsmethoden und ihre Funktionsweise werden in Kapitel 2 vorgestellt. Das Ergebnis und die Diskussion gliedern sich in drei Hauptteile: Kapitel 3, 4 und 5. Kapitel 3 untersucht den Energiespeichermechanismus vom Spinell ZnCo_2O_4 während des 1. Zyklus und wie eine Kohlenstoffbeschichtung die elektrochemische Leistung verbessern kann. In Kapitel 4 wird die Phasenumwandlung während des 1. Zyklus des umweltfreundlicheren ZnMn_2O_4 untersucht und die Vorteile der Kohlenstoffbeschichtung für die Zyklenstabilität und den Ratentest in LIB-Anoden diskutiert. In Kapitel 5 werden die Faktoren, die die Zyklenstabilität von Zink/ Mangan-Oxid-Anoden beeinflussen, eingehend untersucht. Darüber hinaus wird ein Elektrolyt auf Esterbasis (1 M LiPF_6 ; in Cyanopropionsäuremethylester/ Vinylencarbonat) verwendet der sich als nützlich zur Stabilisierung von Kapazitätsschwankungen herausstellte. Abschließend werden Schlussfolgerungen und Ausblicke in Kapitel 6 zusammengefasst. Der experimentelle Teil, die Synthese und die Charakterisierung der Proben wird in Kapitel 7 vorgestellt.

Zusammenfassend zeigt die in dieser Arbeit durchgeführte Studie deutlich, dass ternäre Übergangsmetalloxide vielversprechende Kandidaten für Anodenmaterialien der nächsten Generation von Li-Ionen-Batterien sind. Die Phasenänderung der Zink-Mangan (Kobalt) -oxide während des 1. Zyklus, die Wirkung der Kohlenstoffzusammensetzung auf die Verbesserung der Zyklenstabilität, und die Anwendung eines vielversprechenden Elektrolyten auf Esterbasis, klären den Mechanismus der Lithiuminsertion/ -extraktion in den Elektroden und den Abbauprozess eingehend auf und helfen, die Konversions-/ Legierungsanodenmaterialien zu optimieren.

Die vorliegende Arbeit wurde im Zeitraum vom 1. August 2017 bis 15. October 2019 am Institut für Organische Chemie der Fakultät für Chemie und Biowissenschaften am Karlsruher Institut für Technologie (KIT) unter der Leitung von Prof. Dr. Helmut Ehrenberg angefertigt.

Hiermit versichere ich, die vorliegende Arbeit selbstständig verfasst und keine anderen als die angegebenen Quellen und Hilfsmittel verwendet sowie Zitate kenntlich gemacht zu haben. Die Dissertation wurde bisher an keiner anderen Hochschule oder Universität eingereicht.

.....

Ort, Datum

.....

Unterschrift

Contents

| | |
|---|-----|
| Acknowledgements | I |
| Abstract | III |
| Zusammenfassung | V |
| Contents | IX |
| 1 Introduction | 1 |
| 1.1 Background | 1 |
| 1.2 Li-ion batteries | 4 |
| 1.2.1 History and working principle..... | 4 |
| 1.2.2 Components of a LIB | 5 |
| 1.3 Anode materials for LIBs | 10 |
| 1.3.1 Li metal | 10 |
| 1.3.2 Intercalative materials | 11 |
| 1.3.3 Alloying materials | 14 |
| 1.3.4 Conversion materials..... | 15 |
| 1.3.5 Conversion/alloying materials..... | 17 |
| 1.4 Aims and overview of the work | 18 |
| 2 Experimental methods..... | 21 |
| 2.1 Scanning electron microscopy..... | 21 |
| 2.2 Transmission electron microscopy | 21 |
| 2.3 X-ray powder diffraction..... | 22 |
| 2.4 N ₂ adsorption-desorption..... | 24 |
| 2.5 Raman spectroscopy | 25 |
| 2.6 Fourier transform infrared spectroscopy | 26 |
| 2.7 Thermogravimetric analysis | 26 |

| | | |
|-------|--|----|
| 2.8 | Cyclic voltammetry | 27 |
| 2.9 | Galvanostatic cycling with potential limitation..... | 28 |
| 2.10 | Electrochemical impedance spectroscopy..... | 28 |
| 2.11 | Synchrotron light source | 29 |
| 2.12 | X-ray photoelectron spectroscopy..... | 31 |
| 2.13 | X-ray absorption spectroscopy..... | 31 |
| 2.14 | <i>In situ</i> SRD and XAS | 33 |
| 2.15 | High-temperature SRD..... | 33 |
| 3 | ZnCo ₂ O ₄ and ZnCo ₂ O ₄ carbon cloth composite in LIBs | 35 |
| 3.1 | Introduction | 35 |
| 3.2 | Results and discussion..... | 36 |
| 3.2.1 | Hydrothermal synthesis and characterization of the ZCO and ZCO/CC | 36 |
| 3.2.2 | Mechanism study of the ZCO anode during initial conversion process | 41 |
| 3.2.3 | Electrochemical performance of the ZCO and ZCO/CC | 48 |
| 3.3 | Conclusions | 52 |
| 4 | ZnMn ₂ O ₄ and carbon-coated ZnO-MnO in LiBs | 55 |
| 4.1 | Introduction | 55 |
| 4.2 | Results and discussion..... | 56 |
| 4.2.1 | Phase transition of ZnMn ₂ O ₄ during calcination and carbonization | 56 |
| 4.2.2 | Morphology and structure | 59 |
| 4.2.3 | <i>In situ/ex situ</i> characterizations during the 1 st cycle..... | 68 |
| 4.2.4 | Long-term cycling performance and rate capability | 75 |
| 4.3 | Conclusions | 83 |
| 5 | Cycling stability of the ZnMn ₂ O ₄ and ZnO-MnO anodes in LiBs..... | 85 |
| 5.1 | Introduction | 85 |

| | | |
|-------|--|-----|
| 5.2 | Results and discussion..... | 86 |
| 5.2.1 | <i>Ex situ</i> characterizations of the electrode evolution during cycling..... | 86 |
| 5.2.2 | Electrochemical tests of the bare ZnMn ₂ O ₄ with a CPAME electrolyte..... | 99 |
| 5.3 | Conclusions | 102 |
| 6 | Conclusions and outlook | 103 |
| 7 | Experimental part | 107 |
| 7.1 | Material synthesis..... | 107 |
| 7.1.1 | Hydrothermal preparation of the ZCO and ZCO/CC..... | 107 |
| 7.1.2 | Synthesis of ZnMn ₂ O ₄ nanoparticles | 108 |
| 7.1.3 | Carbon coating on ZnMn ₂ O ₄ nanoparticles | 108 |
| 7.2 | General characterizations | 108 |
| 7.2.1 | XRD | 108 |
| 7.2.2 | SEM and EDS | 109 |
| 7.2.3 | TGA/DSC..... | 109 |
| 7.2.4 | Raman..... | 109 |
| 7.2.5 | FTIR | 109 |
| 7.2.6 | XPS..... | 109 |
| 7.2.7 | TEM | 110 |
| 7.2.8 | N ₂ adsorption-desorption..... | 110 |
| 7.3 | Electrochemical tests..... | 110 |
| 7.3.1 | Working electrode preparation..... | 110 |
| 7.3.2 | Cell configurations | 111 |
| 7.3.3 | Electrochemical tests..... | 112 |
| 7.3.4 | Preparation of <i>ex situ</i> electrodes..... | 112 |
| 7.4 | Synchrotron characterizations | 113 |

| | | |
|-------|---|-----|
| 7.4.1 | Cell preparation | 113 |
| 7.4.2 | Electrochemical test | 113 |
| 7.4.3 | <i>In situ</i> SRD in ALBA | 113 |
| 7.4.4 | <i>In situ</i> SRD in DESY | 113 |
| 7.4.5 | <i>In situ</i> and <i>ex situ</i> XAS in DESY | 113 |
| 7.4.6 | HT-SRD in DESY | 114 |
| 8 | References | 115 |
| 9 | Curriculum Vitae | i |

1 Introduction

1.1 Background

As the development of science & technology and the improvement of living standard, global energy consumption keeps continuously increasing [1]. Nowadays, some serious environmental issues related to energy consumption, such as greenhouse effect, air pollution, and fossil energy exhaustion, have attracted global attentions. Thus, next-generation model of production-storage-consumption of green energy is crucial to a sustainable society. As a response to these concerns, green energy sources like sunlight, wind, tide, geothermal heat, biomass, and nuclear power have been exploited [2]. The construction of green energy supply is in progress to make up the deficiency of the conventional energy model. To take advantage of these sustainable energies, low-cost and high-efficiency energy storage systems are necessary in stationary renewable energy plants to smooth the difference between the intermittent green energy supply and fluctuating demand [3–5]. On the other hand, high energy/power densities and long lifespan are required for energy storage systems in energy consumption devices (portable electronic devices and electric vehicles) to satisfy the request of long using-time and fast charging [6]. Therefore, the demand of high performance and low cost energy storage systems is urgent due to the rapidly growing markets.

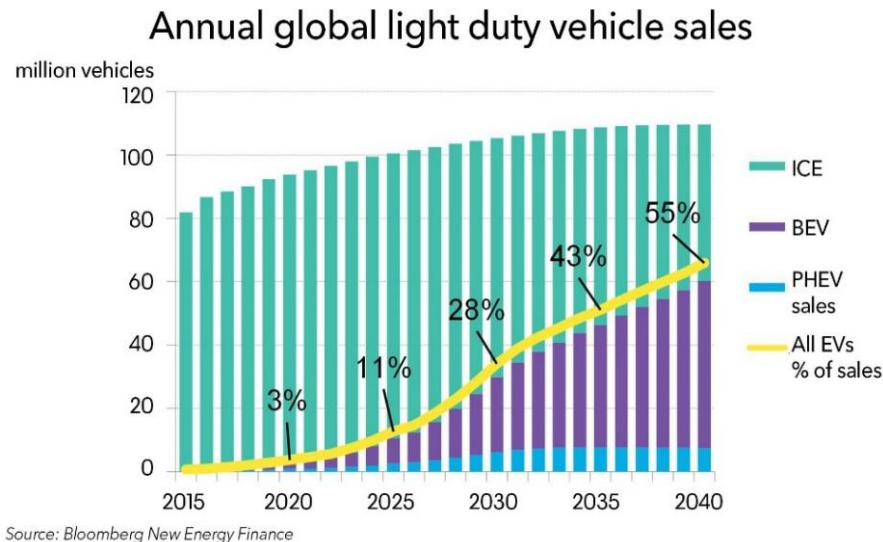


Figure 1.1 The predicted vehicle sales from 2015 to 2040. (Bloomberg New Energy Finance)

Taking electric vehicles (EVs) as an example, transportation electrifying has become a common view all over the world. Since 2010, the EVs have been developed and put into the commercial market, to replace conventional vehicles using internal combustion engines (ICEs). The global

sales of EVs grow rapidly these years with an annual growth rate of over 50 % (from 2010 to 2017) [7]. According to the forecast, EV sales will surpass ICE cars in 2040, owing to larger-scale manufacturing and continuously reduced battery cost (see Figure 1.1), where the BEV represents battery electric vehicle and PHEV is short for plug-in hybrid electric vehicle (combining batteries with a small ICE).

Rechargeable batteries are an important part of energy storage systems especially for movable devices. There are four key types of rechargeable batteries, including lead-acid, Ni-Cd, Ni-MH, and Li-ion batteries (LIBs). The earliest one, the lead-acid battery, which consists of Pb (anode), PbO₂ (cathode), and H₂SO₄ aqueous solution (electrolyte) can be dated back to 1859. The Ni-Cd battery was invented by Waldemar Jungner in 1899 and first manufactured in 1909. Usually, NiO(OH) (cathode), Cd (anode), and KOH alkaline solution (electrolyte) are used in a Ni-Cd battery. In 1989, the Ni-MH battery was firstly commercialized. It is very similar to the Ni-Cd battery, using hydrogen absorbing alloy as anode instead of Cd, which makes Ni-MH batteries more environmental friendly. Nowadays, LIBs, which have been commercialized since 1991, become the most commonly used rechargeable batteries, due to their high energy/power density, high operating voltage and long lifespan [6] (Figure 1.2).

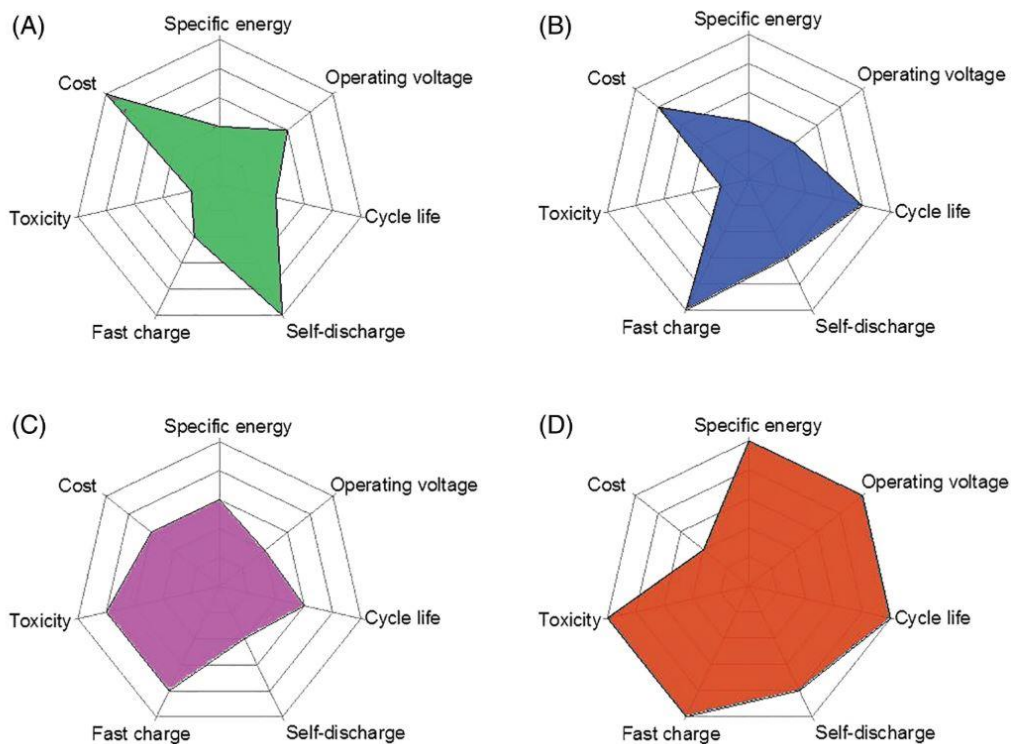


Figure 1.2 Performance comparison of (A), lead-acid, (B), Ni-Cd, (C), Ni-MH, and (D), LIBs. Adapted from Ref. [6].

In addition, electrochemical capacitors (ECs) are another important type of energy storage devices. They can be classified in two groups based on energy storage mechanism, including electric double-layer capacitors (EDLCs) that depend on electrostatic adsorption and pseudo-capacitors (PCs) that involve fast surface redox reactions. Due to the fast surface charge storage mechanism, ECs possess high power density and cycling stability, which can be an effective supplement to LIBs, especially when high power supply is requested [8]. Considering the relative low energy density of ECs, promising hybrid electrochemical capacitors (HECs) are put forward to bridge the gap between the LIBs and ECs (Figure 1.3) [9]. In a HEC, one electrode is battery-type electrode materials to provide a high energy density, and the other electrode is surface-controlled charge storage materials to offer a high power density.

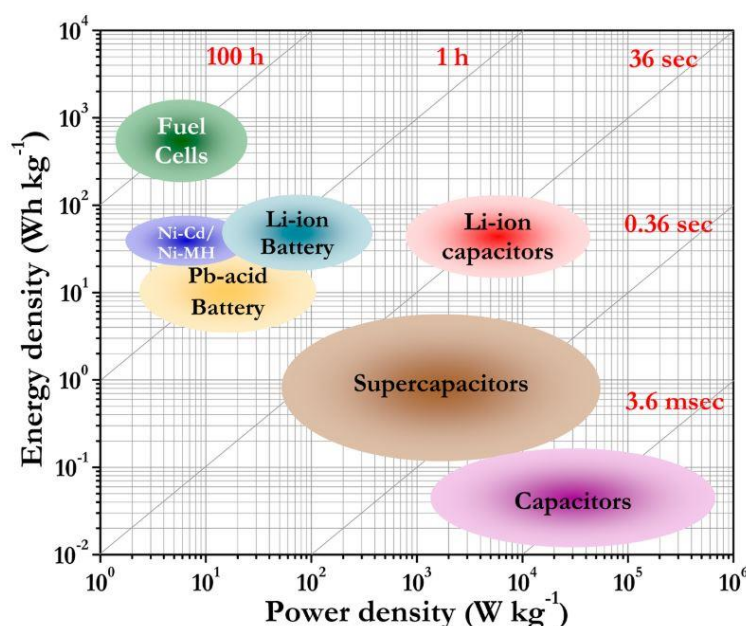


Figure 1.3 Ragone plot of different electrochemical energy storage devices. Adapted from Ref. [9], copyright 2014 American Chemical Society.

Moreover, based on an identical fundamental principle with LIBs, many other rechargeable batteries working with other transmitted ions also attract increasing attentions, including batteries with shuttle of Na^+ [10–12], K^+ [13–15], Zn^{2+} [16,17], Mg^{2+} [18,19], Ca^{2+} [20], Al^{3+} [21], F^- [22], and Cl^- [23,24]. Among them, sodium-ion batteries (SIBs) are the most promising candidates for grid-scale energy storage, given the abundant storage (2.64 wt.% on the earth) and most similar chemical properties of sodium comparing with lithium [25].

1.2 Li-ion batteries

1.2.1 History and working principle

Historically, Li metal batteries (LMBs) were firstly invented in early 1970s. However, safety issue due to lithium dendrite growth, which caused fire, was noticed on commercial lithium/MoS₂ batteries [26]. Therefore, the research had to be switched to LIBs without using lithium metal anode. A rocking-chair concept was introduced by Armand in late 1970s, putting forward to the batteries with lithium ions rocking between two intercalative electrodes [27]. In the next several decades, many efforts have been paid to find suitable electrode materials based on this concept and the rocking-chair LIBs are widely used in our daily life [28,29].

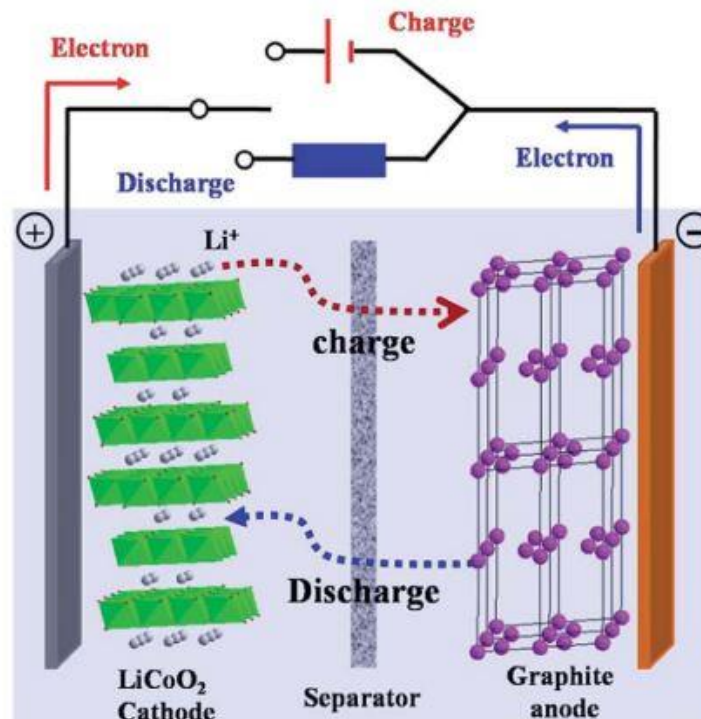


Figure 1.4 Schematic diagram of the working principle of a LIB. Adapted from Ref. [30], copyright of The Royal Society of Chemistry 2014.

In principle, a LIB consists of a positive electrode and a negative electrode which are separated by an electronic insulated separator and immersed in a Li⁺ conductive solution, permitting a closed circuit with an internal Li⁺ transmission and an external e⁻ transmission (Figure 1.4). During charging, Li⁺ ions move from the positive electrode to the negative electrode through electrolyte driven by an external power, supplying an electron flow with the same direction. Conversely, during discharging, Li⁺ ions spontaneously migrate back from the negative to the positive electrode

through the electrolyte, causing an electron flow with the same direction to power the external device. During discharging, the negative electrode is an anode where oxidation reaction occurs, and the positive electrode is a cathode where reduction reaction occurs. The spontaneous Li^+ migration is driven by the difference of the electromotive force (*i.e.* reduction potential of half-cell reaction) between the two half-cell reactions. Therefore, the reversible conversion between electric energy and chemical energy is realized when Li^+ ions shuttle between the two electrodes [31].

1.2.2 Components of a LIB

As discussed above, the core parts of a LIB, in principle, are the cathode, anode, electrolyte and separator. Practically, the electrodes are prepared by doctor-blade technique to coat a slurry on a current collector foil. The slurry contains not only active material for Li^+ insertion and extraction, but also inactive materials including binder and a conductive additive. These components are introduced in detail separately in the following paragraphs.

1.2.2.1 Cathode material

The cathode material is the electrochemical active material in the positive electrode, which is reduced during discharging and oxidized during charging, displaying relatively high reaction potentials. The cathode materials in LIBs have been intensively researched and rapidly developed, from the layered disulfide (TiS_2 , MoS_2 , ect.) used in LMBs to the layered oxide LiCoO_2 (LCO) used in the first commercialized LIBs [32–34]. Later on, layer-structured $\text{LiNi}_x\text{Mn}_y\text{Co}_{(1-x-y)}\text{O}_2$ (NMC) and $\text{LiNi}_x\text{Co}_y\text{Al}_{(1-x-y)}\text{O}_2$ (NCA), spinel-structured LiMn_2O_4 (LMO) and $\text{LiNi}_x\text{Mn}_{(2-x)}\text{O}_4$ (LNMO), and olivine-structured LiFePO_4 and LiMnPO_4 have been investigated [35]. As shown in Figure 1.5, nowadays, the NMC, NCA, LNMO are the most widely used cathode materials. In the next decade, the aim of LIB industry is to gain higher energy density, lower cost and more eco-friendliness [28,36].

1.2.2.2 Anode material

The anode material is the electrochemical active material in the negative electrode, which works as a Li reservoir, donating Li^+ ions and electrons during discharging. In principle, it should exhibit relative low reaction potentials to obtain a high full-cell voltage. Similar with cathode, anode

materials are also desired to possess high energy and power density, long cycling life, and low cost. After a short utilization time of Li metal anode in 1970s, carbonaceous materials were the most used anodes in LIB for several decades until now, including natural and artificial graphite, and disordered hard carbons. They display low reaction potential, long cycle life, low cost and moderate specific capacity (theoretically 372 mAh g^{-1} and practically $330\text{--}350 \text{ mAh g}^{-1}$) [29]. The layered oxide $\text{Li}_4\text{Ti}_5\text{O}_{12}$ (LTO) is also studied due to its superb cycling stability, but it has obvious disadvantages of high reaction potential ($\sim 1.55 \text{ V vs. Li}^+/\text{Li}$) and low specific capacity (theoretically 175 mAh g^{-1}) [37]. Recently, the low rate capability and moderate specific capacity of the carbon anodes cannot satisfy the increasing requirements of the rapid development of LIB industry. Therefore, next generation anode materials with high specific capacity are researched based on alloying or conversion mechanisms [38,39]. As shown in Figure 1.5, Si-graphite composite and Li metal could be the near and far future anodes for LIBs. Besides, conversion-type transition metal oxides (TMO) are also very promising given their high specific capacity, high abundance, and low cost [40,41].

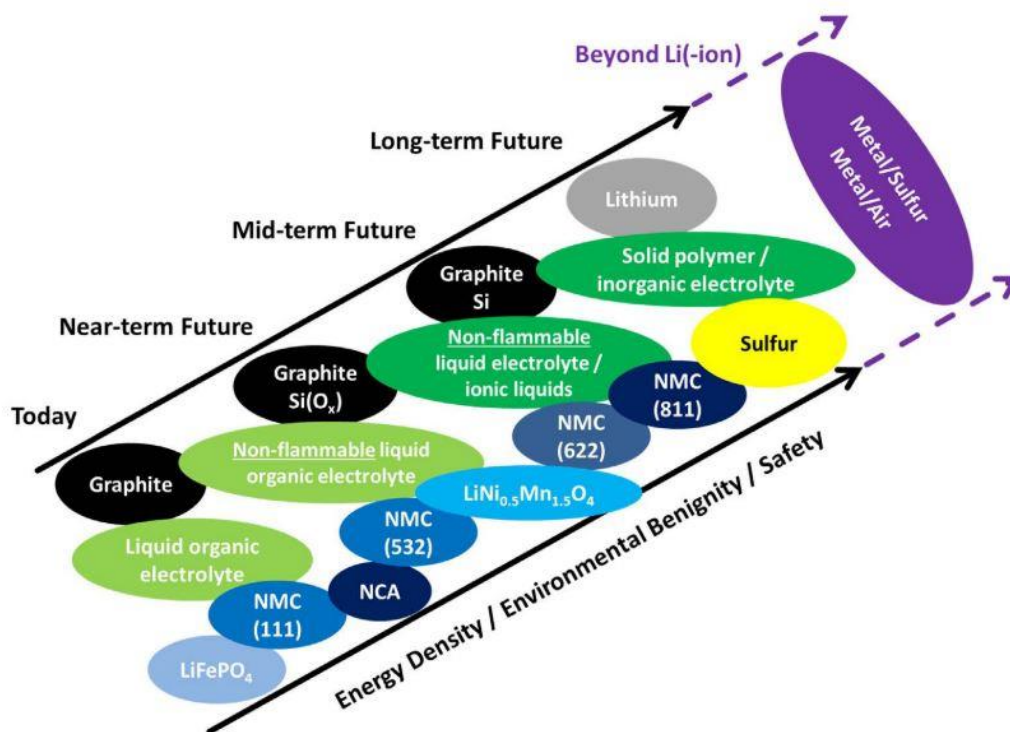


Figure 1.5 Progress and prospect of the cathode, anode, and electrolyte of LIBs. Adapted from Ref. [42], copyright Elsevier B.V.2018.

1.2.2.3 Electrolyte

Electrolyte works as an ionic charge carrier in a battery system. It should have properties of high ionic but low electronic conductivity, low viscosity, wide electrochemical window, wide working temperature range, proper passivation of the electrode surface, and high safety [43]. A normal liquid electrolyte for LIBs consists of a solvent and a Li salt. To state of the art, the solvents can be categorized in three types: ethers, esters, and alkyl carbonates [44]. Among them, the alkyl carbonates are the most intensively used due to their high polarity and solubility, such as ethylene carbonate (EC), dimethyl carbonate (DMC), diethyl carbonate (DEC) and ethyl-methyl carbonate (EMC). The EC with a relative high melting point is a necessary component to passivate the anode surface. Therefore, mixed solvents (alkyl carbonates and esters) are used, such as EC-DMC and EC-DEC-DMC, to obtain a wide working temperature range [45]. The possible Li salts involve LiPF_6 , LiClO_4 , LiBF_4 , $\text{LiN}(\text{SO}_2\text{CF}_2\text{CF}_3)_2$ (LiBETI), $\text{LiB}(\text{C}_2\text{O}_4)_2$ (LiBOB), $\text{LiPF}_3(\text{CF}_2\text{CF}_3)_3$ (LiFAP), and $\text{LiN}(\text{SO}_2\text{CF}_3)_2$ (LiTFSI) [44]. However, many of them have disadvantages, *e.g.* BF_4^- can interfere the anode surface passivation, the LiTFSI can corrode the Al current collector in the cathode, and the LiPF_6 can hydrolyze and decompose to LiF, PF_5 , HF and PF_3O , which are highly toxic and corrosive [46,47]. As a compromise, the electrolyte based on 1 M LiPF_6 dissolved in EC-DMC (1:1 in volume) is the most used in commercial batteries. In future, nonflammable liquid electrolytes and all solid state electrolytes with high safety properties will be developed.

1.2.2.4 Separator

The Separator is an electronic insulate and ionic conductive film used to prevent short circuit induced by direct contact of the cathode and anode. Commercially, a kind of microporous polymer membranes made of polyolefin materials are widely used, such as polyethylene (PE), polypropylene (PP) and their blends (PE-PP). They are extremely thin and the multilayered ones (*e.g.* bilayer PE-PP and trilayer PP-PE-PP) possess a thermal shutdown property, functionalized by PE melting (120~130 °C) to close the ionic pathways, while the PP (melting point of 165 °C) can still work to separate the two electrodes physically [48]. Another type of separator is a non-woven mat made by bonding fibrous materials, including celluloses, polyvinylidene fluoride (PVDF), poly(vinylidene fluoride-co-hexafluoropropylene) (PVDF-HFP) and etc. [49]. They are mostly characterized by high porosity (60~80 %) and low cost [50]. The third type is a ceramic composite

separator, which has excellent wettability and thermal stability (zero shrinkage). It is made of nanosized inorganic particles (*e.g.* Al₂O₃, SiO₂, MgO) bonded by a small amount of binder (*e.g.* PVDF, PVDF-HFP) [50]. Besides, a kind of glass fiber filter membranes (*e.g.* Whatman[®], borosilicate microfiber) are also intensively used as a separator in batteries, especially in Li-S and Li-air batteries due to its high porosity, superior wettability and thermal stability [51].

1.2.2.5 Binder

Except for the electrochemical active materials which are intensively researched, the inactive binder is also an important part in batteries, because it maintains the connection between the electrode materials and current collector and imparts mechanical flexibility. A good binder should not only have high adhesive strength, flexibility, but also high electrochemical stability to keep the integrity of the electrode during cycling and therefore ensuring a high cycling stability. The PVDF is the binder used in the first commercialized LIBs and still dominant in LIB industries. However, many other binders are also investigated and demonstrated better performance than PVDF. Some examples are sodium alginate (SA), carboxyl methyl cellulose (CMC), CMC-SBR (styrene butadiene rubber), poly(acrylic acid) (PAA), and bio-derived polymers, etc.. These binders show higher tensile strength and flexibility than PVDF, due to the hydrogen bonding triggered by their abundant hydroxyl and/or carboxylate groups. They can provide stronger interfacial forces than the weak van der Waals force of PVDF [52]. Moreover, PVDF is not so stable with the lithiated graphite, and the C–F bonds can decompose during charge/discharge [53]. On the other hand, PVDF is only soluble in organic solvents, where the toxic N-methyl-2-pyrrolidone (NMP) is usually used. On the contrary, the others are aqueous-soluble and more eco-friendly [54].

1.2.2.6 Conductive additive

Since some of the electrochemical active materials display intrinsic low electronic conductivity, conductive additive is often necessary to be added in the electrode formulation. The most common conductive additive is acetylene carbon black. Others, like conductive graphite, graphene and carbon nanotubes (CNTs) are also used occasionally [55].

1.2.2.7 Current collector

A current collector is needed for an electrode to enhance its mechanical strength and electronic conductivity. It should also be chemically and electrochemically stable with the electrode active material and the electrolyte at the working conditions. In LIBs, thin Al foils are the most suitable for positive electrodes [56], whereas Cu foil must be used for negative electrodes due to the alloy of Li and Al at low potentials. Moreover, some carbonaceous materials, like carbon cloth, carbon fiber and flexible graphite are used as current collectors for anodes, benefiting from their light weight and extra Li^+ storage capacity [57,58]. Also in anodes, some current collectors with three-dimensional porous structure (e.g. Ni-foam and porous Cu) are employed to increase the contact area of active materials with electrolyte [59,60].

1.2.2.8 Battery configurations

The LIBs are usually manufactured in four kinds of shapes, as shown in Figure 1.6, including cylindrical, coin, prismatic, and thin and flat cell configurations [6,61].

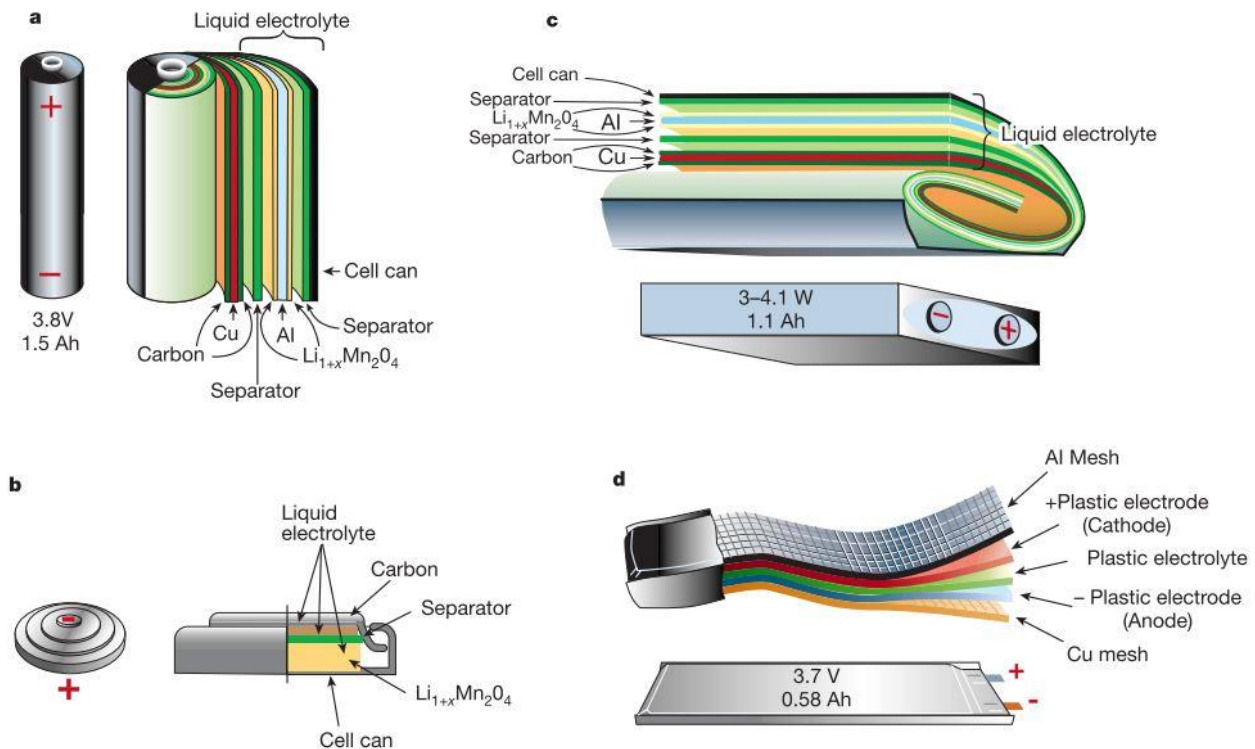


Figure 1.6 Schematic diagrams of various Li-ion battery configurations. Adapted from Ref. [61], copyright 2001 Macmillan Magazines Ltd.

1.3 Anode materials for LIBs

Anode materials for LIBs depending on the different mechanism, can be classified in four types, such as Li metal, intercalative materials, alloying materials, and conversion materials. Figure 1.7 schematically displays the working potentials and specific capacities of the recently used and next generation anode materials for LIBs. These materials are introduced separately in this section.

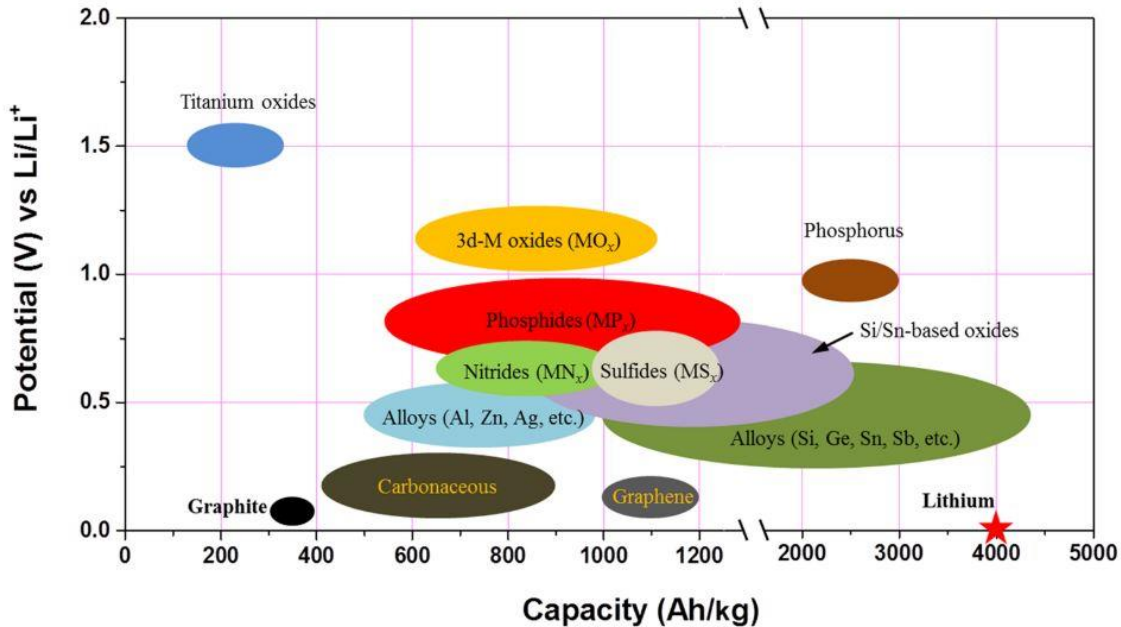


Figure 1.7 Working potential (vs. Li^+/Li) and specific capacity of active anode materials. Adapted from Ref. [62], copyright Shanghai University and Periodicals Agency of Shanghai University 2018.

1.3.1 Li metal

Li metal is the ideal anode material for LIBs, which exhibits the highest theoretical specific capacity (3860 mAh g^{-1}) and the lowest reduction potential (-3.04 V vs. standard hydrogen electrode (SHE)) among all possible material candidates. However, serious safety issues have been raised in early research of LMBs, impeding its further utilization. Lithium dendrites, growing on Li metal anode during cycling, can penetrate the separator to induce internal short-circuit, irreversibly consume active Li and electrolyte resulting in low Coulombic efficiency. Lithium dendrites lead to short cycling life due to electrode polarization and volume expansion. Nowadays, researchers look back to the Li metal anode to pursue high energy density by analyzing the factors that affect Li deposition and searching methods to suppress dendrite growth [63].

In general, except for the intrinsic thermodynamic property of Li with low surface energy and high diffusion energy, the dendrites formation can be attributed to high local current density and inhomogeneity of both electrode surface and current distribution [64]. Therefore, several strategies are proposed in aspects of electrolyte, electrode and separator, including: (1) controlling Li plating and diffusion: applying highly concentrated electrolyte ($> 3 \text{ M}$) [65], and adding electrolyte additives (alkali metal ions [66] or halide ions [67]); (2) introducing stable artificial SEI: adding electrolyte additives (*e.g.* vinylene carbonate, fluoroethylene carbonate [68]), electrode surface pretreatment via chemical, electrochemical, and physical methods [69]; (3) separator modification: reducing membrane pore size to uniform the current distribution and membrane reinforcement [70]; (4) using solid state electrolyte with high mechanical strength [71]; (5) electrode structural modification to increase active area and reduce the local current density: Li loading on ionic [72] or electronic [59] conductive 3D matrix, and mechanically altering the surface shape [73]; and (6) cell operation optimization, like fast discharging, slow charging, and intermittent charging [74]. However, the research on Li metal anodes is still on the way. It will be realized in commercial market in far future.

1.3.2 Intercalative materials

In general, intercalative anode materials are the materials with a layered structure, which can store Li^+ ions in the inter-layers, as shown in Figure 1.8. Carbonaceous materials and layered titanium oxides belong to this kind of materials.

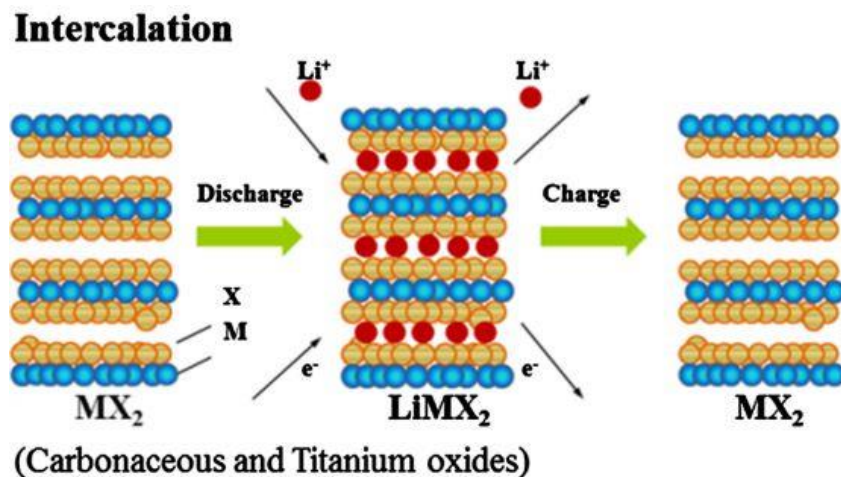


Figure 1.8 Schematic diagram of charge storage in intercalative anode materials. Adapted from Ref. [62], copyright Shanghai University and Periodicals Agency of Shanghai University 2018.

1.3.2.1 Carbonaceous materials

Carbonaceous materials for LIBs anodes are mainly based on graphite, disordered hard carbon, and hydrogen-containing carbon. The graphite is a crystal form of the carbon element with a hexagonal structure. Carbon atoms are covalent bonded through sp^2 hybridization inner a single layer, and the layers are bonded through weak van der Waals force. During lithiation, the Li^+ ions are accommodated between the carbon layers to form a graphite intercalation compound (GIC) with a stoichiometric formula of LiC_6 (theoretical capacity of 372 mAh g^{-1}) [75]. It is proved that the d_{002} spacing (distance between carbon layers) of the carbons plays an important role on the capacity [76]. The soft carbon with d_{002} spacing of $\sim 0.344 \text{ nm}$ exhibits the lowest capacity, whereas the more graphitized carbons (smaller d_{002} spacing) and more disordered hard carbons (larger d_{002} spacing $> 0.372 \text{ nm}$) deliver much higher capacities. Noticeable, hard carbons display higher capacities ($\sim 550 \text{ mAh g}^{-1}$) than the theoretical value of graphite [77]. It can be attributed to extra cluster-type Li storage in nanopores and on both sides of single carbon layers of disordered hard carbons (sloped potential profile), except for the formation of LiC_6 GIC (potential plateau at lower potential) [78]. Two stoichiometric formulas have been proposed, either Li_3C_6 (theoretically capacity of 1116 mAh g^{-1}) with all the center sites of the hexagonal carbon ring occupied [78], or Li_2C_6 (theoretically capacity of 744 mAh g^{-1}) with both sides of carbon layers storing Li^+ displaying two times capacity of graphite [79]. Moreover, a kind of hydrogen-containing carbon also exhibits high capacity due to additional Li atoms bonded by hydrogen atoms [80]. However, the hydrogen-containing carbons display large potential hysteresis, and the hard carbons deliver a large irreversible capacity at the first cycle and a sloped potential profile, which results in large amount of Li consuming and low output cell voltage. Therefore, graphite is until now the most widely used anode materials in industry due to its low cost, low and stable working potential ($0.05 \text{ V vs. } Li^+/Li$), no voltage hysteresis and high reversibility [29].

As anode materials, the so-called solid electrolyte interphase (SEI) layer is always formed during operation due to side reactions with electrolyte. The SEI layer can strongly influence the battery performance concerning the initial capacity loss, self-discharge, cycling life, rate capability and safety. To improve the performance of graphite anodes, much work have been done to analyze the SEI formation on graphite [81]. The graphite crystal has two kinds of surfaces, namely basal surfaces (parallel with the carbon layers) and edge surfaces (perpendicular to the carbon layers).

The electrolyte decomposition and SEI formation prefer to occur on edge surfaces due to the more reactive sites, while the Li^+ ions are intercalated along basal surfaces. Accordingly, a spherical carbon-coated natural graphite with covered edge surfaces and exposed basal surfaces was reported. This material displays much improved Coulombic efficiency [82]. Moreover, the surface chemistry can also influence the SEI formation and electrode resistance, and then the electrochemical performance [83,84].

In addition, graphene, the exfoliated single-layered graphite, is also very popular in utilization as LIB anode materials [85]. It exhibits excellent electronic conductivity, high surface area and good mechanical strength. Similar to the working mechanism of disordered hard carbons with Li storage in single carbon layers, graphene also exhibits high capacity. Experimentally, graphene performs high capacity of more than 1100 mAh g^{-1} at the low current density of 100 mA g^{-1} and $\sim 650 \text{ mAh g}^{-1}$ at 500 mA g^{-1} , displaying poor rate capability [86,87]. A strategy of heteroatom-doping (e.g. N, S, P, B) and hierarchical porous morphology design can improve the energy and power density, due to their benefits on mass transport, fast electrochemical reactions, and preventing graphene layers restacking [88]. However, since a high surface area induces more side reactions and SEI formation, the graphene anode materials always exhibit a high irreversible capacity loss.

1.3.2.2 Layered oxides

Spinel $\text{Li}_4\text{Ti}_5\text{O}_{12}$ is the only other anode material achieving success in LIBs market, due to its excellent safety characters [89]. During lithiation, 3Li^+ are intercalated in the spinel $\text{Li}_4\text{Ti}_5\text{O}_{12}$ transforming it to rock salt structured $\text{Li}_7\text{Ti}_5\text{O}_{12}$. This material exhibits a theoretical capacity of 175 mAh g^{-1} . The charging/discharging process is a two-phase reaction with little volume change, occurring at a stable potential of 1.55 V vs. Li^+/Li . $\text{Li}_4\text{Ti}_5\text{O}_{12}$ has the advantages to provide a long cycle life, to avoid Li dendrite formation (due to the high working potential), as well as to avoid excessive electrolyte decomposition and SEI formation.[90] All characteristics make it a very robust material. Considering the drawback of low electronic conductivity, several strategies have been applied, including hetero-metal-ions doping [91], carbon coating [37], and microstructure design [92]. Regarding the side reaction between the lithiated $\text{Li}_4\text{Ti}_5\text{O}_{12}$ and the organic solvent and its problem of gas generation, surface modification with AlF_3 coating has been proposed [93].

Besides, TiO_2 with a variety of phases, such as anatase, rutile, brookite and bronze, is also very promising, displaying a much higher theoretical capacity of 336 mAh g^{-1} (1 Li inserted in TiO_2) than $\text{Li}_4\text{Ti}_5\text{O}_{12}$ [94].

1.3.3 Alloying materials

As the growing demand of LIBs with high energy density, the well investigated intercalative anode materials are insufficient due to their relative low capacity. The alloying anode materials are potential to become the next generation anodes due to their extremely high capacity. The schematic diagram of the alloy/de-alloy process is shown in Figure 1.9. Considering the cost and toxicity, the most promising ones are Si, Sn, Sb, Al and Mg, and the electrochemical performance is shown in Table 1.1 [89,95]. Among them, Si is the most promising one with the highest theoretical capacity and moderate working potential (avoiding Li deposition), and it has been already tried in industry application in form of Si-C or $\text{SiO}_x\text{-C}$ composites (small Si or SiO_x amount of $< 5 \text{ wt\%}$) [36].

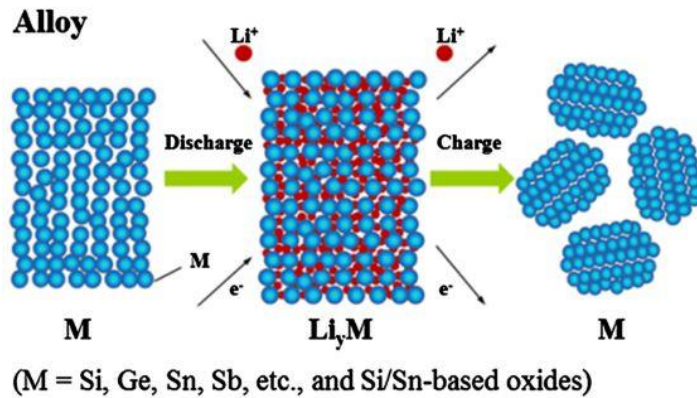


Figure 1.9 Schematic diagram of charge storage in alloying anode materials. Adapted from Ref. [62], copyright Shanghai University and Periodicals Agency of Shanghai University 2018.

Table 1.1 The theoretical specific capacity, charge density, volume change and working potential of several alloying anode materials. Adapted from Ref. [95], copyright 2010 Elsevier B.V.

| Materials | Si | Sn | Sb | Al | Mg |
|---|----------------------------|----------------------------|------------------------|---------------|------------------------|
| Density (g cm^{-3}) | 2.33 | 7.29 | 6.7 | 2.7 | 1.3 |
| Lithiated phase | $\text{Li}_{4.4}\text{Si}$ | $\text{Li}_{4.4}\text{Sn}$ | Li_3Sb | LiAl | Li_3Mg |
| Theoretical specific capacity (mAh g^{-1}) | 4200 | 994 | 660 | 993 | 3350 |
| Theoretical charge density (mAh cm^{-3}) | 9786 | 7246 | 4422 | 2681 | 4355 |
| Volume change (%) | 320 | 260 | 200 | 96 | 100 |
| Potential vs. Li^+/Li (V) | 0.4 | 0.6 | 0.9 | 0.3 | 0.1 |

However, the low initial coulombic efficiency and the fast capacity fading of alloying anodes, which are mainly attributed to the huge volume change and electrode material aggregation during alloy/de-alloy process, block their further application [90]. Thus, several strategies have been developed [95], including: (1) intermetallic, (2) decreasing particle size to nanoscale (< 100 nm) and design of hierarchical structure, (3) composite with conductive matrix, (4) controlling the working potential range, (5) optimizing electrolyte and binder. In detail, the first one, the design of intermetallic materials, consists in creating a Li host structure with a stable sublattice by adding an extra component, such as Cu_2Sb and Cu_6Sn_5 [96,97]. The extra component (*e.g.* Cu) can be substituted by Li during lithiation, resulting in a process without volume expansion. However, the intermetallic anode materials deliver relative low capacities. The second and third methods are the most effective ones and usually used simultaneously [38]. Nanoscaling allows the particles to accommodate large stress without cracking and to decrease the electronic and ionic transport distance [98]. Design of nanostructured composites (especially carbon materials) can suppress the SEI formation induced by the high surface area of nanostructures. Moreover, the conductive matrix can not only improve the conductivity, but also work as a buffer to alleviate the volume change and prevent the active particles from aggregation [99]. The fourth one consists on applying a narrower voltage range to reduce the extent of volume change and avoid particle aggregation [100]. At last, except for the electrode controlling, selection of electrolyte and binder can also influence the electrochemical performance. The electrolyte has direct relation with the SEI formation, the addition of electrolyte additive assisting formation of stable SEI can efficiently improve cycling stability [101]. As also mentioned above, binders like SA, CMC-SBR and PAA works much better than PVDF in electrodes with large volume change, due to their higher tensile strength and flexibility [52].

1.3.4 Conversion materials

Conversion materials are also considered to be the next generation anode materials for LIBs since their high theoretical capacities and abundant resources [41]. As shown in Figure 1.10, conversion anode materials are normally binary or ternary transition metal oxides / sulfides / nitrides / phosphides and even hydrides, which can reversibly react with Li^+ ions to form metallic nanoparticles embedded in amorphous Li containing compounds [62,102]. More than 1 Li^+ per

formula unit (pfu) delivered by this kind of compounds results in a 2~3 times higher specific capacity than the commercial graphite.

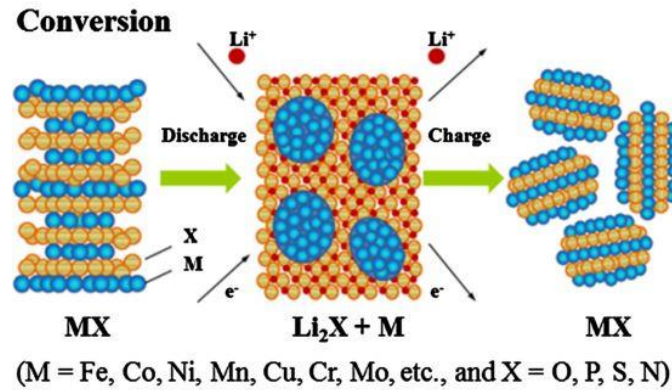


Figure 1.10 Schematic diagram of charge storage in conversion anode materials. Adapted from Ref. [62], copyright Shanghai University and Periodicals Agency of Shanghai University 2018.

Among many compounds based on conversion reactions for LIBs, the oxides are the most promising ones and have been intensively researched due to the easier preparation methods and more stable chemical properties [103]. However, it is still a long way for the conversion anode materials to be used commercially due to several unavoidable issues: high initial irreversible capacity, large volume change and bad cycling stability, as well as large voltage hysteresis. The first and the second ones are problems affecting also the alloying anodes. Similarly to the alloying anodes, also in conversion materials the strategies of nanotechnology and carbon compositing have been intensively used to improve the cycling stability and rate performance [38,40,104]. Moreover, facile and costless synthesis methods (*e.g.* co-precipitation) should be developed to replace the expensive and time consuming methods (*e.g.* multi-stepped hydrothermal method) for preparing well-defined nanostructured materials to make the large-scale fabrication possible [105,106].

The large voltage hysteresis of the conversion anode materials is mostly attributed to the conversion reaction, which is related to the surface energy and the diffusion kinetics of cations and anions, rather than the nanostructure fabrication [41]. The large interfacial area is always created during conversion reactions, which can result in considerable surface/interfacial energy and induce large over potential. On the other hand, there's obviously a correlation between the covalence and the voltage hysteresis. It is concluded that the conversion materials show decreasing voltage hysteresis in the order of fluorides > oxides > sulfides > nitrides > phosphides and hydrides [40].

In addition, transition metal doping is also a possible way to reduce the voltage hysteresis [107–111].

1.3.5 Conversion/alloying materials

Recently, a new class of anodes is gaining increasing attention: conversion/alloying materials. Compared to the anodes only based on conversion or alloying mechanism, lithium storage in this new type of electrodes relies on both the conversion and the alloying mechanisms, which can confer much higher theoretical capacities [112]. As discussed in section 1.3.3 **Alloying materials**, some specific metals like Ge, Sn or Zn can alloy Li. However, their application in LIBs is blocked by the huge volume change upon alloy/de-alloy with up to about 400 vol.% [113,114]. To alleviate the huge volume change, it was proposed to engineer the corresponding oxides or sulfides. After the conversion reaction, metallic nanograins can be generated and dispersed in the $\text{Li}_2\text{O}/\text{Li}_2\text{S}$ matrix, which buffers the volume change during further alloying process. As a representative conversion/alloying type material, the ZnTM_2O_4 (with $\text{TM} = \text{Fe}, \text{Co}, \text{Mn}$) compound exhibits a much promising perspective for LIB application [39]. Therefore, conversion-alloying materials are mainly discussed in this thesis.

Integrating alloying metal into conversion compound shows unique advantages over pure conversion materials, such as high specific capacities, low average operational voltages, and smaller discharge/charge voltage hysteresis. Thus, they can offer enhanced specific energy. Especially, zinc certainly has some advantages concerning its high availability, non-toxicity and relatively small volume variation upon alloy/de-alloy. Apparently, great progress has been achieved in the research field of ZnTM_2O_4 . However, it is still needed to optimize this kind of materials and further improve the energy density and cycling stability.

In general, the intrinsic issues needed to be addressed, such as low electronic conductivity, excessive formation of the SEI layer, large voltage hysteresis, and fast capacity fading, are similar to the conversion and alloying anode materials. The deep understanding of electrochemical storage mechanism and chemical/physical process is beneficial to figure out the solutions. In order to solve the problems, a variety of anode materials for LIBs are comprehensively discussed in this thesis, to offer effective methods and strategies for the eventual commercialization in the near future.

1.4 Aims and overview of the work

As stated above, massive efforts have been devoted to improve the conversion/alloying-type anode materials for LIBs. However, the mechanism study is still inefficient on the evolution of the electrode material during cycling, such as phase composition, metal oxidation state, morphology, and resistance. Elucidating the mechanisms is important for understanding the electrode degradation process and thereafter improving the materials to prolong the cycle life. Therefore, this thesis focuses on the mechanism study of the conversion/alloying-type compounds ZnTM_2O_4 (TM=Co, Mn). It aims to provide a deep understanding of the electrode material phase evolution during energy storage, and the influence of carbon compositing and electrolyte ingredient on cycling stability. Further attempts to find the optimal conversion/alloying-type materials and battery performance are performed in the thesis.

The work is divided into three parts. In the first part, the work mainly focuses on the ZnCo_2O_4 which is hierarchically composited with carbon cloth (ZCO/CC). The aim is to elucidate the Li storage mechanism in ZnCo_2O_4 , via *in situ* synchrotron radiation diffraction (SRD) and X-ray absorption spectroscopy (XAS) during the 1st cycle. The ZCO/CC was synthesized through a hydrothermal method with subsequent calcination. This study reveals the real potentials when the intermediate phases form and vanish during the initial conversion process. Afterwards, the hierarchical ZCO/CC composite was used as binder-free anodes for lithium storage, which displays improved cycling stability and rate capability comparing with the bare ZCO electrodes.

Considering the toxicity of the Co, the substitution of Co to Mn is necessary to develop more environmental friendly electrode materials. Therefore, the second part focuses on the Zn and Mn containing compounds (spinel ZnMn_2O_4 and ZnO-MnO composite). It aims to reveal the phase transformation of spinel ZnMn_2O_4 during the 1st lithiation and to study the influence of the carbon coating on the electrochemical performance. The tetragonal spinel ZnMn_2O_4 nanoparticles were prepared through a facile co-precipitation and calcination method. The carbon composited oxides, including carbon-derivative-coated ZnMn_2O_4 and carbon-coated ZnO-MnO composites, were synthesized by sintering the as-prepared ZnMn_2O_4 with glucose through a carbon-thermal reduction method at different temperatures. *In situ* SRD was conducted to clarify the phase transition of spinel ZnMn_2O_4 during the 1st cycle. Electrochemical performance of the as-prepared

samples were compared through cyclic voltammetry (CV), galvanostatic cycling with potential limitation (GCPL) long-term and rate tests.

Continue to the second part, based on the Zn and Mn containing compounds, the third part aims to elucidate the mechanisms behind the electrode degradation during cycling, and to improve the cycling stability. For this purpose, several *ex situ* techniques were employed. *Ex situ* X-ray photoelectron spectroscopy (XPS) was carried out to reveal the change in the metal oxidation state and the composition of the SEI during the 1st cycle. The kinetic properties of the electrode were investigated by electrochemical impedance spectroscopy (EIS) at varying potentials during the 1st cycle and during the lithiation process (0.4 V vs. Li⁺/Li) upon long-term cycling. *Ex situ* XAS (Mn K-edge and Zn K-edge) study was performed on cycled electrodes to investigate the evolution of the transition-metal oxidation state and local structure. *Ex situ* scanning transmission electron microscopy (STEM) and energy dispersive X-ray spectroscopy (EDS) were used to characterize the morphology evolution and phase segregation of the active particles. Moreover, an ester-based electrolyte (1 M LiPF₆ in cyanopropionic acid methyl ester (CPAME) / vinylene carbonate (VC, 2 wt.%) was studied in order to stabilize the capacity variations. In short, the present results clarify the nature of the additional reversible capacity, reveal the mechanisms behind electrode degradation during cycling, and help to improve the cycling stability of the conversion/alloying-type anode materials for LIBs.

2 Experimental methods

2.1 Scanning electron microscopy

Scanning electron microscopy (SEM) is a powerful technique to reveal information of sample external morphology and chemical composition, using a focused beam of high-energy electrons to scan specimen surface. As shown in [Figure 2.1](#), electrons are firstly generated from an electron gun of either thermionic emission mode (tungsten or LaB₆) or field emission mode (cold-cathode type (tungsten single crystal) or thermally assisted Schottky type (zirconium oxide)). Then, the electron beam is focused by two condenser lenses and adjusted by pairs of deflection coils to scan the sample surface with a raster fashion. When the electrons interact with the specimen surface atoms, different signals are produced, including secondary electrons, reflected or back-scattered electrons, characteristic X-rays and cathodoluminescence light. Normally, secondary electron imaging is used to produce high-resolution (< 1 nm) images of a sample surface, since that secondary electrons are emitted from very close to the specimen surface. On the other side, back-scattered electrons emerge from deeper positions of the specimen, resulting in a less resolution. Characteristic X-rays are emitted when an inner shell electron is excited by the electron beam, causing an outer-shell electron to fill the residual hole and release X-rays with specific energy (the energy difference between the outer shell and the inner shell) [\[115\]](#). The energy of these characteristic X-rays can be measured by Energy-dispersive X-ray spectroscopy to identify the abundance of elements in the specimen and map their distribution. For common imaging in SEM, specimens must be electrically conductive to prevent accumulation of electrostatic charge, avoiding scanning faults and other image artifacts. Non-conductive materials are usually coated with an ultrathin layer of gold or graphite by sputter coating.

2.2 Transmission electron microscopy

Transmission electron microscopy (TEM) is another powerful tool for specimen imaging. The electron beam is generated by either thermionic emission or field emission, and then accelerated by a high voltage. The specimen is required to be less than 100 nm thick. The obtained images are with a significantly higher resolution (0.1 nm) than light microscopes due to the much smaller de Broglie wavelength of electrons. The images contain information of not only the amplitude of beam, but also the phase of the electrons. As shown in [Figure 2.2](#), there are two basic operation

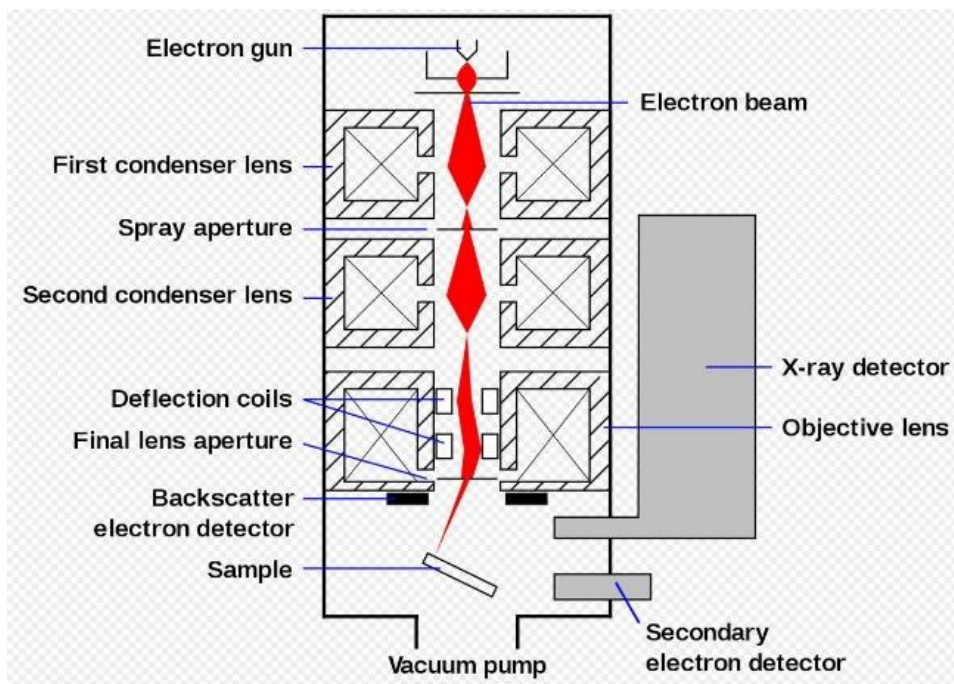


Figure 2.1 Schematic diagram of SEM. Open access under Wikipedia, https://en.wikipedia.org/wiki/Scanning_electron_microscope.

modes of TEM - imaging and diffraction modes. In imaging mode, Objective aperture is inserted in a back focal plane of Objective lens, therefore the bright field image is obtained if the central beam is selected and the dark field image is received if the diffracted beam is selected. In diffraction mode, Selected area aperture is used to determine the observed specimen area, and the Diffraction pattern is obtained by changing the strength of Intermediate lens. Diffraction is a very powerful tool for doing crystal orientation determination. Moreover, electron energy loss spectroscopy (EELS) can be used to identify elemental composition by selecting electrons with particular velocities, which are associated with the way how the electrons interact with the sample.

2.3 X-ray powder diffraction

X-ray powder diffraction (XRD) is a nondestructive analytical method for determining the atomic and molecular structure of crystal materials. Crystals are considered as regular arrays of atoms, which scatter X-ray (electromagnetic waves) primarily through the atoms' electrons. The scattering produces a regular array of secondary spherical waves, which can add constructively in a few specific directions through interference. These specific directions are determined according to Bragg's Law: $2d \sin \theta = n\lambda$ (see [Figure 2.3](#)), where d is the spacing between diffracting planes,

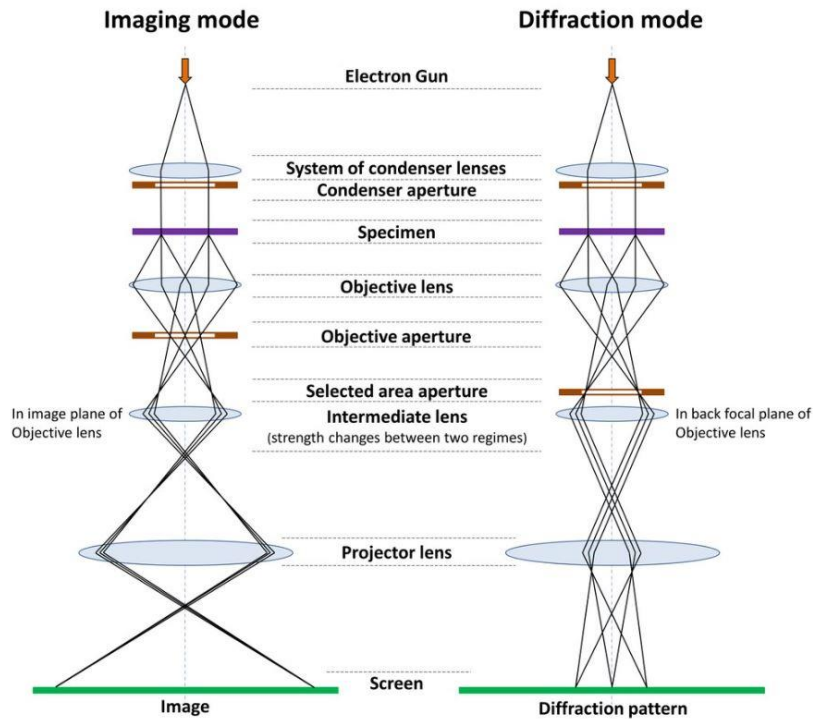


Figure 2.2 Schematic diagram of TEM. Open access under Wikipedia,
https://en.wikipedia.org/wiki/Transmission_electron_microscopy.

θ is the diffraction angle, n is any integer, and λ is the wavelength of the X-ray. Unlike anisotropic single crystals, a powdered sample can be considered as an isotropic case, where every possible crystalline orientation is represented equally. Therefore, each plane will be represented in the signal, and crystallographic information of a powdered crystal material can be revealed by measuring the angles and intensities of the diffracted beams. An X-ray diffractometer can be operated in transmission, reflection and Debye-Scherrer modes. The sample is loaded in a small disc-like container or a glass capillary and put on one axis of the diffractometer while a detector rotates around it on an arm forming a 2θ angle with the X-ray tube.

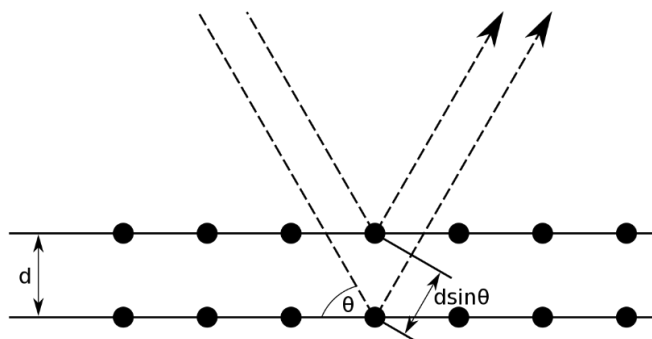


Figure 2.3 Schematic diagram of Bragg's law.

2.4 N₂ adsorption-desorption

Gas adsorption-desorption measurement is an effective method to characterize porous materials, revealing their specific surface area (SSA) and pore size distribution (PSD). The gaseous adsorbates can be N₂, Ar, CO₂, H₂O, which are not reactive with the adsorbents. In the most common case, measurement is conducted with N₂ adsorption-desorption at the boiling point of N₂ (77 K). In the measurement, a BET SSA can be calculated based on the adsorption data in the relative pressure (P/P_0) range of 0.05~0.35 according to the BET (Brunauer-Emmett-Teller) theory of gas adsorption in multimolecular layers [116], where the P and P_0 are the equilibrium and saturation pressure, respectively.

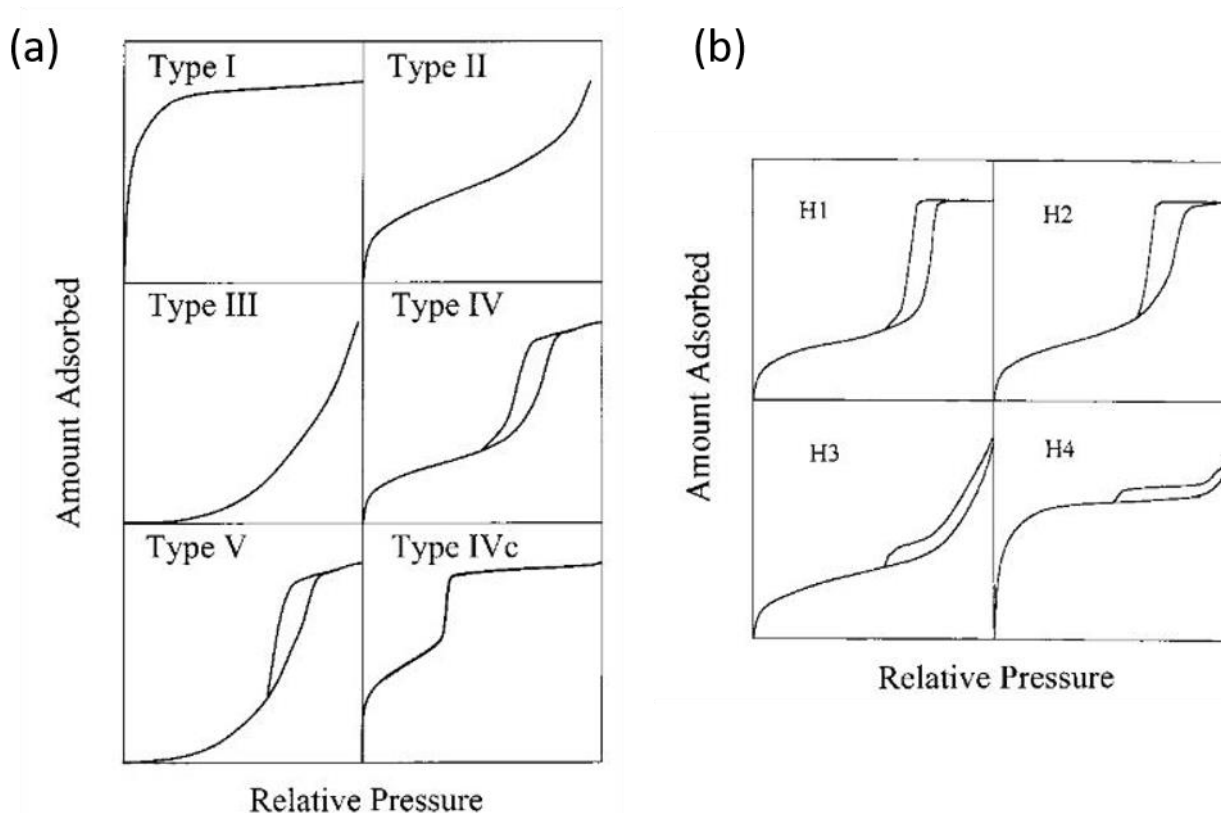


Figure 2.4 Classification of adsorption-desorption isotherms (a) and hysteresis loops (b). Adapted from Ref. [117], copyright 2001 American Chemical Society.

Moreover, an adsorption-desorption isotherm is obtained in a wide P/P_0 range of 0~1, whose shape can give information of the pores (*i.e.* size and shape) [117]. As shown in Figure 2.4a, the adsorption-desorption isotherms can be classified in five types. Type I isotherms display a main adsorption at low P/P_0 range (< 0.1), indicating a monolayer adsorption in micropores (< 2 nm) or

mesopores (2~50 nm) with size near the micropore range. In Type II and Type III, the adsorbed amount increases along with the relative pressure and displays no adsorption-desorption hysteresis. It is attributed to unrestricted multilayer formation in macropores (> 50 nm). The difference between Type II and Type III in low P/P_0 range is due to the different solid surface properties, where N_2 adsorption isotherms of surfactant-containing materials can be similar to Type II with a pronounced stage of the monolayer adsorption, and water adsorption isotherms of hydrophobic materials can be similar to Type III with no obvious monolayer formation process. Adsorption-desorption hysteresis loops are observed in Type IV and V isotherms, which correspond to capillary condensation-evaporation in mesopores occurring at different relative pressures. The hysteresis loops can be sorted into four categories by shape, relating to different pore shapes (Figure 2.4b). The Type H1 exhibits parallel and nearly vertical branches, corresponding to materials uniformly compacted with near spherical particles or uniform cylindrical pores. The Type H2 displays a triangular shape and a steep desorption branch, indicating a uniform channel-like pores or cage-like pores. The Type H3, displaying a hysteresis loop which is not level off near the saturation vapor pressure, represents slit-like pores compacted by plate-like particles. The Type H4 shows parallel and horizontal branches, indicating a network of large mesopores surrounded by smaller pores, or possibly collapse of the structure of compacted plate-like particles. Additionally, materials with accessible mesopores can display particular Type IV isotherms without hysteresis (Type IVc). In many cases, materials can possess different types of pores, resulting in isotherms as a combination of the mentioned types. Furthermore, many methods are developed to calculate the PSD of the materials, such as BJH (Barrett, Joyner and Halenda), NLDFT (nonlocal density functional theory) methods [118].

2.5 Raman spectroscopy

Raman spectroscopy is a technique used to observe vibrational, rotational, and other low-frequency modes in a system, providing a structural fingerprint for molecular identification. In the Raman test, a monochromatic light (visible, near-infrared or near-ultraviolet) interacts with molecular vibrations or phonons in the system, resulting in energy decreasing (Stokes Raman scattering) and increasing (Anti-Stokes Raman scattering) of the laser photons which can be finally detected. The Raman effect mainly depends on the electric dipole-electric dipole polarizability derivative of a bond. Therefore, the neutral bonds (*e.g.* C–C, C–H, C=C) display strong Raman

signals due to their large changes in polarizability during a vibration, while the polar bonds (*e.g.* C–O, N–O, O–H) display weak Raman signals since the small effect on polarization from a vibration.

2.6 Fourier transform infrared spectroscopy

Fourier transform infrared spectroscopy (FTIR) is a useful analysis technique for chemical identification and study through detecting absorption or emission of an infrared spectrum by the specimen. In an FTIR spectrometer, a broadband light source (contains all wavelengths to be measured) are modulated by a Michelson interferometer to obtain different wavelengths of light at different rates. Then, either a straightforward way of measuring each wavelength time by time, or a less intuitive way of Fourier-transform method (measuring many frequencies at one time) can be used to obtain an absorption spectrum. At last, a Fourier transform is needed to convert the raw data obtained from Fourier-transform method into the actual spectrum.

In the infrared portion, the mid-infrared region ($4000\sim 400\text{ cm}^{-1}$, $2.5\sim 25\text{ }\mu\text{m}$) is intensively used to study the vibrations and rotations of the structure. IR absorption mainly depends on the electric dipole moment derivative. Therefore, the polar bonds (*e.g.* C–O, N–O, O–H) are more IR active than the neutral bonds (*e.g.* C–C, C–H, C=C) due to their larger net dipole moment change during a vibration. The Raman and IR are complementary, giving a same frequency for a given vibrational transition, but different relative intensities due to the different types of interaction between the molecule and the incoming photons.

2.7 Thermogravimetric analysis

Thermogravimetric analysis (TGA) is a thermal analysis by measuring the mass change as a function of heating temperature or heating time. It can provide information about phase transition, absorption and desorption, thermal decomposition and solid-gas reactions. In a thermogravimetric analyzer, the most important part is a thermobalance, which consists of a precision balance, a furnace, a temperature control system, and a recording system. Moreover, the TGA can be conducted under a variety of atmospheres including: ambient air, vacuum, inert gas, oxidizing/reducing gases, etc.; as well as different pressures including: a high vacuum, high pressure, constant pressure, or a controlled pressure.

2.8 Cyclic voltammetry

Cyclic voltammetry (CV) is a potentiodynamic electrochemical method to investigate the electrochemical redox potentials and reaction rates of electrolytes and electrode materials. In CV measurement, the working electrode potential is ramped linearly versus time to reach a set potential, and then ramped reversely to return to another set potential. The cycle of ramps between the two set potentials can be repeated. The rate of potential change over time is named scan rate (V s^{-1}). At the same time, the current (between the working and counter electrode) is recorded and plotted versus the potential (between the working and reference electrode). As shown in Figure 2.5, the negative current curve recorded when the potential decreases corresponds to a cathodic process (reduction reaction), while the positive current curve recorded when the potential increases is attributed to an anodic process (oxidation reaction). A more similar oxidation peak compared with the reduction peak (potential and shape) implies a more reversible redox couple.

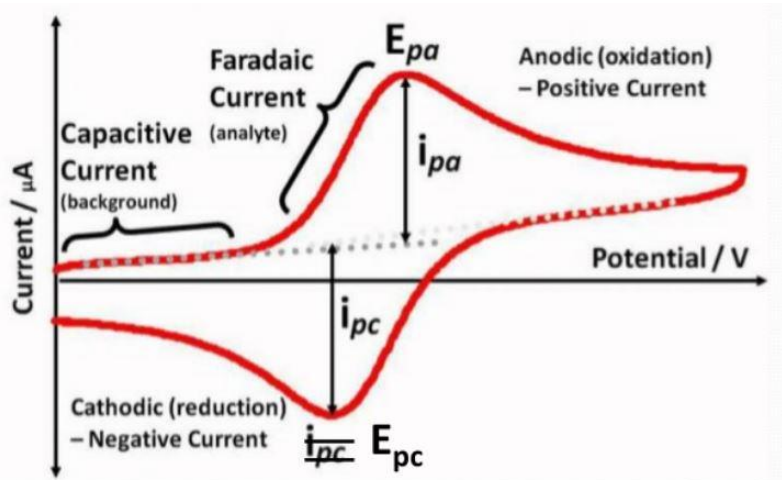


Figure 2.5 Schematic diagram of a CV curve. Open access under:

<http://urrjaa.blogspot.com/2013/08/cyclic-voltammetry-urrjaa-p0110-2013.html>.

According to the Randles-Sevcik equation (Equation 2.1), the peak current i_p in a CV curve depends not only on the diffusion of species to the electrode surface but also on scan rate [119]. A faster potential sweep causes a larger concentration gradient near the electrode, resulting in a higher current.

$$i_p = 0.4463 nFAC \left(\frac{nFvD}{RT} \right)^{\frac{1}{2}} \quad (\text{Equation 2.1}),$$

where i_p is the maximum current (A), n is the number of electrons transferred in the redox event, F is the Faraday Constant (C mol^{-1}), A is the electrode area (cm^2), C is the concentration of charge

carriers (mol cm^{-3}), ν is the scan rate (V s^{-1}), D is the diffusion coefficient ($\text{cm}^2 \text{s}^{-1}$), R is the Gas constant ($\text{J K}^{-1} \text{mol}^{-1}$), and T is the temperature (K). Therefore, the diffusion coefficient (D) can be calculated by recording peak currents at different scan rates.

2.9 Galvanostatic cycling with potential limitation

The batteries are normally charged/discharged with a constant current or a constant voltage. In laboratory, the constant current mode is often used to test the energy storage behavior of an electrode material, named galvanostatic cycling with potential limitation (GCPL). In detail, a constant current density (A g^{-1} or A cm^{-2}) is applied between the working and the counter electrode, and the generating potential is monitored and recorded between the working and the reference electrode. When the potential reaches the upper or lower limitations, the current direction is changed. In addition, GCPL test is also conducted with different current densities to evaluate the rate performance of electrode materials.

2.10 Electrochemical impedance spectroscopy

Electrochemical impedance spectroscopy (EIS) is an important technique to investigate an electrochemical system to reveal the frequency-dependent processes occurring in it without making measurements inside the system. Especially for batteries, EIS can be used to evaluate the internal resistance, as well as the state of charge and the state of aging. EIS is usually measured by applying a modulated sinusoidal AC potential excitation over a wide range of frequencies (*i.e.*, $10^6 \sim 10^{-2}$ Hz) to an electrochemical cell with a static potential and then measuring the response current and its phase. To keep the linearity of the system (a response with the same frequency but shifted phase), the excitation signal is normally very small (less than 10 mV in amplitude). As shown in [Figure 2.6](#), the EIS data are normally expressed in Bode plots (log frequency *vs.* the absolute value of the impedance and the phase shift) and Nyquist plots (real part impedance *vs.* imaginary part impedance). Since mainly capacitances occur, the negative imaginary axis in Nyquist plots is normally used. In the plots, if curves are known for certain states in a system, a qualitative graphical analysis of the plots is possible. Furthermore, equivalent electrical circuits depicting the presumed chemical and physical processes in the system can be designed and used for fitting the EIS plots. A variety of circuit elements are applied, including resistors (solution resistance, charge transfer resistance), capacitors (electrochemical double layer capacitance), constant phase elements (CPEs,

representing non-ideal capacitors due to surface roughness and non-uniform current distribution, etc.), Warburg elements (diffusion phenomena) and virtual inductors (probably due to the formation of a passive surface layer or errors in the measurement like potentiostat non-idealities).

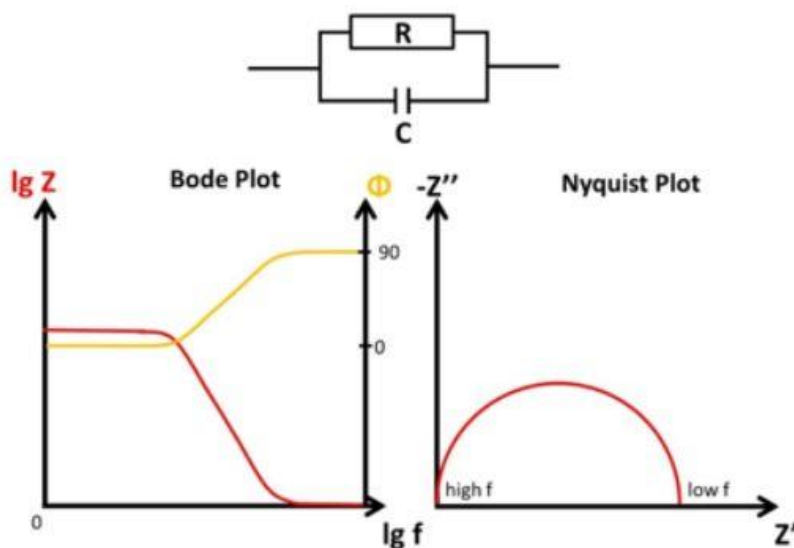


Figure 2.6 Examples of EIS Bode and Nyquist plots. Open access under:

<https://www.palmsenscorrosion.com/knowledgebase/bode-and-nyquist-plot/>.

2.11 Synchrotron light source

A synchrotron light source is a source of electromagnetic radiation generated by accelerating high-energy particles by a magnetic field (forcing the particles to travel in a curved path). It is an ideal tool for many types of research in materials science, physics and chemistry. The word “synchrotron” is evolved from “cyclotron”, the first cyclic particle accelerator. Different from a cyclotron using both a constant guiding magnetic field and a constant-frequency electromagnetic field, a synchrotron works by variation of the magnetic field strength in time, to adapt the increasing relativistic mass of particles during acceleration and constrain the circulation path to be constant. Hence, a large thin torus, instead of a disk, vacuum chamber for the particles can be used, potentiating a more efficient use of magnetic fields. As shown in [Figure 2.7](#), a synchrotron light source usually contains a linear accelerator, a booster ring and a storage ring. The particles (electrons, positrons or protons) are successively accelerated to their final energy (in GeV range) by the linear accelerator and the booster ring, and then injected into the storage ring by injection

kicker magnets. The storage ring is a type of synchrotron with constant particle kinetic energy for photon generation. A key benefit of this design of pre-acceleration and injection is that the storage ring can accumulate a high beam flux from an injection accelerator with a much lower flux. The storage ring is separated into components with specialized functions, displaying a round-cornered polygon shape. The bending magnets are located at the round sections. The straight sections are equipped with radio frequency cavities (compensating energy loss of particles after synchrotron radiation), and insertion devices (wigglers and undulators) for photon generation. Wigglers or undulators consist of a series of dipole magnets in a periodic array which can provide a sinusoidal magnetic field enhancing the beam intensity. Undulators can produce intense spectrum concentrated in narrow energy bands.

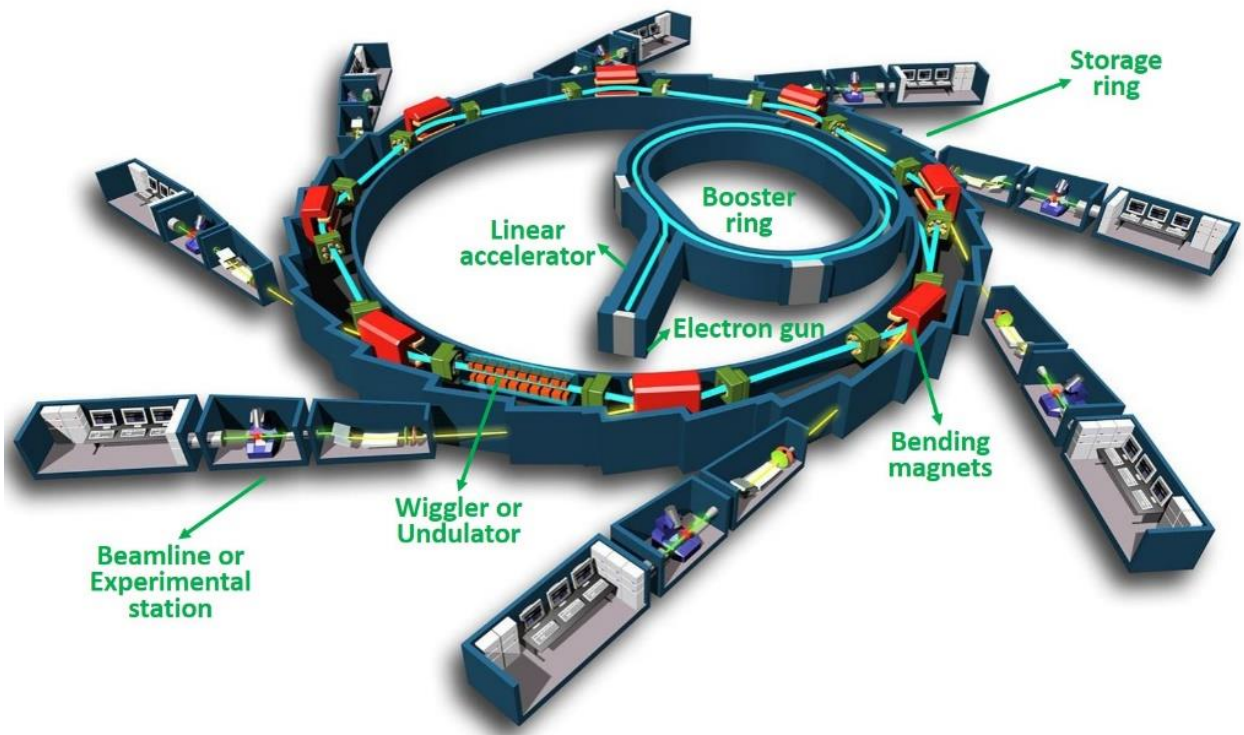


Figure 2.7 Schematic diagram of a synchrotron light source. Open access under:

<https://simple.wikipedia.org/wiki/Synchrotron>.

The synchrotron radiation has the following properties: (1) Continuum radiation which covers a wide frequency range, from microwaves to hard X-rays; (2) High intensity which allows rapid experiments or measurements for weakly scattering crystals; (3) Highly collimated photon beam with a small angular divergence; (4) High level of polarization (linear, elliptical or circular); (5) Pulsed light emission with pulse durations from one nanosecond down to tens of picoseconds which

allows the high resolution on time scale. Due to these superiorities, the synchrotron radiation is mainly used in three kinds of experiments: (1) Diffraction and scattering: *in situ* synchrotron X-ray diffraction (SRD), small angle X-ray scattering (SAXS), and X-ray pair distribution function (PDF) analysis, etc.; (2) Spectroscopy: X-ray absorption spectroscopy (XAS), soft X-ray photoelectron spectroscopy (SXPS), hard X-ray photoelectron spectroscopy (HAXPES), and X-ray fluorescence (XRF), etc.; and (3) Imaging: phase-contrast X-ray imaging and scanning transmission X-ray microscopy (STXM), etc..

2.12 X-ray photoelectron spectroscopy

X-ray photoelectron spectroscopy (XPS) is a surface-sensitive quantitative technique, that can be used to analyze the elemental composition of a sample surface (0~10 nm in depth), revealing empirical formula, chemical state and electronic state of the concerning elements (except H and He). In XPS measurement, when a specimen is irradiated with a beam of X-ray with a constant frequency, photoelectrons are excited from inner shells of atoms. After simultaneously measuring the kinetic energy and number of the escaped electrons, the binding energy of the elements can be obtained based on the work of Ernest Rutherford: $E_{\text{binding}} = E_{\text{photon}} - (E_{\text{kinetic}} + \varphi)$, where E_{binding} is the binding energy (BE) of the electron, E_{photon} is the energy of the incident X-ray photon, E_{kinetic} is the kinetic energy of the electron as measured and φ is the work function. The X-ray source of a XPS system can be monochromatic Al K_{α} (1486.6 eV) or Mg K_{α} (1253.6 eV) X-rays, or a synchrotron light source with soft (100~2100 eV) or hard (2.1~20 keV) X-rays. Considering that higher photon energy probing deeper in a specimen, information in different depths of a specimen can be obtained when applying different photon energies. Moreover, XPS can also be measured through line profiling, mapping, and depth profiling to test the uniformity of elemental composition. Ion beam or cluster etching is used to expose deeper layers of the sample in depth profiling.

2.13 X-ray absorption spectroscopy

X-ray absorption spectroscopy (XAS) is a powerful technique for determining the local geometric structure and oxidation state of concerned elements in a specimen. XAS is a type of absorption spectroscopy, which can be obtained by tuning photon energy in range where the inner

electrons of the target element can be excited (0.1~100 keV). Therefore, synchrotron radiation is normally used as light source due to its wide frequency range and high intensity.

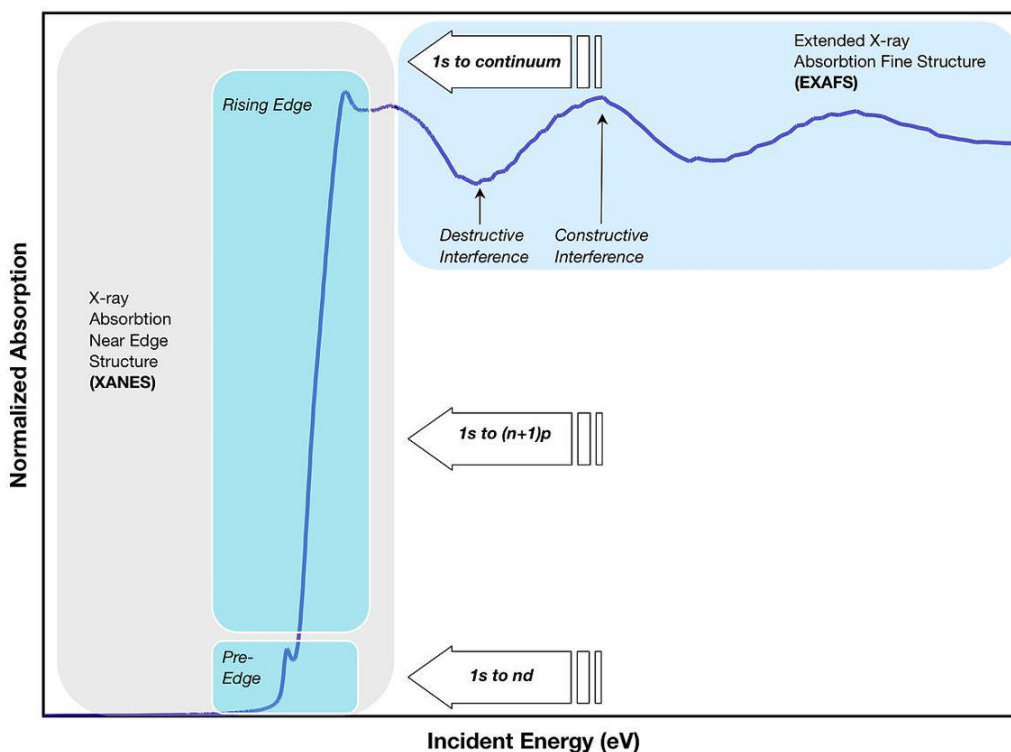


Figure 2.8 An example of XAS spectrum which can be divided in XANES and EXAFS. Open access under: https://en.wikipedia.org/wiki/X-ray_absorption_spectroscopy.

As shown in [Figure 2.8](#), a XAS spectrum can be interpreted in three main regions. (1) The absorption threshold in pre-edge region is determined by the transition of electrons to the lowest unoccupied states. It displays an arc tangent shape for metals given the transition to the Fermi energy states, while a Lorentzian line-shape for insulators that occur at energies lower than the transitions to the lowest unoccupied states due to the bound core excitons. (2) The X-ray absorption near-edge structure (XANES) region, displaying a Fano line-shape, represents mainly the core transitions of electrons to quasi bound states with kinetic energy in the range of 10~150 eV above the chemical potential. In this region, photoelectrons are multiple scattered in strongly correlated systems. (3) The extended X-ray absorption fine structure (EXAFS) locates in the high photon energy region, where photoelectrons with high kinetic energy are excited and weakly scattered by neighbor atoms which can be approximated by single scattering events. A IFEFFIT method has been used for interpretation of EXAFS spectra [120].

2.14 *In situ* SRD and XAS

For electrode materials, it is important to analyze the evolution of their chemical properties (crystal structure and oxidation state) during electrochemical charge and discharge processes. Hence, *in situ* measurements, such as *in situ* SRD and *in situ* XAS are introduced based on synchrotron radiation, due to its high intensity and short acquisition time. In the measurements, electrochemical coin cells with a small window are assembled and fixed on a 8-fold plate which can repeatedly rotate forth and back to locate the target cell under the beam successively [121]. On the other hand, the plate is connected with a potentialstat to perform a galvanostatic charge/discharge (GCPL) process, and the SRD or XAS measurements are conducted simultaneously. The overview of the *in situ* SRD instrument is shown in Figure 2.9.

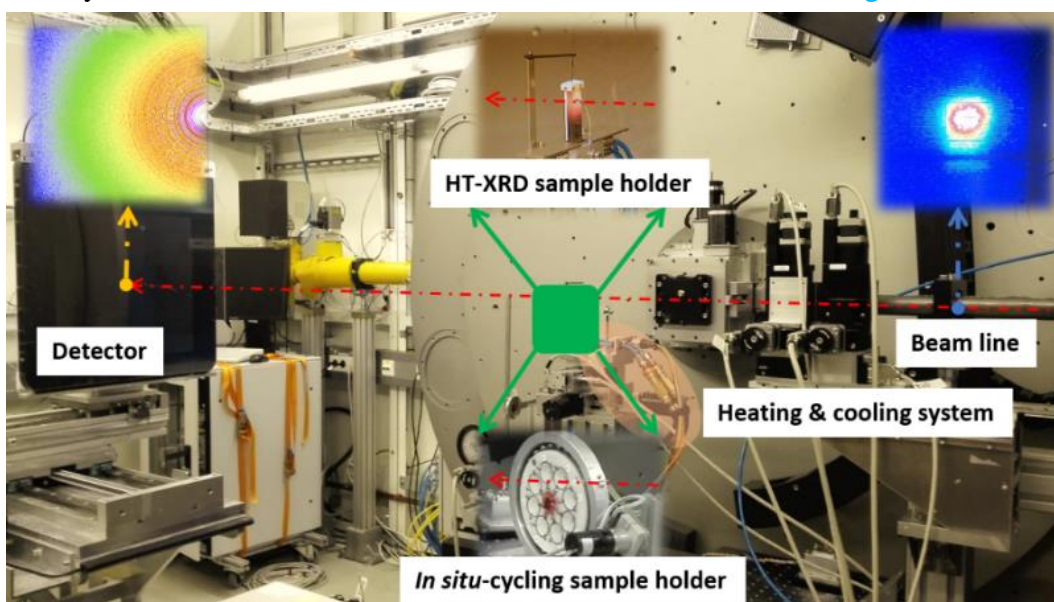


Figure 2.9 Overview of the *in situ* SRD and HT-SRD instruments in the P02.1, Petra-III DESY.

2.15 High-temperature SRD

High-temperature SRD (HT-SRD) is a useful method to detect phase evolution of a sample at increasing temperatures based on synchrotron radiation. The sample is prepared by putting fine powder in a quartz capillary, and then either keeping the capillary open to air or sealing it under inert gas (e.g. Ar). Afterwards, the capillary is heated in a ceramic heater equipped with a cooling system (Figure 2.9), which can control the temperature programmly in range of 20~850 °C. At the same time, the SRD is conducted at settled temperatures, and thus temperature-dependent phase transitions of the sample can be achieved.

3 ZnCo₂O₄ and ZnCo₂O₄ carbon cloth composite in LIBs

3.1 Introduction

So far, many transition metal oxides have been intensively studied as anode materials for LIBs [122]. As it is known, cobalt oxides have high structural and cycling stability, compared to other transition metal oxides [123]. However, the high-cost and high-toxicity of cobalt block the large-scale application of cobalt oxides. One strategy to reduce the usage of cobalt, is its partial substitution with inexpensive and nontoxic elements. Thus, some ternary oxides have been developed, like such as ZnCo₂O₄ [123–125], CoFe₂O₄ [126–128], and NiCo₂O₄ [129–131]. Among them, ZnCo₂O₄ is very promising since its conversion-alloying-combined charge storage mechanism. This material delivers high specific capacity, theoretically 789 mAh g⁻¹ with 7 Li⁺ pfu [132,133]. Further, some hierarchical ZnCo₂O₄ structures load on conductive matrix were designed to alleviate volume change, increase electron conductivity and shorten Li⁺ pathway, such as peanut-like ZnCo₂O₄/rGO/CNTs [134], ZnCo₂O₄-urchins/carbon-fibers [135], ZnCo₂O₄ nanowire arrays/carbon cloth [132], ZnCo₂O₄ nanosheets on nickel foam [136], and ZnCo₂O₄ nanoflowers/carbon nanotube/N-doped graphene [137].

Despite the wide available literature related to the synthesis of ZnCo₂O₄ and hierarchical ZnCo₂O₄/matrix composites and their improved electrochemical performance, there is still no deep understanding of the working mechanism of ZnCo₂O₄. Up to now, *ex situ* XRD, TEM, and SAED have been employed as tools for elucidating the conversion mechanism, revealing the process of $\text{LiZn} \rightleftharpoons \text{Zn} \rightleftharpoons \text{ZnO}$ and $\text{Co} \rightleftharpoons \text{CoO} \rightleftharpoons \text{Co}_3\text{O}_4$ during cycling [138]. Some reports involving other transition metal oxides, such as ZnO/ZnFe₂O₄ [139] and Mn₃O₄ [140], clearly demonstrate the phase evolution in the initial cycle via *in situ* XRD method. Therefore, *in situ* techniques are powerful methods to understand the mechanism of (de)lithiation. However, it is difficult to do this directly on hierarchical ZnCo₂O₄/matrix because of the low ZnCo₂O₄ loading. Very recently, Deng *et al.* used *in situ* XRD to study the ZnCo₂O₄ spheres for lithium storage, but they only observed gradual fading of characteristic diffraction peaks of ZnCo₂O₄ upon the initial lithiation [125]. Because the initial lithiation process is crucial to electrochemically activate ZnCo₂O₄, it is necessary to investigate in-depth this material via *in situ* techniques.

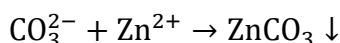
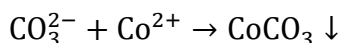
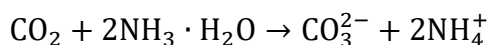
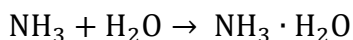
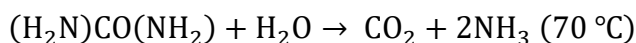
Inspired by the above discussion, this work aims to elucidate the Li storage mechanism of parallelepipedal ZnCo₂O₄ particles (named ZCO) via *in situ* SRD and *in situ* XAS. This study reveals the real potentials when the intermediate phases form and vanish during the conversion process. Notably, a carbon cloth (CC) supported ZnCo₂O₄ (named ZCO/CC) was synthesized under the same hydrothermal condition with the ZCO. Afterwards, the hierarchical ZCO/CC was used as binder-free anodes for lithium storage. The electrochemical performance of the ZCO/CC and the bare ZCO electrodes were measured and compared.

The results in this chapter are published in the following publication: **Z. Zhao**, G. Tian, V. Trouillet, L. Zhu, J. Zhu, A. Missiul, E. Welter, S. Dsoke, *In Operando* analysis of the charge storage mechanism in a conversion ZnCo₂O₄ anode and the application in flexible Li-ion batteries, *Inorg. Chem. Front.* 6 (2019) 1861–1872. Reproduced by permission of The Royal Society of Chemistry, <https://pubs.rsc.org/en/content/articlelanding/2019/QI/C9QI00356H#/divAbstract>.

3.2 Results and discussion

3.2.1 Hydrothermal synthesis and characterization of the ZCO and ZCO/CC

The ZCO and ZCO/CC were synthesized through a hydrothermal method. The XRD pattern in [Figure 3.1a](#) confirms that the precursor of the ZCO is composed of metal carbonates (CoCO₃ and ZnCO₃). During the hydrothermal process, Co²⁺ and Zn²⁺ ions can co-precipitate with carbonate in a weak alkaline environment (pH value of 6 ~ 9). Herein, urea can react with H₂O and then converts to NH₃ (NH₄⁺) and CO₂ (CO₃²⁻), which can provide the alkaline environment and serve as the precipitant, respectively. The overall reactions during the hydrothermal process can be, therefore, described as following:



To determine the optimal sintering temperature, TGA was performed from 35 °C to 1000 °C under O₂/Ar (1:3 by volume) flow. In [Figure 3.1b](#), the ZCO precursor exhibits a major weight loss at 360~470 °C due to decomposition of the metal carbonates (CoCO₃ at 350 °C and ZnCO₃ at 400 °C). At 470 °C, 68 wt.% of mass remains, which is in agreement with the theoretical value of 68 wt.% ($\text{ZnCO}_3 + 2\text{CoCO}_3 + 0.5\text{O}_2 \rightarrow \text{ZnCo}_2\text{O}_4 + 3\text{CO}_2 \uparrow$). Due to the presence of the CC, the mass loss of the ZCO/CC precursor in step I is only 7 wt.%, which is related to the decomposition of the Zn and Co-containing compounds. The ZCO/CC precursor displays an additional step at 600~700 °C (step II) where the mass loss is 51 wt.%. This is related to the combustion of the CC. Finally, the residual mass of 42 wt.% at 750 °C can be associated with the amount of ZnCo₂O₄ attached on the CC. [Figure 3.1c](#) shows the presence of residual materials after step III (above 930 °C). This material is a mixture of ZnCo₂O₄, ZnO, Co₃O₄, and possible CoAlO₃ or ZnAl₂O₄, which is due to the decomposition of ZnCo₂O₄ ($3\text{ZnCo}_2\text{O}_4 \rightarrow 3\text{ZnO} + 2\text{Co}_3\text{O}_4 + 0.5\text{O}_2 \uparrow$) and contamination from the Al₂O₃ crucible, respectively. Based on these results, the sintering temperature was set at 500 °C, and the ZnCo₂O₄ accounts for 46 wt.% in the ZCO/CC. The Raman spectrum of the CC ([Figure 3.1d](#)) exhibits two distinct peaks located at 1336 cm⁻¹ (D-band) and 1589 cm⁻¹ (G-band), ascribed to the defected- and graphitized- carbon structure, respectively. However, these bands disappear in the spectrum of the ZCO/CC, indicating the homogeneous surface covering of ZnCo₂O₄ on the CC. Similar to the ZCO, the ZCO/CC shows also the characteristic bands located at 182, 487, 527, 625 and 717 cm⁻¹, corresponding to the F_{2g}, E_g, F_{2g}, and A_{1g} modes of ZnCo₂O₄, respectively [141,142]. Based on these experimental evidences, we can conclude that ZnCo₂O₄ was successfully synthesized and homogeneously grown on the CC surface via hydrothermal reaction.

As shown in [Figure 3.2a](#), the pink rhombohedral ZCO precursor displays a wide size distribution (5 ~ 100 μm). However, the well-crystallized micrometer scale particles display a prismatic shape with a smooth exterior and distinct edges, apparently suggesting high crystallinity for these crystals. The sintering process can induce the removal of CO₃²⁻ and volume change, leading to the pulverization of large particles into small ones (see [Figure 3.2b](#)). The SEM image ([Figure 3.2c](#)) of the ZCO show parallelepiped-like shaped particles, with angles of $\alpha = 90^\circ$, $\beta = 90^\circ$ and $\gamma = 150^\circ$. The formation mechanism of ZnCo₂O₄ with a similar morphology was also reported by Cheng *et al.* [143]. The particle shape is related to hydrothermal condition and inorganic additive. As

demonstrated by EDS mapping (see Figure 3.2d~f), a fairly uniform elemental distribution of Zn, Co and O elements are observed over the entire particles. Longtime hydrothermal reaction can enable sufficient dissolution-precipitation reaction between metal ions and metal carbonate, forming the phase-pure parallelepiped-like shaped ZnCo₂O₄ particles.

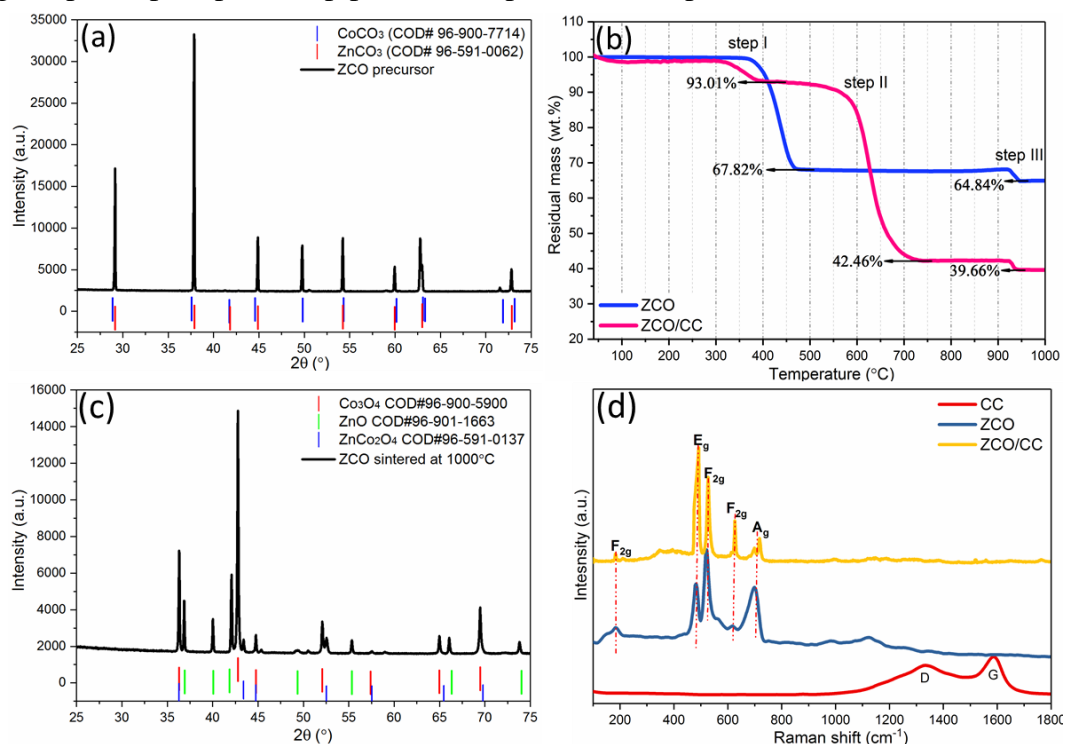


Figure 3.1 XRD patterns (Co-K_{α1}) of the ZCO precursor (a) before and (c) after TGA test, (b) TGA curves of the ZCO precursor and the ZCO/CC precursor under O₂/Ar (1:3 by volume) flow with heating rate of 5 °C min⁻¹, and (d) Raman (532 nm) spectra of the CC, ZCO and ZCO/CC.

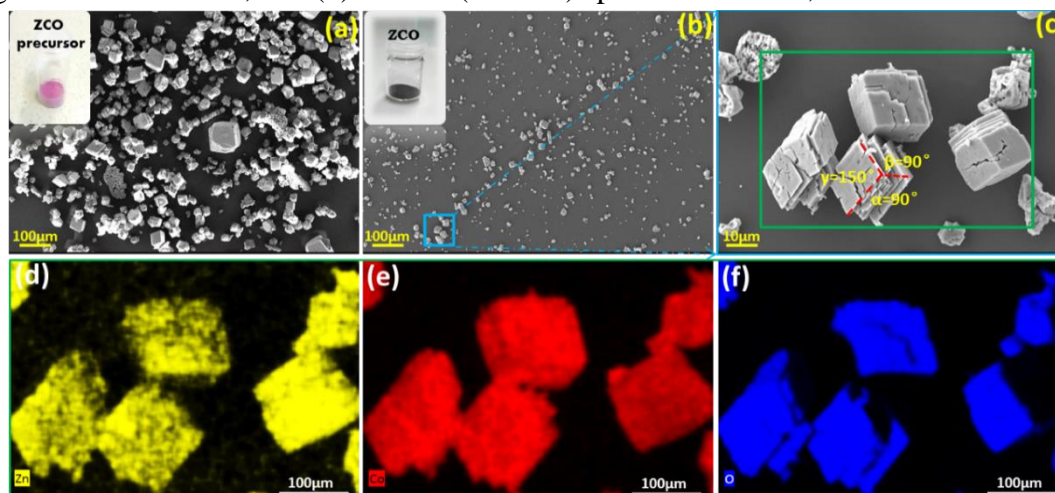


Figure 3.2 SEM images: (a) the ZCO precursor after hydrothermal reaction, (b, c) the ZCO after 450 °C calcination, and EDS mapping of the ZCO: Zn (d), Co (e) and O (f).

The XRD pattern (Mo-K_{α1}) of the ZCO is shown in [Figure 3.3a](#). The Rietveld refinement confirms the main cubic phase (space group: $Fd\bar{3}m$, COD #96-591-0137, 95 wt.%) and tiny hexagonal phase (space group: $P6_3mc$, COD #90-153-3021, 5 wt.%) in the ZCO. Satisfactory agreement factors ($R_{wp} = 8.55\%$, $R_p = 6.32\%$) with the cell parameter $a = 8.108 \text{ \AA}$ and cell volume $= 533.052(6) \text{ \AA}^3$ were obtained in this crystal refinement. As depicted in [Figure 3.3b](#), the schematic crystal structure of cubic spinel ZnCo₂O₄ consists of octahedral (blue CoO₆) and tetrahedral structures (yellow ZnO₄) [144]. The surface chemical composition and chemical states of the ZCO were analyzed by XPS. The XPS spectra in [Figure 3.3c~f](#) confirm the presence of Zn, Co and O. The Zn LMM Auger line at ~989 eV ([Figure 3.3c](#)) indicates the presence of Zn²⁺. Furthermore, two components can be observed in the Zn 2p_{3/2} spectrum ([Figure 3.3d](#)), at 1021.2 eV and 1022.7 eV, indicating the presence of Zn²⁺ in tetrahedral and octahedral oxygen coordination, respectively, and the tiny amount of Zn²⁺ in octahedral oxygen coordination is due to Zn²⁺ and Co³⁺ exchanging their positions [145]. According to the previous work from Azmi *et al.* [146,147], the 2p spectrum of cobalt ([Figure 3.3e](#)) was fitted by considering the typical occurring multiplet splitting observed for transition metals. Similar to the results from Kumar *et al.* [148], the fitted multiplet defined as in the study of Biesinger *et al.* [149], accompanied with the absence of the Co³⁺ satellite (785.6 eV), proves the presence of Co³⁺ only. The O 1s spectrum ([Figure 3.3f](#)) can be resolved into three components, and the most intensive one is attributed to the oxygen in the metal oxide (529.9 eV), whereas C=O (531.6 eV) and C–O (532.7 eV) stem from contamination. The quantitative analysis of the spectra leads to a Zn:Co:O ratio of 1:2.3:3.9, which well agrees with the expected stoichiometry of the ZnCo₂O₄.

The phase purity of the ZCO/CC was also studied by XRD. [Figure 3.4a](#) confirms that the reflections are well indexed with the $Fd\bar{3}m$ cubic phase ZnCo₂O₄ (96 wt.%), accompanied with tiny $P6_3mc$ hexagonal phase ZnCo₂O₄ (4 wt.%). Two broad and tiny diffraction peaks at ~11° and ~20° are due to the existence of the CC in the composite (see [Figure 3.5](#)). The XRD and SEM confirm the homogeneous growth of the crystal ZCO on the CC after annealing of the ZCO/CC precursor ([Figure 3.4b](#)). From the SEM image of [Figure 3.4c](#), one can observe the ZCO nanoflakes (~116 nm thickness) grown on the fibers. The open space between the nanoflakes allows efficient accommodation of large volume changes and releases structural stress. From the inserted image in [Figure 3.4b](#), it is clear that the highly flexible and self-supported ZCO/CC electrode can suffer a

180° mechanical bending. In short, the hierarchical ZCO/CC composite as a self-supporting electrode can combine the advantages of high electronic conductivity, high surface-to-volume ratio and short Li-ion diffusion length.

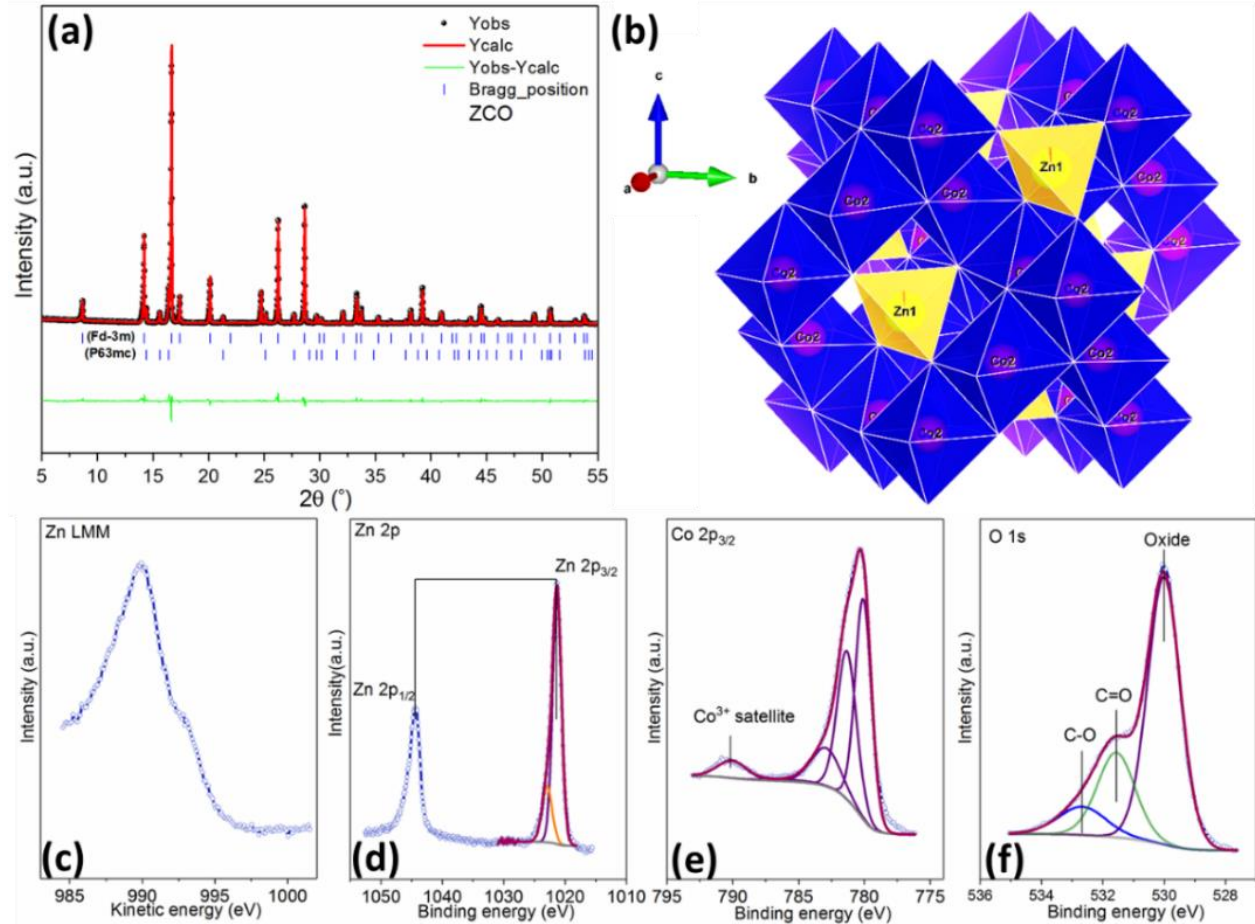


Figure 3.3 (a) The XRD (Mo-K_{α1}) pattern with Rietveld refinement fitting of the ZCO and (b) the corresponding visualized diagram of crystal structure, (c~f) the XPS spectra of the ZCO: (c) Zn LMM, (d) Zn 2p_{3/2}, (e) Co 2p_{3/2} and (f) O 1s.

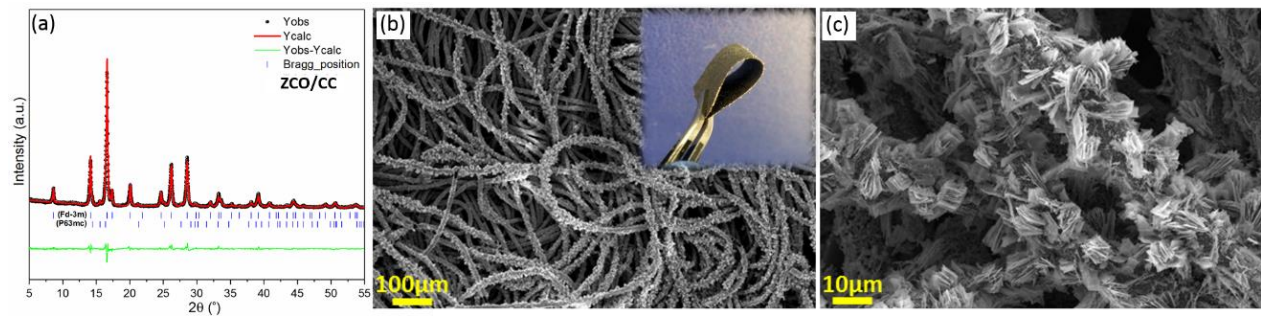


Figure 3.4 (a) The XRD (Mo-K_{α1}) pattern of the ZCO/CC, and (b, c) SEM images of the ZCO/CC. The inserted figure in (b) is a photo of a bending ZCO/CC electrode.

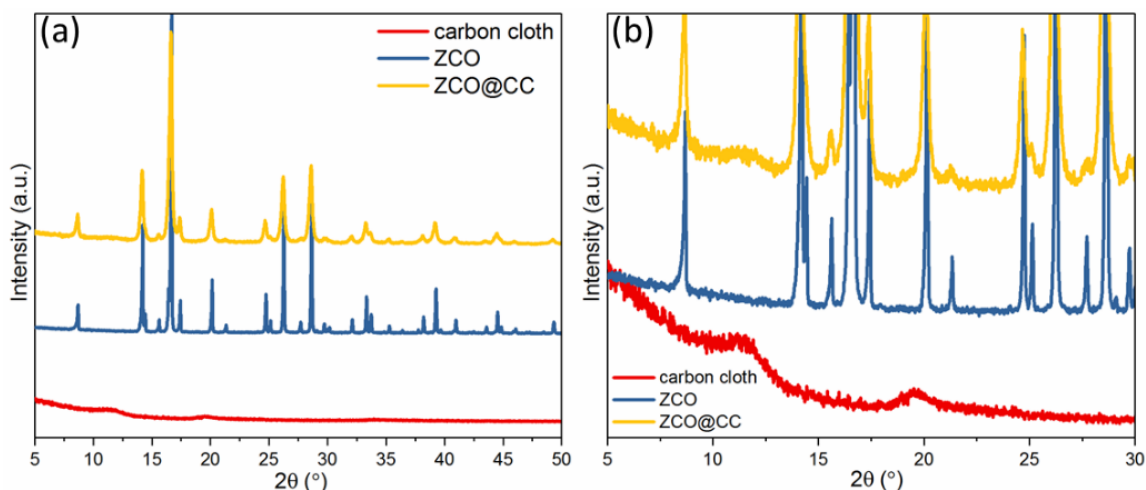


Figure 3.5 XRD patterns (Mo K α 1) of the CC, ZCO and ZCO/CC.

3.2.2 Mechanism study of the ZCO anode during initial conversion process

Figure 3.6a shows the CV curves of the ZCO electrode over 50 cycles. Based on previous reports, during the first cathodic scan, the weak peak at 1.7 V is related to the initial Li⁺ insertion into the ZnCo₂O₄ structure [150]. Then, the CV shows an intensive irreversible peak at ~0.7 V followed by a minor peak at ~0.4 V, corresponding to the conversion of ZnCo₂O₄ to metallic Zn and Co, and a further alloying of Zn with Li. In the following cycles, the main reduction peak (~0.7 V) shifts to ~1.0 V, a phenomenon which is in agreement with literature [133]. During the anodic sweep, Li de-alloy from LiZn at ~0.6 V, and the two peaks located at around 1.7 V and 2.2 V correspond to the formation of ZnO and CoO, respectively [138,151]. After tens cycles, the cathodic peaks apparently shift to lower potential, ~0.3 V, while the anodic peaks gradually disappear, indicating the decrease in reaction kinetics [152]. Figure 3.6b shows the potential profiles recorded at 0.1 A g⁻¹. The 1st lithiation and delithiation capacities are 1087 and 806 mAh g⁻¹, respectively, which are beyond theoretical values of 976 mAh g⁻¹ and 789 mAh g⁻¹ based on 9 and 7 Li⁺ pfu delivered, respectively. The extra capacity can be attributed to a space charge storage mechanism due to nanosize effect [153,154]. The high irreversible capacity during the 1st cycle corresponds to the initial formation of SEI layer and the irreversible conversion from Co³⁺ to Co²⁺ [155–158]. A severe capacity fade is observed after 20 cycles, which can be mainly ascribed to the pulverization of the active material and reducing of electronic conductivity.

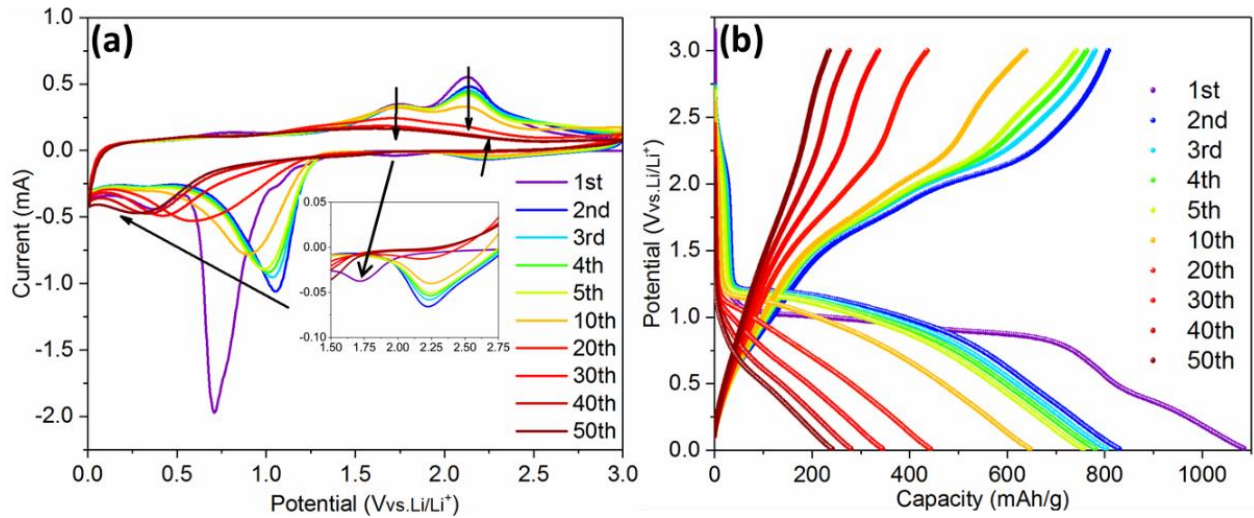


Figure 3.6 The CV curves at a scan rate of 0.1 mV s⁻¹ (a) and GCPL potential profiles recorded at 0.1 A g⁻¹ (b) of the ZCO.

In order to further understand the electrochemical reaction mechanism of the ZCO, *in situ* SRD was performed during the 1st GCPL cycle at 75 mA g⁻¹. Based on the above discussed electrochemical behavior (Figure 3.6), the potential plateaus and current peaks can be related to specific phase changes. The SRD patterns, containing a total of 145 scans, can be separated into five steps (named from A to E in Figure 3.7 and Figure 3.8).

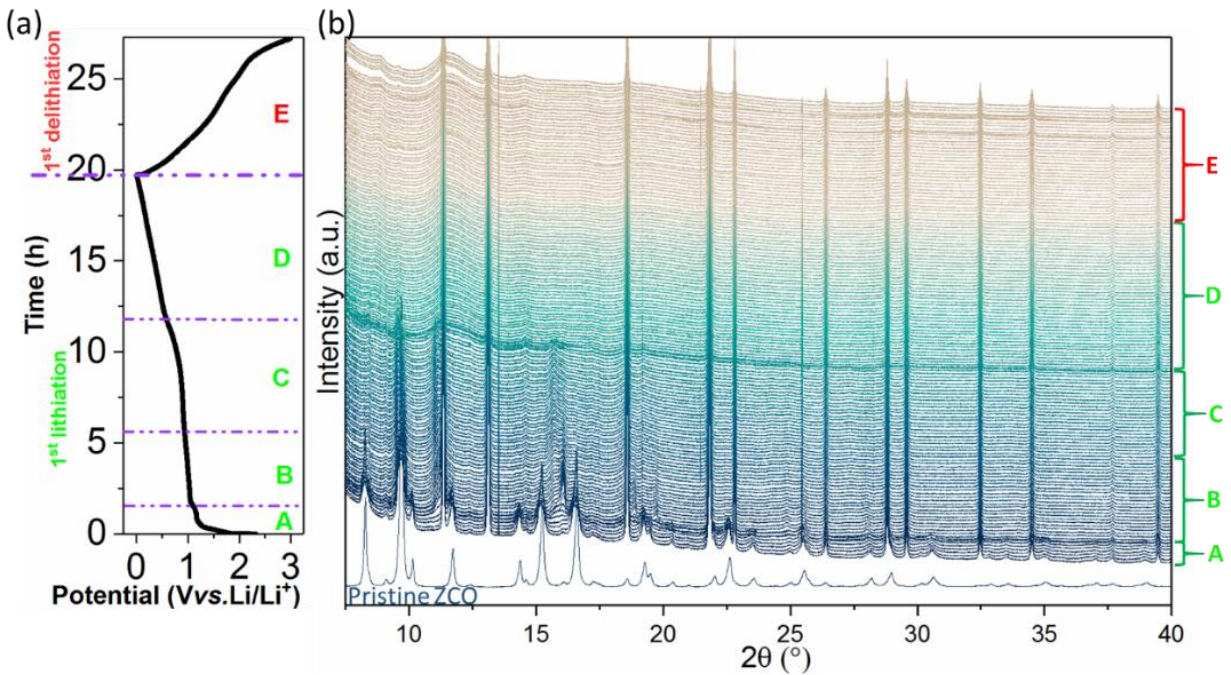


Figure 3.7 *In situ* SRD ($\lambda=0.41266 \text{ \AA}$) measurement of the ZCO electrode: (a) potential profile (75 mA g⁻¹) and (b) SRD patterns during the 1st lithiation/delithiation.

In step A (scan 1~7, [Figure 3.8a&b](#)), where the potential rapidly drops and forms a short plateau at ~1.16 V, the intensity of the ZnCo₂O₄ peaks decreases slightly. In this region, the Li-ion insertion into cubic ZnCo₂O₄ leads to an increase of cell parameters (*e.g.*, lattice parameter *a*: 8.108 Å at scan1 → 8.111 Å at scan3 → 8.113 Å at scan5 → 8.114 Å at scan7, see [Figure 3.9a](#)). Between the step A and step B (scan 7~9), when there is a small steep potential slope (1.16 V → 1.07 V), a new series of reflections appear at 9.8°, 11.3°, 16.1°, 18.8° and 19.7°, as depicted in [Figure 3.8a](#) and [Figure 3.9c&d](#). These peaks correspond to LiCo₂O₃ (Li_{0.33}Co_{0.67}O, COD #96-154-1452), indicating that the Li⁺ intercalated ZnCo₂O₄ (LiZnCo₂O₄) converts to LiCo₂O₃ and ZnO. Step B covers the scan 8~31, corresponding to the potential plateau at 1.05~0.93 V. As shown in [Figure 3.8c&d](#) and the enclosed red dash line of [Figure 3.9e&f](#), the peak intensity of the LiCo₂O₃ reaches the maximum value at scan 10 and then gradually decreases until scan 31. Meanwhile, the intensity of the CoO reflections (at 9.6°, 11.1°, 15.7° and 19.3° enclosed in pink dash line in [Figure 3.9e&f](#), COD #96-154-1663) increases, indicating the conversion from LiCo₂O₃ to CoO and Li₂O during Li⁺ insertion. Moreover, a series of weak reflections related to ZnO (at 8.4°, 9.1°, 14.6° and 17.3° in [Figure 3.9e&f](#), COD #96-230-0114) can also be observed. Simultaneously, the diffraction peaks related to ZnCo₂O₄ gradually weaken until completely vanish at scan 17 at around 1.01 V. In step C (scan 32~63), corresponding to a potential plateau at 0.93~0.85 V (scan 48) and a gentle slope (0.85~0.59 V), the intensity of the new reflections (LiCo₂O₃, CoO and ZnO) decreases and finally vanishes (see [Figure 3.8c&d](#) and [Figure 3.9g&h](#)). It relates to the continuous reduction reaction of CoO and ZnO to metallic Co and Zn. In step D (scan 64~106), related to a potential slope at 0.57~0.01 V, the diffraction peaks related to CoO and ZnO disappear (see [Figure 3.8e](#) and [Figure 3.10a&b](#)), and an extra amount of Li is stored in the interface between Li₂O and metal nanodomains based on the space charge storage mechanism [153,154]. The typical alloying reaction of Zn with Li occurs below 0.5 V, and the SEI forms at ~0.8 V [139,159,160]. Unfortunately, due to the nature of the nanoparticles produced by the electrochemical conversion reaction, the LiZn alloy cannot be observed in the SRD patterns.

During the delithiation process (step E, scan 107~145), at potential above 1.34 V (scan 121), the reflections located at 8.6°, 14.8° and 9.6° slightly increase in intensity (see [Figure 3.8e](#) and [Figure 3.10c&d](#)), indicating the formation of the oxidation products, ZnO and CoO. The nanosized products block further analysis based on phase change during the continuous (de)lithiation process.

Herein, this is the first time that the multiple conversion processes are observed on the ZnCo₂O₄ anode. In general, the first conversion reaction is $\text{LiZnCo}_2\text{O}_4 \rightarrow \text{LiCo}_2\text{O}_3 + \text{ZnO}$, followed by the second conversion of $\text{LiCo}_2\text{O}_3 \rightarrow \text{CoO} + \text{Li}_2\text{O}$, and finally, the CoO and ZnO are reduced to metallic Co and Zn (LiZn alloy) nanograins. After delithiation, the segregated metal oxides ZnO and CoO are reconstructed.

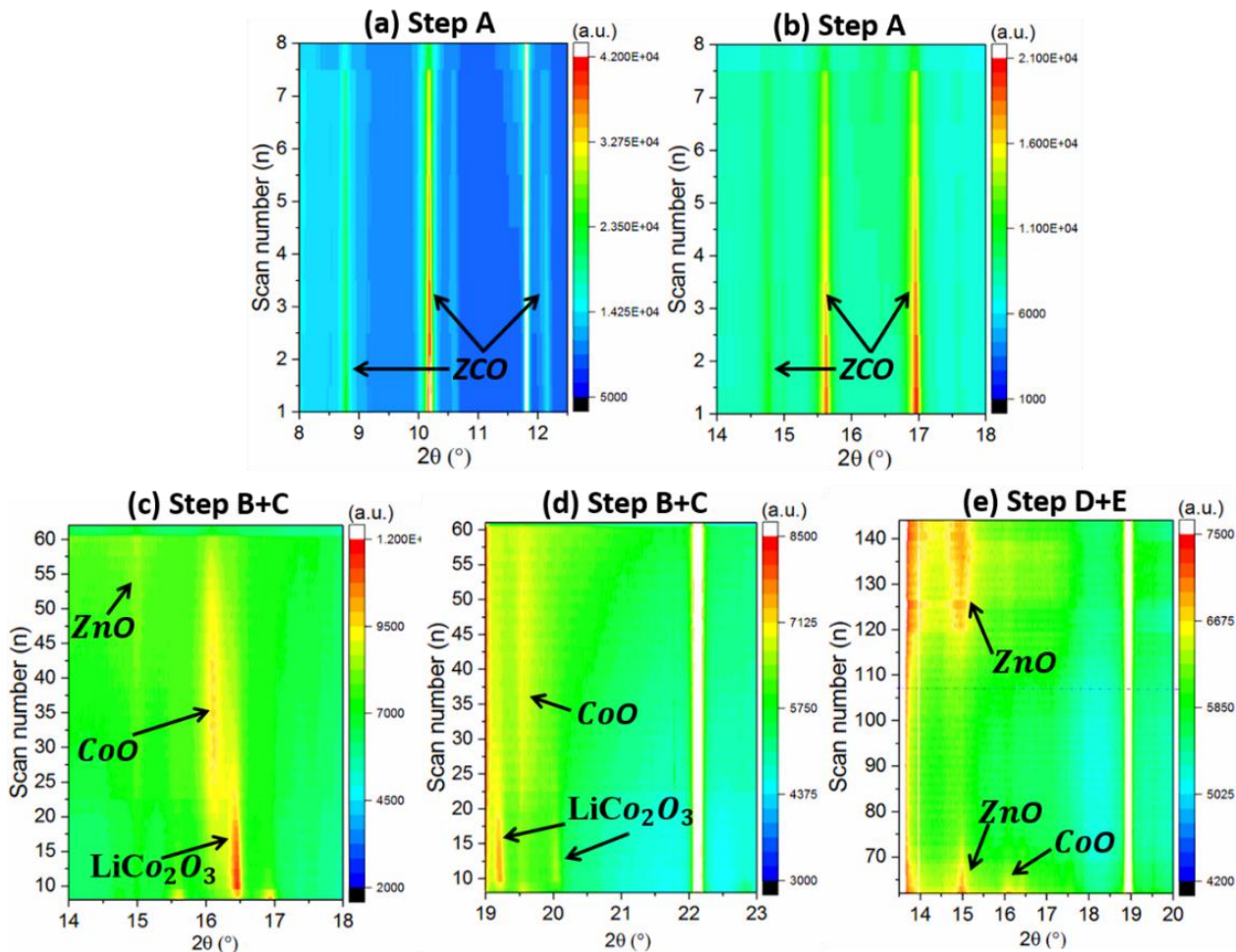


Figure 3.8 *In situ* SRD contour map of the ZCO with different reaction steps: (a, b) step A, (c, d) step B+C and (e) step D+E.

To clarify the evolution of the cobalt valence in the ZCO electrode, *in situ* XAS measurement was carried out at Co K-edge during the 1st lithiation performed at 80 mA g⁻¹ (see Figure 3.11a). Figure 3.11b depicts that Co³⁺ (scan1) in the pristine electrode is gradually reduced to Co²⁺ (scan6), corresponding to the step A+B concluded in the *in situ* SRD test. During scan 1~2 (step A), the cobalt valence change dramatically from higher than Co₃O₄ to lower than Co₃O₄, which is in agreement with the conversion from ZnCo₂O₄ to LiCo₂O₃. Later on, LiCo₂O₃ converts to CoO

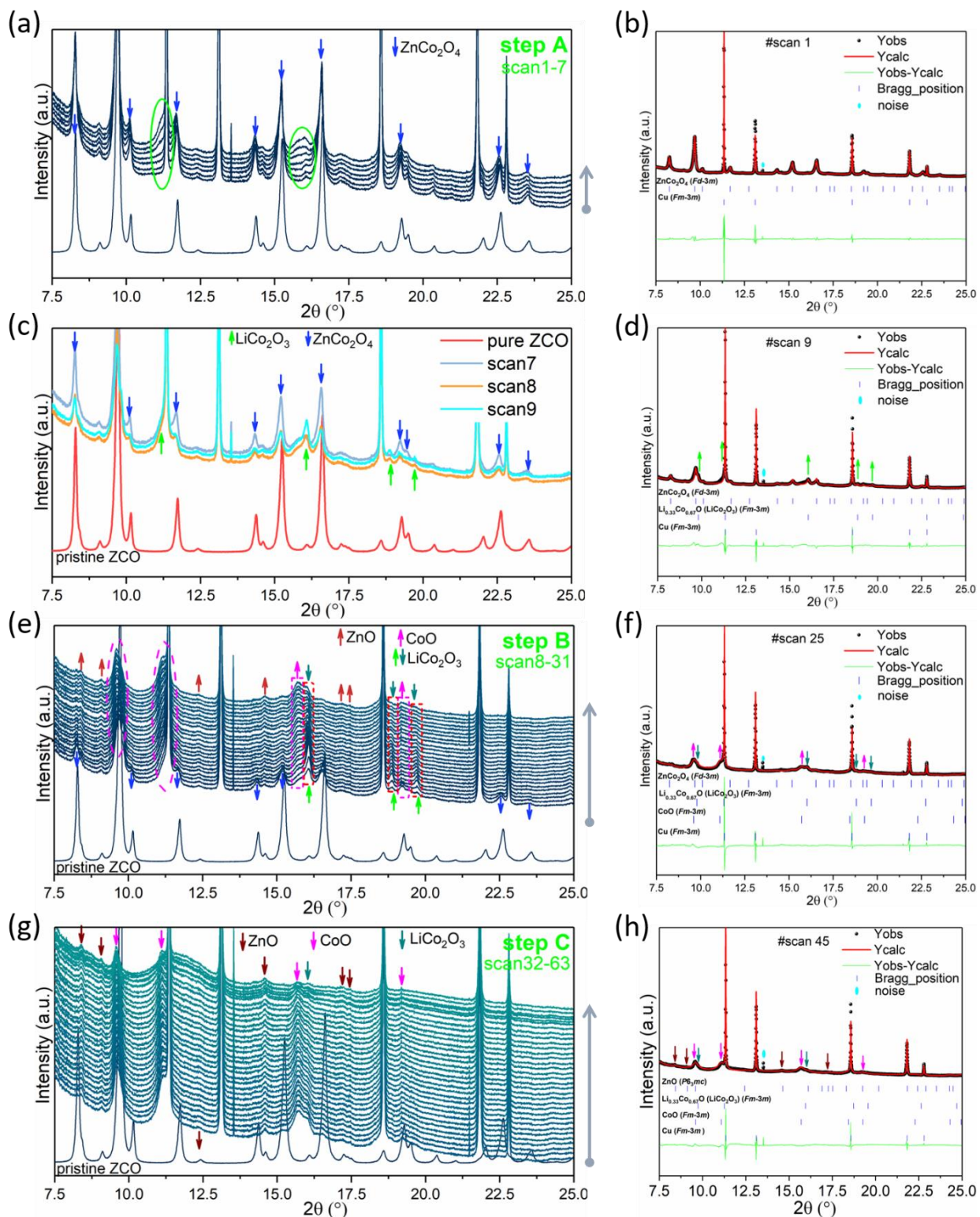


Figure 3.9 Evolution of the *in situ* SRD patterns of the ZCO electrode: step A (a, b), step A+B (c, d), step B (e, f) and step C (g, h).

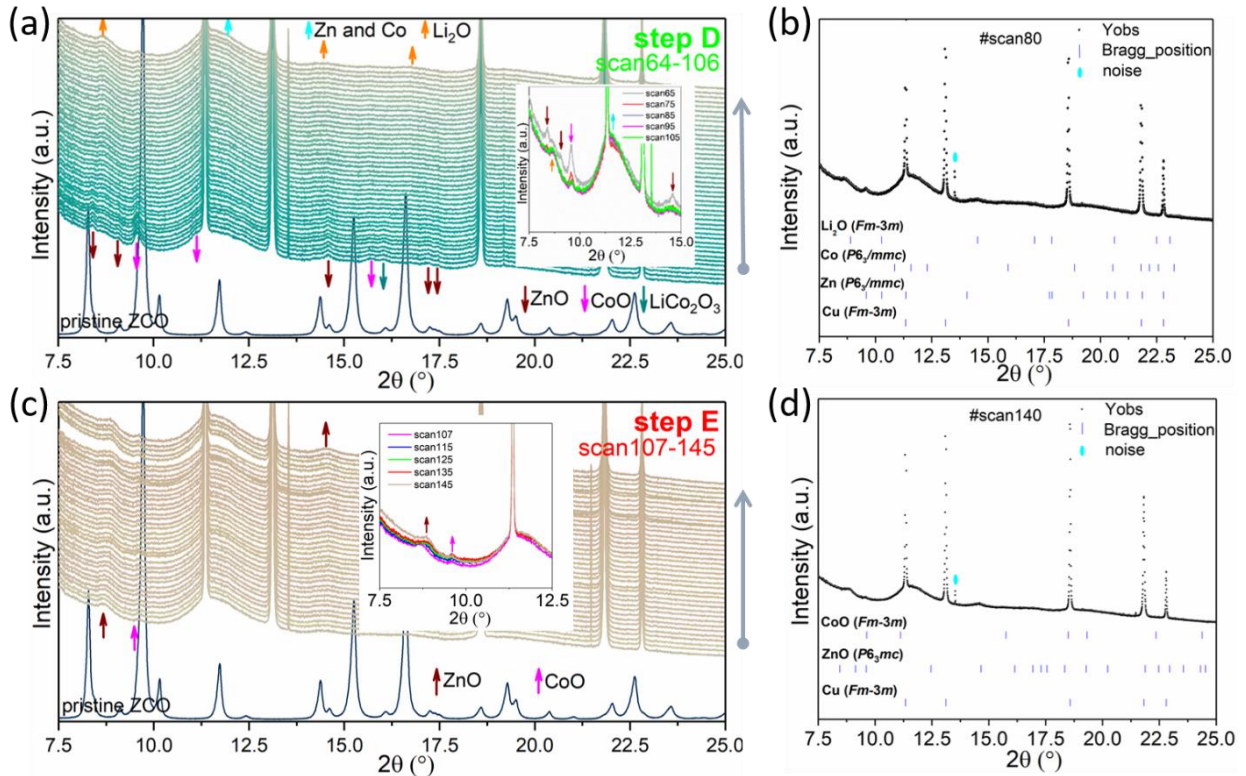
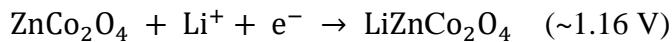


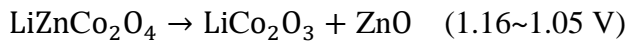
Figure 3.10 Evolution of the *in situ* SRD patterns: step D (a, b) and step E (c, d).

gradually during scan 3~6 (step B). From scan 7 to scan 11, CoO converts to Co continuously, which can be related to step C (see [Figure 3.11c](#)). At last, from scan 12 to scan 17 (see [Figure 3.11d](#)), the spectra are overlapped and consistent with the spectrum of Co foil, corresponding to step D with no more conversion reaction. The capacity stored in step D is attributed to the space charge storage [153,154]. Therefore, the evolution of the cobalt valence is well in agreement with the *in situ* SRD results. Based on the combination of the *in situ* SRD and XAS analysis, the lithiation/delithiation process in the ZCO electrode is concluded in the following equations:

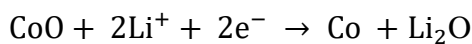
Step A (OCV~1.16 V):

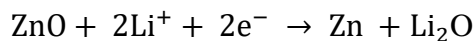


Step B (1.16~0.93 V):

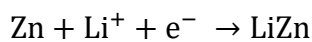


Step C (0.93~0.59V):





Step D (0.57~0.01 V):



Step E (0.01~3.00 V):

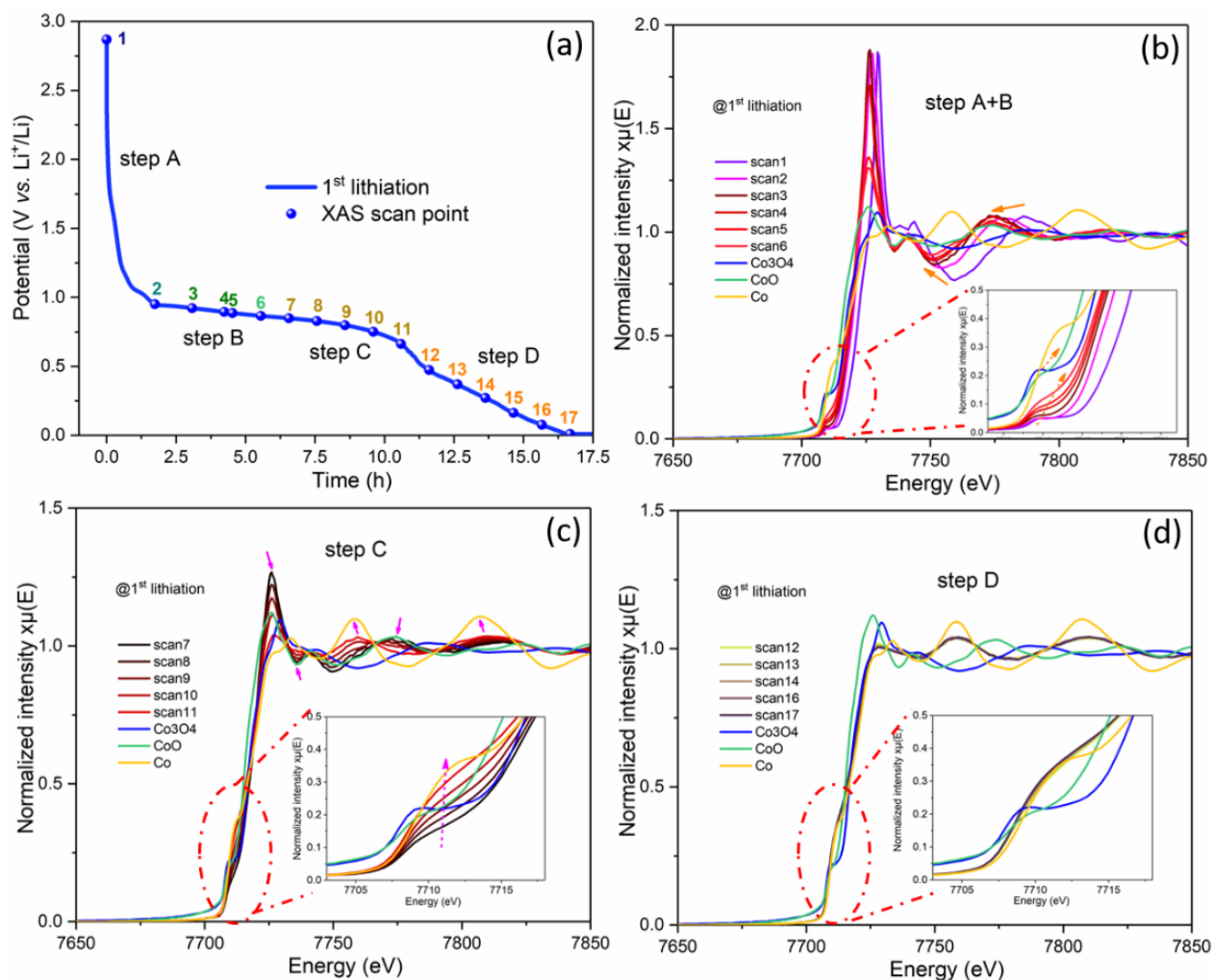
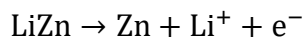


Figure 3.11 (a) The potential profile of the ZCO half-cell during the *in situ* XAS with a current density of 80 mA g^{-1} , and the NEXAS spectra on Co K-edge during the 1st lithiation process: (b) step A+B, (c) step C and (d) step D.

3.2.3 Electrochemical performance of the ZCO and ZCO/CC

To verify the improvement of the electrochemical performance for the composited electrode due to the ZnCo₂O₄ nanoflakes growing on the 3D conductive substrate, CV measurements were carried out for both ZCO and ZCO/CC samples. Figure 3.12a&b show that the main cathodic peaks of the ZCO are located at 1.0~0.5 V, corresponding to the reductions of Co²⁺ to Co⁰ and Zn²⁺ to Zn⁰. In addition, two anodic peaks at ~1.8 V and ~2.1 V appear during the delithiation process, ascribed to the oxidation reactions of Zn→ZnO and Co→CoO, respectively [161,162]. In contrast, the ZCO/CC electrode exhibits additional redox reactions at low potential (~0.4 V at lithiation process/~0.6 V at delithiation process), which can be attributed to Li⁺ storage in the CC. Moreover, the anodic/cathodic peaks shift towards each other slightly in the ZCO/CC electrode compared with the ZCO one, indicating a lower polarization induced by the enhanced electronic conductivity. Different from the opinion of Liu. *et al* [135], the contribution of the CC to the capacity (~80 mAh g⁻¹ at 0.1 A g⁻¹, see Figure 3.13) is not negligible.

Herein, two mechanisms are considered to elucidate the Li⁺ storage in the CC: (i) Li⁺ insertion into graphitic carbon to form LiC₆ and (ii) Li⁺ storage on the carbon surface via capacitive effect [163,164]. The two effects can be distinguished by analyzing the power-law dependence relationship between generated current (*i*) and scan rate (*v*) from the CV data (*i_v* = *av^b*) [165]. Figure 3.12c shows the linear fitting according to the relationship of *ln i_v* = *lna* + *blnv*. The fitting result for the both cathodic peak at ~0.4 V (*b* = 0.920±0.027) and anodic peak at ~0.6 V (*b* = 0.973±0.058) for the ZCO/CC displays *b* value of around 1.0, meaning that the contribution of the capacitive charge storage in the CC is the main reason for the enhanced capacity at low potential. Figure 3.12a&b shows that voltage hysteresis of the CV peaks are gradually enlarged as the scan rate increasing. To further investigate the reaction kinetics, the Li⁺ diffusion coefficient is calculated from the peak currents based on the Randles-Sevcik equation [166]:

$$i_p^2 = 0.2n^3F^3c^2A^2D_{Li}v/(RT) \quad (\text{Eq. 3.1})$$

where *i_p* is the peak current (A), *n* is the number of electrons transferred in the redox reaction, *F* is Faraday constant (96485 C mol⁻¹), *c* is the concentration of Li⁺ species (0.15 mol cm⁻³ for the ZCO), *A* is the effective contact area between ZCO and electrolyte, *D_{Li}* is the Li⁺ diffusion coefficient (cm² s⁻¹), *v* is the scan rate (V s⁻¹), *R* is the gas constant (8.314 J mol⁻¹ K⁻¹) and *T* is

the absolute temperature (298 K). As shown in Figure 3.12d, the linear relationship between peak currents (i_p) and the square root of scan rate ($v^{1/2}$) suggests that the electrochemical storage process is limited by the diffusion process. Because the effective contact area (A) of these compounds is rather complex due to the huge difference in morphology between the ZCO particles and the ZCO/CC composite, we propose to use a comprehensive parameter ($AD_{Li}^{1/2}$ (cm³/s^{1/2})) to describe the apparent effective diffusion in the solid phase. From this calculation, $AD_{Li}^{1/2}$ related to the ZCO/CC is 1.2 times higher than the one related to the pure ZCO (anodic: 2.48×10^{-7} vs. 2.97×10^{-7} cm³/s^{1/2}; cathodic: 3.81×10^{-7} vs. 4.53×10^{-7} cm³/s^{1/2} for the ZCO vs. ZCO/CC).

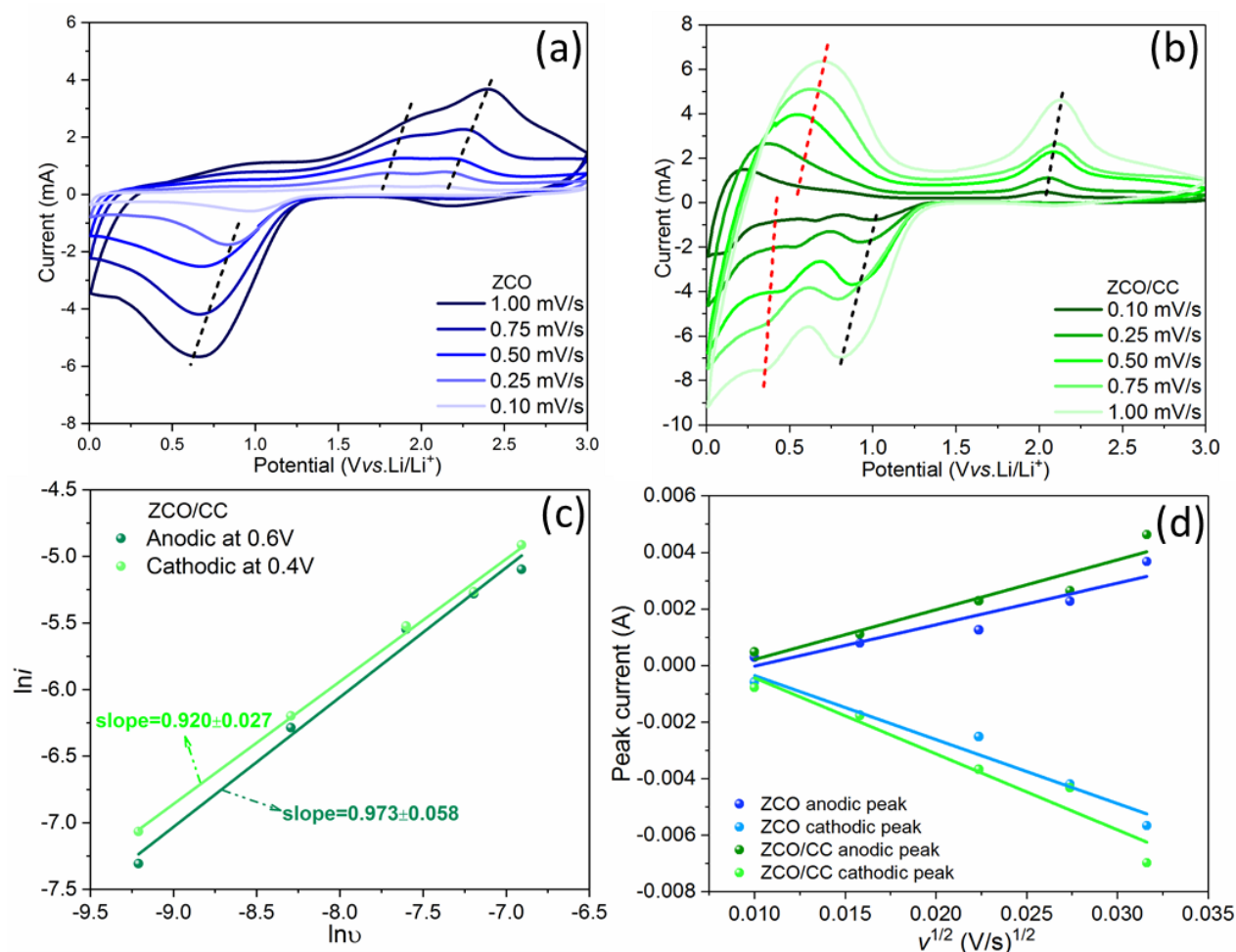


Figure 3.12 CV curves of the ZCO (a) and the ZCO/CC (b) at different scan rates of 0.1~1.0 mV s⁻¹, (c) power-law dependence of generated currents on scan rates and corresponding linear fitting of the pair of redox peaks at ~0.4 V (cathodic) and ~0.6 V (anodic) for the ZCO/CC, and (d) profiles of the peak current (i_p) vs. the square root of scan rate ($v^{1/2}$) and corresponding linear fitting for the ZCO and the ZCO/CC at ~0.7 V (cathodic) and ~2.1 V (anodic).

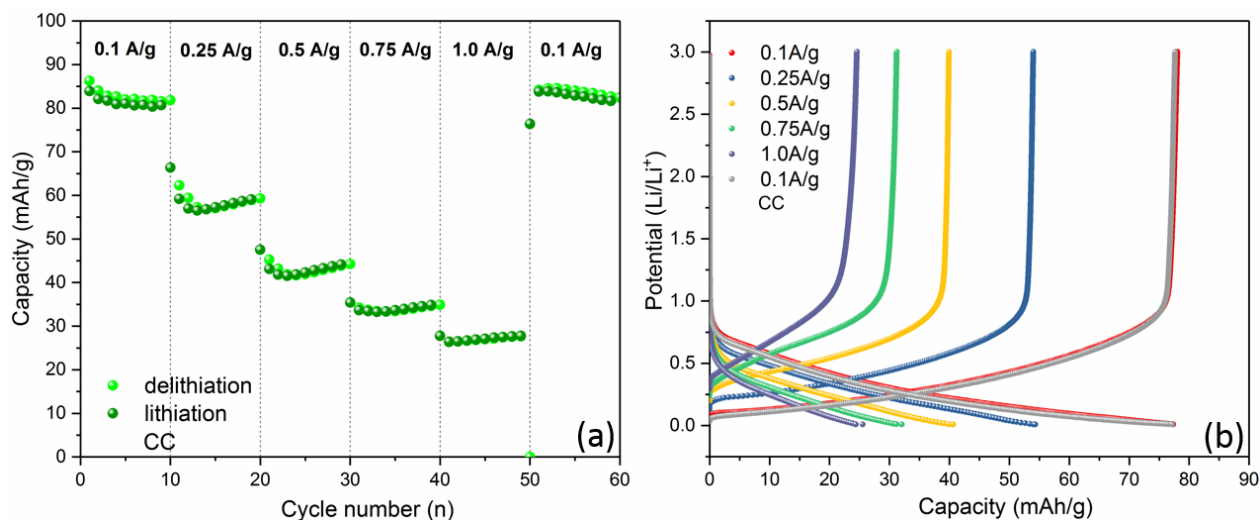


Figure 3.13 Electrochemical performance of the CC: (a) GCPL specific capacity and (b) potential profiles at different current densities.

Figure 3.14a compares rate capability of the ZCO and ZCO/CC at different current densities from 0.1 to 1.0 A g⁻¹, whereas the capacity decreases with rising current density due to the sluggish Li⁺ diffusion kinetics [167]. For a fair comparison, the capacity contribution from the CC in the ZCO/CC electrodes is not included, by subtracting the capacity of pure CC (see Figure 3.13). The ZCO/CC electrode exhibits a much better rate performance (delithiation capacity: 1013, 948, 760, 664 and 603 mAh g⁻¹ at 0.1, 0.25, 0.5, 0.75 and 1.0 A g⁻¹, respectively) compared to the ZCO electrode, while the ZCO displays capacities of 1049, 832, 451, 249 and 131 mAh g⁻¹ at 0.1, 0.25, 0.5, 0.75 and 1.0 A g⁻¹, respectively. When the current density is reduced again to 0.1 A g⁻¹, the capacity of the ZCO/CC electrode (1207 mAh g⁻¹) is beyond the original value. Furthermore, in commercial application, capacity density of cells should be valued considering the total mass of all cell parts. Actually, the mass of inactive components in electrode, such as binder, conductive additive and current collector, should be also taken into account. In this work, the apparent specific capacities of the ZCO and the ZCO/CC electrodes are also compared based on the total electrode mass, namely ZCO+carbon black+polymer binder+copper foil and ZCO+CC, respectively. As shown in Figure 3.15, the apparent specific capacity of the ZCO/CC is 296 mAh g⁻¹ at 0.1 mA g⁻¹, which is almost twice of the value of the ZCO (170 mAh g⁻¹). At higher current densities, the disparity becomes even wider (176 mAh g⁻¹ for the ZCO/CC vs. 22 mAh g⁻¹ for the ZCO at a current density of 1.0 A g⁻¹). This is not only due to the light weight of the CC but also to its contribution to providing extra energy storage at low potential and enhancing electronic

conductivity. This result indicates the potential of such carbon cloth supported flexible electrode, due to its well improved electrochemical performance and much higher apparent specific capacity.

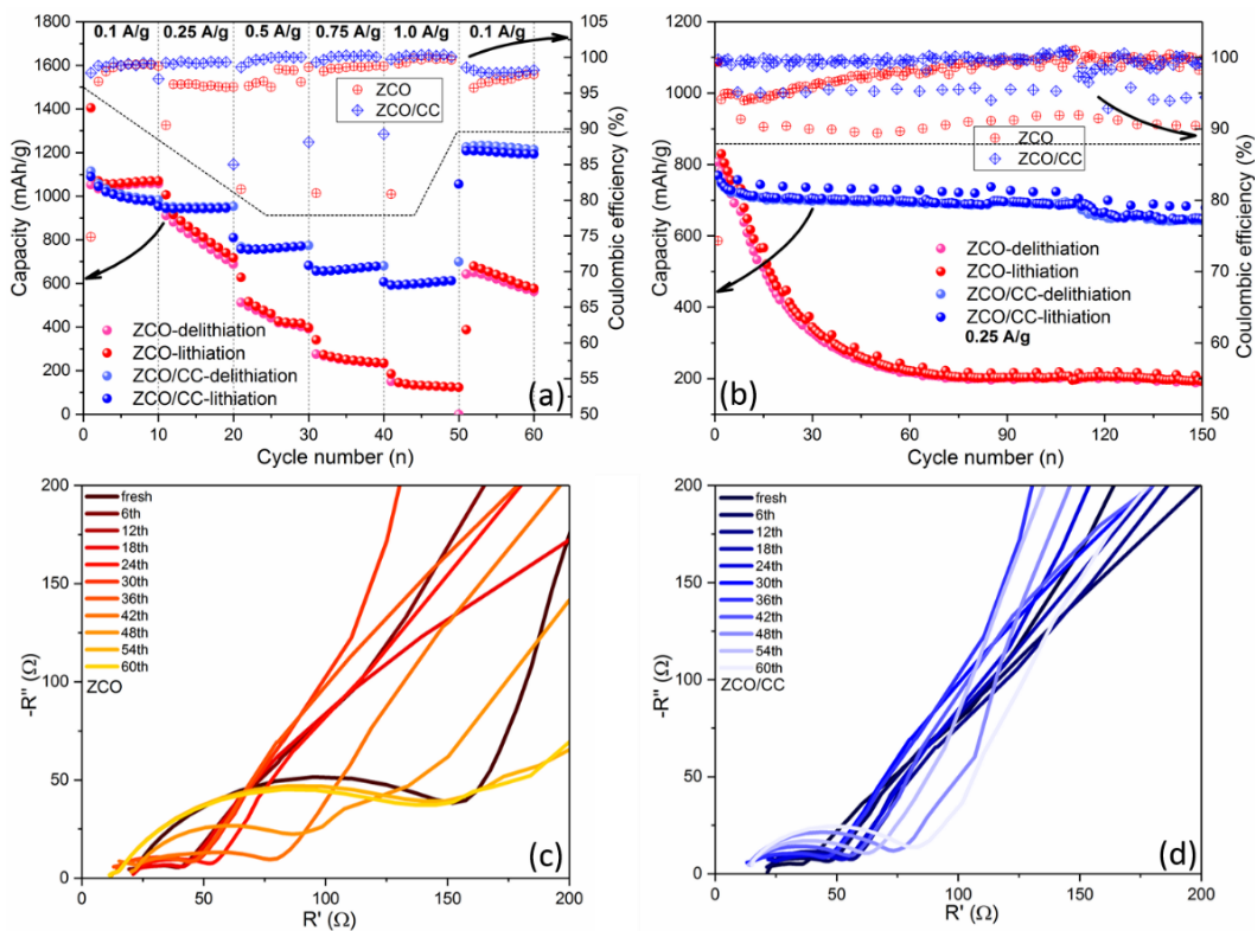


Figure 3.14 Electrochemical performance of the ZCO and ZCO/CC: (a) the rate capability, (b) the cycling stability at 0.25 A g^{-1} , and the selected Nyquist plots of the ZCO (c) and ZCO/CC (d) during GCPL test at 3.0 V.

The long-term GCPL test performed with a current density of 0.25 A g^{-1} is presented in Figure 3.14b. The ZCO displays serious capacity loss within 60 cycles, while the capacity of the ZCO/CC is still stable until the $\sim 110^{\text{th}}$ cycle. The delithiation capacities at the 60^{th} cycle of the ZCO/CC and ZCO electrodes are around 701 and 225 mAh g^{-1} , respectively. It is also noteworthy that the Coulombic efficiency of the ZCO/CC is always higher than the ZCO in both rate test and cycling test. Therefore, it is confirmed by the improved reaction reversibility the benefits of the combination of the conductive matrix and ZnCo₂O₄ nanoflakes, which not only allows the progressive penetration of the liquid electrolyte into the interior ZnCo₂O₄ but also facilitates

electron conduction through the CC. To examine the resistance evolution during long-term cycling test, the EIS plots were recorded every six cycles at 3.0 V during the cycling test. As shown in Figure 3.14c&d, a Nyquist plot consists of a semicircle at medium frequency and an inclined line at low frequency, related to the interface resistance and Li-ion diffusion in electrode, respectively. The ZCO electrode displays a high interface resistance at pristine state, which apparently decreases after the 1st cycle due to the formation of ionic conductive SEI layer, and increases dramatically after 36 cycles due to the electrode pulverization. In comparison, the interface resistance of the ZCO/CC electrode is low at the beginning and only increases slightly during long-term cycling, suggesting a fast reaction kinetics, which can be related to the well-maintained integrity of active particles and fast Li⁺ and electrons diffusion in the ZCO/CC electrode. [139,157,159,160,168] Such attractive properties are ascribed to the unique morphology of this binder-free electrode.

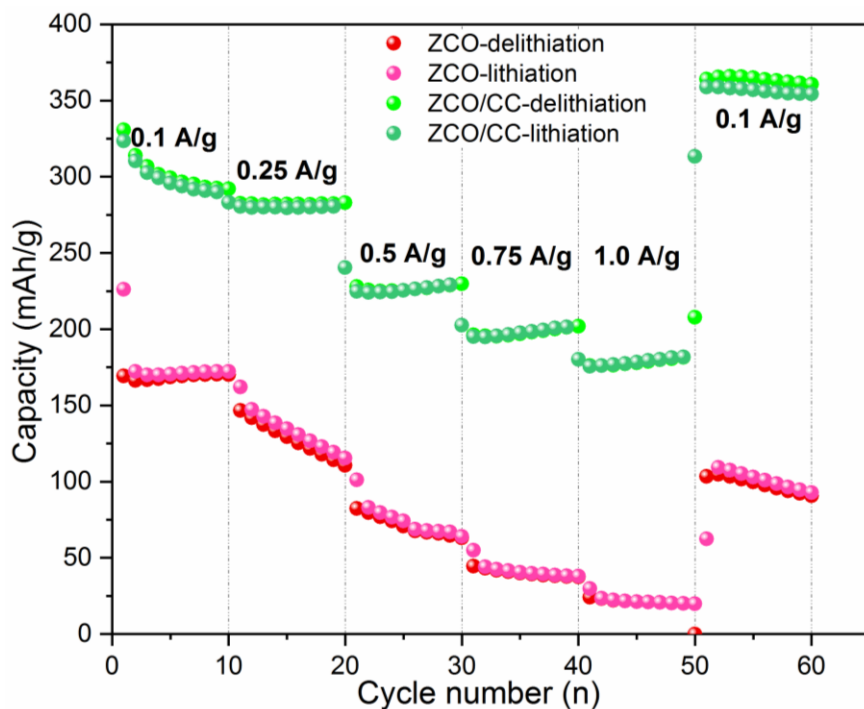


Figure 3.15 Rate capability of the ZCO and ZCO/CC based on the apparent specific capacity calculated from the whole electrode (including all electrode parts).

3.3 Conclusions

In this study, phase pure ZnCo₂O₄ was prepared by a hydrothermal method and used as anode material for LIBs. The mechanism of Li storage in spinel ZnCo₂O₄ is investigated by *in situ* SRD and XAS during galvanostatic cycling. Electrochemical insertion, conversion and alloying

reactions of the ZnCo₂O₄ electrode are discussed in detail. It is the first time that the intermediate phases (LiCo₂O₃ (at 1.16 V), CoO (at ~0.9 V) and ZnO (at ~1.1 V)) are evidenced during the 1st lithiation process. After the formation of CoO and ZnO, the two oxides can be further converted to metallic Zn (following by formation of LiZn), Co and Li₂O. In contrast to previous conclusion, during the first delithiation, CoO instead of Co₃O₄ is formed. As a binder-free anode for LIBs, the hierarchical ZCO/CC enables to deliver high specific capacity and shows excellent cycling stability (701 mAh g⁻¹ at 60th cycle at a specific current of 0.25 A g⁻¹). This appealing electrochemical behavior can be attributed to the large electrochemical active area and fast ion/electron transfer in the hierarchical ZCO/CC composite. However, since that Co is toxic and expensive, substituting Co by more environmental friendly Mn is more promising. Thus, the ZnMn₂O₄ anode material is investigated and discussed in the next chapter.

4 ZnMn₂O₄ and carbon-coated ZnO–MnO in LiBs

4.1 Introduction

Compared with ZnCo₂O₄, the spinel ZnMn₂O₄ is more appealing due to its lower redox potentials, lower toxicity, lower cost and environmental friendliness [169,170]. Similar with ZnCo₂O₄, the Li⁺ storage in ZnMn₂O₄ relies not only on the redox mechanism, but also on the alloying mechanism, which induces the reversible storage of 7 Li⁺ pfu (784 mAh g⁻¹). The spinel ZnMn₂O₄ converts to Li-Zn alloy and metallic Mn nanoparticles embedded in amorphous Li₂O during the 1st lithiation, then converts to MnO, ZnO and Li₂O during the subsequent delithiation [104,171]. Similarly, nanoscale particle size is proposed to enhance the cycling stability and rate capability, which can effectively alleviate the strains induced by volume change and improve the reaction kinetics through the large surface area and short Li⁺ diffusion pathway [102,172]. Moreover, the carbonaceous compositing can enhance the electronic conductivity and suppress excessive electrolyte decomposition by preventing direct contact between active particles and electrolyte [173,174].

This work focuses on the ZnMn₂O₄, carbon-derivative-coated ZnMn₂O₄ and carbon-coated ZnO–MnO, both for the preparation process and the electrochemical characterizations. The ZnMn₂O₄ nanoparticles were synthesized via a facile co-precipitation method and a subsequent calcination. The carbon-derivative-coated ZnMn₂O₄ and carbon-coated ZnO–MnO were prepared through a carbon-thermal reduction method. The calcination and carbonization processes were analyzed by HT-SRD and TGA to elucidate the phase formation and transition of ZnMn₂O₄. *In situ* SRD and EIS at different potentials during the 1st cycle were conducted to clarify the initial conversion process. The cycling and rate performances of the bare ZnMn₂O₄ and the carbon composites are measured and compared through GCPL and CV tests. The results of this work clarify the initial conversion process of the ZnMn₂O₄ during the 1st cycle and demonstrate that the carbon coating can effectively improve the cycling stability of the ZnMn₂O₄ anodes in LIBs.

The results in this chapter are partially published in the following publications:

Z. Zhao, G. Tian, A. Sarapulova, V. Trouillet, Q. Fu, U. Geckle, H. Ehrenberg, S. Dsoke, Elucidating the energy storage mechanism of ZnMn₂O₄ as promising anode for Li-ion batteries, *J.*

Mater. Chem. A. **6** (2018) 19381–19392. Reproduced by permission of The Royal Society of Chemistry, <https://pubs.rsc.org/en/content/articlelanding/2018/TA/C8TA06294C#!divAbstract>.

Z. Zhao, G. Tian, A. Sarapulova, G. Melinte, J.L. Gómez-Urbano, C. Li, S. Liu, E. Welter, M. Etter, S. Dsoke, Mechanism Study of Carbon Coating Effects on Conversion-Type Anode Materials in Lithium-Ion Batteries: Case Study of ZnMn₂O₄ and ZnO–MnO Composites, *ACS Appl. Mater. Interfaces.* **11** (2019) 29888–29900.
<https://pubs.acs.org/doi/10.1021/acsami.9b08539>.

4.2 Results and discussion

4.2.1 Phase transition of ZnMn₂O₄ during calcination and carbonization

The ZnMn₂O₄ nanoparticles were synthesized through oxalic acid co-precipitation method and calcination in air. The calcination process was studied by TGA/DSC and HT-SRD. The precursor obtained from co-precipitation (ZMO-pre) was subjected to TGA/DSC under O₂/Ar flow (11/31 mL min⁻¹) in order to study the formation of ZnMn₂O₄ (Figure 4.1a). This process involves two steps: (i) the endothermic dehydration at 145~175 °C producing the anhydrous oxalate, and (ii) the exothermic decomposition of the anhydrous oxalate at 300 ~ 350 °C, which is similar to the reported thermal decomposition of MnC₂O₄·2H₂O [175]. The weight fractions of the bound H₂O and the residual ZnMn₂O₄ are 19.2 wt. % and 44.3 wt. %, respectively, which are very close to the theoretical values: 19.7 wt. % (bound H₂O) and 43.7 wt. % (ZnMn₂O₄).

The pre-sintered precursor, ZMO-350, was subjected to HT-SRD measurement (Figure 4.1b). The patterns scanned at 20 °C and 350 °C indicate that the tetragonal spinel ZnMn₂O₄ (space group *I4₁/amd* with origin choice 2, ICSD #15305) forms after sintering at 350 °C for 3 h, even though the reflections are relatively weak and broad. Afterwards, the reflections become stronger and sharper as temperature goes up. However, some new reflections appear above 650 °C. Some reports assigned them to the formation of ZnMnO₃ [176]. In our case, there are neither an increase in mass (consequence of the oxidization from Mn(III) to Mn(IV), see TGA in Figure 4.1a) nor MnO characteristic reflections (disproportionation of Mn(III) to Mn(II) and Mn(IV), see Figure 4.1b) observed. It is not in agreement with ZnMnO₃ (Mn(IV)) formation. The Rietveld refinement (Figure 4.2) reveals that a cubic spinel phase ZnMn₂O₄ (space group *Fd $\bar{3}m$*) forms above 650 °C.

It was reported that the c/a ratio in the tetragonal phase is higher than 1 at room temperature, and can abruptly fall to unity after reaching a critical transformation temperature [177]. For this material, 650 °C is the critical transformation temperature. The lattice parameter of the cubic spinel phase at 800 °C is $a = 8.457(1)$ Å. Notably, the reflections corresponding to the cubic spinel phase completely disappear after cooling down to 20 °C. This reversible phase transformation also confirms that it is cubic spinel phase ZnMn₂O₄, rather than ZnMnO₃. Finally, the precursor was sintered at 500 °C for 1 h and 3 h for further analysis, named ZMO-1h and ZMO-3h, respectively.

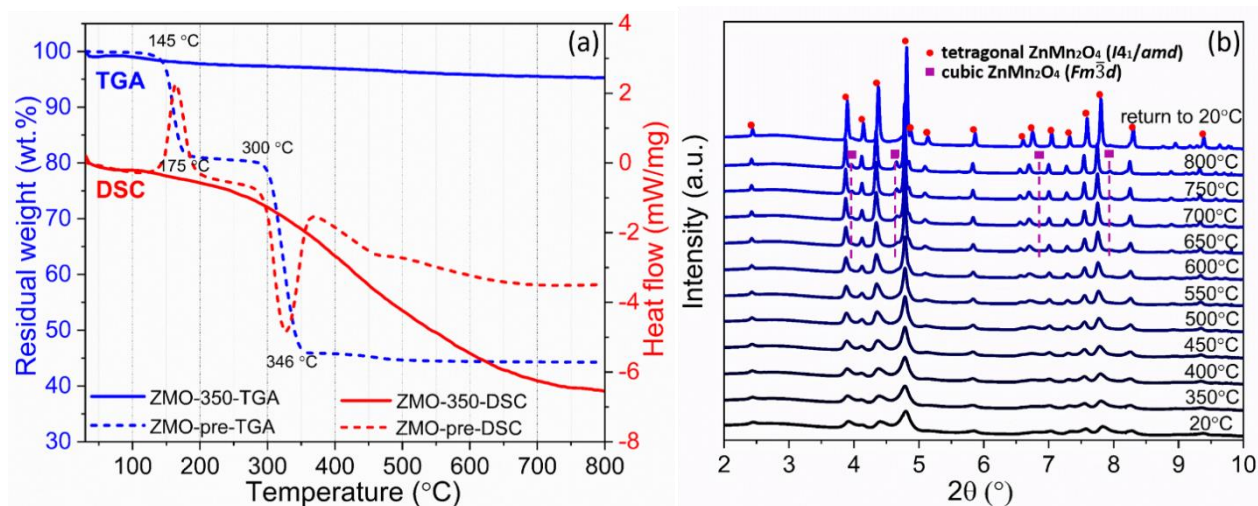


Figure 4.1 (a) TGA (blue) and DSC (red) curves of the ZMO-350 (solid line) and the ZMO-pre (dash line) with a heating rate of 10 °C min⁻¹ under O₂/Ar flow (11/31 mL min⁻¹), (b) HT-SRD ($\lambda=0.20714$ Å) patterns of the ZMO-350 during calcination up to 800 °C.

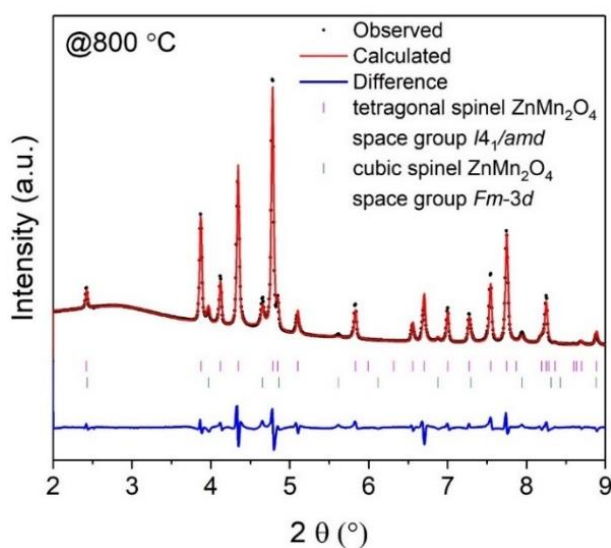


Figure 4.2 The SRD pattern of the scan at 800 °C in HT-SRD and the Rietveld refinement result for the ZMO-350 calcination in air.

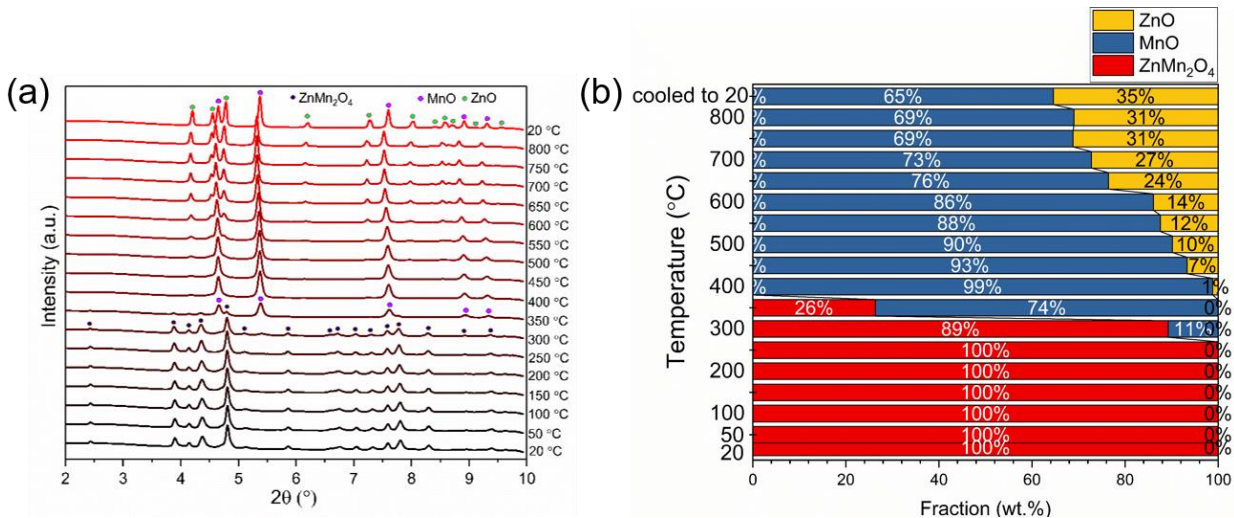


Figure 4.3 (a) HT-SRD ($\lambda=0.20737$ Å) patterns of the ZMO-1h/glucose precursor and (b) the evolution of the crystallized phase fractions during carbonization process.

Afterwards, the ZMO-1h was coated with carbon through a carbon-thermal reduction method with glucose as carbon source (ZMO-1h : glucose=2:1 by mass). However, the ZnMn₂O₄ can be partially reduced to ZnO–MnO composite during carbonization. Therefore, HT-SRD has been used to monitor the phase transition. As shown in Figure 4.3a, the ZnMn₂O₄ phase (#COD 96-901-2843, *I4₁amd*) forms after sintering at 500 °C in air (the 20 °C pattern at the bottom). The ZnMn₂O₄ phase remains stable below 250 °C, and then gradually converts to MnO (#COD 96-101-0394, *Fm $\bar{3}$ m*) and amorphous ZnO (250~400 °C). Above 400 °C, the amorphous ZnO starts to crystallize (ZnO, #COD 96-210-7060, *P6₃mc*). Based on Rietveld refinement calculation (Figure 4.3b), it is revealed that the phase fraction of crystallized ZnO increases slowly upon heating (400~750 °C), whereas the crystallized MnO forms faster at lower temperatures (300~400 °C). This can be attributed to the different rates of nuclei formation and growth for the ZnO and MnO. After cooling down from 800 °C to 20 °C, the sample is composed of MnO (65 wt.%) and ZnO (35 wt.%), which well agrees with the theoretical molar ratio Mn:Zn=2:1 (63.55 wt.% MnO and 36.45 wt.% ZnO). Moreover, the unit cells of ZnMn₂O₄ and MnO expand as the temperature increases. In detail, ZnMn₂O₄ expands mainly along the *c* axis. The parameter *c* enlarges linearly from 9.227 Å at 20 °C to 9.306 Å at 350 °C ($\Delta c/c = 0.86\%$), while the parameter *a*(*b*) shows less changes ($\Delta a/a = 0.28\%$), as shown in Figure 4.4a&b. In contrast, the unit cell of ZnO shrinks from 400 °C to 500 °C, indicating the crystallization of ZnO (Figure. 4.4c). Besides, the carbonization of glucose mainly occurs in the temperature range of 200~400 °C, and the weight losses of pure glucose are ~50 wt. % at 300

°C and 80 wt. % at 400 °C [178]. Therefore, 300 °C, 400 °C and 500 °C have been chosen as carbonization temperatures for further study, namely carbon-derivative-coated ZnMn₂O₄ (CZMO-300), and carbon-coated ZnO–MnO (CZMO-400 and CZMO-500).

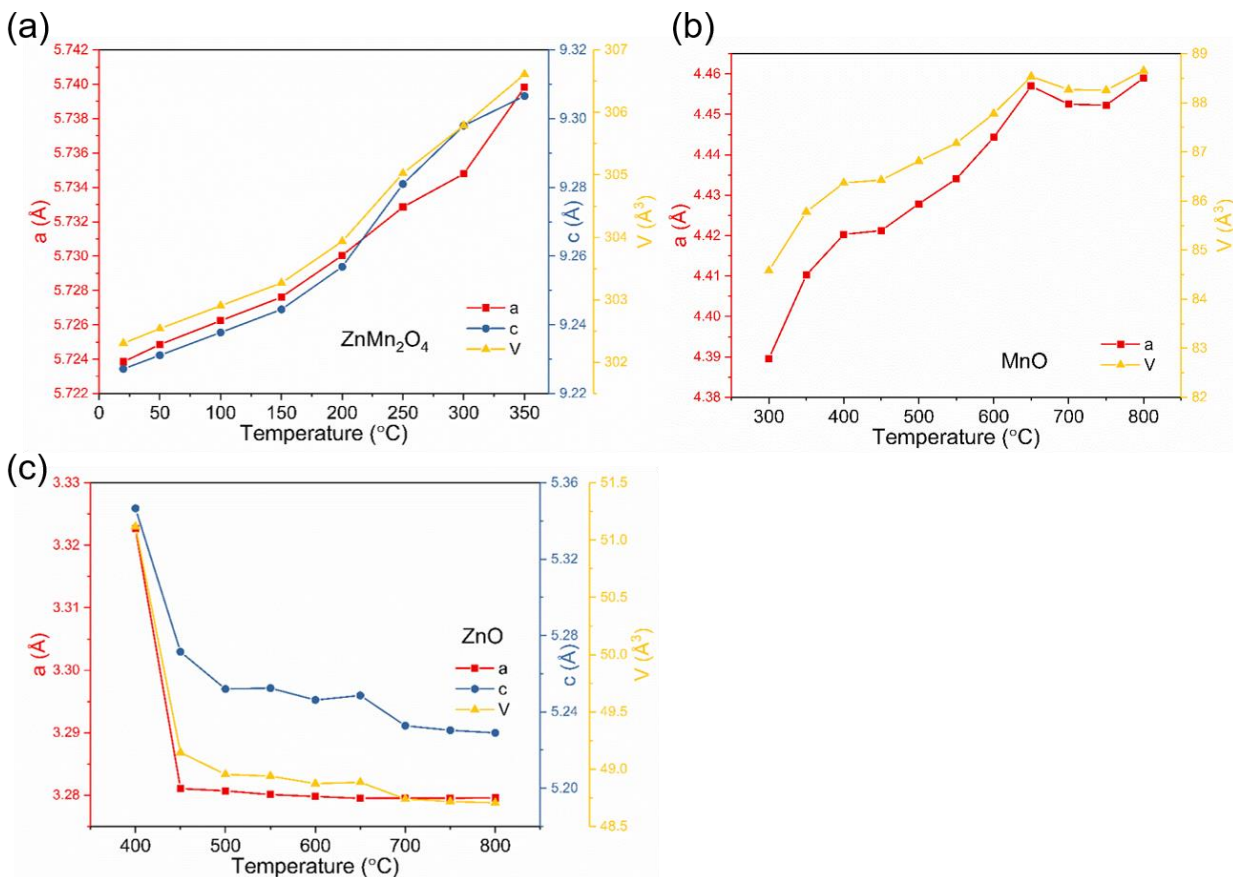


Figure 4.4 The change of lattice parameters of (a) ZnMn₂O₄, (b) MnO and (c) ZnO upon temperature increasing.

4.2.2 Morphology and structure

The morphology and phase composition of the as-prepared samples are analysed. As shown in [Figure 4.5a](#), the ZMO-3h displays a layered octahedral shape which comes from the shape of co-precipitation precursor. The open space between the layers can facilitate the transfer of Li⁺ between the electrolyte and the metal oxide. An overview image is shown in [Figure 4.6](#) which confirms the uniform morphology. In [Figure 4.5b](#), it can be seen that the layered structure consists of a number of nanoparticles with the average size of 33 ± 7 nm ([Figure 4.5c](#)). As confirmed by EDS mapping ([Figure 4.5d](#)), the elements O, Zn, and Mn are homogeneously distributed. Such uniform

nanoparticles are beneficial to relieve the capacity fading induced by volume variation and particle pulverization [179].

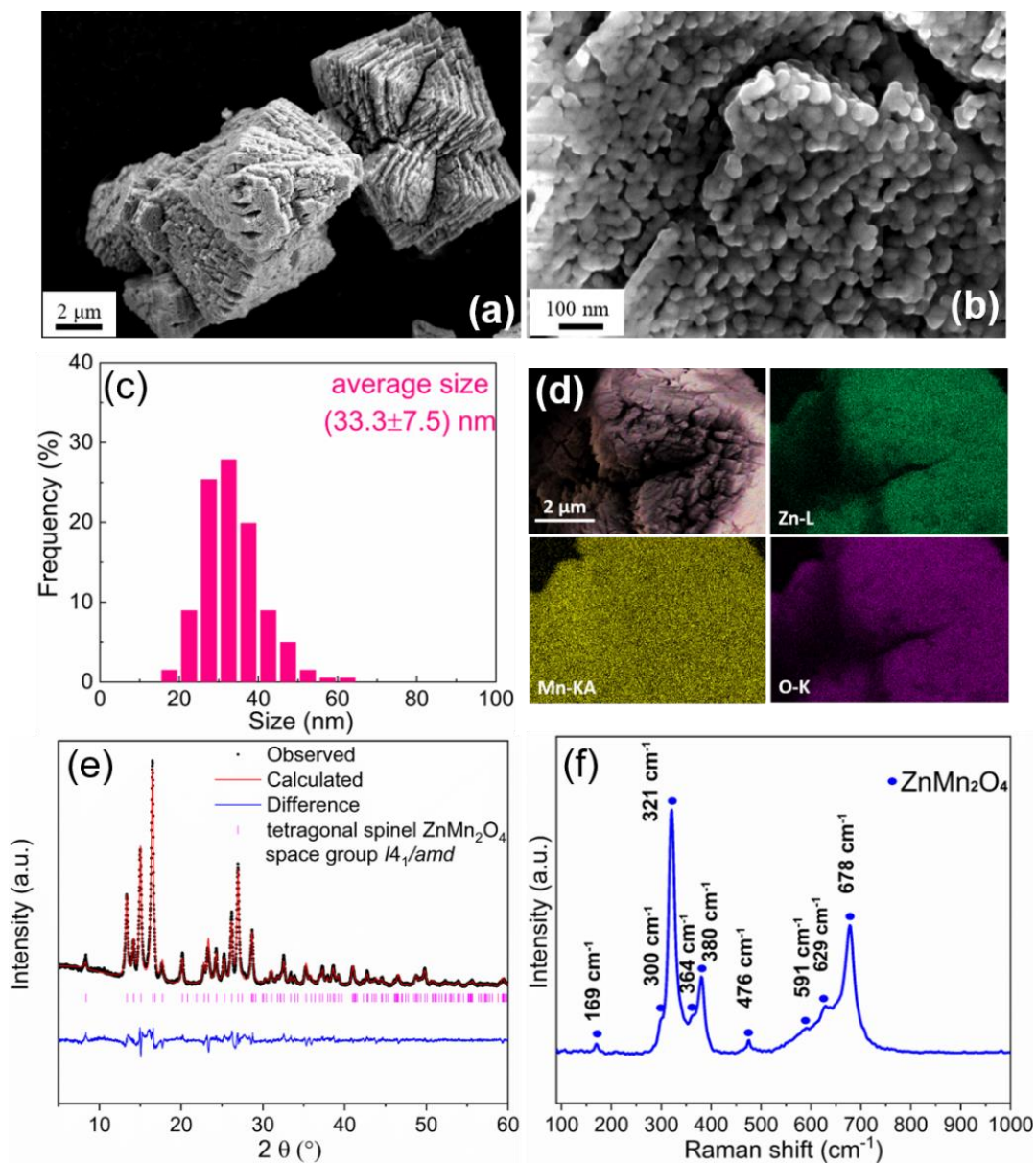


Figure 4.5 (a, b) SEM images at different magnifications, (c) the statistical particle size distribution, (d) EDS mapping, (e) XRD pattern (Mo-K_{α1}) and the Rietveld refinement result and (f) Raman (532 nm) spectrum of the ZMO-3h.

XRD (Mo-K_{α1}) test and the Rietveld refinement were conducted to analyse the phase composition of the ZMO-3h (Figure 4.5e). The refinement confirms the single phase tetragonal spinel ZnMn₂O₄, with space group of *I4₁/amd* with origin choice 2 (ICSD #15305). In the given structure model, the Zn atoms occupy the 4a tetrahedral sites and the Mn atoms occupy the 8d

octahedral sites. The lattice parameters of the obtained compound are as following: $a = 5.726(2)$ Å, $c = 9.204(4)$ Å ($c/a = 1.61$), and the unit cell volume is $301.8(2)$ Å³. Raman spectroscopy provides the local crystal structure information. According to the factor group theory, the tetragonal spinel ZnMn₂O₄ possesses 10 Raman modes: $\Gamma = 2A_{1g} + 3B_{1g} + B_{2g} + 4E_g$ [180]. On the experimental spectrum, only 9 bands attributed to the tetragonal spinel ZnMn₂O₄ vibration modes are visible (Figure 4.5f). In detail, it is assumed that the bands above 600 cm⁻¹ are modes due to the oxygen motion in the tetrahedral AO₄ (ZnO₄) sites, which can be considered as A_{1g} symmetry modes [181]. While the modes attributed to the oxygen motion in the octahedral BO₆ (MnO₆) sites are mostly at lower frequencies [182]. The band at 300 cm⁻¹ is directly influenced by the stretching vibration of Zn–O bond in tetrahedral units [180]. In summary, Raman and XRD confirm the successful synthesis of the tetragonal spinel ZnMn₂O₄.

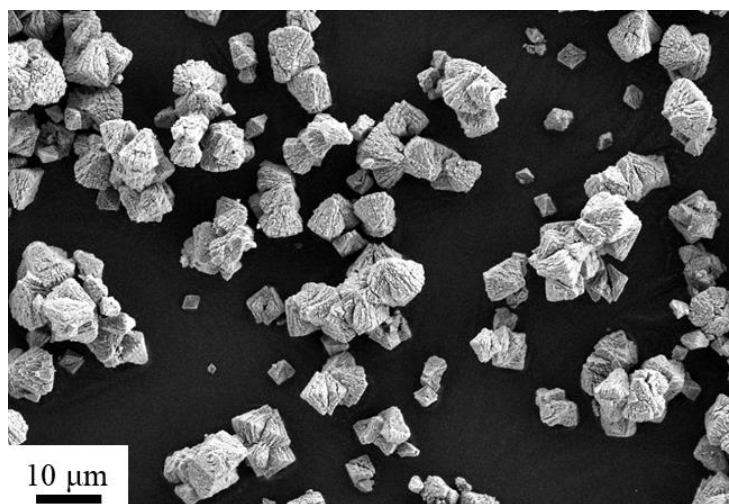


Figure 4.6 FESEM image of the ZMO-3h at low magnification.

The morphology of the ZMO-1h and CZMO samples is shown in Fig. 4.7. As observed from Figure 4.7a&b, the ZMO-1h displays clusters of flakes with a size of 2~5 μm composed of interconnected nanoparticles (30~50 nm), while the CZMO-300 looks like large blocks, due to the linking of carbon derivative (Figure 4.7c). As shown in Figure 4.7d, metal oxide nanoparticles are surrounded by the carbon derivative. When calcined at 400 °C and 500 °C, the glucose is well carbonized into thin carbon layers. In detail, the CZMO-400 looks like porous blocks consisting of carbon-coated nanoparticles (Figure 4.7e). The CZMO-500 (Figure 4.7g) shows a similar morphology like the bare ZMO-1h. Moreover, the CZMO-400 and CZMO-500 are composed of smaller nanoparticles (average size of 15~30 nm) due to the collapse of the original particles during

the phase transition from ZnMn₂O₄ to ZnO–MnO composite (Figure 4.7f&h). The smaller particle sizes benefit to the rate performance of the electrode materials [183]. The EDS result confirms that Zn, Mn and O are homogeneously distributed in all the as-prepared samples, and the surface of the CZMO samples are fully covered with carbon (Figure 4.8).

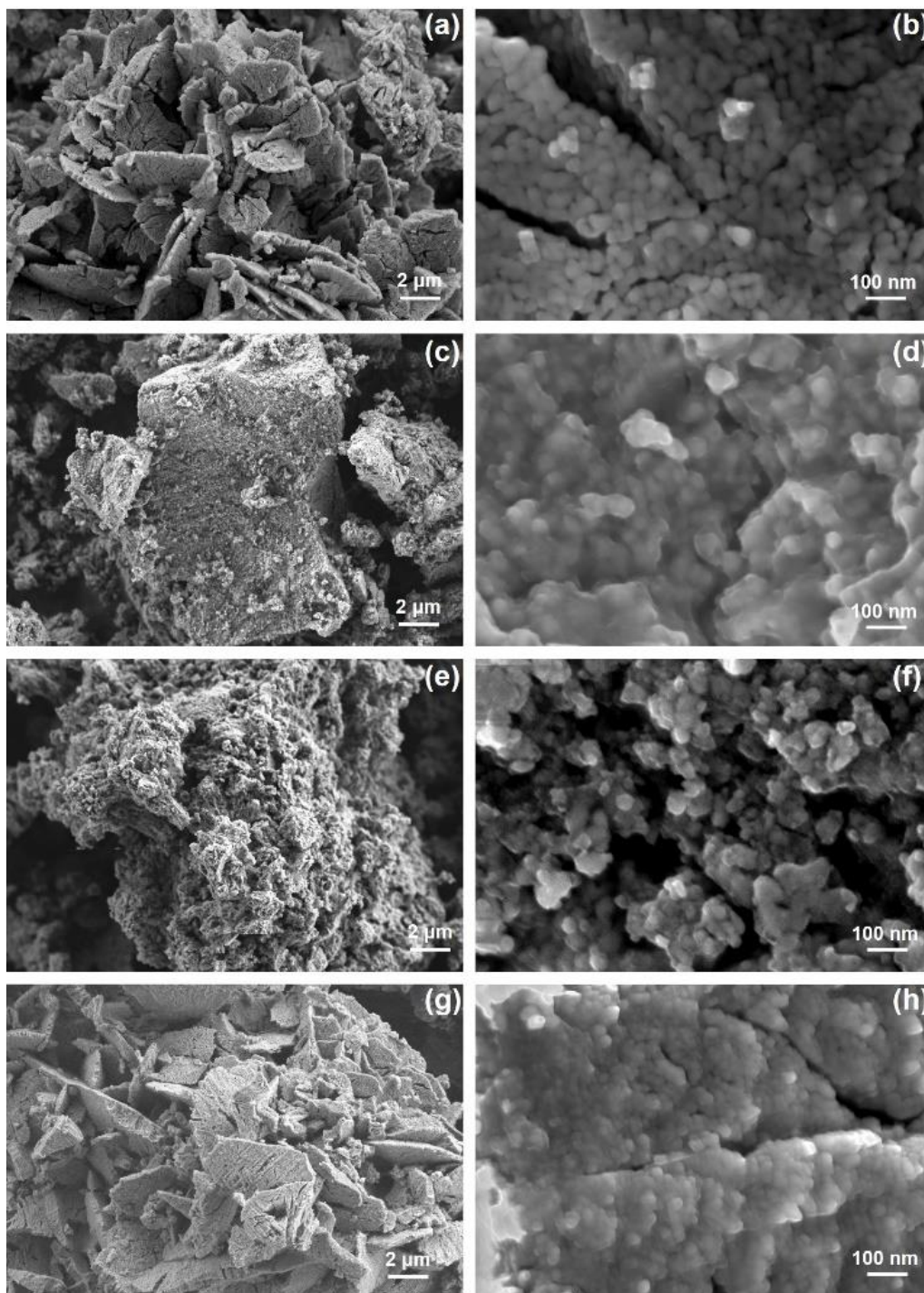


Figure 4.7 SEM images: (a,b) ZMO-1h, (c,d) CZMO-300, (e,f) CZMO-400 and (g,h) CZMO-500.

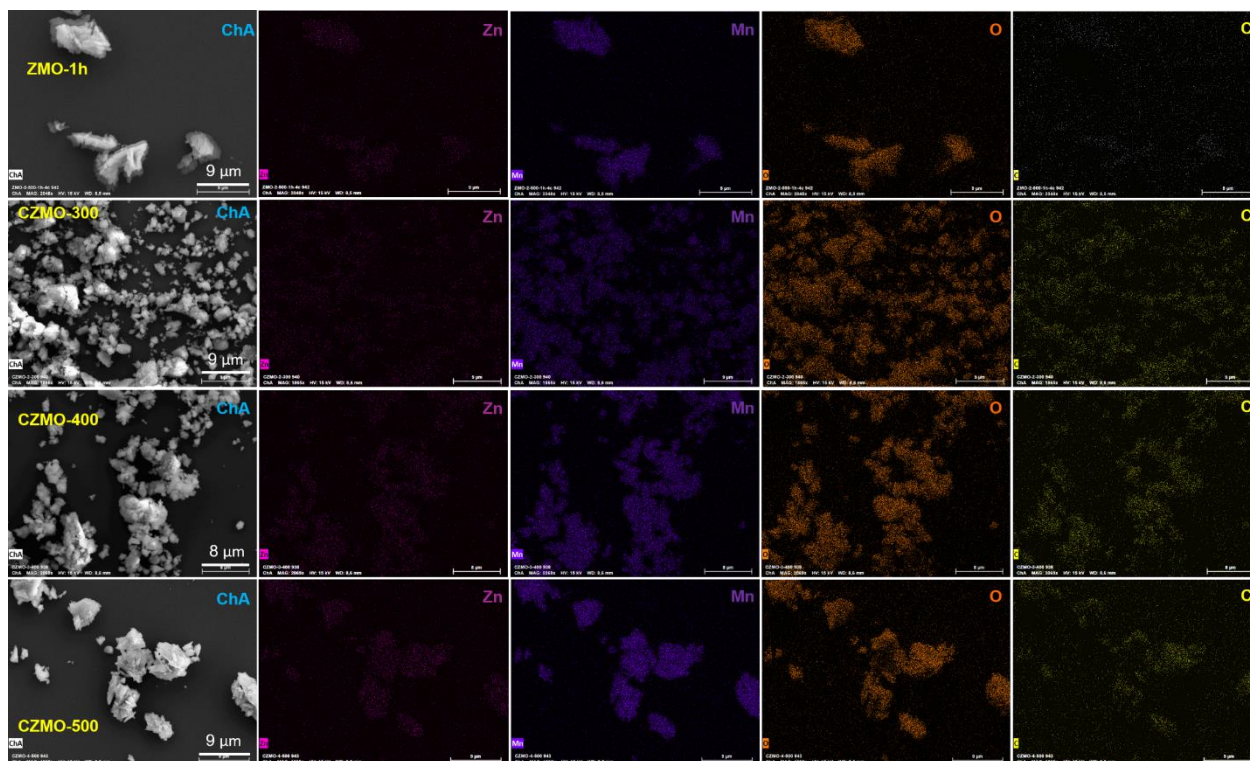


Figure 4.8 EDS mapping figures of the as-prepared samples: ZMO-1h, CZMO-300, CZMO-400 and CZMO-500.

The crystal structure of the ZMO-1h and the CZMO samples has been characterized by XRD (Mo $K_{\alpha 1}$), as shown in [Figure 4.9a](#). It is evident that the tetragonal spinel ZnMn₂O₄ is successfully synthesized, as previously confirmed by HT-SRD. The carbon-coated samples (CZMO-400 and CZMO-500) show a clear reduction from ZnMn₂O₄ to ZnO–MnO. Crystallized phase composition of the as-prepared samples has been calculated according to Rietveld refinement (see [Figure 4.10](#)), and it is in good agreement with the HT-SRD results. In detail, the CZMO-300 is composed of 89 wt.% ZnMn₂O₄ and 11 wt.% MnO, whereas the CZMO-400 consists of 91 wt.% MnO and 9 wt.% ZnO, and the CZMO-500 is composed of 81 wt.% MnO and 19 wt.% ZnO. It is noteworthy that amorphous ZnO in these samples can't be detected by XRD.

To determine the content of coated carbon or carbon-derivative, TGA was performed from 30 °C to 800 °C in Ar/O₂ flow (3:1 by volume). As shown in [Figure 4.9b](#), the ZMO-1h shows high thermal stability with no obvious weight loss during heating, while the other three samples display a weight main loss at ~300 °C, due to the combustion of the coated carbon or carbon-derivative. Except for the CZMO-300, the weight of the CZMO-400 and CZMO-500 increases at an onset

temperature of ~ 284 °C, which can be attributed to the oxidation of MnO. Therefore, the weight change due to both the MnO oxidation and the carbon combustion results in a fluctuation of the residual weight around 370 °C. Finally, the carbon or carbon-derivative contents of the coated layers in CZMO-300, CZMO-400 and CZMO-500 are calculated to be 22.2 wt.%, 15.7 wt.% and 12.3 wt.%, respectively. The EDS result also shows a similar trend for their carbon contents of 25.3 wt.%, 12.5 wt.%, 10.4 wt.%, respectively.

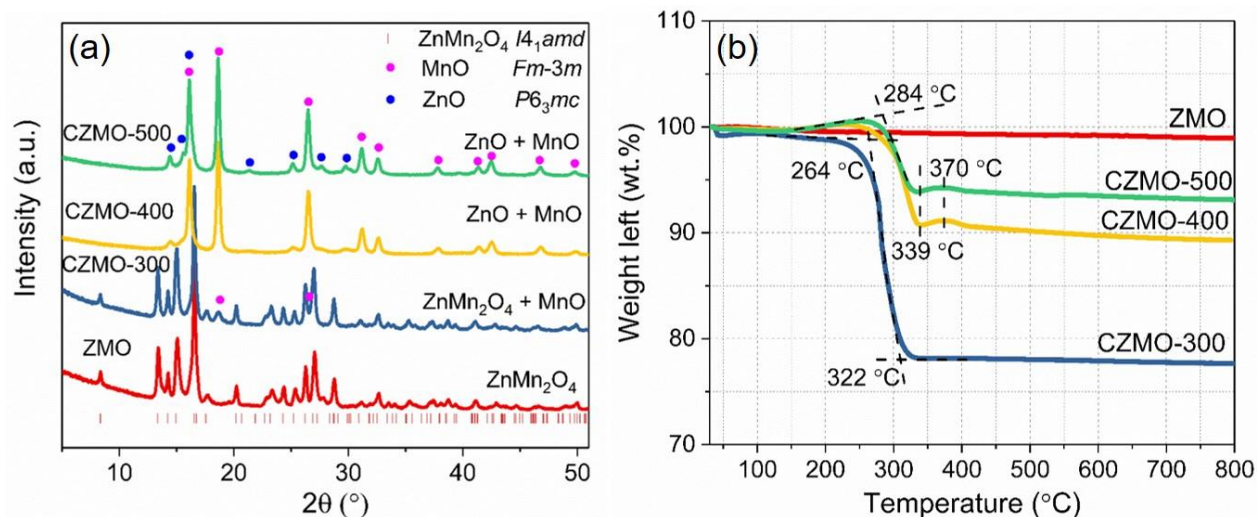


Figure 4.9 (a) XRD (Mo K_{α1}) patterns and (b) TGA curves of the noted samples.

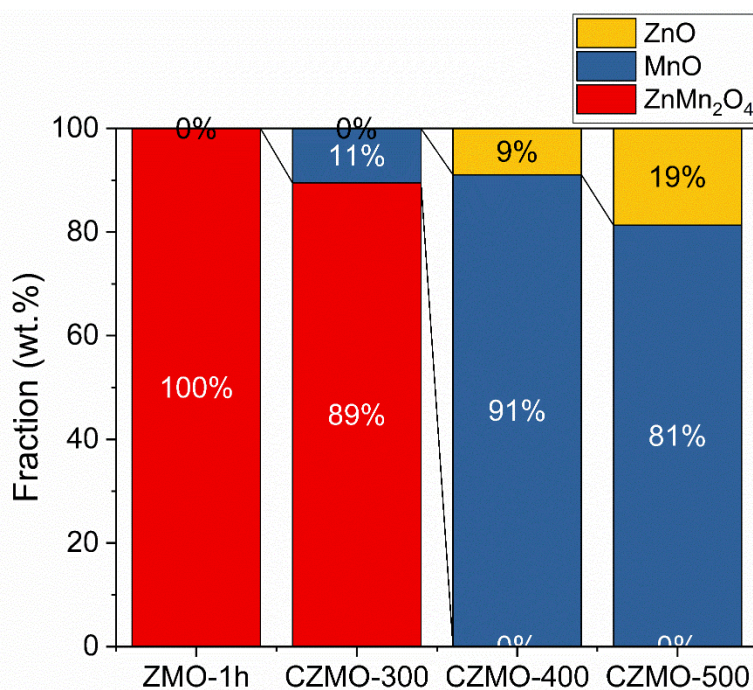


Figure 4.10 Crystallized phase composition of the as-prepared samples obtained by XRD (Mo K_{α1}) test and Rietveld refinement.

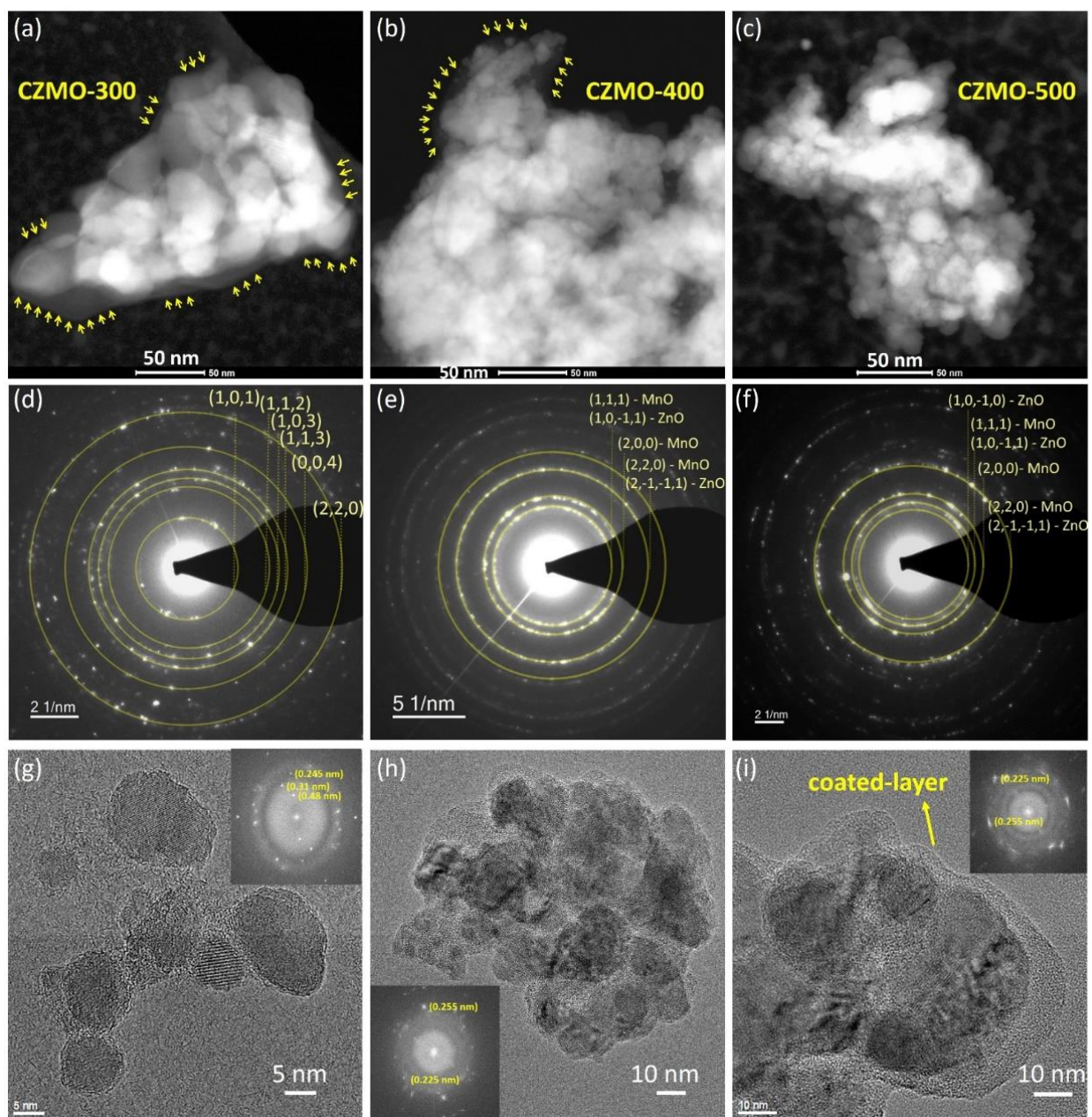


Figure 4.11 STEM - HAADF, SAED and HRTEM images of the CZMO-300 (a, d&g), CZMO-400 (b, e&h), and CZMO-500 (c, f&i). The insets in g, h and i represent the fast Fourier transform (FFT) of the corresponding HRTEM images.

The morphology and phase composition of the CZMO samples are also investigated by transmission electron microscopy. The HAADF images presented in [Figure 4.11 a~c](#) show a few nanometers thick carbon layer coating the CZMO-300 particles, a thinner and less homogeneously distributed layer around the CZMO-400 sample and a barely visible coating for the CZMO-500. Moreover, STEM-HAADF imaging shows that CZMO-400 and CZMO-500 nanoparticles are

smaller as compared with the CZMO-300 sample, in agreement with the analysis of SEM imaging. The results of the SAED analysis of the crystal phase evolution throughout the heat treatment are shown in Figure 4.11d~f. The diffraction patterns of the CZMO-300 sample can be identified as the ones of the ZnMn₂O₄ spinel structure, whereas the ones of the CZMO-400 and CZMO-500 samples correspond to the MnO and ZnO phases. The corresponding patterns of the ZnMn₂O₄ phase are not present in the CZMO-400 and CZMO-500 diffractions and this can be easily highlighted by following the $d_{(101)} \sim 0.48\text{nm}$ reflection that cannot be observed in the last two samples. High-resolution TEM imaging (Figure 4.11g~i) shows a similar evolution of the crystal phases as the electron diffraction. The crystal lattice fringes exhibited by the CZMO-300 nanoparticles can be indexed as the $d_{(101)} \sim 0.48\text{nm}$, $d_{(112)} \sim 0.31\text{nm}$ and $d_{(113)} \sim 0.245\text{nm}$ spacing of the ZnMn₂O₄ spinel phase. These reflections disappear for the CZMO-400 and CZMO-500 samples. Moreover, the HRTEM image of the CZMO-500 sample shows the presence of a homogenous carbon layer around some nanoparticles.

Furthermore, N₂ adsorption-desorption isotherms and the corresponding pore size distributions are shown in Figure 4.12. The ZMO-1h and the CZMO-400 display SSAs of 44 m² g⁻¹ and 31 m² g⁻¹, respectively. The pore sizes of the two samples are mainly distributed in 2~20 nm. This is because that the coated carbon layer can block some mesopores (2~10 nm), leading to the lower SSA of the CZMO-400 sample [184].

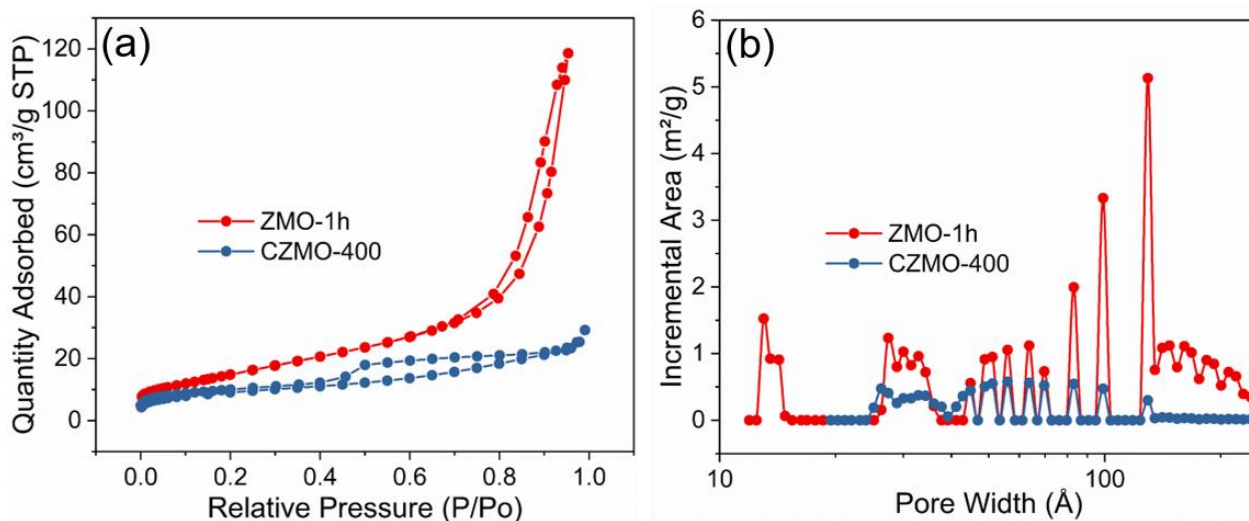


Figure 4.12 Nitrogen adsorption-desorption isotherms (a) and the related pore size distributions (b) of the ZMO-1h and CZMO-400.

To further analyze the coated carbon or carbon-derivative in the CZMO samples, Raman and FTIR studies were conducted (Figure 4.13). In low Raman shift range (100~800 cm⁻¹), the modes of the ZMO-1h and CZMO-300 are similar, confirming the formation of tetragonal spinel ZnMn₂O₄ [158,185], whereas the modes of the CZMO-400 and CZMO-500 become broader and shift to lower Raman shift, indicating the phase transition from ZnMn₂O₄ to MnO [186]. The two broad modes at 1000~1800 cm⁻¹, corresponding to defective and graphitic carbon (D band and G band), appear in the spectra of the CZMO-400 and CZMO-500, confirming that the carbon-coated layer is fully formed above 400 °C and that the coated layer in the CZMO-300 is a carbon-derivative. In Figure 4.14, the fitting of the D band and G band are performed by using four vibration modes (G ~1580 cm⁻¹, D1 ~1350 cm⁻¹, D3 ~1500 cm⁻¹, and D4 ~1200 cm⁻¹) [187]. The I_{D1}/I_G intensity (peak area) ratios of the CZMO-400 and CZMO-500 are calculated to be 2.44 and 1.57, respectively. This indicates a higher degree of graphitization of the coated carbon in the CZMO-500. In Figure 4.13b, the FTIR spectra show that the bands of glucose disappear after the heat treatment. In the spectra of the CZMO-300, the bands located at ~1580 cm⁻¹, ~1408 cm⁻¹, and ~1084 cm⁻¹ correspond to the functional groups of C=C, O–H, and C–O, respectively [188]. Above 400 °C, these peaks related to the organic functional groups almost disappear, demonstrating the formation of the graphitic carbon.

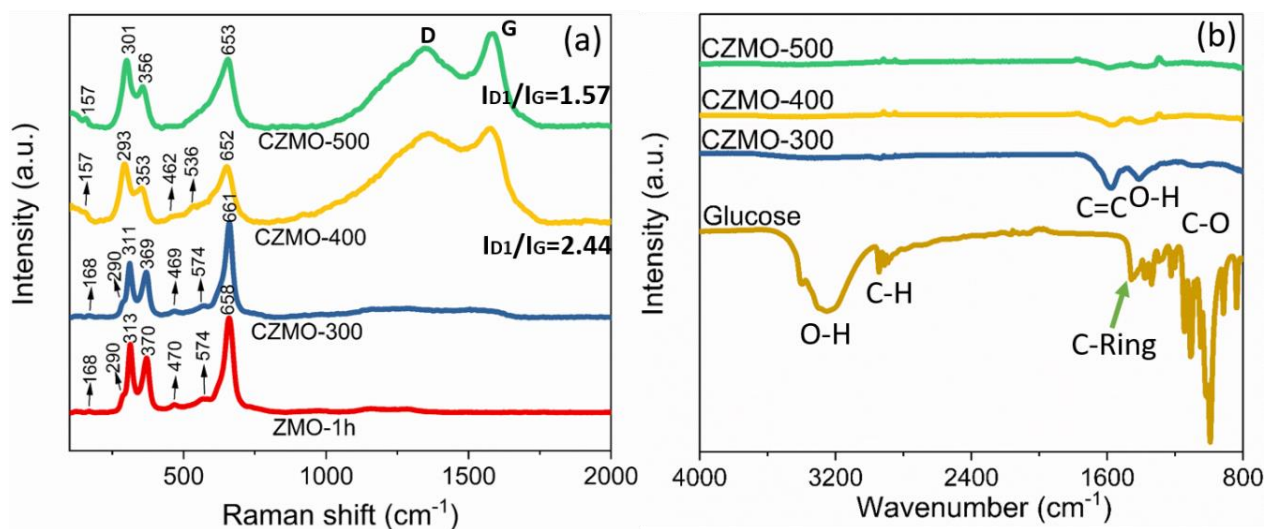


Figure 4.13 (a) Raman (633 nm) spectra and (b) FTIR spectra of the ZMO-1h and CZMO samples.

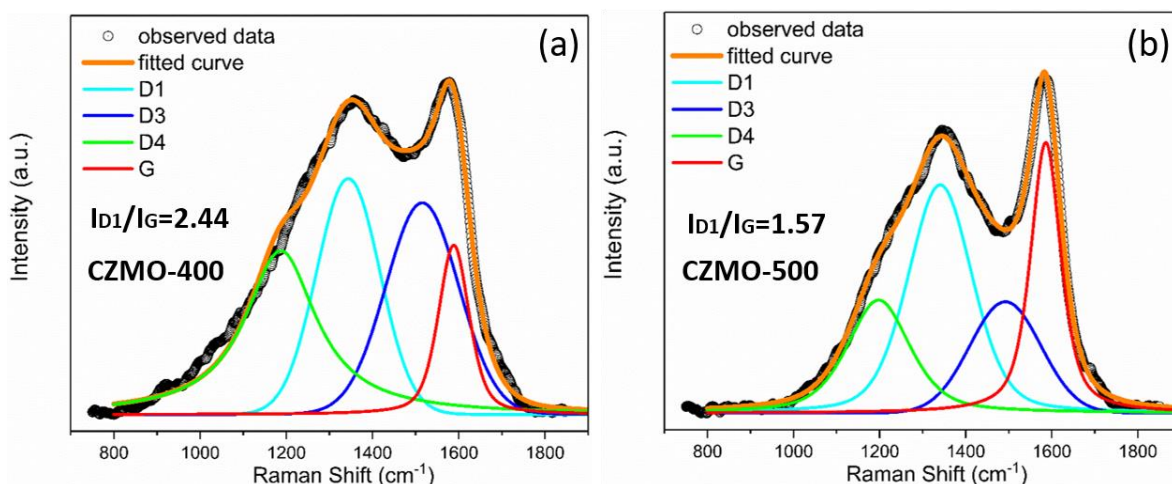


Figure 4.14 Raman (633 nm) spectra of the CZMO-400 (a) and CZMO-500 (b), curve fitting was performed using four Gaussian shape bands.

4.2.3 *In situ/ex situ* characterizations during the 1st cycle

To analyze the electrochemical properties during the 1st cycle, GCPL and CV tests were performed on the ZMO-3h (Figure 4.15). The initial lithiation and delithiation capacities are ~1400 and ~900 mAh g⁻¹, respectively, which are both higher than the theoretical capacities. During lithiation, there is a short potential plateau at ~1.4 V in the galvanostatic profile. It can be related to the broad peak at 1.28 V in the CV curve, indicating the reduction of Mn(III) to Mn(II) [189]. The subsequent sloped decline (1.4 V ~ 0.5 V) in the potential profile can be attributed to SEI formation, evidenced by a weak peak at ~0.9 V in the CV curve [190,191]. The long potential plateau at ~0.40 V corresponds to the pronounced peak at 0.26 V in the CV curve. It is attributed to the reduction of Mn(II) and Zn(II) to Mn(0) and Zn(0) [189]. Metallic Zn is readily alloyed with Li (form LiZn₄) once it is formed and continuous alloying reactions occur below 0.5 V [192,193]. At last, a sloped potential appears between 0.30 V and 0.01V. It is related to the current plateau near 0.10 V in the CV curve, corresponding to the Li-Zn alloying reaction and extra Li storage in the interface of metal nanograins and Li₂O due to space charge storage mechanism caused by nanosize effect [153,154]. Upon delithiation, the sloped potential from 0.01 V to ~1.00 V can be attributed to the Li-Zn de-alloy [194]. Then two separated plateaus appear at ~1.20 V and ~1.50 V, corresponding to the two broad oxidation peaks at 1.21 V and 1.52 V in the CV curve. They are assigned to the oxidation of Mn(0) and Zn(0) to Mn(II) and Zn(II), respectively [181]. The subsequent increase slope in the potential profile from ~1.70 V to 3.00 V (~100 mAh g⁻¹) can be

related to the decomposition of the SEI film, which is in agreement with S. Laruelle *et al.*'s report [195].

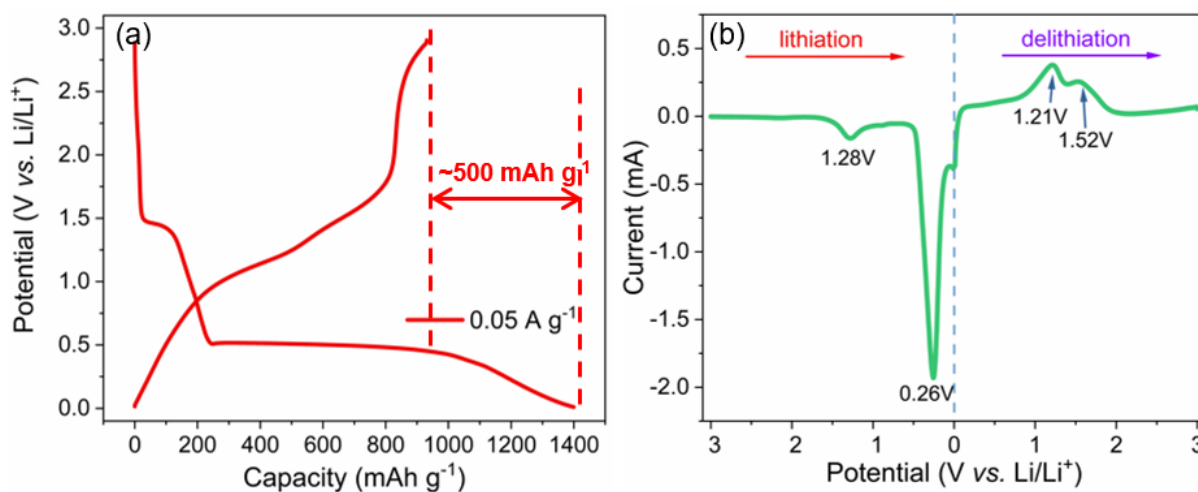


Figure 4.15 Electrochemical characterization of the ZMO-3h during the 1st cycle: (a) the potential profile at specific currents of 0.05 A g⁻¹, (b) the CV curve scanned at 0.1 mV s⁻¹.

To investigate the phase transformation of the ZnMn₂O₄ anode during the 1st cycle, *in situ* SRD was performed during 70 mA g⁻¹ GCPL cycling, and the SRD patterns and the relevant potential profile are shown in Figure 4.16a&b. During lithiation, the reflections related to ZnMn₂O₄ gradually fade out until the scan 90 (8.8 Li pfu, 0.20 V), indicating the conversion from crystalline phase to amorphous phase. At the same time, a series of new reflections appear at scan 10 and disappear at scan 90 (1.0~8.8 Li pfu, 0.41~0.20 V), which can be attributed to the formation and the decomposition of an intermediate phase LiZnMn₂O₄ [176]. The coexistence of LiZnMn₂O₄ and ZnMn₂O₄ during the conversion process, related to the long potential plateau from scan 10 ~ scan 90, can be ascribed to slow insertion kinetics (ZnMn₂O₄ → LiZnMn₂O₄). The Li ions intercalate into the residual ZnMn₂O₄, and at the same time the LiZnMn₂O₄ converts to the metallic Zn, Mn and the Li₂O, which cannot be observed in the SRD patterns due to their nanoscale and amorphous structure [159]. The most intensive LiZnMn₂O₄ reflections are observed at scan 28 (2.6 Li pfu at 0.42 V). As shown in Figure 4.17, the refinement fitting of scan 28 confirms that the LiZnMn₂O₄ shares a similar tetragonal spinel structure with ZnMn₂O₄ (space group *I4₁/amd* with origin choice 2, ICSD #15305), where Zn ions move from tetrahedral 4a sites to octahedral 8c sites, and Li ions occupy 4a Zn sites and also octahedral 8c sites. The refined lattice parameters of the intermediate phase are as following: $a = 6.008(2) \text{ \AA}$, $c = 8.965(4) \text{ \AA}$ ($c/a = 1.492$). And the unit cell volume is

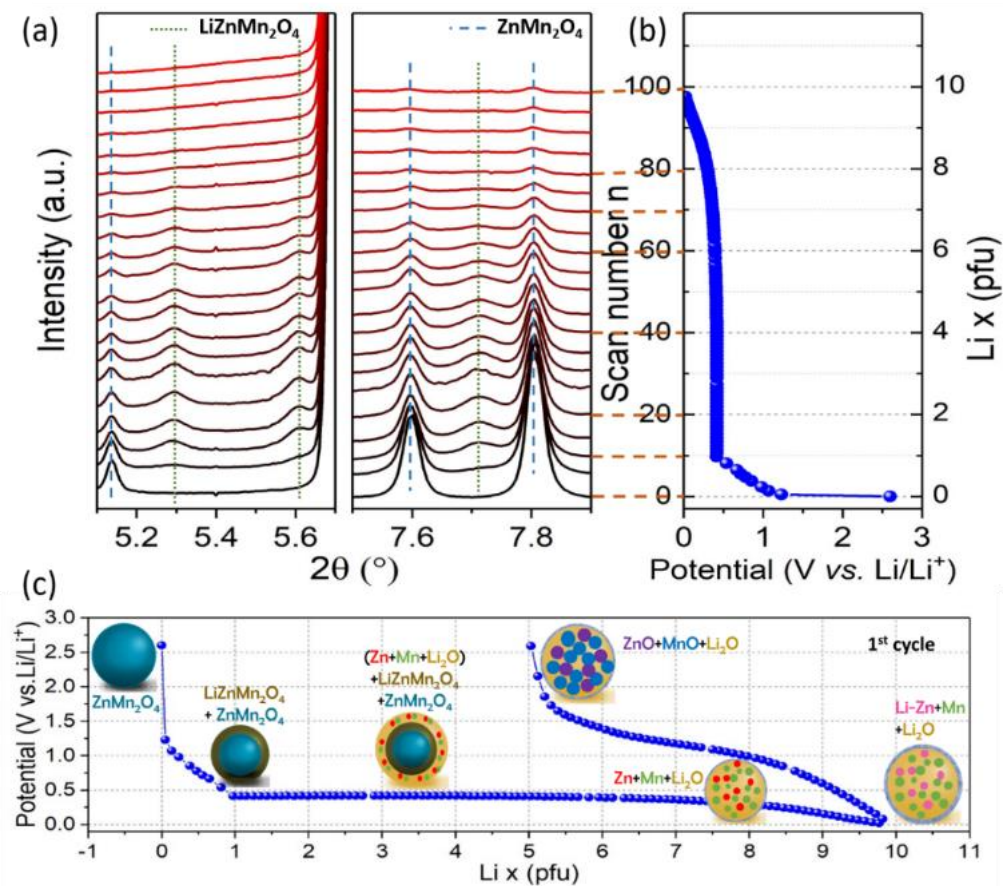


Figure 4.16 (a) The *in situ* SRD ($\lambda=0.20720$ Å) patterns for the ZMO-3h during 1st lithiation and (b) the relevant potential profile (70 mA g⁻¹), (c) the schematic diagram of the ZnMn₂O₄ phase transition during the 1st cycle.

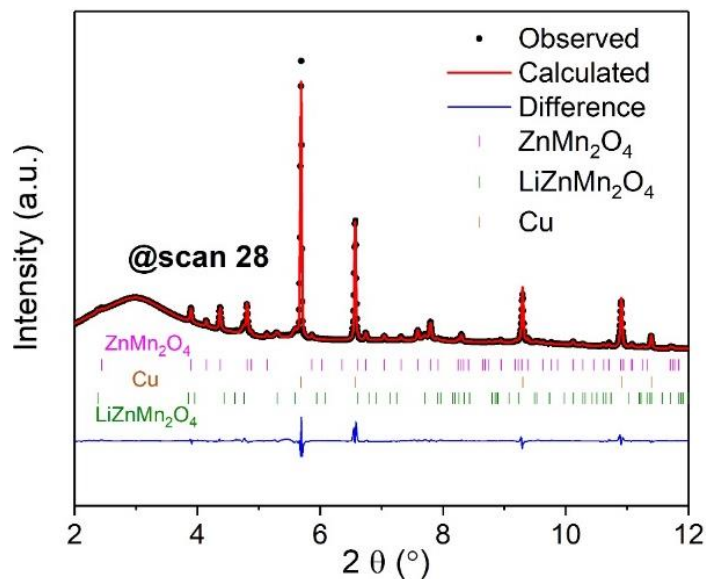
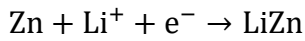
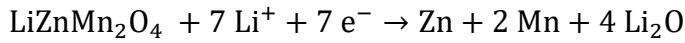
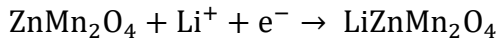


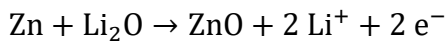
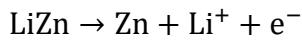
Figure 4.17 *In situ* SRD pattern of scan 28 and the Rietveld refinement result (ZMO-3h).

323.7(2) Å³. After scan 90 (8.8 Li pfu at 0.20 V), the reflections corresponding to ZnMn₂O₄ and LiZnMn₂O₄ are not detected anymore, indicating the end of the further phase transformation to Zn+2Mn+4Li₂O. From scan 90 to scan 98 (8.8~9.8 Li pfu insertion, 0.20~0.02 V), 1.0 Li pfu are inserted due to the Li-Zn alloying and extra space charge [154,196]. During delithiation, the SRD patterns display no obvious reflections because the electrode material becomes amorphous [197]. The phase transition process of ZnMn₂O₄ anode during the 1st cycle is summarized in the schematic graph of Figure 4.16c and the following equations:

1st lithiation:



1st delithiation:



The Nyquist plots recorded at different (de)lithiation potentials during the 1st cycle with a constant current density of 0.1 A g⁻¹, as shown in Figure 4.18a, can be fitted with three equivalent circuits (Figure 4.18b). The circuit (1) is applied to fit the plots obtained on the cells at delithiated state (OCV and 3.0 V). The circuit (2) is used for fitting the plots of the cells at half-lithiated/half-delithiated state (lithiated: 1.7 V, 1.0 V; delithiated: 1.4 V, 2.2 V). And the circuit (3) is used for fitting the cells at lithiated state (lithiated: 0.6 V, 0.1 V; delithiated: 0.01 V, 0.6 V). The fitting plots are shown in Figure 4.19. In the equivalent circuit, the resistance of electrolyte (R_{el}) is related to the intercept with the real axis at high-frequency. The resistance related to the SEI film (R_{SEI}) and the relative double layer capacitance (Q_{dl1}) correspond to the first semicircle at mid-high frequency (400~3 Hz) [198]. The second semicircle at lower frequency (2~0.06 Hz) is assigned to the resistance of charge transfer (R_{ct}) and the related double layer capacitance (Q_{dl2}) [198]. The inclined line at low frequency represents the Warburg diffusion (solid Li⁺ diffusion in the bulk electrode material), where a C is series connected with the Warburg element (W) and corresponds to the capacitive charge storage after finite-length diffusion. Constant phase elements (CPEs) are used to

fit the double-layer capacitance at the active material surface (Q_{dl1}) and at the surface of crystallites (Q_{dl2}), considering the deviations from the ideal behavior of a perfect capacitor [199]. The diffusion coefficient (D_{Li}) can be calculated according to the Eq. 4.1 [200]:

$$D_{Li} = \frac{1}{2} \left(\frac{RT}{Az^2 F^2 c_{Li} \sigma} \right)^2 \quad (\text{Eq. 4.1})$$

where z is the number of electrons transferred per charge carrier (z is 1 for Li⁺), F is the Faraday constant (96485.3 C mol⁻¹), R is the gas constant (8.314 J mol⁻¹ K⁻¹), T is the temperature (298 K), A is the area of the electrode, c_{Li} is the molar concentration of Li⁺ and σ is the Warburg coefficient obtained from the slope of Z' vs. $\omega^{-0.5}$ at low frequencies (Figure 4.20).

From the fitting results, one can see a stable and low electrolyte resistance (R_{el}) of 2.0 ~ 3.0 Ω at varying (de)lithiated potentials in Figure 4.18c. It indicates high conductivity of the electrolyte, which is not influenced by the initial formation of the SEI film. The variation of R_{SEI} with the potential is plotted in Figure 4.18d. During lithiation, the R_{SEI} steeply decreases from 29.1 Ω at OCV (2.9 V) to 4.4 Ω at 1.0 V, then increases again and keep stable to ~11 Ω at 0.6~0.01 V. The low R_{SEI} at 1.7~1.0 V indicates the initial formation of conductive SEI which facilitate the Li⁺ insertion process (ZnMn₂O₄ → LiZnMn₂O₄). While, the R_{SEI} increases at lower potential (1~0.6 V), which can be attributed to the formation of thicker SEI film. During delithiation, the R_{SEI} gradually increases to the maximum value of 18.5 Ω at 1.4 V. It can be ascribed to the fact that the formed SEI become less conductive induced by Li extraction. Then, R_{SEI} declines to 14.1 Ω (3.0 V), indicating the SEI decomposition at high potential, which is also in agreement with the ref. [195]. The final R_{SEI} at 3.0 V is much lower than the initial value, demonstrating that the initial formation of the SEI during the 1st cycle is beneficial to the Li⁺ charge transfer.

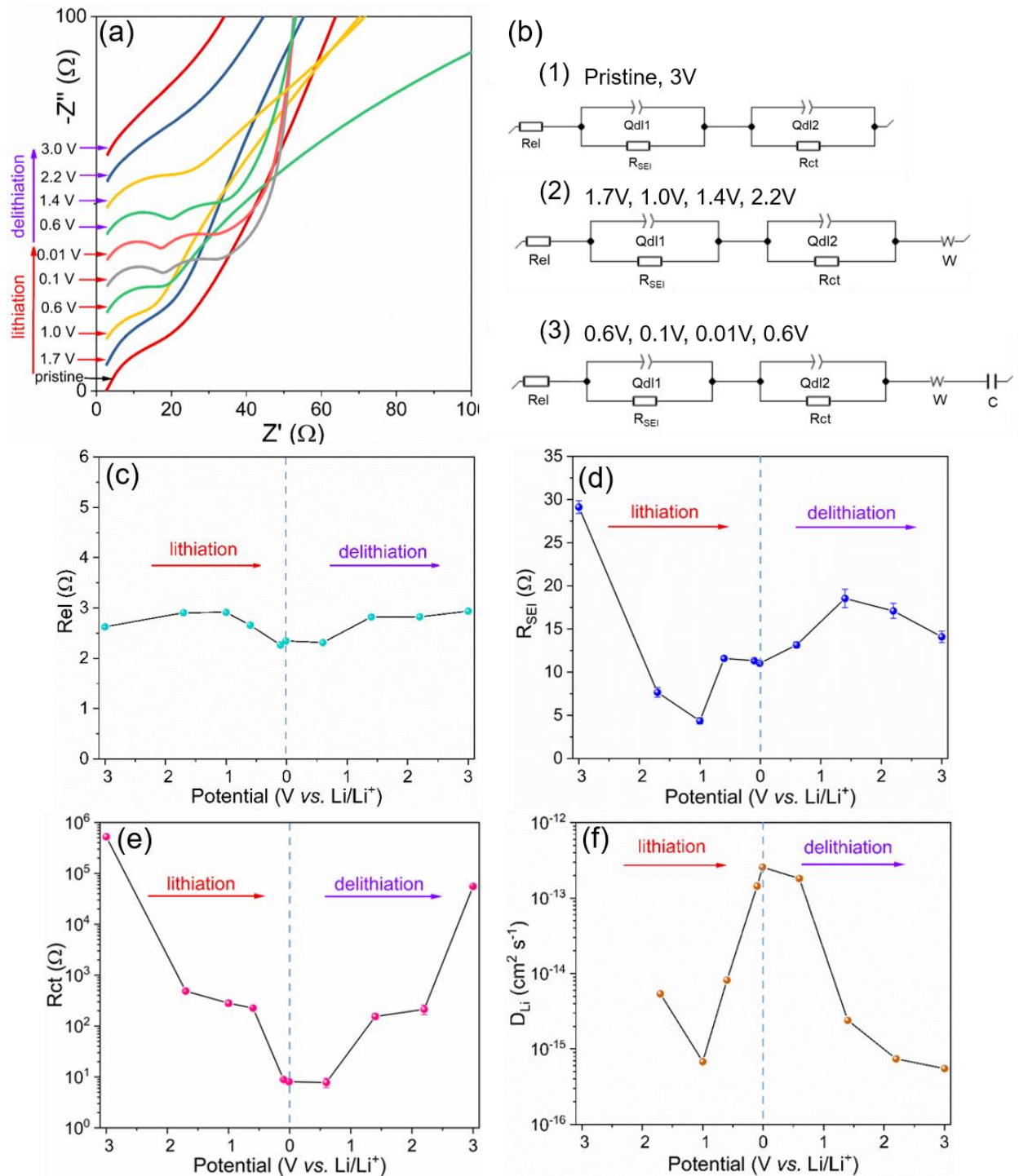


Figure 4.18 (a) The Nyquist plots obtained from EIS test on the ZMO-3h during the 1st GCPL cycle (100 mA g^{-1}), (b) the equivalent circuits for EIS fitting; and the EIS fitting results: (c) resistance of the electrolyte, R_{el} , (d) resistance related to charge transfer, R_{SEI} , (e) the electronic conductive resistance, R_{ct} and (f) diffusion coefficient, D_{Li} .

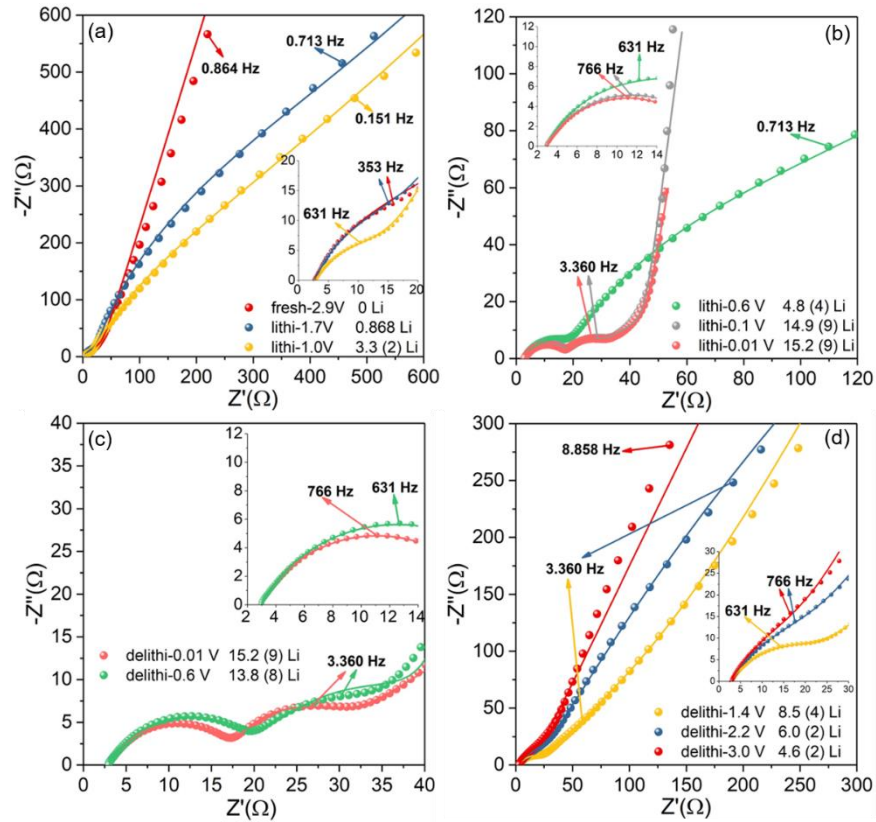


Figure 4.19 EIS Nyquist plots (points) and the fitting curves (solid line) of the 1st cycle (0.1 A g^{-1}) of the ZMO-3h half-cell.

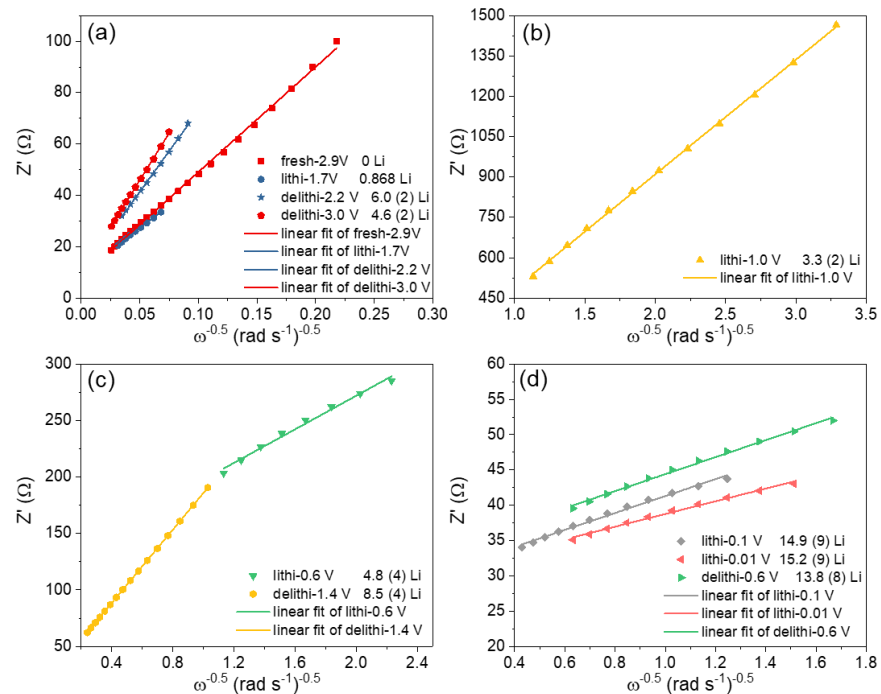


Figure 4.20 The linear relationship between the Z' and the $\omega^{-0.5}$ according to the EIS plots scanned at different (de)lithiation states for the ZMO-3h.

The variation tendencies of the charge transfer resistance (R_{ct}) and the diffusion coefficient (D_{Li}) are shown in Figure 4.18e&f, respectively. The R_{ct} of the electrode is extremely high of $5.2 \times 10^5 \Omega$ at the delithiated state (3.0 V). During lithiation, the R_{ct} decreases to 500~200 Ω at 1.7~0.6 V, and proceeds to 8.0 Ω at 0.1~0.01 V. It implies the improved reaction kinetics of the intermediate phase LiZnMn₂O₄ compared to the pristine ZnMn₂O₄, and indicates that the lithiated phase (LiZn+2Mn+4Li₂O) is well conductive. Meanwhile, the D_{Li} decreases from $5.4 \times 10^{-15} \text{ cm}^2\text{s}^{-1}$ to $6.8 \times 10^{-16} \text{ cm}^2\text{s}^{-1}$ at 1.7 ~ 1.0 V, indicating the lower Li⁺ diffusion rate of the intermediate phase LiZnMn₂O₄ than that of the pristine ZnMn₂O₄. It can be assigned to that the abundant insertion of the Li⁺ ions in ZnMn₂O₄ reduces the number of voids available for the Li⁺ movement in the spinel structure, resulting in a low D_{Li} at 1.0 V. Thereafter, the D_{Li} dramatically increases to $2.6 \times 10^{-13} \text{ cm}^2\text{s}^{-1}$ at the end of lithiation (0.01 V), indicating the faster Li⁺ diffusion of the lithiated phase (LiZn+2Mn+4Li₂O) at low potential. During delithiation, the R_{ct} increases while the D_{Li} decreases again, with 154 Ω and $2.4 \times 10^{-15} \text{ cm}^2\text{s}^{-1}$ at half-delithiated state (1.4 V) and with $5.5 \times 10^4 \Omega$ and $5.5 \times 10^{-16} \text{ cm}^2\text{s}^{-1}$ at fully-delithiated state (3.0 V).

4.2.4 Long-term cycling performance and rate capability

The electrochemical performance was evaluated by CV, GCPL. Figure 4.21 displays the CV curves of the ZMO-1h and CZMO samples measured with a scan rate of 0.1 mV s^{-1} . For the initial conversion process (Figure 4.21a), the ZMO-1h behaves similar with the ZMO-3h as depicted beforehand (Figure 4.15). In contrast, the CZMO samples display higher electrode polarization in the 1st cathodic curve. The peaks shift towards lower potential, and current tails are also observed in the low potential region (Figure 4.21d, g and j). This can be ascribed to the carbon layer, which covers the active sites of the active materials [201,202].

In subsequent cycles, two anodic peaks at ~1.2 V (Mn⁰ to Mn²⁺) and ~1.5 V (Zn⁰ to Zn²⁺) and one cathodic peak at ~0.5 V (Mn²⁺ to Mn⁰ and Zn²⁺ to Zn⁰) can be observed, indicating the occurrence of conversion reactions [189]. In Figure 4.21b&c, the cathodic peak of the ZMO-1h shifts to lower potential and the intensities of redox peaks decrease upon cycling. This indicates that the electrode polarization continuously increases, which is accompanied by a decrease in capacity. In contrast, the CZMO samples display much higher cycling stability. The CZMO-300 displays a tiny decrease in peak current after ~120 cycles, without an increase of electrode

polarization (see Figure 4.21e&f). As for the CZMO-400 and CZMO-500, a tiny increase in the peak intensities during 30th~70th cycles can be noted (see Figure 4.21h&k). A weak increase of electrode polarization occurs after ~120 cycles (see Figure 4.21i&l).

Interestingly, the ZMO-1h shows an increasing additional capacitive charge storage after ~30th cycles (see Figure 4.21b&c). This corresponds to extra reversible charge storage in the SEI [157,190,191,195]. The new pair of redox peaks observed during 60~100 cycles can be assigned to the Mn³⁺/Mn²⁺ redox reaction [203]. It is reported that this reaction can only occurs on materials with superior kinetic properties (electronic conductivity and Li⁺ diffusion) [152,203]. In our case, the reaction occurs not from the beginning but after ~60 GCPL cycles. This can be explained considering that the nanoscaled pristine ZnMn₂O₄ particles evolves to smaller ZnO and MnO particles upon cycling which can shorten the Li⁺ diffusion pathways. A similar, but much weaker phenomenon, can also be observed in the CZMO samples. These results evidence that carbon coating not only prevents an excessive electrode polarization but also improves the reversibility of charge storage processes.

In CV measurement, the currents response to the applied scan rates can be used to distinguish the two diffusion kinetics: the diffusion(bulk)-controlled reaction and the surface-controlled reaction [204]. The current response to the scan rate at a particular potential can be written as the following Eq. 4.2&4.3 [205]-[163]:

$$|i(v)| = k_1 v + k_2 v^{1/2} \quad (\text{Eq. 4.2});$$

$$|i(v)|v^{-1/2} = k_1 v^{1/2} + k_2 \quad (\text{Eq. 4.3});$$

where v is the scan rate, $i(v)$ is the current response, and k_1 and k_2 are the coefficients denoted to the proportion of the surface-controlled process and the diffusion(bulk)-controlled process, respectively. Thereafter, k_1 and k_2 can be obtained by linear fitting the relationship of $|i(v)|v^{-1/2}$ and $v^{1/2}$. The CV-rate measurement was performed after 55 GCPL cycles (when the capacitive current and the additional redox process appear) (Figure 4.22a). The currents related to the new redox peaks (cathodic peak at ~1.09 V and anodic peak at ~2.16 V) are depicted as the relationship

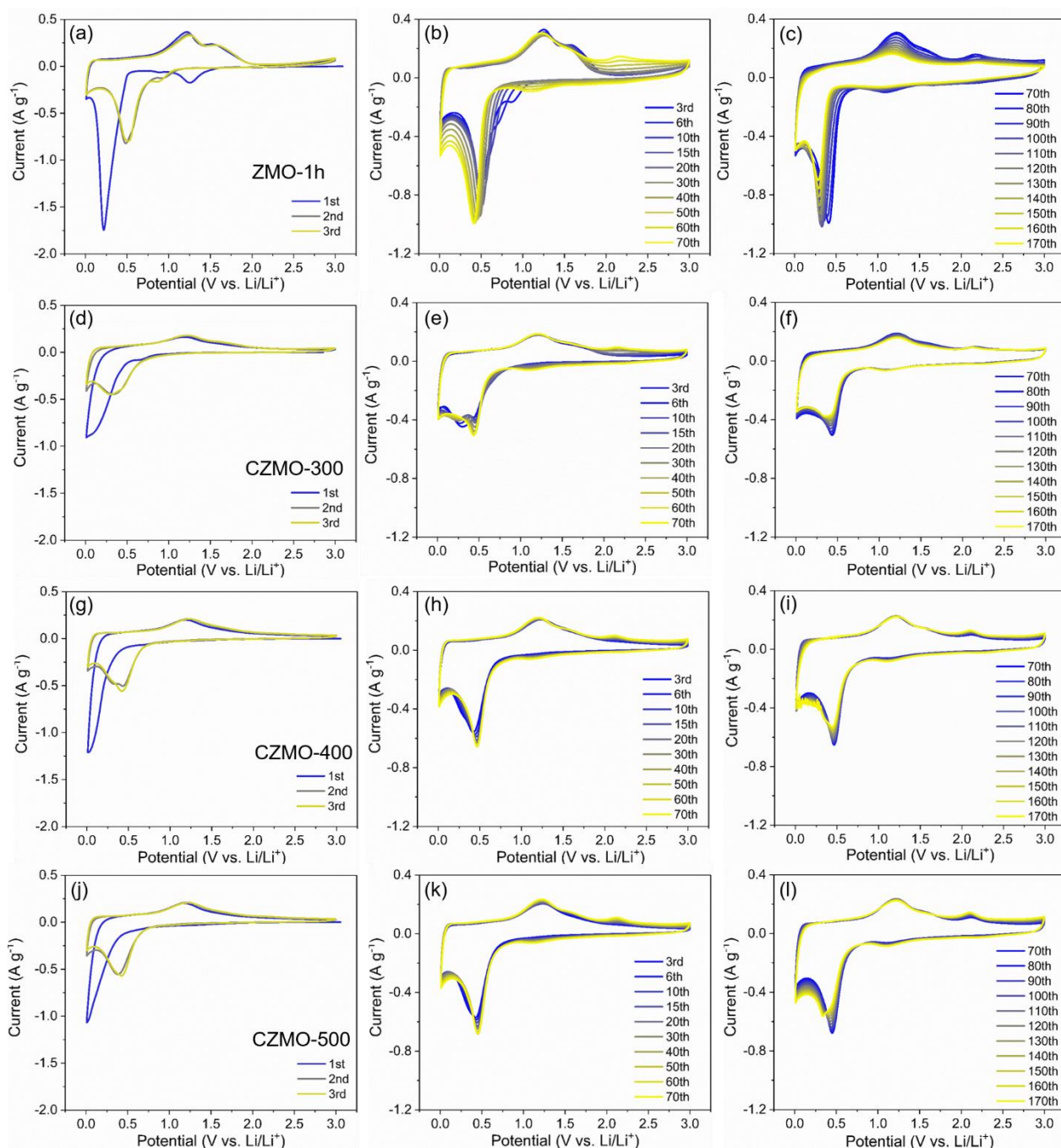


Figure 4.21 CV curves: (a~c) ZMO-1h, (d~f) CZMO-300, (g~i) CZMO-400, (j~l) CZMO-500 scanned at 0.1mV s^{-1} .

of $|i(v)|v^{-1/2}$ and $v^{1/2}$, and the corresponding coefficients k_1 and k_2 are shown in [Figure 4.22b](#). The surface-controlled process contribution can be evaluated by the parameter $k_1/(k_1+k_2)$, which can change between 0 and 1.0. The higher value means the more capacitive (surface-type) contribution. For the cathodic and the anodic peaks, the values of $k_1/(k_1+k_2)$ are 0.71 and 0.62,

respectively. In addition, the peak current also obeys the power-law relationship: $i = av^b$, according to Y. Meng *et al.*'s work [206]. The v is the scan rate and the i is the current response. The b value can change from 0.5 to 1.0, and $b=0.5$ when it is a diffusion(bulk)-controlled process, while $b=1.0$ when it is a surface-controlled process. As shown in Figure 4.23e, the b values can be calculated as the slope of $\lg(i)$ vs. $\lg(v)$, which are 0.81 and 0.74 for the cathodic and the anodic peaks, respectively. Furthermore, some points at different potentials on the CVs have been chosen to calculate the surface-controlled current (k_1v) contribution and the reconstructed CVs are shown in Figure 4.23a~d. The ratio of the shadow area (surface-controlled) is 61.56% at scan rate of 1 mV s⁻¹. Apparently, both, the surface-controlled and the diffusion(bulk)-controlled processes contribute to the additional capacity. The surface-controlled charge storage process can be assigned to both, the pseudocapacitive mechanism (charge storage in SEI and metal/Li₂O interface) and the electric double-layer mechanism (static electrical charge storage on high-area electrode material surface). The diffusion(bulk)-controlled process can be assigned to the redox reaction of Mn³⁺/Mn²⁺.

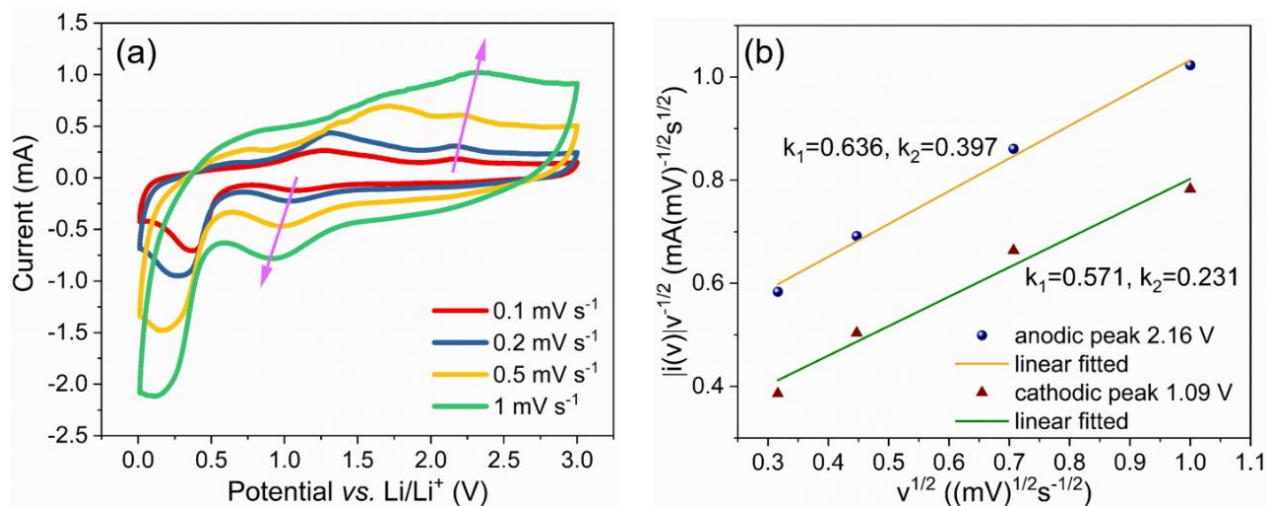


Figure 4.22 (a) The CV curves of the ZMO-3h (after 55 cycles) scanned at varied rates 0.1~1 mV s⁻¹ and (b) the relationship of $|i(v)|v^{-1/2}$ and $v^{1/2}$ at the selected potentials.

Figure 4.24a displays the long-term cycling performance at a current density of 0.5 A g⁻¹, and selected potential profiles are shown in Figure 4.25 & 4.26. The ZMO-1h shows a high capacity during the initial cycles (~800 mAh g⁻¹), followed by dramatic variations, as previously reported [158]. Specifically, the capacity increases intensively up to ~1100 mAh g⁻¹ at the 80th cycle, and then suddenly decreases, to ~400 mAh g⁻¹ at the 150th cycle. In contrast, the CZMO samples deliver much more stable capacities. Within the initial 100 cycles, the capacity gradually increases

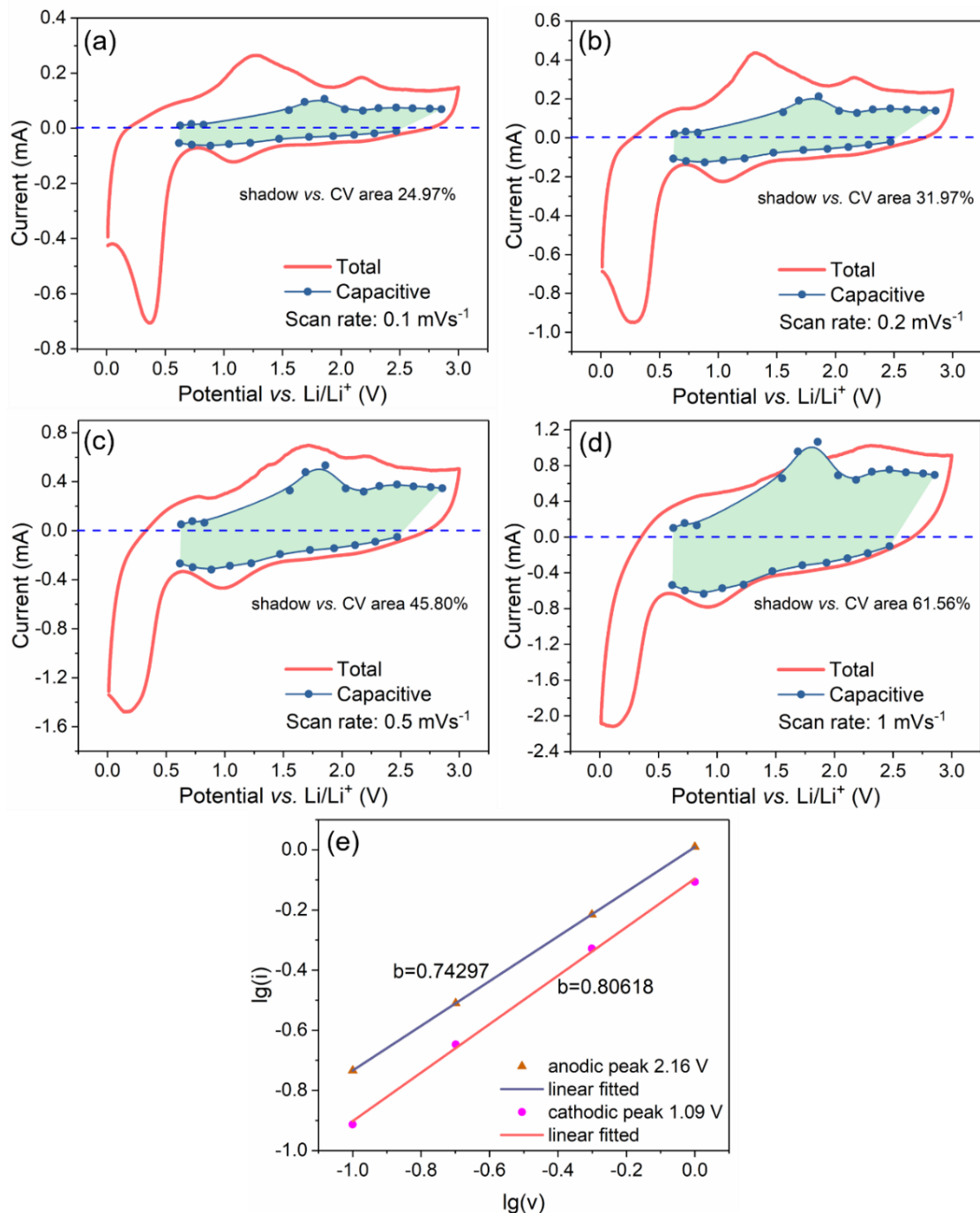


Figure 4.23 (a~d) The CV curves of the ZMO-3h (after 55 cycles) scanned at varied rates 0.1~1 mV s⁻¹ with fitted capacitive contribution (shadow area) and (e) linear fitting of the $\lg(i)$ vs. $\lg(v)$ plots.

from 500 to 700 mAh g⁻¹. After that, the capacity remains stable for the next hundreds of cycles. Regarding the coulombic efficiency, it can be noted that the ZMO-1h displays the highest value of 66.2% at the 1st cycle, whereas the coulombic efficiencies of the CZMO-300, CZMO-400 and

CZMO-500 are 47.3%, 52.3% and 51.9%, respectively. These results indicate that the carbon- and carbon-derivative-coated layers induce higher irreversible capacity during the 1st lithiation. In the subsequent cycles, the ZMO-1h and the CZMO-300 possess lower coulombic efficiencies than that of the CZMO-400 and CZMO-500. The coulombic efficiencies of the ZMO-1h and CZMO-300 gradually increase to 99.2 % after ~40 and ~50 cycles, respectively. The highest coulombic efficiency is obtained after ~10 and ~20 cycles for the CZMO-400 and CZMO-500, respectively (see the inset image in Figure 4.24a). This result indicates that a stable SEI can be faster formed on the carbon layer, whereas the bare ZMO-1h needs more cycles to stabilize the interface.

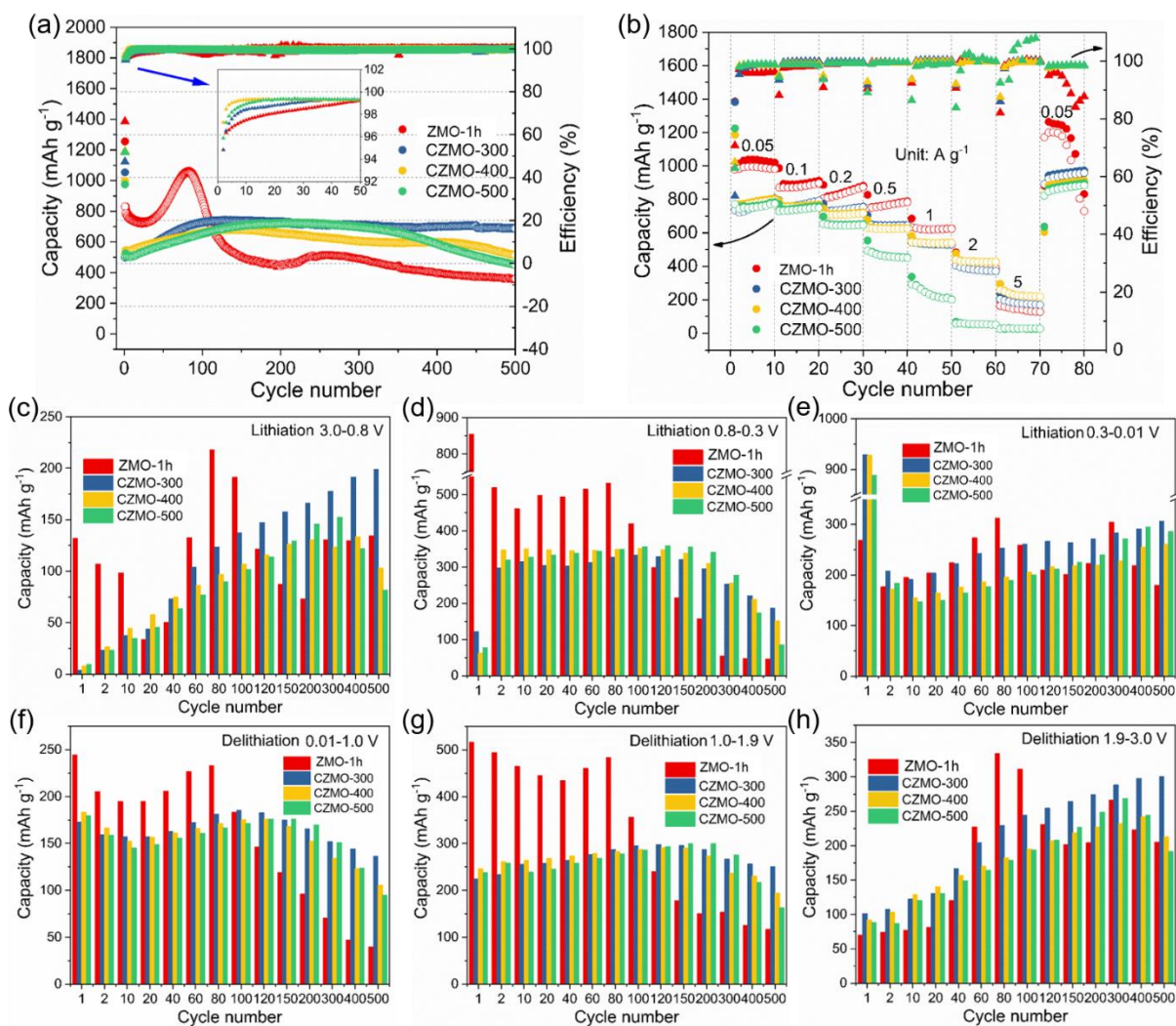


Figure 4.24 GCPL lithiation (solid spots) and delithiation (circles) capacities (a) with 0.5 A g^{-1} for long-term cycling and (b) with varied current densities; the inset in (a) shows the coulombic efficiency in the initial 50 cycles; and (c~h) capacity vs. cycle number separated into different potential ranges: (c) 3.0~0.8 V, (d) 0.8~0.3 V, and (e) 0.3~0.01 V during lithiation, and (f) 0.01~1.00 V, (g) 1.0~1.9 V and (h) 1.9~3.0 V during delithiation.

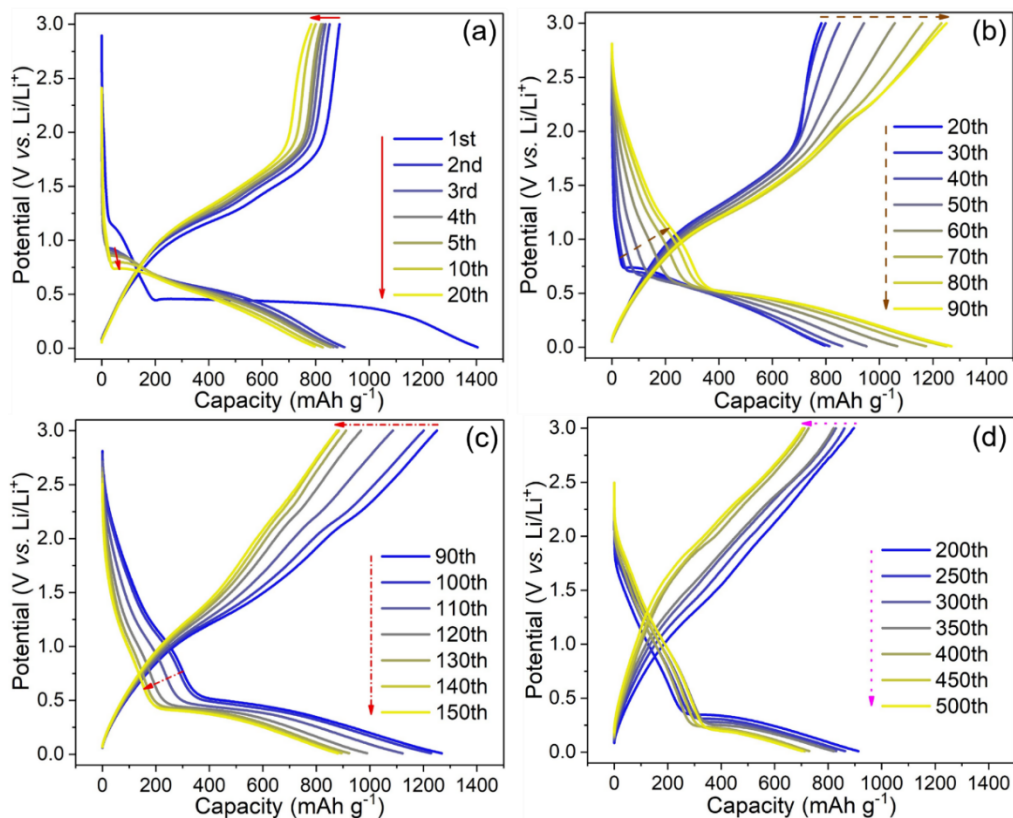


Figure 4.25 The selected potential profiles of the long-term cycling at 0.5 A g^{-1} of the ZMO-3h anode.

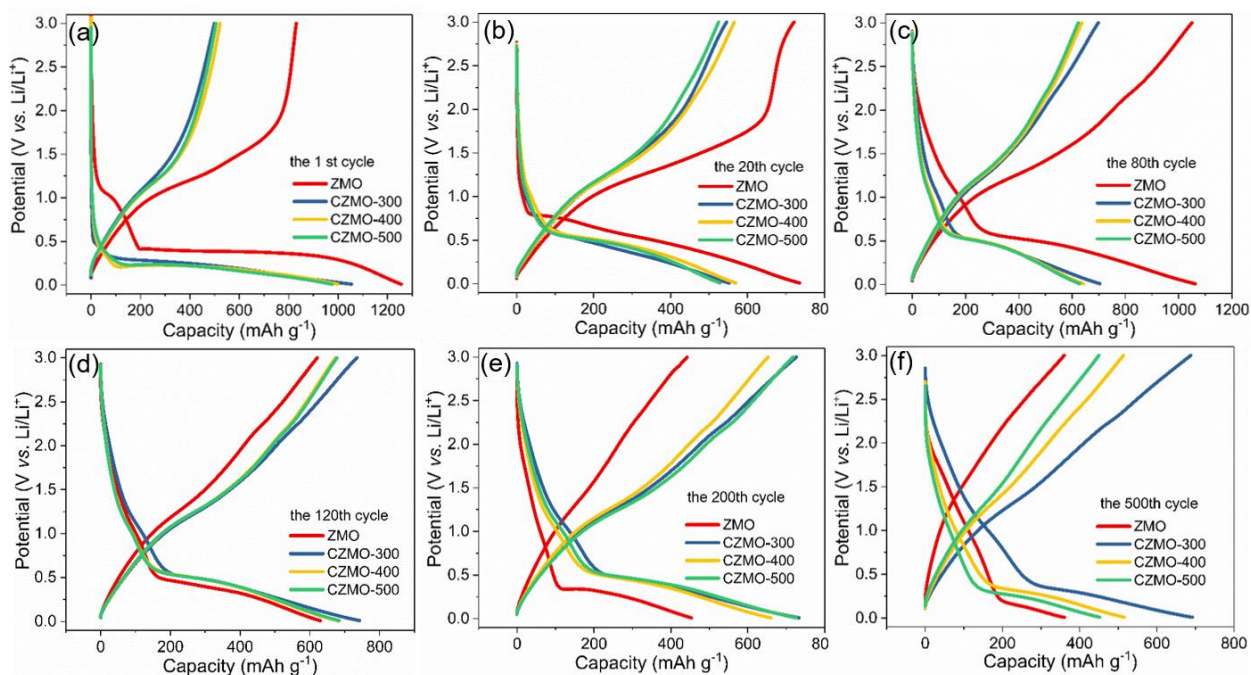


Figure 4.26 Potential profiles of GCPL with current density of 0.5 A g^{-1} at different cycle numbers for the ZMO-1h and CZMO samples.

A rate capability test was performed to evaluate the electrochemical performance of the samples at different current densities (Figure 4.24b). At lower current densities, the ZMO-1h shows the highest capacity with $\sim 994 \text{ mAh g}^{-1}$ at 0.05 A g^{-1} and $\sim 620 \text{ mAh g}^{-1}$ at 1 A g^{-1} , while the CZMO-300 and CZMO-400 deliver similar capacities of $\sim 771 \text{ mAh g}^{-1}$ at 0.05 A g^{-1} and 538 mAh g^{-1} at 1 A g^{-1} . In contrast, the CZMO-500 shows a poor rate capability, delivering only 233 mAh g^{-1} at 1 A g^{-1} . At higher current densities, the CZMO-400 shows the highest capacity with 428 mAh g^{-1} at 2 A g^{-1} and 225 mAh g^{-1} at 5 A g^{-1} . Moreover, when the current density returns to 0.05 A g^{-1} , the ZMO-1h electrode shows a failure in cycling stability. The corresponding capacity retention is shown in Figure 4.27. Among these samples, the CZMO-400 displays the best rate capability. This can be attributed to the coated carbon layer with proper coated amount and degree of graphitization. In the CZMO-300, the coated layer is not graphitized, inducing a limited electronic conductivity, whereas, in the CZMO-500, the carbon content is too low to connect all the metal oxide particles.

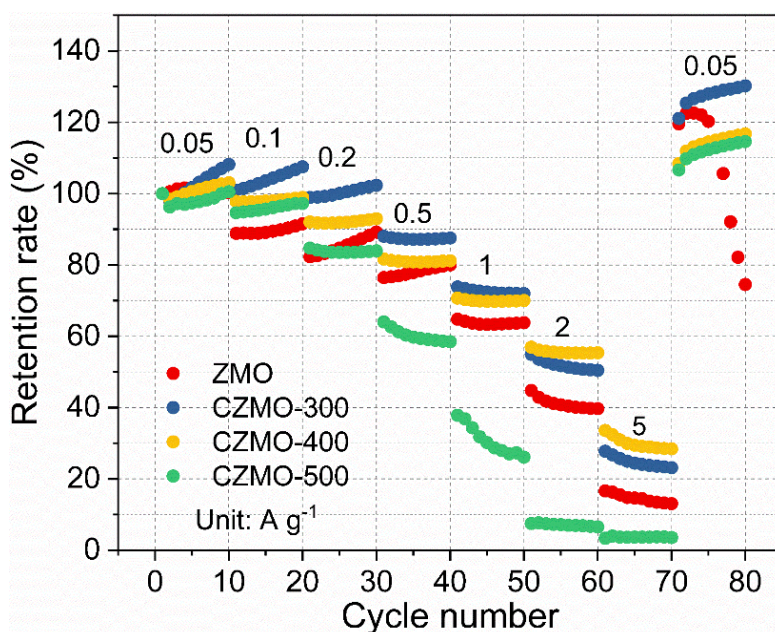


Figure 4.27 Retention rate of the GCPL delithiation capacities using varied current densities.

As discussed in the CV study, the capacity of the conversion electrodes can be separated into different potential ranges based on the specific charge storage processes. Figure 4.24d&g show the capacity related to the main conversion processes ($\text{Mn}^0/\text{Mn}^{2+}$ and $\text{Zn}^0/\text{Zn}^{2+}$). The ZMO-1h exhibits a capacity which is $150\sim 200 \text{ mAh g}^{-1}$ higher than the CZMO samples during the initial 80 cycles. This indicates the higher conversion capacity in the ZMO-1h sample. In contrast, the CZMO samples show much higher capacity retention within 200 cycles. The evolution of the $\text{Mn}^{3+}/\text{Mn}^{2+}$

conversion and the SEI charge storage can be observed in [Figure 4.24c&h](#). The ZMO-1h shows a higher reduction capacity during the initial 10 cycles, indicating that the Mn³⁺/Mn²⁺ conversion reaction is partially reversible and that the Mn³⁺ converts to Mn²⁺ gradually at the delithiated state. During the 60th~80th cycles the capacity of ZMO-1h rapidly increases, and then fast fades in the subsequent cycles. On the other hand, the capacity of the CZMO samples increase gradually, due to the slow increase in the Mn³⁺/Mn²⁺ redox reaction and charge storage in SEI. [Figure 4.24f](#) shows the capacity originated from the de-alloy reaction and the extra space charge [153,154]. The capacity evolution related to the alloy/de-alloy process is similar to the one related to the main conversion process. Besides the capacity of alloy mechanism and extra space charge, the capacity displayed in [Figure 4.24e](#) also contains the extra capacity due to the SEI. The capacity of the ZMO-1h rapidly increases and decreases at the 60th~100th cycles, in contrast to the modest capacity growth of the CZMO samples. Among the samples, the CZMO-300 shows the highest SEI extra capacity. It can be attributed to its higher amount of surface functional groups, –OH, which is detected by FTIR ([Figure 4.13b](#)). Yan-Yan Hu, *et al.* have reported that the surface –OH groups of electrode materials can involve the formation of LiOH in SEI, which can contribute to extra capacity [191].

4.3 Conclusions

In summary, the ZnMn₂O₄ nanoparticles have been successfully synthesized through a coprecipitation and calcination method. Then, the ZnMn₂O₄ was coated with carbon by a carbon-thermal reduction method. During calcination in air, the TGA and HT-SRD reveal that the tetragonal spinel ZnMn₂O₄ phase forms at around 350 °C, then partially transforms to a cubic spinel phase ZnMn₂O₄ above 650 °C, and finally returns to tetragonal spinel phase after cooling down to 20 °C. During the carbonization process, the HT-SRD shows that the ZnMn₂O₄ is converted to ZnO-MnO composite at 250~400 °C, and the crystallized MnO and ZnO are formed above 350 °C and 600 °C, respectively. *In situ* SRD performed on the ZnMn₂O₄ electrode during the 1st cycle reveals the formation of the intermediate tetragonal spinel phase LiZnMn₂O₄ which coexists with the original ZnMn₂O₄ during lithiation. Combined with the EIS analysis, it is concluded that low bulk electronic conductivity is the main reason for the slow initial insertion kinetics (ZnMn₂O₄ → LiZnMn₂O₄). While during the conversion process (0.6~0.01 V), the material shows fast reaction kinetics, resulting in high rate performance. During long-term cycling, the bare ZnMn₂O₄ displays

obvious capacity increase. It is illustrated by CV that the increase in Mn→Mn₃O₄ conversion reaction occurs after ~60 cycles, which contributes to the capacity increase. In comparison, the carbon coated samples shows slower conversion kinetics than the bare ZnMn₂O₄ during the 1st lithiation. This is ascribed to the fact that the carbon layer covers the active sites on metal oxide. However, the carbon coating improves efficiently the cycling stability and rate capability, compared to the significant capacity variations of the bare ZnMn₂O₄.

5 Cycling stability of the ZnMn₂O₄ and ZnO-MnO anodes in LiBs

5.1 Introduction

As learned from the last section, conversion-type anodes deliver a high irreversible capacity during the 1st cycle, and an increasing amount of extra capacity upon cycling [207]. This can be attributed to the initial formation and the extra charge storage in the SEI [105,208]. Amount of work has been done on solid electrolyte interphase (SEI) through multiple methods, such as TEM, soft XAS, XPS and NMR [157,190,191,195]. In case of ZnMn₂O₄, some papers also report that the further redox reaction between Mn(II) and Mn(III) can also lead to an additional capacity [203,208]. Therefore, the study on the evolution of intrinsic conversion redox chemistry is also necessary. In contrast, the carbon-coated ZnO-MnO delivers much higher cycling stability than the bare ZnMn₂O₄.

In order to clarify the as-mentioned arguments, multiple methods have been applied on the *ex situ* electrodes at different cycling states, including XPS, TEM and XAS. *Ex situ* XPS was carried out to reveal the change of the metal oxidation state and the composition of the SEI during the 1st cycle. *Ex situ* TEM was used to measure the morphology change and phase segregation of active material after cycling. Last but not least, *ex situ* XAS and long-term EIS were measured to investigate the phase and resistance evolution of electrode upon long-term cycling. The results clarify the nature of the additional reversible capacity and elucidate the effects of carbon coating comprehensively.

Moreover, considering that the SEI layer plays a very important role in triggering capacity variations and active material isolation, the strategy of using a different electrolyte to prevent excessive SEI formation is also promising. An ester-based electrolyte solvent, cyanopropionic acid methyl ester (CPAME), is reported to be promising in EDLCs, displaying high thermal and electrochemical stability [209,210]. Vinylene carbonate (VC) is one of the most frequently studied SEI-forming additives which can lead to an enhanced LIB cycling stability [211]. Therefore, in this work, a new electrolyte (1 M LiPF₆ in CPAME / VC (2 wt.%)) was used to improve the cycling stability of the bare ZnMn₂O₄ anodes. GCPL, CV were used to evaluate the electrochemical performances.

The results in this chapter are partially published in the following publication:

Z. Zhao, G. Tian, A. Sarapulova, V. Trouillet, Q. Fu, U. Geckle, H. Ehrenberg, S. Dsoke, Elucidating the energy storage mechanism of ZnMn₂O₄ as promising anode for Li-ion batteries, *J. Mater. Chem. A*. 6 (2018) 19381–19392. Reproduced by permission of The Royal Society of Chemistry, <https://pubs.rsc.org/en/content/articlelanding/2018/TA/C8TA06294C#!divAbstract>.

Z. Zhao, G. Tian, A. Sarapulova, G. Melinte, J.L. Gómez-Urbano, C. Li, S. Liu, E. Welter, M. Etter, S. Dsoke, Mechanism Study of Carbon Coating Effects on Conversion-Type Anode Materials in Lithium-Ion Batteries: Case Study of ZnMn₂O₄ and ZnO–MnO Composites, *ACS Appl. Mater. Interfaces*. 11 (2019) 29888–29900.

<https://pubs.acs.org/doi/10.1021/acsami.9b08539>.

5.2 Results and discussion

5.2.1 *Ex situ* characterizations of the electrode evolution during cycling

In order to obtain deeper information regarding the SEI formation and the involved redox reactions, XPS analysis was conducted on the ZMO-3h, on pristine electrode as well as on electrodes after the 1st lithiation and the 1st delithiation with current density of 0.5 A g⁻¹. Since no Zn and Mn could be detected at the lithiated and delithiated electrode surface, it was necessary to etch the samples by argon clusters. The ZMO-3h powder, the pristine electrode and the electrode after the 1st delithiation show similar spectra with an Auger-electron line Zn LMM at ~989 eV kinetic energy (Figure 5.1a), indicating the existence of Zn(II) [148]. It confirms that the Zn(II) is reversibly formed after the 1st cycle. However, the overlap of the Mn 3s peak and Zn 3p doublet hinders the identification of the oxidation state of Mn. For this reason, only Mn 2p can be here considered. In addition, the weak intensity of the signal - attenuated by the SEI - hampers the evaluation of the oxidation state. Nevertheless, Mn(III) and Mn(II) ions contain unpaired electrons in their 3d valence level which can couple with the unpaired electrons in the core formed by photoionization, so that show multiplet splitting in their 2p spectra [212]. Azmi *et al.* demonstrated the possibility of determining the different oxidation states of transition metals by consideration of this multiplet splitting [146,147]. Therefore, this approach was applied here considering the parameters defined by Biesinger *et al.* [149], e.g. number of peaks and their binding energy. As

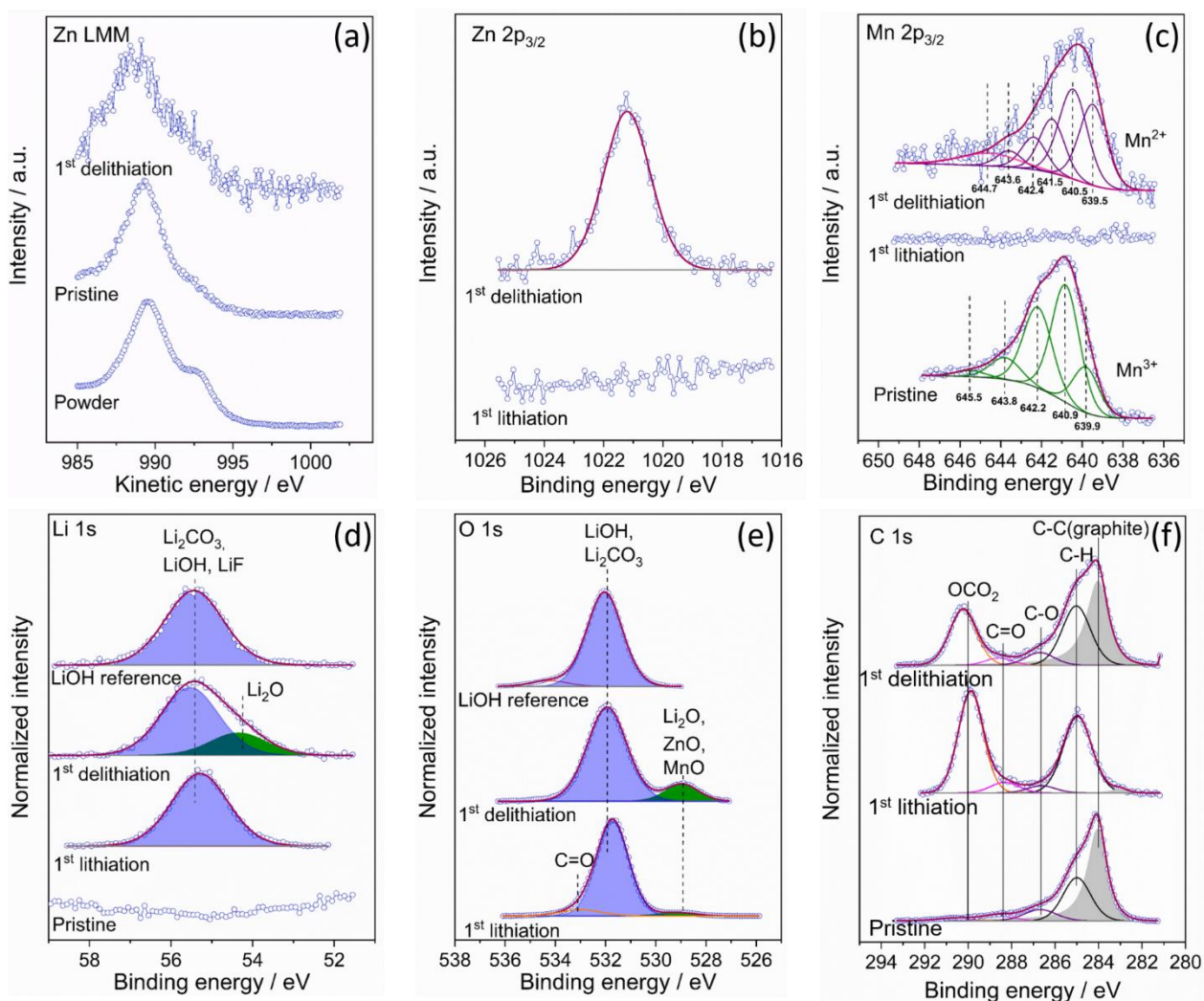


Figure 5.1 Zn LMM Auger line (a) and XPS spectra: (b) Zn 2p_{3/2}, (c) Mn 2p_{3/2}, (d) Li 1s, (e) O 1s, (f) C 1s of the ZMO-3h electrodes (pristine, after 1st lithiation and 1st delithiation by 0.5 A g⁻¹ GCPL) and of the LiOH reference.

shown in [Figure 5.1c](#), the Mn 2p_{3/2} spectrum of the pristine sample splitted into 5 peaks can be attributed to Mn(III), while the Mn 2p_{3/2} spectrum of the sample after 1st delithiation splitted into 6 peaks determines the attribution of Mn(II), comparing fitted spectra parameters with the reported literature [\[149\]](#). It indicates that, after the 1st cycle, the Mn(III) in ZnMn₂O₄ is irreversibly reduced to Mn(II). In addition, the delithiated sample shows a peak at 54.4 eV which can be attributed to the irreversible formation of Li₂O ([Figure 5.1d](#)). The Zn 2p_{3/2} and Mn 2p_{3/2} spectra of the 1st lithiated and the 1st delithiated electrodes are shown in [Figure 5.1b&c](#), respectively. These peaks and the O 1s peak related to the metal oxide (at 528.9 eV), as well as the C 1s graphite component (at 284.4 eV), which compose the inside real electrode, can only be detected on the delithiated

electrode, indicating the thinner SEI at the delithiation state than at the lithiation state. This phenomenon confirms the formation of the SEI during lithiation and the decomposition during delithiation [195]. The composition of the SEI is given by qualitative as well as quantitative analysis of the Li 1s, O 1s and C 1s spectra (shown in Figure 5.1d~f), respectively. As expected, the pristine electrode is free of Li whereas one major peak appears at 55.3 eV (43.7 at%) for the lithiated sample. At the same time, a clear peak at 290.2 eV (4.2 at%) appears in the C 1s spectrum, which proves the presence of Li_2CO_3 . Considering the stoichiometry of this carbonate, an excess of Li is observed and reveals the presence of another lithium compound in the SEI. Simultaneously, the O 1s signal at 531.6 eV (40.1 at%) can also be attributed to the carbonate but shows in the same manner, an excess of oxygen. The residual concentrations of both lithium and oxygen in a ratio of 1:1 evidence the presence of LiOH or Li_2O_2 . Since the binding energy values of Li 1s reported in the literature for both compounds are distributed in the range of 55.0 ± 0.5 eV [213], the measurement of a reference is necessary to properly identify the compound. LiOH (with Li_2CO_3 at the surface) shows Li 1s at 55.4 eV and O 1s at 532.0 eV, which are in accordance with the observed peaks of the electrode (Figure 5.1d&e). Similarly, Li_2CO_3 and LiOH can also be reliably attributed to the peaks observed in the spectra for the delithiated sample: C 1s 290.2 eV (6.8 at%), Li 1s 55.5 eV (24.5 at%) and O 1s, 531.9 eV (32 at%). Based on the carbonate concentration given by the quantitative analysis, the estimated content of Li_2CO_3 and LiOH can be ~4 at% and ~30 at% for the lithiated sample, and ~7 at% and ~10 at% for the delithiated one, respectively. H. Duncan *et al.* also confirmed high carbonate content in the delithiated ZnMn_2O_4 electrodes [157]. Importantly, Zhang *et al.* found that Li_2CO_3 can reversibly store Li^+ in the Li-ion battery with CoCO_3 anode [214]. In addition, Hu *et al.* reported that the LiOH generated on the RuO_2 anode can reversibly react with Li and store Li^+ [191]. Therefore, the formation of LiOH and Li_2CO_3 in the SEI can be the crucial factors that contribute to the additional capacity.

To study the morphology and phase composition evolution of the active particles after cycling, *ex situ* TEM was conducted on ZMO-3h electrode materials after cycling. As shown in Figure 5.2, the measuring points are at the initial cycle (1st cycle), the cycle with the lowest capacity (25th cycle), the cycle with the highest capacity (90th cycle), and the cycle after capacity fading (150th cycle).

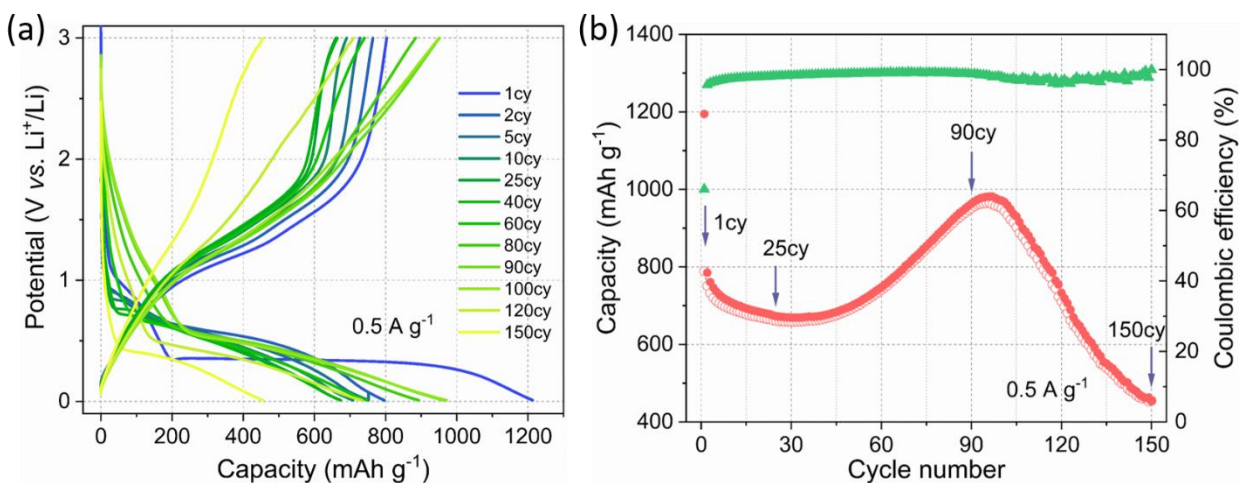


Figure 5.2 GCPL potential profiles (a) and specific capacities (b) of the ZMO-3h electrodes with a current density of 0.5 A g^{-1} . The points labelled in image b display the states of the electrodes for *ex situ* TEM measurement.

As shown by the STEM-HAADF imaging (Figure 5.3a) the pristine sample consists of interconnected nanoparticles with clear edges. The diffraction patterns of the SAED analysis shown in Figure 5.3d can be indexed as the (1,0,1), (1,1,2), (1,0,3) and (1,1,3) planes of the ZnMn_2O_4 spinel structure. Although, the 1st lithiation process drastically changes the morphology of the initial nanoparticles due to Li insertion and the subsequent volume expansion, most of particles retain a nano-sized morphology (Figure 5.3b). Moreover, a few nanometers thick SEI layer can be observed covering the active particles (Figure 5.3b - inset). No major morphological difference between the 1st lithiated and delithiated samples could be observed by HAADF imaging (Figure 5.3c). The new Mn and Zn species created during the 1st cycle for both lithiation and delithiation reactions are forming pseudo-amorphous aggregates embedded in an oxide framework. This pseudo-amorphous character is shown by SAED analysis (Figure 5.3e), that presents relatively diffuse diffraction rings for both samples. Together with the characteristic reflections of the Li_2O phase, the lithiated samples shows the (2,1,1) plane of the metallic Mn (Figure 5.3e - top). This diffraction plane disappears after the 1st delithiation, and instead, the (1,1,0) plane of MnO is shown (Figure 5.3e - bottom). Figure 5.3f presents the elemental distribution of Li and Mn in the 1st lithiated sample. It shows that Mn/Zn nanoparticles resulted after the lithiation are surrounded by Li_2O .

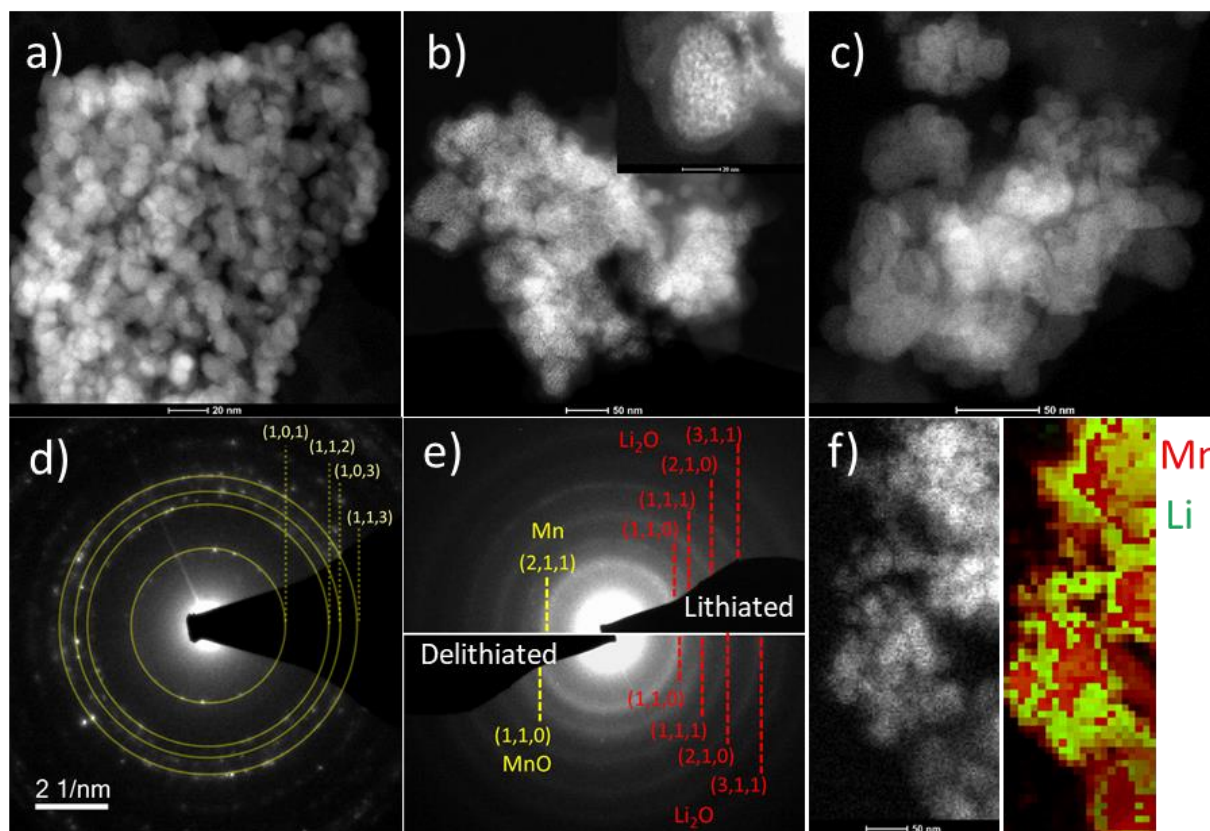


Figure 5.3 STEM - HAADF imaging of the *ex situ* ZMO-3h samples: pristine (a), 1st cycle lithiated (b) and 1st cycle delithiated state (c). SAED analysis of the pristine (d) and cycled samples (e). STEM-EELS based elemental mapping of the 1st cycled lithiated sample (f).

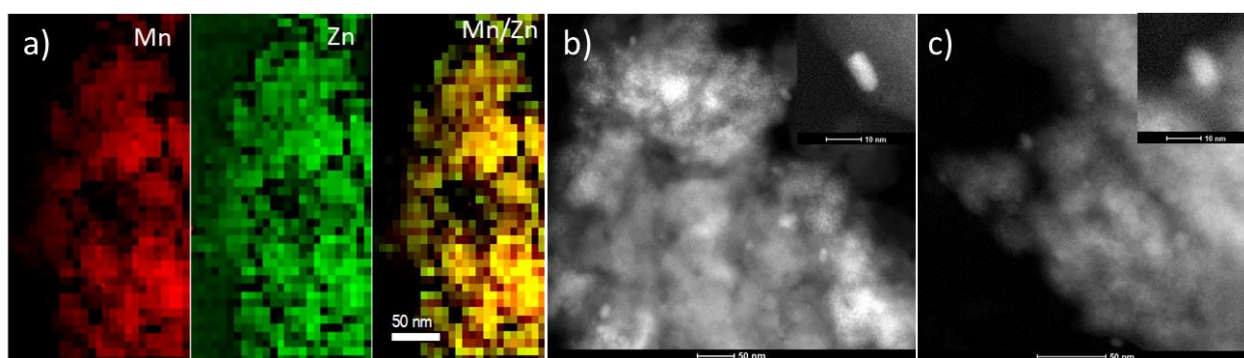


Figure 5.4 (a) EELS-based elemental mapping of Mn and Zn metals for the 1st cycle delithiated specimen. (b) STEM-HAADF image of the 25th cycle lithiated sample showing separated Zn nanoparticles distributed around cycled aggregates. The inset shows a magnified image of a metallic Zn nanoparticle. (c) STEM-HAADF image of the 25th cycle delithiated sample showing ZnO nanoparticles around the aggregates. The inset shows a magnified ZnO nanoparticle.

After the 1st cycle, there is no sign of separation between Mn and Zn phases. [Figure 5.4a](#) shows an elemental map for the 1st cycle delithiated sample that depicts a homogenous distribution at the nano-scale of the two metals. The separation of the Zn phase from the pseudo-amorphous cycled aggregates is first observed in the 25th cycle lithiated sample ([Figure 5.4b](#) with inset). EDX analysis shows a pure metallic Zn phase forming nanoparticles around a few tens of nanometer in size and with a predominantly rod-like shape. STEM-HAADF imaging ([Figure 5.4c](#) with inset) and EDX analysis of the subsequent delithiated sample reveal the oxidation of these nanoparticles to ZnO. These bigger and well-distinguished particles may become isolated and irreversible, which can give reason to the capacity decrease in initial cycles.

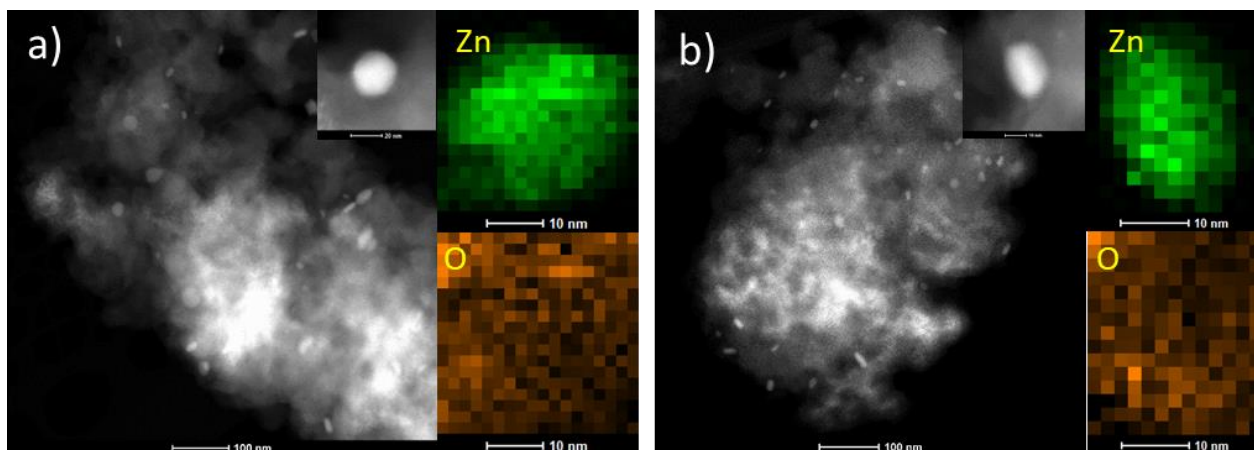


Figure 5.5 (a) STEM-HAADF image of the 90th cycle lithiated sample showing separated Zn nanoparticles distributed around cycled aggregates. The right column shows the EDX-based elemental map of Zn and O proving the metallic Zn character of the nanoparticles. (b) STEM-HAADF image of the 90th cycle delithiated sample. The right column shows the EDX-based elemental map of Zn and O.

After 90 cycles, the Zn-based nanoparticles are presented around each cycled aggregate ([Figure 5.5](#)). Their density seems to be increased compared with the 25th cycle specimen but a quantitative evaluation is difficult. The EDX-based elemental mapping ([Figure 5.5a](#) –right column) shows that these nanoparticles are a pure Zn metal phase at lithiated state. The metallic phase is maintained even after the subsequent delithiation cycle as shown by the elemental mapping presented in [Figure 5.5b](#) –right column. The samples after 150 cycles display a similar morphology. This phenomenon indicates a phase segregation of Zn and an irreversible formation of metallic Zn during long-term cycling. This degradation process of ZnO conversion reaction can induce a capacity decrease.

XANES and EXAFS are powerful methods to characterize the valence and local structure of related elements [215]. To further reveal the redox chemistry evolution and the effect of the coated carbon, *ex situ* XAS was performed on ZMO-1h and CZMO-400 electrodes. The *ex situ* samples analyzed are listed in the following: the electrodes (de)lithiated with a current of 0.05 A g^{-1} after the 1st cycle, and the electrodes (de)lithiated with a current of 0.5 A g^{-1} after the 40th cycle, the 60th cycle, the 80th cycle and the 100th cycle. This allows to understand the redox processes during the 1st cycle and to relate the evolution of the redox pairs to the capacity variations of the ZMO-1h (Figure 5.6&5.7).

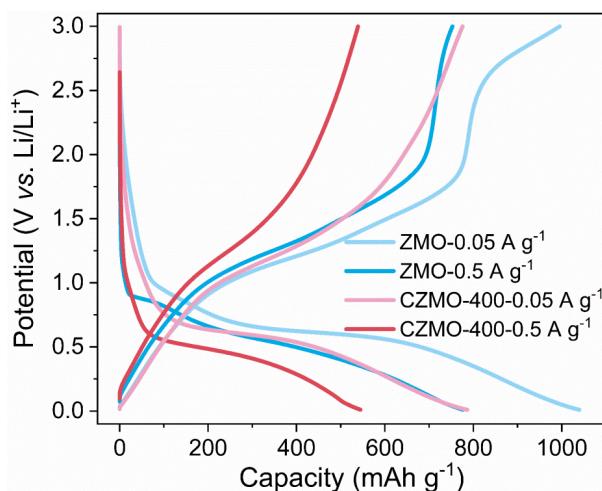


Figure 5.6 Potential profiles of the 5th GCPL cycle for the ZMO-1h and CZMO-400 with 0.05 and 0.5 A g^{-1} current densities.

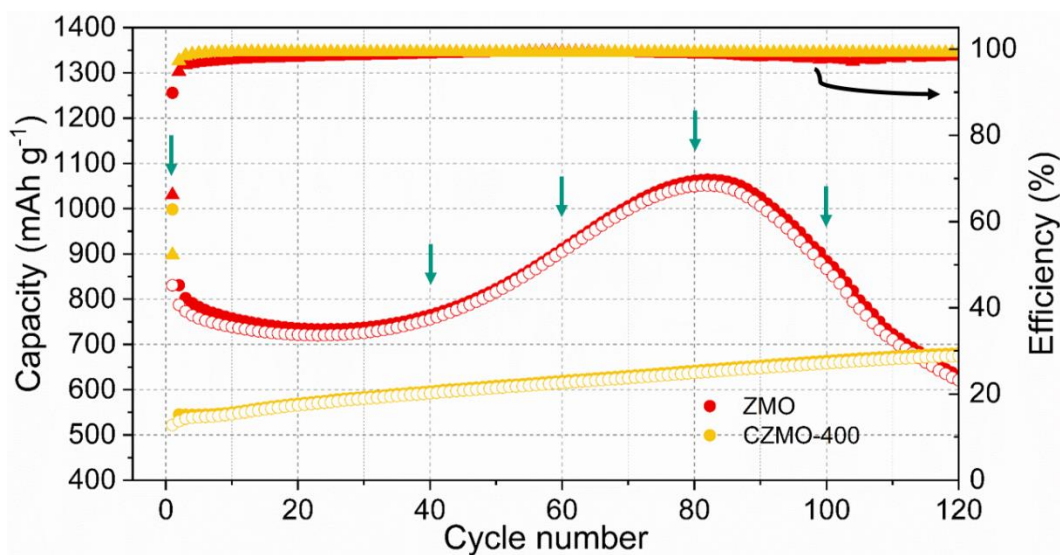


Figure 5.7 Specific capacity of GCPL cycling of the ZMO-1h and CZMO-400 electrodes at a current density of 0.5 A g^{-1} .

A detailed analysis of the Mn K-edge XANES spectra is shown in [Figure 5.8](#). Compared with the spectra of standard Mn₂O₃ and MnO, the pristine ZMO-1h sample displays a valence near to Mn³⁺, while the pristine CZMO-400 sample displays a lower Mn oxidation state (between Mn³⁺ and Mn²⁺), which is due to the reduction of ZnMn₂O₄ during carbonization ([Figure 5.8a&d](#)). The spectra of delithiated samples show slight differences in the edge energy in comparison with the standard MnO spectrum. This implies the presence of other species, like Mn³⁺ and Mn⁰. On the other hand, the edge energy of the lithiated samples locates between the MnO and Mn, demonstrating the reduction of manganese oxides to metallic Mn ([Figure 5.8b&e](#)). Moreover, an isosbestic point at 6544 eV can be observed in the spectra of the lithiated samples, implying a phase transition process upon cycling. This confirms that MnO and Mn, whose spectra intersect at the isosbestic point, are involved in this process [\[216\]](#).

Since both the lithiated and delithiated samples are composed of different valences, linear combination fitting was performed on XANES data. The spectra of standard Mn₂O₃, MnO and Mn are used as references for linear combination fitting to evaluate the fractions of different Mn components, Mn³⁺, Mn²⁺ and Mn⁰ [\[126,217\]](#). Firstly, the delithiated samples are discussed. The ZMO-1h electrode after the 1st cycle ([Figure 5.8c](#)) contains a certain amount of Mn³⁺, which agrees with the plateau near 3 V (Mn²⁺ to Mn³⁺) observed in the galvanostatic profile ([Figure 5.6](#)). This indicates that Mn can be partially oxidized to Mn³⁺ when applying a low current density (0.05 A g⁻¹ in this case). At the same time, a small amount of Mn⁰ is also observed, suggesting some irreversibility during the oxidation reaction. After the 40th cycle, the amount of Mn³⁺ decreases while the amount of Mn⁰ increases. This demonstrates a decrease of reversibility for the oxidation reaction, and it can be well correlated to the capacity fading observed during the initial cycles. Interestingly, at the 60th and 80th cycle, the amount of Mn³⁺ increases and Mn⁰ decreases, evidencing an enhanced oxidation reaction, which can be the main reason for the obvious capacity increase. This is attributed to the shorter Li diffusion distances and faster reaction kinetics induced by the conductive SEI growing into the active particles through the cracks formed during cycling. At the 100th cycle, repeated conversion process and excessive SEI formation induce particle pulverization, resulting in a decreased reaction activity and leading to the subsequent capacity loss. This is evidenced by a decreased amount of Mn³⁺ and an increased amount of Mn⁰. In contrast, the fitting results of the CZMO-400 electrodes show a stable amount of Mn³⁺, and a decreased amount of Mn⁰ during long-term cycling ([Figure 5.8f](#)), indicating a limited oxidation reaction to Mn³⁺ and

improved reaction reversibility of the Mn⁰/Mn²⁺ oxidation. These phenomena imply a suppressed phase composition evolution process, which can be attributed to the fact that the coated layer inhibits excessive SEI growth and suppresses particle pulverization.

On the lithiated ZMO-1h electrodes (Figure 5.8c), the fraction of Mn⁰ decreases to the lowest value at the 40th cycle, then increases to high values from the 60th to the 80th cycle, and finally decreases again at the 100th cycle. This also agrees with the trend as described above, displaying a well-improved reaction activity from the 60th to the 80th cycle and capacity fading at the 100th cycle. In comparison, in the lithiated CZMO-400 electrodes (Figure 5.8f), the fraction of Mn⁰ is much higher than that in the ZMO-1h, and it even reaches 100 % at the 100th cycle, demonstrating an improved reduction conversion and enhanced efficiency induced by carbon coating.

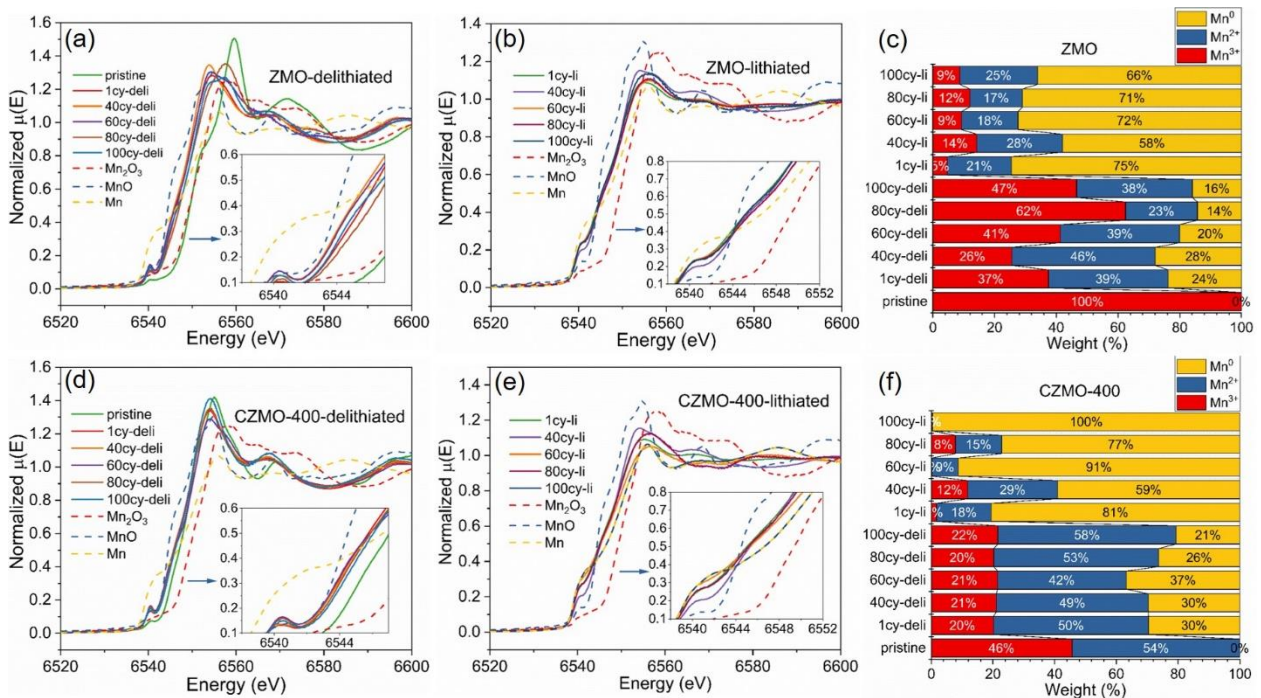


Figure 5.8 *Ex situ* XANES spectra for Mn K-edge: (a) delithiated ZMO-1h, (b) lithiated ZMO-1h, (d) delithiated CZMO-400 and (e) lithiated CZMO-400 and the LCF results based on the relative derivative normalized energy spectra in XANES region: (c) ZMO-1h and (f) CZMO-400.

The Mn local structure obtained from Fourier transform of EXAFS spectra is shown in Figure 5.10. The fitting results of the electrodes after 1 cycle, 40 cycles and 80 cycles at delithiated state are shown in Figure 5.9 and Table 5.1. The results indicate that both, the ZMO-1h and CZMO-400, are composed of MnO and Mn₃O₄ mixture after the 1st cycle, and composed of only MnO after the 40th cycle. Thereafter, the ZMO-1h changes to a mixed composition of MnO and Mn₃O₄ after the 80th cycle, whereas the CZMO-400 still exhibits the MnO composition. This is in agreement with the oxidation state analysis based on the XANES spectra. Moreover, the long-range orderliness of the crystal structure is weakened during cycling. As for the lithiated samples (Figure 5.9d&h and Figure 5.10c&d), the single broad peak is attributed to the overlapped Mn-Mn interaction (~ 2.6 Å) of Mn metal (ICSD 163411 $P4_13_2$) and Mn-O interaction (~ 2.1 Å) of MnO (ICSD 162039 $Fm\bar{3}m$). The long-range orderliness is not constructed after the conversion process.

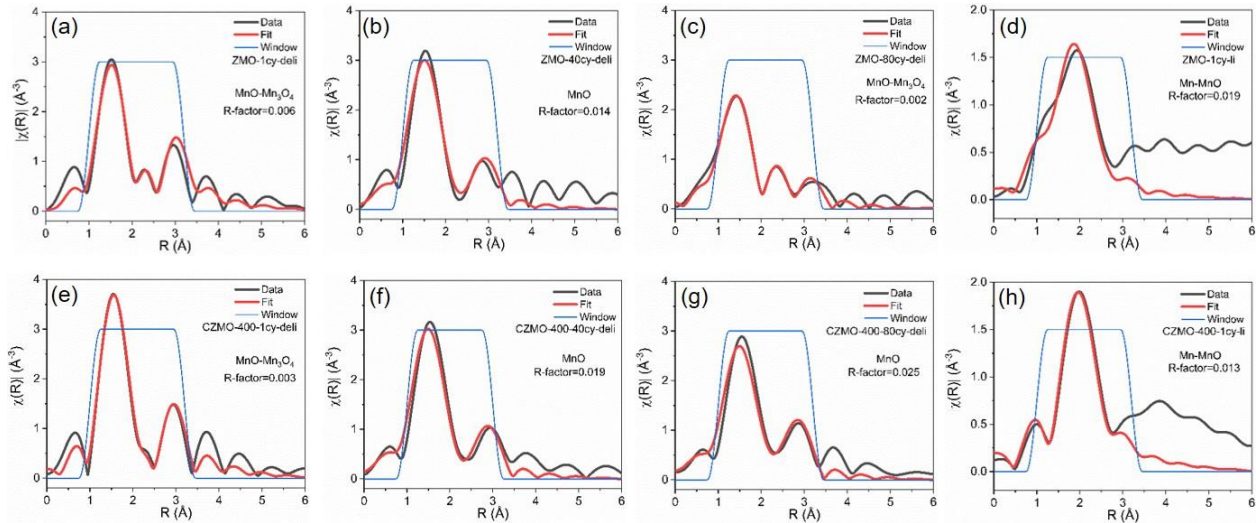


Figure 5.9 Fitting of the Fourier transformed EXAFS spectra for selected *ex situ* electrodes: (a~c) delithiated ZMO-1h at the 1st cycle (a), the 40th cycle (b) and the 80th cycle (c); (d) lithiated ZMO-1h at the 1st cycle; (e~g) delithiated CZMO-400 at the 1st cycle (e), the 40th cycle (f) and the 80th cycle (g); (h) lithiated CZMO-400 at the 1st cycle.

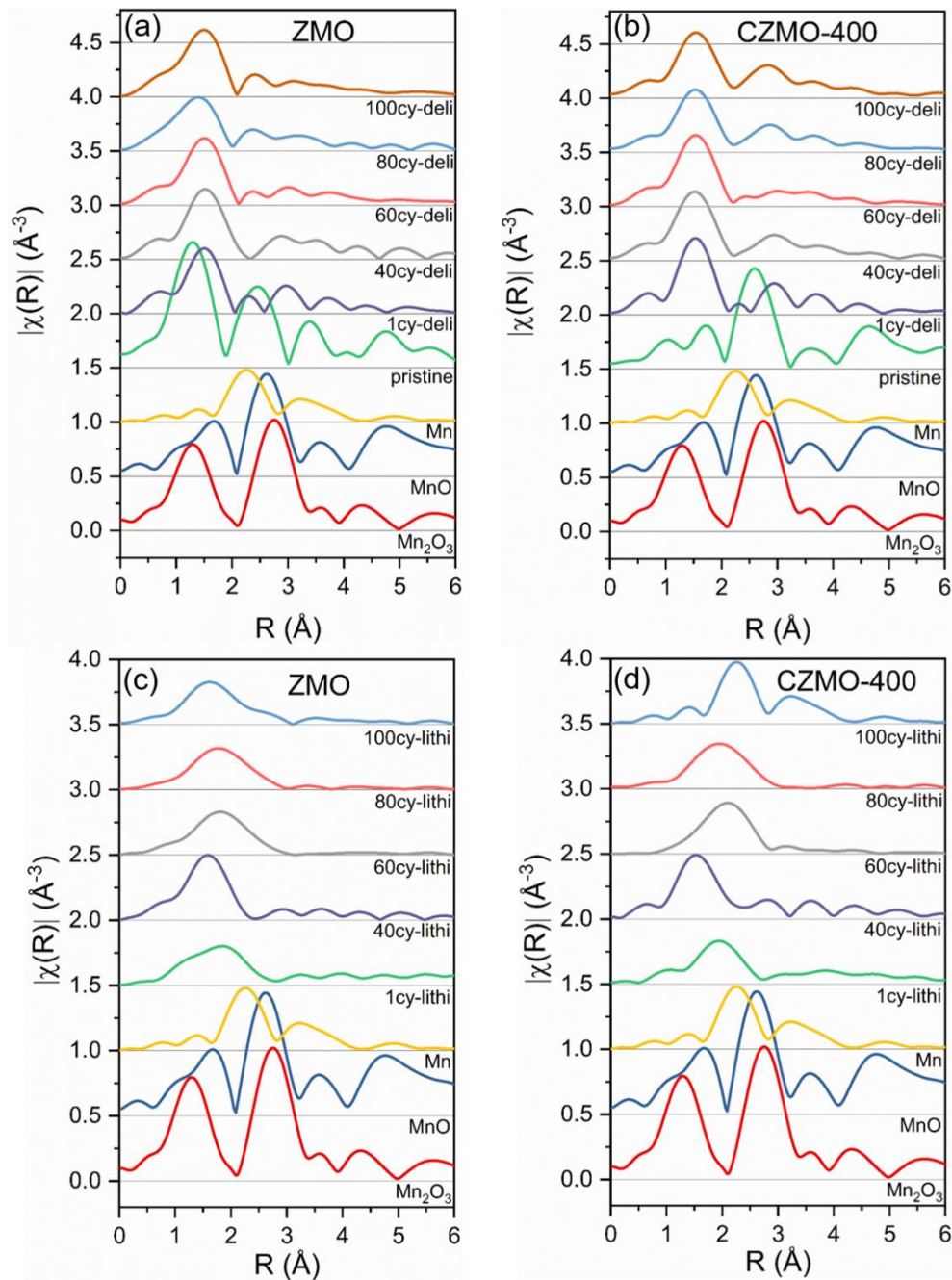


Figure 5.10 Mn local structure obtained from Fourier transform of EXAFS spectra: (a) delithiated ZMO-1h, (b) delithiated CZMO-400, (c) lithiated ZMO-1h, and (d) lithiated CZMO-400.

Table 5.1 The fitted parameters based on the EXAFS spectra for the delithiated electrodes.

| Parameters | Coordination numbers | The delithiated ZMO-1h electrodes | | | The delithiated CZMO-400 electrodes | | |
|--|----------------------|-----------------------------------|------------------------|------------------------|-------------------------------------|------------------------|------------------------|
| | | 1 st cycle | 40 th cycle | 80 th cycle | 1 st cycle | 40 th cycle | 80 th cycle |
| ΔE_0 | -- | -7.93 | -4.26 | -2.78 | -1.06 | -5.39 | -5.39 |
| R_{Mn-O1} (MnO) | 6 | 1.99 | 2.04 | 2.03 | 2.06 | 2.03 | 2.04 |
| R_{Mn-O2} (Mn ₃ O ₄) | 4 | 1.74 | -- | 1.98 | 2.08 | -- | -- |
| R_{Mn-O3} (Mn ₃ O ₄) | 2 | 2.06 | -- | 2.43 | 2.43 | -- | -- |
| R_{Mn-Mn1} (MnO) | 12 | 3.01 | 3.26 | 3.06 | 3.39 | 3.23 | 3.22 |
| R_{Mn-Mn2} (Mn ₃ O ₄) | 2 | 2.99 | -- | 3.07 | 2.98 | -- | -- |
| R_{Mn-Mn3} (Mn ₃ O ₄) | 4 | 3.23 | -- | 3.31 | 3.21 | -- | -- |
| σ^2_{O1} (MnO) | -- | 0.0115 | 0.0128 | 0.0384 | 0.0405 | 0.0122 | 0.0138 |
| σ^2_{O2} (Mn ₃ O ₄) | -- | 0.0288 | -- | 0.0147 | 0.0040 | -- | -- |
| σ^2_{Mn1} (MnO) | -- | 0.0387 | 0.0317 | 0.0383 | 0.0320 | 0.0312 | 0.0292 |
| σ^2_{Mn2} (Mn ₃ O ₄) | -- | 0.0033 | -- | 0.0118 | 0.0079 | -- | -- |
| R-factor | -- | 0.0055 | 0.0146 | 0.0015 | 0.0033 | 0.0188 | 0.0254 |

To further understand the different electrochemical behavior of the ZMO-1h and CZMO-400, EIS measurements were conducted every 6 cycles at 0.4 V during the lithiation process at the current density of 0.5 A g⁻¹ (see Figure 5.11a&c). Figure 5.11b shows the capacity variation of the ZMO-1h upon cycling. The maximum capacity of the ZMO-1h is achieved at the ~48th cycle, while the CZMO-400 shows a monotonous increase of the specific capacity. This is also in agreement with the above GCPL results. The Nyquist plots consist of two semicircles and an inclined line. In the high-frequency region (100~20 kHz), the intercept between the first semicircle and the real axis is related to the resistance of the cell system (R_s), including the cell parts, electrolyte, separator, and working electrode contact. In the mid-frequency range (400~3 Hz), the first semicircle corresponds to the parallel connection of the resistance of SEI (R_{SEI}) and the corresponding capacitance (CPE1). The second semicircle at lower frequencies (2~0.06 Hz) is attributed to the parallel connection of the charge transfer resistance (R_{ct}) and the corresponding capacitance (CPE2). The inclined line appearing at even lower frequencies indicates the diffusion process, which is represented by a constant phase element (CPE3) [218,219]. The equivalent circuit is shown in Figure 5.11d and the fitted Nyquist plots are depicted in Figure 5.11a&c.

The evolution of the fitted resistances is shown in Figure 5.11d. The R_s variation reflects the change of the electrode contact resistance. The R_s of the ZMO-1h obviously increases from the 50th cycle (~1 Ω) to the 120th cycle (~3 Ω), whereas the CZMO-400 has a stable R_s (~1.5 Ω). This result demonstrates that the coated carbon layer can delay the pulverization process, and help to keep the

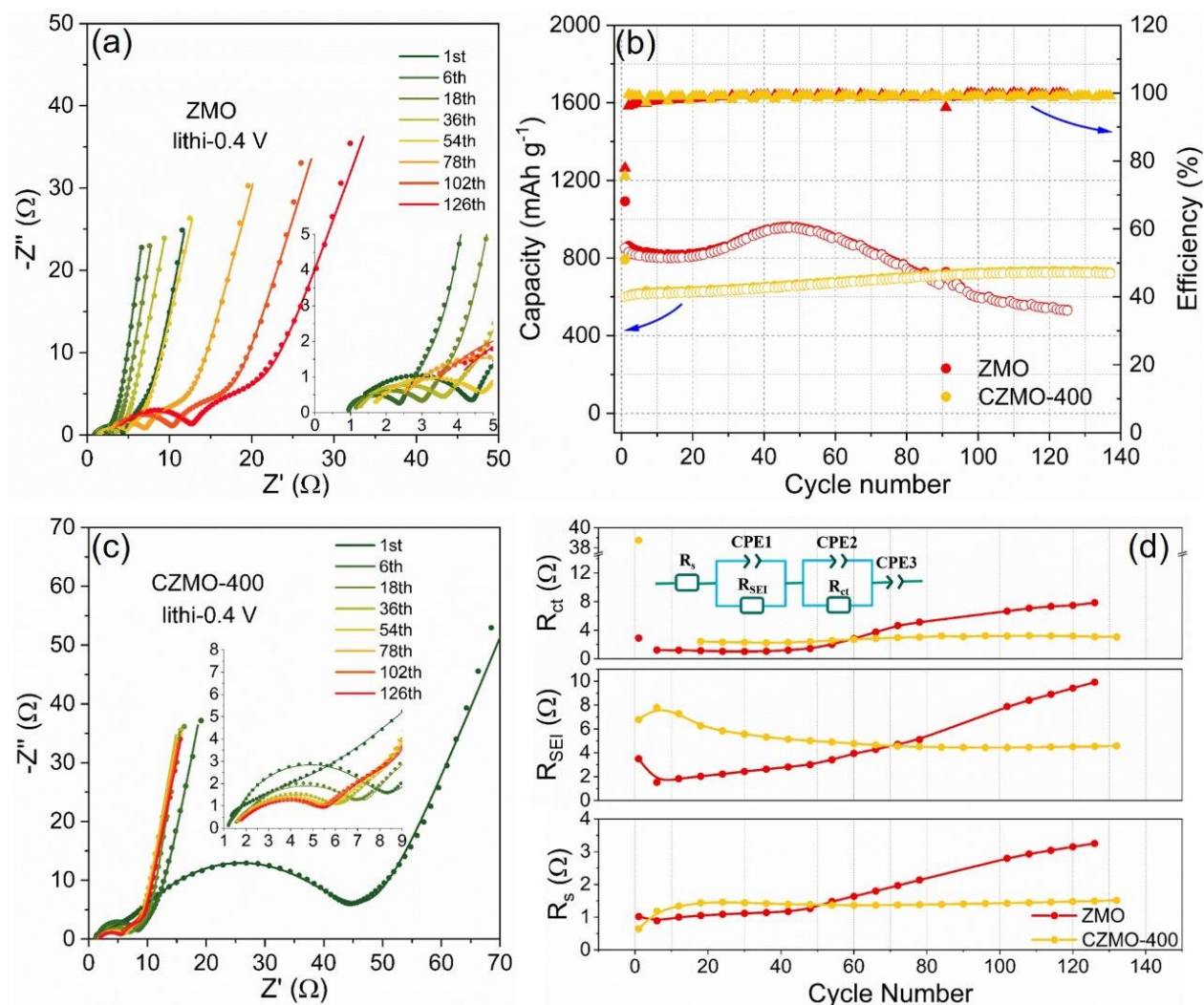


Figure 5.11 EIS test during GCPL cycling: (a&c) Nyquist plots recorded at 0.4 V during lithiation (point: raw data, line: fitted data) for (a) the ZMO-1h and (c) the CZMO-400; (b) capacities during lithiation (solid spots) and delithiation (circles) at 0.5 A g^{-1} , and (d) R_s , R_{SEI} , and R_{ct} obtained by fitting the Nyquist plots.

integrity of the electrode, thus avoiding the loose of contact between the active particles. The R_{SEI} of the ZMO-1h displays a dramatic decrease from 3.5 to 1.5Ω after the initial SEI formation. By contrast, the much higher R_{SEI} ($\sim 7 \Omega$) of the CZMO-400 indicates that the SEI formed on the carbon-coated surface is less conductive. Furthermore, the evolution of R_{SEI} is different for the two samples. The R_{SEI} of the ZMO-1h slowly increases before that the electrodes reach their highest capacities: the increase of additional capacity occurs in parallel with the increase of R_{SEI} . This confirms that the growth of conductive SEI can accommodate more and more Li^+ ions. Afterwards, the R_{SEI} of the ZMO-1h rapidly increases, while, in parallel, a fast capacity fading occurs. It can be

speculated that the SEI becomes less conductive after repeated charge/discharge cycles and seriously impedes the Li^+ migration. In comparison, the R_{SEI} of the CZMO-400 decreases gradually and keeps a low value after ~ 80 cycles. It indicates that the less conductive SEI formed on the coated carbon is activated as the cycling proceeding. The initial R_{ct} of the ZMO-1h and CZMO-400 are 3Ω and 39Ω , respectively. The higher R_{ct} of the CZMO-400 can explain the high electrode polarization observed during the 1st lithiation process in the CVs (Figure 4.21d, g and j). However, after the 1st cycle, the R_{ct} becomes very low ($\sim 1 \Omega$ for the ZMO-1h and $\sim 2 \Omega$ for the CZMO-400). Thereafter, the R_{ct} of the ZMO-1h obviously increases after ~ 50 cycles, corresponding to the phase transformation and segregation upon cycling. In contrast, the stable R_{ct} of the CZMO-400 confirms the role of the coated carbon on the suppression of phase changes.

5.2.2 Electrochemical tests of the bare ZnMn_2O_4 with a CPAME electrolyte

CV and GCPL tests are carried out on the ZMO-3h anodes with the CPAME electrolyte (1 M LiPF_6 in CPAME), as shown in Figure 5.12. The CV curve indicates the instability of the CPAME electrolyte in this system at potentials higher than 2.67 V vs. Li^+/Li . Thus, the potential window for the further tests is set to 0.01~2.6 V. However, the capacity fades fast during cycling, which can be attributed to the strong side reactions consuming the electrolyte. Therefore, 2 wt.% VC is added in order to form a protective SEI layer, preventing the electrolyte decomposition. The electrochemical performance is further investigated with the CPAME-VC electrolyte (1 M LiPF_6 in CPAME / VC (2 wt.%)). The results are compared with the ones with the LP30 electrolyte. As

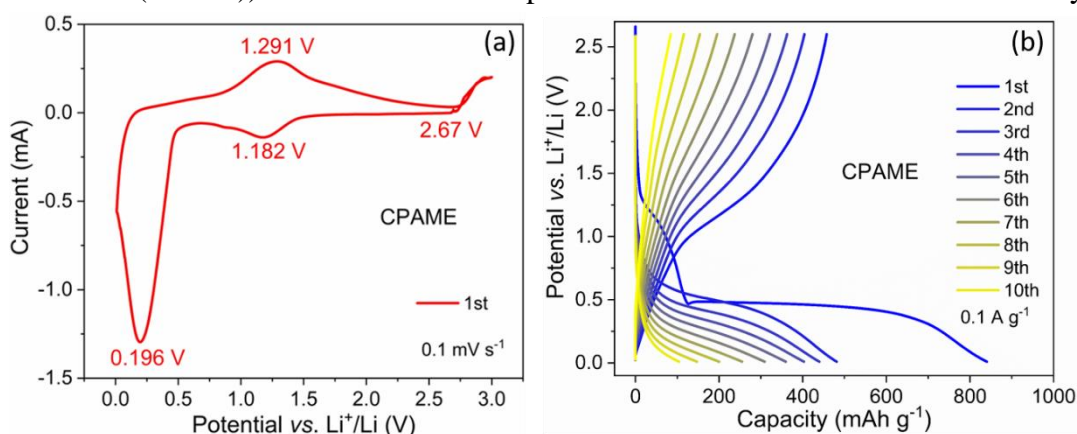


Figure 5.12 Electrochemical test of the ZMO-3h anodes in the CPAME electrolyte (1 M LiPF_6 in CPAME): (a) CV with a scan rate of 0.1 mV s^{-1} , (b) GCPL potential profiles with a current density of 0.1 mA g^{-1} .

shown in Figure 5.13, the CVs of the cell with the CPAME-VC electrolyte show stronger electrode polarization than the ones with the LP30, illustrated by the slightly shifted and broader redox peaks. It can be attributed to the lower conductivity, higher viscosity of the CPAME-VC electrolyte than the LP30. The weak peak at around 0.8 V in the cathodic part can be related to the SEI formation. In the CPAME-VC electrolyte, this peak appears at almost the same potential in subsequent cycles, whereas in the LP30, it shifts to lower potentials continuously during cycling. It indicates that the CPAME-VC electrolyte leads to a stable SEI formation process, while this process in the EC/DMC electrolyte varies during cycling.

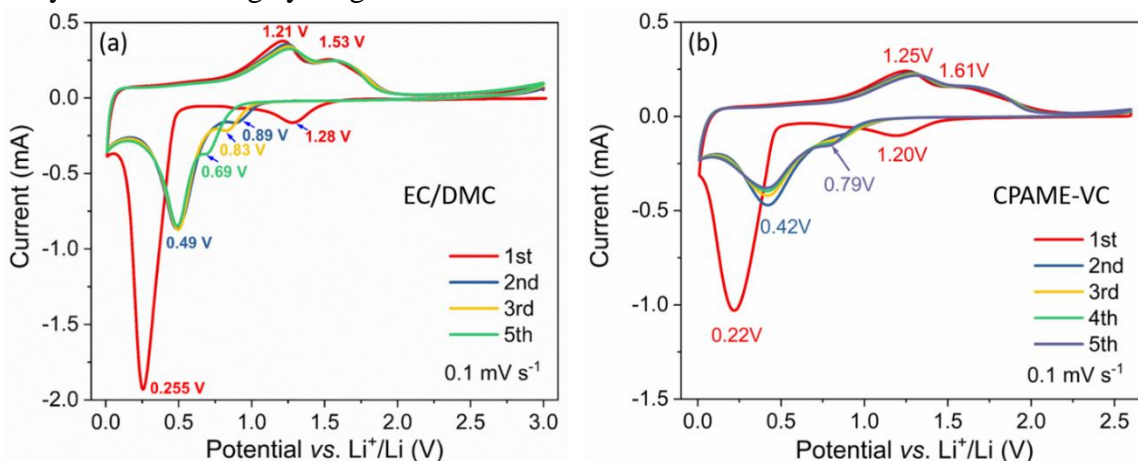


Figure 5.13 CV curves of the ZMO-3h anodes in different electrolytes with a scan rate of 0.1 mV s^{-1} : (a) the LP30 (1 M LiPF_6 in EC/DMC), (b) 1 M LiPF_6 in CPAME / VC (2 wt.%).

Long-term cycling performance with the CPAME-VC electrolyte has been tested at the current density of 0.5 A g^{-1} . The capacity of the cell with the CPAME-VC electrolyte decreases slowly and continuously during cycling (Figure 5.14a). In contrast, the capacity of the cell with the LP30 electrolyte decreases slightly in the initial ~ 30 cycles, then increases dramatically during $30\sim 100$ cycles and finally decreases again ($100\sim 150$ cycles). The potential profiles of the CPAME-VC cell are shown in Figure 5.14c&d, displaying a degradation of the transition metal redox reaction during cycling without extra capacity increase induced by the SEI layer, which is instead observed in the LP30 electrolyte. However, the capacities with these two electrolytes become identical after 150 cycles. Therefore, it can be concluded that the activity of the SEI formed on the transition metal oxide surface can be suppressed by replacing the more reactive EC/DMC electrolyte solvent with a more stable ester-based one (CPAME) with 2 wt.% VC additive. To test the rate performance with the CPAME-VC electrolyte, GCPLs at different current densities have been conducted (0.1 A

$\text{g}^{-1} \sim 5 \text{ A g}^{-1}$). As shown in Figure 5.14b, e&f, the cell with the CPAME-VC electrolyte delivers worse rate capability than the one with the LP30 electrolyte. It can be related to the lower conductivity and higher viscosity of the CPAME-VC electrolyte. Moreover, the loss of capacity upon cycling without any extra capacity increase with the CPAME-VC electrolyte can be another reason. In summary, even though a lower rate capability is delivered, the CPAME-VC electrolyte performs a much higher stability than the LP30 electrolyte against the capacity fluctuation during cycling.

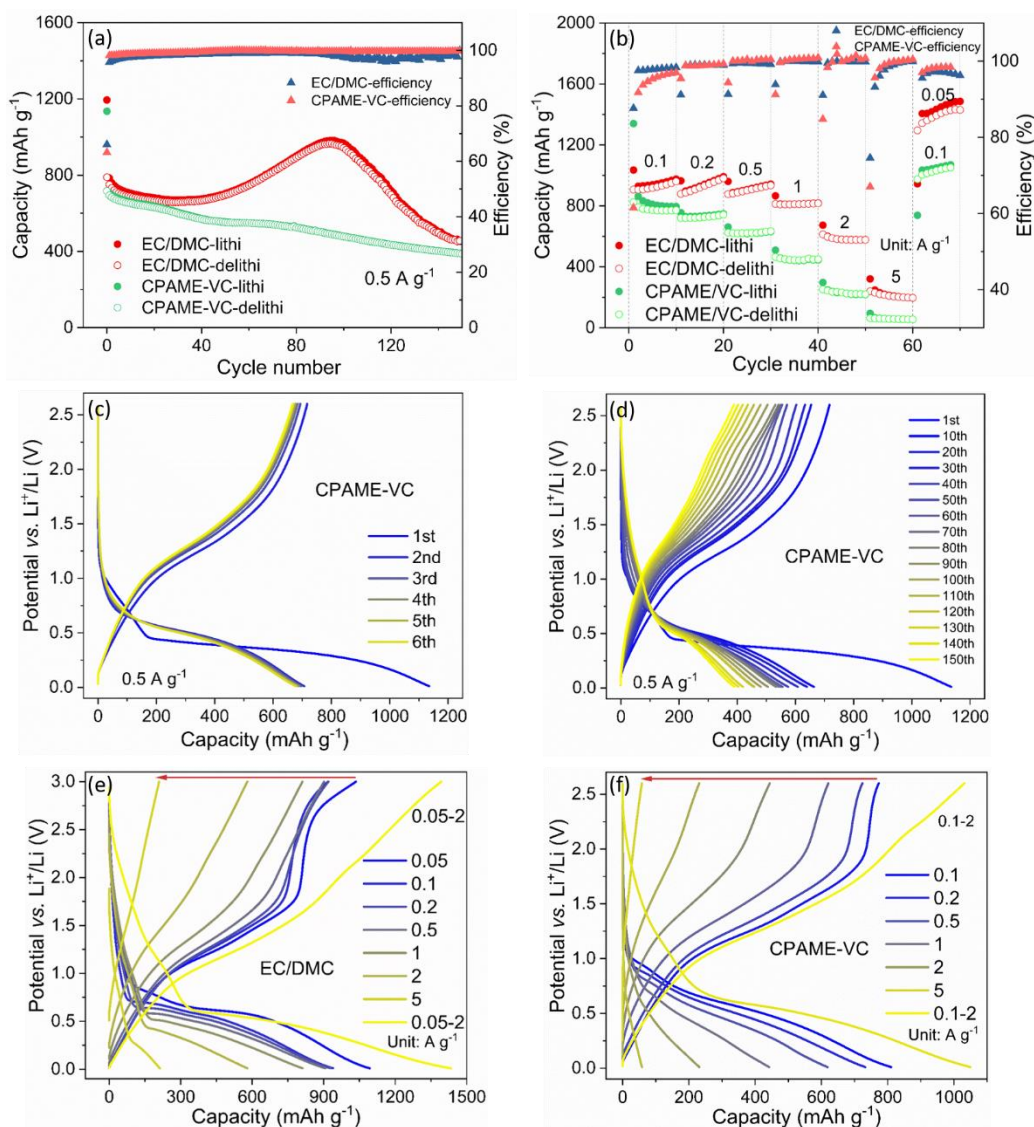


Figure 5.14 GCPL cycling tests of the ZMO-3h with the LP30 and CPAME-VC electrolytes: (a) cycling performance with a current density of 0.5 A g^{-1} , (b) rate performance, (c&d) potential profiles with the CPAME-VC electrolyte, and (e&f) potential profiles with different current densities: (e) the EC/DMC electrolyte (LP30) and (f) the CPAME-VC electrolyte.

5.3 Conclusions

In summary, the reasons for the extra capacity increase and the fast electrode degradation of the bare ZnMn_2O_4 electrode are deeply elucidated. The *ex situ* XPS reveals that the SEI film is composed of Li_2CO_3 and LiOH , both of which can contribute to the capacity increase. The *ex situ* TEM evidences the formation of Zn-based nanoparticles after the 25th cycle, which results in capacity fading of conversion reaction. Moreover, *ex situ* XAS and CV illustrate the evolution of the metal oxides during repeated conversion reaction. It is confirmed that the increase in $\text{Mn} \rightarrow \text{Mn}_3\text{O}_4$ conversion reaction occurs after ~60 cycles, which contributes to the capacity increase. The long-term EIS test reveals that the fast capacity fading after the extra capacity increase of the bare ZnMn_2O_4 electrode is related to the fast resistance increase of the electrode. It can be attributed to the excessive SEI formation and active particle pulverization. Moreover, the carbon-coating is demonstrated to be an effective method to improve the electrode cycling stability and to stabilize the significant capacity variations. This work reveals that the coated layer can not only suppress the active material pulverization and inhibit SEI excessive growth, but also restrain the phase evolution of the active material from MnO to Mn_3O_4 and enhance the reduction conversion to metallic Mn, inducing a stabilized conversion reaction. In addition, the using of the CPAME-VC electrolyte also prevents the capacity fluctuations. It indicates that the composition of the electrolyte plays an important role in the SEI formation and the cycling performance of the conversion-type transition metal oxide. Except for the development of the electrode materials, optimizing the electrolyte is another important way to improve the electrochemical performance. In future, understanding of the SEI composition with the CPAME-VC electrolyte can be conducted by *ex situ* XPS, as well as, further optimization of the electrolyte through properly tuning the SEI is also needed. This study gives a deeper understanding on the electrochemical energy storage mechanism of the ZnMn_2O_4 anode and gives explanations on the influence of carbon coating. The results can provide a deep insight to understand the degradation of conversion-type materials.

6 Conclusions and outlook

In this thesis, the conversion-type ternary transition metal oxides ZnCo_2O_4 and ZnMn_2O_4 , as well as their carbon composites have been comprehensively studied as conversion/alloying anode materials in LIBs.

For the material synthesis, different methods are applied and studied. The ZnCo_2O_4 and a ZnCo_2O_4 -carbon cloth composite have been prepared by a hydrothermal method, resulting in a morphology of a hierarchical layered ZnCo_2O_4 attached on the conductive carbon fibers. In contrast, the ZnMn_2O_4 nanoparticles have been synthesized through a co-precipitation and calcination method, which is much easier for up-scaling. The obtained samples are agglomerated nanoparticles with a uniform size of 15~30 nm, depending on the sintering temperature and time. During the calcination process, the TGA and HT-SRD reveal that the tetragonal spinel ZnMn_2O_4 phase forms at around 350 °C, then partially transforms to a cubic spinel phase ZnMn_2O_4 above 650 °C, and finally returns to tetragonal spinel phase after cooling down to 20 °C. Based on the as-prepared spinel ZnMn_2O_4 nanoparticles, a carbon-thermal reduction method has been used for carbon coating. The phase transition of the ZnMn_2O_4 during the carbonization process has been studied by HT-SRD. The result shows that the ZnMn_2O_4 is converted to ZnO-MnO composite at 250~400 °C, and the crystallized MnO and ZnO are formed above 350 °C and 600 °C, respectively.

The mechanism of Li storage in spinel ZnCo_2O_4 is investigated by *in situ* SRD and XAS during GCPL. The intermediate phases (LiCo_2O_3 (at 1.16 V), CoO (at ~0.9 V) and ZnO (at ~1.1 V)) are evidenced during the 1st lithiation process. After the formation of CoO and ZnO, the two oxides can be further converted to metallic Zn (following by formation of LiZn), Co and Li_2O . Similarly, *in situ* SRD performed on the ZnMn_2O_4 electrode during the 1st cycle reveals the formation of the intermediate tetragonal spinel phase $\text{LiZnMn}_2\text{O}_4$ which coexists with the original ZnMn_2O_4 during lithiation. Combined with the EIS analysis, it is concluded that low bulk electronic conductivity is the main reason for the slow initial insertion kinetics ($\text{ZnMn}_2\text{O}_4 \rightarrow \text{LiZnMn}_2\text{O}_4$). While during the conversion process (0.6~0.01 V), the material shows fast reaction kinetics, resulting in high rate performance. These results indicate that the initial lithiation of the conversion-type materials always start from a Li insertion process which facilitates the further conversion reaction.

As a binder-free anode for LIBs, the hierarchical ZCO/CC enables to deliver high specific capacity and shows excellent cycling stability (701 mAh g⁻¹ at 60th cycle at a specific current of 0.25 A g⁻¹). This appealing electrochemical behavior can be attributed to the higher electronic conductivity and shorter diffusion path in the hierarchical ZCO/CC composite. It is elucidated that the hierarchical nanostructure design and carbon-compositing can effectively improve the rate capability and cycling stability.

Different from the ZCO electrodes, the bare ZnMn₂O₄ displays obvious capacity increase during long-term cycling. The reasons for the extra capacity increase and the fast electrode degradation of the bare ZnMn₂O₄ electrode are deeply elucidated. The *ex situ* XPS reveals that the SEI film is composed of Li₂CO₃ and LiOH, both of which can contribute to the capacity increase. Moreover, *ex situ* XAS and CV illustrate the evolution of the metal oxides during repeated conversion reaction. It is confirmed that the increase in Mn→Mn₃O₄ conversion reaction occurs after ~60 cycles, which contributes to the capacity increase. The long-term EIS test reveals that the fast capacity fading after the extra capacity increase of the bare ZnMn₂O₄ electrode is related to the fast resistance increase of the electrode. It can be attributed to the excessive SIE formation and active particle pulverization.

Moreover, covering the ZnMn₂O₄ nanoparticles with carbon or carbon-derivative layers also improves efficiently the cycling stability and rate capability, compared to the significant capacity variations of the bare ZnMn₂O₄. The *ex situ* XAS and long-term EIS reveal that the coated layer can not only suppress the active material pulverization and inhibit SEI excessive growth, but also restrain the phase evolution of the active material from MnO to Mn₃O₄ and enhance the reduction conversion to metallic Mn, inducing a stabilized conversion reaction.

In addition, except for the development of the electrode materials, optimizing the electrolyte composition is another important way to improve the electrochemical performance. The use of the CPAME-VC electrolyte leads to a higher cycling stability comparing with the LP30 electrolyte. It can be attributed to the less reactivity of the CPAME solvent than the EC/DMC and the more stable SEI formed in the CPAME-VC electrolyte. Further understanding of the SEI composition with the CPAME-VC electrolyte can be conducted by *ex situ* XPS in future.

In summary, the strategies of nanosizing, coating with carbon layer, including a conductive matrix in the composite are important to prepare an optimize conversion anode material with higher cycling stability and rate capability. The SEI layer plays an important role on the conversion-type anode materials, especially in aspect of cycling life. Thus, using electrolyte additives and adjusting electrolyte solvent to control the SEI formation and growth is another useful strategy to improve the cell-performance with conversion/alloying electrodes. Furthermore, more breakthrough is still needed on decreasing the large voltage hysteresis to increase the energy efficiency. One way is to adjust the covalence by changing from oxides towards sulfides, nitrides, phosphides and hydrides. However, more efforts on both experimental and theoretical calculation are required to elucidate the origin of the voltage hysteresis and to find the way to reduce it.

7 Experimental part

7.1 Material synthesis

7.1.1 Hydrothermal preparation of the ZCO and ZCO/CC

Following the schematic diagram depicted in [Figure 7.1](#), $\text{ZnSO}_4 \cdot 6\text{H}_2\text{O}$ (2 mmol, 99.0%, Acros), $\text{Co}(\text{NO}_3)_2 \cdot 6\text{H}_2\text{O}$ (4 mmol, 98.0%, Sigma-Aldrich) and urea (15 mmol, 98.0%, Sigma-Aldrich) were dissolved in 70 mL deionized water by magnetic stirring for 30 min. Then, the CC (25 mm×25 mm, H2315/H23, Quin Tech) was vertically fixed in the center of a 100 mL Teflon-lined autoclave. Later, the mixed solution was put into the autoclave and heated at 200 °C for 16 h. After cooling down, the two precursors of the ZCO particles (the sediment) and of the ZCO/CC composite (the CC) were obtained in one pot. After that, the two obtained precursors were washed separately with deionized water and absolute ethanol several times and then dried at 80 °C overnight. Finally, the ZCO precursor was sintered at 500 °C for 6 h in air, whereas the ZCO/CC precursor was annealed at 500 °C for 6 h under N_2 flow and afterwards sintered at 450 °C for 15 min in air for further oxidation of Co^{2+} to Co^{3+} . A heating rate of $5\text{ }^\circ\text{C min}^{-1}$ was used until the annealing temperature was reached.

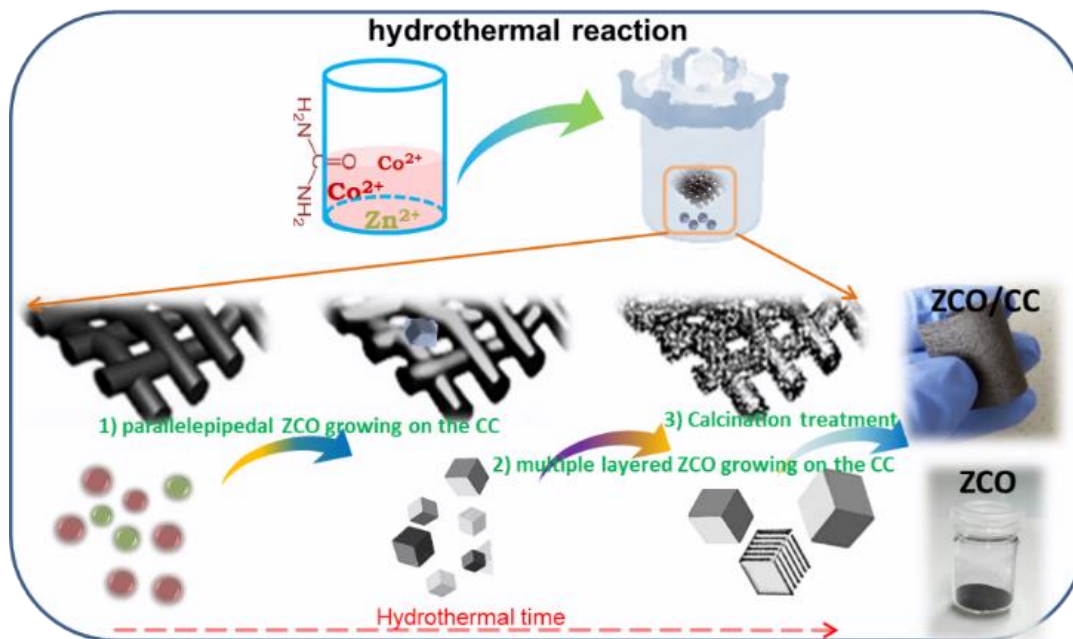


Figure 7.1 Schematic diagram of the hydrothermal synthesis process of the ZCO and the ZCO/CC.

7.1.2 Synthesis of ZnMn₂O₄ nanoparticles

The ZnMn₂O₄ nanoparticles were prepared via oxalic acid co-precipitation method [105]. Zinc acetate dihydrate (Zn(CH₃COO)₂·2H₂O, Alfa-Aesar, 98%), manganese acetate tetrahydrate (Mn(CH₃COO)₂·4H₂O, Aldrich, 99%), and oxalic acid (H₂C₂O₄, Aldrich, 99%) were used without further purification. 16 mmol zinc acetate and 32 mmol manganese acetate were dissolved in deionized water to form solution A, as well as 72 mmol oxalic acid was dissolved in deionized water to form solution B. Solution A was added into solution B during vigorous stirring and the mixed solution was stirred at 600 rpm for 0.5 h. The obtained precipitate was washed and centrifuged several times with deionized water and ethanol. The precursor was obtained after drying at 80 °C for 12 h and named ZMO-pre. Subsequently, the ZMO-pre was calcined at 350 °C for 3h, and at 500 °C for 1h and 3 h in air, named ZMO-350, ZMO-1h and ZMO-3h, respectively.

7.1.3 Carbon coating on ZnMn₂O₄ nanoparticles

D-(+)-Glucose anhydrous (C₆H₁₂O₆, Alfa Aesar, 99%) was used as carbon source without further purification. The ZMO-1h was mixed with glucose with mass ratio of ZMO-1h : glucose=2:1 through dissolving in water and dried at 80 °C for 12 h. Then, the precursor was sintered at 300, 400, 500 °C for 1 h under Ar flow, named CZMO-300, CZMO-400, CZMO-500, respectively.

7.2 General characterizations

7.2.1 XRD

XRD was carried out by a STOE Stadi P X-ray powder diffractometers (50 kV, 40 mA) in Debye-Scherrer geometry equipped with Mythen1K detectors. Mo-K_{α1} radiation (λ=0.70932 Å) and Co-K_{α1} radiation (λ=1.78896 Å) were used to characterize the crystal structure. Rietveld refinement was performed to analyze the diffraction data using the FullProf software package [220].

7.2.2 SEM and EDS

A field emission scanning electron microscope Merlin (FESEM, Carl Zeiss SMT AG) was used to study the morphology of the samples. The particle size was statistically calculated by the imageJ software. The elemental distribution of the samples was determined by energy dispersive X-ray spectroscopy (EDS, Bruker, Quantax 400 SDD).

7.2.3 TGA/DSC

TGA/DSC were conducted through a thermogravimetric analyzer (STA 449C, Netzsch GmbH) under O₂/Ar flow (11/31 mL min⁻¹).

7.2.4 Raman

Raman Spectroscopy was performed by a Raman spectrometer (LabRam Evolution HR, HORIBA Jobin Yvon) with 532 nm laser excitation and laser power of 10 mW, and 633 nm laser excitation and laser power of 17 mW.

7.2.5 FTIR

FTIR was conducted by using a Bruker Tensor 27 FT-IR spectrometer.

7.2.6 XPS

XPS was performed using a K-Alpha+ XPS spectrometer (ThermoFisher Scientific, East Grinstead, UK). The Thermo Avantage software is used in data acquisition and processing as described by K.L. Parry *et al.*[221]. All samples were analyzed using a microfocused, monochromated Al K α X-ray source (400 μ m spot size). The K-Alpha+ charge compensation system was employed during analysis, using electrons of 8 eV energy and low-energy argon ions to prevent localized charge accumulating. The spectra were fitted with one or more Voigt profiles (binding energy uncertainty: ± 0.2 eV) and Scofield sensitivity factors were applied for quantification [222]. All spectra were referenced to the C 1s peak (C–C, C–H) at 285.0 eV binding energy and the C 1s (graphite) at 284.4 eV controlled by means of the photoelectron peaks of metallic Cu, Ag, and Au, respectively. All *ex situ* electrodes were prepared in an Argon-filled glove

box and transferred under inert gas in the spectrometer. The electrodes were etched using clusters of 1000 argon atoms and 4 keV energy (MAGCIS, ThermoFisher Scientific).

7.2.7 TEM

The samples were examined using a Titan 80–300 electron microscope, equipped with a CEOS image aberration corrector, high angle annular dark field (HAADF) scanning transmission electron microscopy (STEM) detector and a Tridiem Gatan image filter (GIF). The microscope was operated at an accelerating voltage of 300 kV. To investigate the morphology and phase composition, high-angle annular dark field (HAADF), selected area electron diffraction (SAED), high-resolution TEM imaging (HRTEM), and electron energy loss spectroscopy (EELS) were performed. The pristine samples were prepared by dispersing the sample powder into ethanol through ultra-sonication and then drop casting on a copper grid. For the *ex situ* samples, all samples were prepared under an argon atmosphere inside a glovebox. The samples dispersed onto a carbon-coated grid were transferred to the microscope using a Gatan TEM vacuum transfer holder. All EELS spectra were re-calibrated using the π^* transition of the carbon edge at 285 eV and the plural scattering was removed using the Fourier-ratio method. The elemental map of Li was extracted from STEM spectrum imaging of Li-K edge from a relatively thin specimen region ($t/\lambda < 1$). After removing the zero loss peak a second derivative of the low loss region was used to enhance the separation of the Mn M-edge and the Li-K edge. Selected area electron diffraction (SAED) was performed on micro-sized agglomerated using a 40 μm aperture.

7.2.8 N₂ adsorption-desorption

Nitrogen adsorption-desorption isotherms were obtained in an ASAP2460 instrument from micromeritics at -195.8 °C. Samples were degassed at 120 °C for 12 h prior to the analysis. SSAs were calculated based on the BET in the 0.05~0.25 relative pressure range.

7.3 Electrochemical tests

7.3.1 Working electrode preparation

The ZCO electrodes were prepared by mixing ZCO powder, carbon black (Super-C65, Timcal Ltd.) and PVDF binder (R6020/1001, Solvay) in a weight ratio of 8:1:1 using NMP (GC 99.5%,

Merck KGaA). The slurry was cast on Cu foil using an Erichsen coatmaster with a doctor-blade. After drying, the coated foil was cut into disks (ϕ 12 mm, ~ 14 μm thick and ~ 1.1 mg ZCO loading on ~ 10 mg Cu foil). In contrast, the as-prepared ZCO/CC composite was also cut into disks (ϕ 12 mm, ~ 147 μm thick, and ~ 1.9 mg ZCO loading on 4.5 mg carbon cloth).

The ZMO and CZMO electrodes were prepared by coating a uniform slurry on a 10 μm thick copper foil with the mass loading of ~ 2 mg cm^{-2} and the dry thickness of ~ 15 μm . The slurry mixed through deionized water was consisted of active material (60 wt.%), sodium carboxymethyl cellulose (NaCMC, CRT2000, WaloCel, 10 wt.%), styrene-butadiene (SBR) co-polymer latex (TRD2001, JSR Micro, 10 wt.%), and carbon black (Super P Li, Timcal Ltd., 20 wt.%).

7.3.2 Cell configurations

For the ZCO and ZCO/CC working electrodes, CR2032 type coin cells were built for all the electrochemical measurements. One coin cell was composed of a working electrode, polypropylene separator (ϕ 17 mm, Celgard 2325-1750-A), Li foil counter electrode (ϕ 15 mm, Alfa Aesar) and LP30 electrolyte (1 M LiPF_6 in ethylene carbonate/dimethyl carbonate =1:1 in mass, BASF).

For the ZMO and CZMO working electrodes, CR2032 type coin cells were built for CV and GCPL measurements. The coin cell consists of a working electrode, a glass fiber separator (Whatman[®]-GF/D), a Li foil counter electrode, and LP30 electrolyte.

The ZMO-3h electrodes were also tested with an ester-based electrolyte (1 M LiPF_6 in cyanopropionic acid methyl ester (CPAME) / vinylene carbonate (VC, 2 wt.%), supplied by Prof. Dr. Andrea Balducci of the Friedrich-Schiller-University Jena), in CR2032 type coin cells. A glass fiber separator and a Li foil counter electrode were used.

The EIS measurement during the 1st cycle of the ZMO-3h electrode was conducted on a T-shape Swagelok[®] cell. It was assembled with a working electrode, two glass fiber separators, a Li foil counter electrode, LP30 electrolyte, and a Li tip reference electrode placed close to the working electrode.

PAT-cells (EL-CELL[®]) were used in long-term GCPL and EIS measurements for the ZMO-1h, CZMO-300 and CZMO-400 electrodes. The cells were assembled with a PAT-Core, which was

composed of a working electrode, a thin glass fiber separator, a Li foil counter electrode, LP30 electrolyte between two stainless steel plungers, and a Li-ring reference electrode.

All the cells were built in an Ar-filled glovebox (Labstar glove box workstation and MB200, MBraun GmbH).

7.3.3 Electrochemical tests

GCPL, CV and EIS were carried out utilizing a multichannel potentiostat (VMP3, Bio-Logic Science Instruments). The cells were kept in a climate chamber (Binder GmbH) at 25 °C during the electrochemical experiments. GCPL tests were measured in a potential range of 0.01~3.0 V vs. Li⁺/Li with varying specific currents (0.05, 0.1, 0.2, 0.5, 1, 2 and 5 A g⁻¹). The cell with the CPAME-VC and CPAME electrolytes were measured in a potential range of 0.01~2.6 V vs. Li⁺/Li. CVs were conducted in a same potential range with scan rates of 0.1, 0.2, 0.5, 1 mV s⁻¹. EIS measurements were conducted at specific potentials and specific cycle numbers upon an alternating current signal with an amplitude of 5 mV in a frequency range from 500 kHz to 10 mHz. The cells were hold at the selected potential for 3 h to reach equilibrium prior to each EIS test. The impedance spectra were fitted using RelaxIS3 software (rdh Instruments GmbH & Co. KG).

7.3.4 Preparation of *ex situ* electrodes

For the *ex situ* XPS measurement on the ZMO-3h, the working electrodes were cycled with 0.5 A g⁻¹ and stabilized at the 1st lithiated (0.01 V vs. Li/Li⁺) and the 1st delithiated (3.0 V vs. Li⁺/Li) states.

For the *ex situ* TEM measurement on the ZMO-3h, the working electrodes were cycled with 0.5 A g⁻¹ current density and stabilized at the lithiated (0.01 V vs. Li⁺/Li) and the delithiated (3.0 V vs. Li⁺/Li) states at the 1st, 25th, 90th, and 150th cycles.

For the *ex situ* XAS measurement on the ZMO-1h and CZMO-400, the working electrodes were cycled with 0.05 A g⁻¹ (1cy) and 0.5 A g⁻¹ (40cy, 60cy, 80cy, 100cy) current densities and stabilized at both lithiated and delithiated states at specific cycle numbers.

The cycled electrodes were taken out and washed with dimethyl carbonate three times, and dried through vacuum in room temperature. The process was proceeded in an Ar-filled glovebox.

7.4 Synchrotron characterizations

7.4.1 Cell preparation

The working electrodes (WEs) for *in situ* SRD and *in situ* XAS were prepared by mixing 70 wt.% of active material (ZCO, ZMO-3h), 20 wt.% of carbon black (Super P Li, Timcal Ltd.) and 10 wt.% of polytetrafluoroethylene (PTFE, white beads, Aldrich) binder by dry grinding and pressing on Cu mesh. About 3 mg of the mixture was pressed on the center of a copper mesh (ϕ 12 mm) and dried in vacuum at 80 °C for 24 h. Li|LP30|WE *in situ* CR2025 coin cells with a glass (for SRD) or Kapton foil (for XAS) window (ϕ 5 mm) in the center, were assembled by the same method stated above with glass fiber separators.

7.4.2 Electrochemical test

GCPL was conducted utilizing a multichannel potentiostat (VMP3, Bio-Logic) in a potential range of 0.01~3.0 V vs. Li⁺/Li at room temperature.

7.4.3 *In situ* SRD in ALBA

In situ SRD data of the ZCO electrode was collected by using monochromatic synchrotron radiation ($\lambda = 0.41266 \text{ \AA}$) at the MSPD beamline, ALBA [121]. Si and LaB₆ were used as standard samples for calibration. Glass capillaries (ϕ 0.5 mm) were used for *ex situ* SRD test.

7.4.4 *In situ* SRD in DESY

In situ SRD measurement of the ZMO-3h electrode was carried out by monochromatic synchrotron diffraction ($\lambda = 0.20720 \text{ \AA}$) at the beamline P02.1 in PETRA-III, DESY [121,223]. LaB₆ was used as standard sample for calibration. 2D diffraction images were collected and transformed to intensity- 2θ data by the software Fit2D [220].

7.4.5 *In situ* and *ex situ* XAS in DESY

In situ XAS measurement of the ZCO electrode and *ex situ* XAS measurements of the ZMO-1h and CZMO-400 electrodes were performed at the beamline P65 of PETRA III in DESY. The XAS spectra were recorded in transmission geometry with the conventional step-scan mode at Co K-

edge and Mn K-edge. The double-crystal fixed exit monochromator was equipped with Si (111) crystal, and the ionization chambers were optimized. A multichannel potentiostat (VMP3, Bio-Logic) was supplied by the beamline P02.1 (PETRA III, DESY) for electrochemical cycling. The spectra were processed by using the Demeter software [120].

7.4.6 HT-SRD in DESY

HT-SRD data were collected by monochromatic synchrotron diffraction at the beamline P02.1 of PETRA-III in DESY. The HT-SRD subjected on the ZMO-350 was conducted in air with a radiation wavelength of $\lambda = 0.20714 \text{ \AA}$. The HT-SRD investigation on the carbonization process of the ZMO-1h / glucose mixture (m:m=2:1) was conducted in Ar with a radiation wavelength of $\lambda = 0.20737 \text{ \AA}$. Quartz capillaries (ϕ 0.5 mm) were used as HT-SRD sample holder. The heating rate was $20 \text{ }^\circ\text{C min}^{-1}$ and the cooling rate was $50 \text{ }^\circ\text{C min}^{-1}$. The temperature was stabilized during data collection (less than 5 min per temperature point). LaB_6 was used as a standard reference sample for wavelength calibration. The as-obtained 2D image data were transformed to intensity- 2θ data using the software Fit2D [220].

8 References

- [1] D. Larcher, J.-M. Tarascon, Towards greener and more sustainable batteries for electrical energy storage, *Nat. Chem.* 7 (2015) 19–29. doi:10.1038/nchem.2085.
- [2] M.Z. Jacobson, M.A. Delucchi, Z.A.F. Bauer, S.C. Goodman, W.E. Chapman, M.A. Cameron, C. Bozonnat, L. Chobadi, H.A. Clonts, P. Enevoldsen, J.R. Erwin, S.N. Fobi, O.K. Goldstrom, E.M. Hennessy, J. Liu, J. Lo, C.B. Meyer, S.B. Morris, K.R. Moy, P.L. O’Neill, I. Petkov, S. Redfern, R. Schucker, M.A. Sontag, J. Wang, E. Weiner, A.S. Yachanin, 100% Clean and Renewable Wind, Water, and Sunlight All-Sector Energy Roadmaps for 139 Countries of the World, *Joule*. 1 (2017) 108–121. doi:10.1016/j.joule.2017.07.005.
- [3] M. Esteban, J. Portugal-Pereira, B.C. McLellan, J. Bricker, H. Farzaneh, N. Djalilova, K.N. Ishihara, H. Takagi, V. Roeber, 100% renewable energy system in Japan: Smoothing and ancillary services, *Appl. Energy*. 224 (2018) 698–707. doi:10.1016/j.apenergy.2018.04.067.
- [4] L. Kong, Z. Li, L. Liang, Y. Xia, J. Xie, A capacity-investment model of wind power with uncertain supply-price under high penetration rate, *J. Clean. Prod.* 178 (2018) 917–926. doi:10.1016/j.jclepro.2017.12.284.
- [5] C. Zöphel, S. Schreiber, T. Müller, D. Möst, Which Flexibility Options Facilitate the Integration of Intermittent Renewable Energy Sources in Electricity Systems?, *Curr. Sustain. Energy Reports*. 5 (2018) 37–44. doi:10.1007/s40518-018-0092-x.
- [6] Y. Liang, C. Zhao, H. Yuan, Y. Chen, W. Zhang, J. Huang, D. Yu, Y. Liu, M. Titirici, Y. Chueh, H. Yu, Q. Zhang, A review of rechargeable batteries for portable electronic devices, *InfoMat*. 1 (2019) 6–32. doi:10.1002/inf2.12000.
- [7] N. Lutsey, The rise of electric vehicles: The second million, *Int. Counc. Clean Transp.* (2017).
- [8] Y. Wang, Y. Song, Y. Xia, Electrochemical capacitors: mechanism, materials, systems, characterization and applications, *Chem. Soc. Rev.* 45 (2016) 5925–5950. doi:10.1039/C5CS00580A.
- [9] V. Aravindan, J. Gnanaraj, Y.-S. Lee, S. Madhavi, Insertion-Type Electrodes for Nonaqueous Li-Ion Capacitors, *Chem. Rev.* 114 (2014) 11619–11635. doi:10.1021/cr5000915.
- [10] Y. Fang, Z. Chen, L. Xiao, X. Ai, Y. Cao, H. Yang, Recent Progress in Iron-Based Electrode Materials for Grid-Scale Sodium-Ion Batteries, *Small*. 14 (2018) 1–19. doi:10.1002/sml.201703116.
- [11] V. Palomares, P. Serras, I. Villaluenga, K.B. Hueso, J. Carretero-González, T. Rojo, Na-ion batteries, recent advances and present challenges to become low cost energy storage systems, *Energy Environ. Sci.* 5 (2012) 5884. doi:10.1039/c2ee02781j.
- [12] S. W. Wang, W. Li, H.L. and S.C. Wang, Z. Miao, Structural Design of Anode Materials for Sodium-Ion Batteries, *J. Mater. Chem. A*. 6 (2018) 6183–6205. doi:10.1039/C7TA10823K.

- [13] C. Zhang, Y. Qiao, P. Xiong, W. Ma, P. Bai, X. Wang, Q. Li, J. Zhao, Y. Xu, Y. Chen, J.H. Zeng, F. Wang, Y. Xu, J. Jiang, Conjugated Microporous Polymers with Tunable Electronic Structure for High-Performance Potassium-Ion Batteries, *ACS Nano*. 13 (2019) 745–754. doi:10.1021/acsnano.8b08046.
- [14] J. Zheng, Y. Yang, X. Fan, G. Ji, X. Ji, H. Wang, S. Hou, M.R. Zachariah, C. Wang, Extremely stable antimony–carbon composite anodes for potassium-ion batteries, *Energy Environ. Sci.* 12 (2019) 615–623. doi:10.1039/C8EE02836B.
- [15] T. Masese, K. Yoshii, M. Kato, K. Kubota, Z.-D. Huang, H. Senoh, M. Shikano, A high voltage honeycomb layered cathode framework for rechargeable potassium-ion battery: P2-type $\text{K}_{2/3}\text{Ni}_{1/3}\text{Co}_{1/3}\text{Te}_{1/3}\text{O}_2$, *Chem. Commun.* 55 (2019) 985–988. doi:10.1039/C8CC07239F.
- [16] C. Pan, R. Zhang, R.G. Nuzzo, A.A. Gewirth, $\text{ZnNi}_x\text{Mn}_x\text{Co}_{2-2x}\text{O}_4$ Spinel as a High-Voltage and High-Capacity Cathode Material for Nonaqueous Zn-Ion Batteries, *Adv. Energy Mater.* 1800589 (2018) 1–11. doi:10.1002/aenm.201800589.
- [17] N. Zhang, F. Cheng, Y. Liu, Q. Zhao, K. Lei, C. Chen, X. Liu, J. Chen, Cation-Deficient Spinel ZnMn_2O_4 Cathode in $\text{Zn}(\text{CF}_3\text{SO}_3)_2$ Electrolyte for Rechargeable Aqueous Zn-Ion Battery, *J. Am. Chem. Soc.* 138 (2016) 12894–12901. doi:10.1021/jacs.6b05958.
- [18] M.-Q. Zhao, C.E. Ren, M. Alhabeab, B. Anasori, M.W. Barsoum, Y. Gogotsi, Magnesium-Ion Storage Capability of MXenes, *ACS Appl. Energy Mater.* 2 (2019) 1572–1578. doi:10.1021/acsaem.8b02253.
- [19] X. Deng, Y. Xu, Q. An, F. Xiong, S. Tan, L. Wu, L. Mai, Manganese ion pre-intercalated hydrated vanadium oxide as a high-performance cathode for magnesium ion batteries, *J. Mater. Chem. A*. 7 (2019) 10644–10650. doi:10.1039/C8TA11236C.
- [20] M. Wang, C. Jiang, S. Zhang, X. Song, Y. Tang, H.-M. Cheng, Reversible calcium alloying enables a practical room-temperature rechargeable calcium-ion battery with a high discharge voltage, *Nat. Chem.* 10 (2018) 667–672. doi:10.1038/s41557-018-0045-4.
- [21] H. Yang, H. Li, J. Li, Z. Sun, K. He, H.-M. Cheng, F. Li, The Rechargeable Aluminum Battery: Opportunities and Challenges, *Angew. Chemie.* (2019). doi:10.1002/ange.201814031.
- [22] I. Mohammad, R. Witter, M. Fichtner, M.A. Reddy, Introducing Interlayer Electrolytes: Toward Room-Temperature High-Potential Solid-State Rechargeable Fluoride Ion Batteries, *ACS Appl. Energy Mater.* 2 (2019) 1553–1562. doi:10.1021/acsaem.8b02166.
- [23] X. Zhao, Z. Zhao-Karger, D. Wang, M. Fichtner, Metal Oxychlorides as Cathode Materials for Chloride Ion Batteries, *Angew. Chemie Int. Ed.* 52 (2013) 13621–13624. doi:10.1002/anie.201307314.
- [24] C. Chen, T. Yu, M. Yang, X. Zhao, X. Shen, An All-Solid-State Rechargeable Chloride Ion Battery, *Adv. Sci.* 6 (2019) 1802130. doi:10.1002/advs.201802130.
- [25] H. Pan, Y.-S. Hu, L. Chen, Room-temperature stationary sodium-ion batteries for large-

- scale electric energy storage, *Energy Environ. Sci.* 6 (2013) 2338. doi:10.1039/c3ee40847g.
- [26] C. Julien, A. Mauger, A. Vijn, K. Zaghbi, *Lithium Batteries*, Springer International Publishing, Cham, 2016. doi:10.1007/978-3-319-19108-9.
- [27] B. Scrosati, Lithium Rocking Chair Batteries: An Old Concept?, *J. Electrochem. Soc.* 139 (1992) 2776. doi:10.1149/1.2068978.
- [28] M. Li, J. Lu, Z. Chen, K. Amine, 30 Years of Lithium-Ion Batteries, *Adv. Mater.* 30 (2018) 1800561. doi:10.1002/adma.201800561.
- [29] G.E. Blomgren, The Development and Future of Lithium Ion Batteries, *J. Electrochem. Soc.* 164 (2017) A5019–A5025. doi:10.1149/2.0251701jes.
- [30] G.-L. Xu, Q. Wang, J.-C. Fang, Y.-F. Xu, J.-T. Li, L. Huang, S.-G. Sun, Tuning the structure and property of nanostructured cathode materials of lithium ion and lithium sulfur batteries, *J. Mater. Chem. A* 2 (2014) 19941–19962. doi:10.1039/C4TA03823A.
- [31] D. Guyomard, Li Metal-Free Rechargeable LiMn_2O_4 /Carbon Cells: Their Understanding and Optimization, *J. Electrochem. Soc.* 139 (1992) 937. doi:10.1149/1.2069372.
- [32] M.S. Whittingham, Electrical Energy Storage and Intercalation Chemistry, *Science* (80-.). 192 (1976) 1126–1127. doi:10.1126/science.192.4244.1126.
- [33] K. Mizushima, P.C. Jones, P.J. Wiseman, J.B. Goodenough, Li_xCoO_2 ($0 < x < 1$): A new cathode material for batteries of high energy density, *Mater. Res. Bull.* 15 (1980) 783–789. doi:10.1016/0025-5408(80)90012-4.
- [34] M.S. Whittingham, Lithium Batteries and Cathode Materials, *Chem. Rev.* 104 (2004) 4271–4302. doi:10.1021/cr020731c.
- [35] C. Liu, F. Li, L.-P. Ma, H.-M. Cheng, Advanced Materials for Energy Storage, *Adv. Mater.* 22 (2010) E28–E62. doi:10.1002/adma.200903328.
- [36] R. Schmich, R. Wagner, G. Hörpel, T. Placke, M. Winter, Performance and cost of materials for lithium-based rechargeable automotive batteries, *Nat. Energy*. 3 (2018) 267–278. doi:10.1038/s41560-018-0107-2.
- [37] G.J. Wang, J. Gao, L.J. Fu, N.H. Zhao, Y.P. Wu, T. Takamura, Preparation and characteristic of carbon-coated $\text{Li}_4\text{Ti}_5\text{O}_{12}$ anode material, *J. Power Sources*. 174 (2007) 1109–1112. doi:10.1016/j.jpowsour.2007.06.107.
- [38] S. Goriparti, E. Miele, F. De Angelis, E. Di Fabrizio, R. Proietti Zaccaria, C. Capiglia, Review on recent progress of nanostructured anode materials for Li-ion batteries, *J. Power Sources*. 257 (2014) 421–443. doi:10.1016/j.jpowsour.2013.11.103.
- [39] D. Bresser, S. Passerini, B. Scrosati, Leveraging valuable synergies by combining alloying and conversion for lithium-ion anodes, *Energy Environ. Sci.* 9 (2016) 3348–3367. doi:10.1039/C6EE02346K.
- [40] Y. Lu, L. Yu, X.W. (David) Lou, Nanostructured Conversion-type Anode Materials for

- Advanced Lithium-Ion Batteries, *Chem.* 4 (2018) 972–996. doi:10.1016/j.chempr.2018.01.003.
- [41] J. Cabana, L. Monconduit, D. Larcher, M.R. Palacín, Beyond intercalation-based Li-ion batteries: The state of the art and challenges of electrode materials reacting through conversion reactions, *Adv. Mater.* 22 (2010) 170–192. doi:10.1002/adma.201000717.
- [42] D. Bresser, K. Hosoi, D. Howell, H. Li, H. Zeisel, K. Amine, S. Passerini, Perspectives of automotive battery R&D in China, Germany, Japan, and the USA, *J. Power Sources.* 382 (2018) 176–178. doi:10.1016/j.jpowsour.2018.02.039.
- [43] D. Aurbach, Y. Talyosef, B. Markovsky, E. Markevich, E. Zinigrad, L. Asraf, J.S. Gnanaraj, H.J. Kim, Design of electrolyte solutions for Li and Li-ion batteries: A review, *Electrochim. Acta.* 50 (2004) 247–254. doi:10.1016/j.electacta.2004.01.090.
- [44] K. Xu, Electrolytes and Interphases in Li-Ion Batteries and Beyond, *Chem. Rev.* 114 (2014) 11503–11618. doi:10.1021/cr500003w.
- [45] M.C. Smart, B. V. Ratnakumar, S. Surampudi, Use of Organic Esters as Cosolvents in Electrolytes for Lithium-Ion Batteries with Improved Low Temperature Performance, *J. Electrochem. Soc.* 149 (2002) A361. doi:10.1149/1.1453407.
- [46] K. Kanamura, W. Hoshikawa, T. Umegaki, Electrochemical Characteristics of $\text{LiNi}_{0.5}\text{Mn}_{1.5}\text{O}_4$ Cathodes with Ti or Al Current Collectors, *J. Electrochem. Soc.* 149 (2002) A339. doi:10.1149/1.1448818.
- [47] D. Aurbach, K. Gamolsky, B. Markovsky, G. Salitra, Y. Gofer, U. Heider, R. Oesten, M. Schmidt, The Study of Surface Phenomena Related to Electrochemical Lithium Intercalation into Li_xMO_y Host Materials ($M = \text{Ni}, \text{Mn}$), *J. Electrochem. Soc.* 147 (2000) 1322. doi:10.1149/1.1393357.
- [48] W.-C. Yu, M.W. Geiger, Shutdown, bilayer battery separator, U.S. Patent, No. 5,565,281, 1996.
- [49] J.R. Kim, S.W. Choi, S.M. Jo, W.S. Lee, B.C. Kim, Characterization and Properties of P(VdF-HFP)-Based Fibrous Polymer Electrolyte Membrane Prepared by Electrospinning, *J. Electrochem. Soc.* 152 (2005) A295. doi:10.1149/1.1839531.
- [50] S.S. Zhang, A review on the separators of liquid electrolyte Li-ion batteries, *J. Power Sources.* 164 (2007) 351–364. doi:10.1016/j.jpowsour.2006.10.065.
- [51] J. Zhu, M. Yanilmaz, K. Fu, C. Chen, Y. Lu, Y. Ge, D. Kim, X. Zhang, Understanding glass fiber membrane used as a novel separator for lithium–sulfur batteries, *J. Memb. Sci.* 504 (2016) 89–96. doi:10.1016/j.memsci.2016.01.020.
- [52] H. Chen, M. Ling, L. Hencz, H.Y. Ling, G. Li, Z. Lin, G. Liu, S. Zhang, Exploring Chemical, Mechanical, and Electrical Functionalities of Binders for Advanced Energy-Storage Devices, *Chem. Rev.* 118 (2018) 8936–8982. doi:10.1021/acs.chemrev.8b00241.
- [53] K.Y. Cho, Y. Il Kwon, J.R. Youn, Y.S. Song, Interaction analysis between binder and particles in multiphase slurries, *Analyst.* 138 (2013) 2044. doi:10.1039/c3an36720g.

- [54] D. Bresser, D. Buchholz, A. Moretti, A. Varzi, S. Passerini, Alternative binders for sustainable electrochemical energy storage—the transition to aqueous electrode processing and bio-derived polymers, *Energy Environ. Sci.* 11 (2018) 3096–3127. doi:10.1039/c8ee00640g.
- [55] Y. Shi, L. Wen, S. Pei, M. Wu, F. Li, Choice for graphene as conductive additive for cathode of lithium-ion batteries, *J. Energy Chem.* 30 (2019) 19–26. doi:10.1016/j.jechem.2018.03.009.
- [56] C. Iwakura, Y. Fukumoto, H. Inoue, S. Ohashi, S. Kobayashi, H. Tada, M. Abe, Electrochemical characterization of various metal foils as a current collector of positive electrode for rechargeable lithium batteries, *J. Power Sources.* 68 (1997) 301–303. doi:10.1016/S0378-7753(97)02538-X.
- [57] J. Guo, A. Sun, C. Wang, A porous silicon–carbon anode with high overall capacity on carbon fiber current collector, *Electrochem. Commun.* 12 (2010) 981–984. doi:10.1016/j.elecom.2010.05.006.
- [58] M. Yazici, D. Krassowski, J. Prakash, Flexible graphite as battery anode and current collector, *J. Power Sources.* 141 (2005) 171–176. doi:10.1016/j.jpowsour.2004.09.009.
- [59] Q. Li, S. Zhu, Y. Lu, 3D Porous Cu Current Collector/Li-Metal Composite Anode for Stable Lithium-Metal Batteries, *Adv. Funct. Mater.* 27 (2017) 1606422. doi:10.1002/adfm.201606422.
- [60] Q. Sa, Y. Wang, Ni foam as the current collector for high capacity C–Si composite electrode, *J. Power Sources.* 208 (2012) 46–51. doi:10.1016/j.jpowsour.2012.02.020.
- [61] J.-M. Tarascon, M. Armand, Issues and challenges facing rechargeable lithium batteries, *Nature.* 414 (2001) 359–367. doi:10.1038/35104644.
- [62] J. Lu, Z. Chen, F. Pan, Y. Cui, K. Amine, High-Performance Anode Materials for Rechargeable Lithium-Ion Batteries, *Electrochem. Energy Rev.* 1 (2018) 35–53. doi:10.1007/s41918-018-0001-4.
- [63] X.-B. Cheng, R. Zhang, C.-Z. Zhao, Q. Zhang, Toward Safe Lithium Metal Anode in Rechargeable Batteries: A Review, *Chem. Rev.* 117 (2017) 10403–10473. doi:10.1021/acs.chemrev.7b00115.
- [64] A. Pei, G. Zheng, F. Shi, Y. Li, Y. Cui, Nanoscale Nucleation and Growth of Electrodeposited Lithium Metal, *Nano Lett.* 17 (2017) 1132–1139. doi:10.1021/acs.nanolett.6b04755.
- [65] L. Suo, Y.-S. Hu, H. Li, M. Armand, L. Chen, A new class of Solvent-in-Salt electrolyte for high-energy rechargeable metallic lithium batteries, *Nat. Commun.* 4 (2013) 1481. doi:10.1038/ncomms2513.
- [66] F. Ding, W. Xu, G.L. Graff, J. Zhang, M.L. Sushko, X. Chen, Y. Shao, M.H. Engelhard, Z. Nie, J. Xiao, X. Liu, P. V. Sushko, J. Liu, J.-G. Zhang, Dendrite-Free Lithium Deposition via Self-Healing Electrostatic Shield Mechanism, *J. Am. Chem. Soc.* 135 (2013) 4450–

4456. doi:10.1021/ja312241y.
- [67] Y. Lu, Z. Tu, L.A. Archer, Stable lithium electrodeposition in liquid and nanoporous solid electrolytes, *Nat. Mater.* 13 (2014) 961–969. doi:10.1038/nmat4041.
- [68] H. Kuwata, H. Sonoki, M. Matsui, Y. Matsuda, N. Imanishi, Surface Layer and Morphology of Lithium Metal Electrodes, *Electrochemistry.* 84 (2016) 854–860. doi:10.5796/electrochemistry.84.854.
- [69] Y. Gao, Z. Yan, J.L. Gray, X. He, D. Wang, T. Chen, Q. Huang, Y.C. Li, H. Wang, S.H. Kim, T.E. Mallouk, D. Wang, Polymer–inorganic solid–electrolyte interphase for stable lithium metal batteries under lean electrolyte conditions, *Nat. Mater.* 18 (2019) 384–389. doi:10.1038/s41563-019-0305-8.
- [70] M.-H. Ryou, D.J. Lee, J.-N. Lee, Y.M. Lee, J.-K. Park, J.W. Choi, Excellent Cycle Life of Lithium-Metal Anodes in Lithium-Ion Batteries with Mussel-Inspired Polydopamine-Coated Separators, *Adv. Energy Mater.* 2 (2012) 645–650. doi:10.1002/aenm.201100687.
- [71] S. Xin, Y. You, S. Wang, H. Gao, Y. Yin, Y. Guo, Solid-State Lithium Metal Batteries Promoted by Nanotechnology: Progress and Prospects, *ACS Energy Lett.* 2 (2017) 1385–1394. doi:10.1021/acseenergylett.7b00175.
- [72] D. Lin, J. Zhao, J. Sun, H. Yao, Y. Liu, K. Yan, Y. Cui, Three-dimensional stable lithium metal anode with nanoscale lithium islands embedded in ionically conductive solid matrix, *Proc. Natl. Acad. Sci.* 114 (2017) 4613–4618. doi:10.1073/pnas.1619489114.
- [73] M.H. Ryou, Y.M. Lee, Y. Lee, M. Winter, P. Bieker, Mechanical surface modification of lithium metal: Towards improved Li metal anode performance by directed Li plating, *Adv. Funct. Mater.* 25 (2015) 834–841. doi:10.1002/adfm.201402953.
- [74] H. Yang, E.O. Fey, B.D. Trimm, N. Dimitrov, M.S. Whittingham, Effects of Pulse Plating on lithium electrodeposition, morphology and cycling efficiency, *J. Power Sources.* 272 (2014) 900–908. doi:10.1016/j.jpowsour.2014.09.026.
- [75] D. Aurbach, The Study of Li-Graphite Intercalation Processes in Several Electrolyte Systems Using In Situ X-Ray Diffraction, *J. Electrochem. Soc.* 142 (1995) 1746. doi:10.1149/1.2044188.
- [76] A. Satoh, Electrochemical intercalation of lithium into graphitized carbons, *Solid State Ionics.* 80 (1995) 291–298. doi:10.1016/0167-2738(95)00149-Z.
- [77] T. Zheng, High-Capacity Carbons Prepared from Phenolic Resin for Anodes of Lithium-Ion Batteries, *J. Electrochem. Soc.* 142 (1995) L211. doi:10.1149/1.2048450.
- [78] K. Sato, M. Noguchi, A. Demachi, N. Oki, M. Endo, A Mechanism of Lithium Storage in Disordered Carbons, *Science* (80-.). 264 (1994) 556–558. doi:10.1126/science.264.5158.556.
- [79] Y. Liu, J.S. Xue, T. Zheng, J.R. Dahn, Mechanism of lithium insertion in hard carbons prepared by pyrolysis of epoxy resins, *Carbon N. Y.* 34 (1996) 193–200. doi:10.1016/0008-6223(96)00177-7.

- [80] T. Zheng, Lithium Insertion in High Capacity Carbonaceous Materials, *J. Electrochem. Soc.* 142 (1995) 2581. doi:10.1149/1.2050057.
- [81] S.J. An, J. Li, C. Daniel, D. Mohanty, S. Nagpure, D.L. Wood, The state of understanding of the lithium-ion-battery graphite solid electrolyte interphase (SEI) and its relationship to formation cycling, *Carbon N. Y.* 105 (2016) 52–76. doi:10.1016/j.carbon.2016.04.008.
- [82] M. Yoshio, H. Wang, K. Fukuda, Spherical Carbon-Coated Natural Graphite as a Lithium-Ion Battery-Anode Material, *Angew. Chemie Int. Ed.* 42 (2003) 4203–4206. doi:10.1002/anie.200351203.
- [83] J. Collins, G. Gourdin, M. Foster, D. Qu, Carbon surface functionalities and SEI formation during Li intercalation, *Carbon N. Y.* 92 (2015) 193–244. doi:10.1016/j.carbon.2015.04.007.
- [84] C. Lee, Y.-J. Han, Y.D. Seo, K. Nakabayashi, J. Miyawaki, R. Santamaría, R. Menéndez, S.-H. Yoon, J. Jang, C₄F₈ plasma treatment as an effective route for improving rate performance of natural/synthetic graphite anodes in lithium ion batteries, *Carbon N. Y.* 103 (2016) 28–35. doi:10.1016/j.carbon.2016.02.060.
- [85] M.R. Al Hassan, A. Sen, T. Zaman, M.S. Mostari, Emergence of graphene as a promising anode material for rechargeable batteries: a review, *Mater. Today Chem.* 11 (2019) 225–243. doi:10.1016/j.mtchem.2018.11.006.
- [86] P. Lian, X. Zhu, S. Liang, Z. Li, W. Yang, H. Wang, Large reversible capacity of high quality graphene sheets as an anode material for lithium-ion batteries, *Electrochim. Acta.* 55 (2010) 3909–3914. doi:10.1016/j.electacta.2010.02.025.
- [87] G. Wang, X. Shen, J. Yao, J. Park, Graphene nanosheets for enhanced lithium storage in lithium ion batteries, *Carbon N. Y.* 47 (2009) 2049–2053. doi:10.1016/j.carbon.2009.03.053.
- [88] Z.-L. Wang, D. Xu, H.-G. Wang, Z. Wu, X.-B. Zhang, In Situ Fabrication of Porous Graphene Electrodes for High-Performance Energy Storage, *ACS Nano.* 7 (2013) 2422–2430. doi:10.1021/nm3057388.
- [89] V. Aravindan, Y.-S. Lee, S. Madhavi, Research Progress on Negative Electrodes for Practical Li-Ion Batteries: Beyond Carbonaceous Anodes, *Adv. Energy Mater.* 5 (2015) 1402225. doi:10.1002/aenm.201402225.
- [90] B.N. Loeffler, D. Bresser, S. Passerini, M. Copley, Secondary Lithium-Ion Battery Anodes: From First Commercial Batteries to Recent Research Activities, *Johnson Matthey Technol. Rev.* 59 (2015) 34–44. doi:10.1595/205651314X685824.
- [91] Q. Zhang, M.G. Verde, J.K. Seo, X. Li, Y.S. Meng, Structural and electrochemical properties of Gd-doped Li₄Ti₅O₁₂ as anode material with improved rate capability for lithium-ion batteries, *J. Power Sources.* 280 (2015) 355–362. doi:10.1016/j.jpowsour.2015.01.124.
- [92] L. Shen, C. Yuan, H. Luo, X. Zhang, K. Xu, Y. Xia, Facile synthesis of hierarchically porous

- Li₄Ti₅O₁₂ microspheres for high rate lithium ion batteries, *J. Mater. Chem.* 20 (2010) 6998. doi:10.1039/c0jm00348d.
- [93] W. Xu, X. Chen, W. Wang, D. Choi, F. Ding, J. Zheng, Z. Nie, Y.J. Choi, J. Zhang, Z.G. Yang, Simply AlF₃-treated Li₄Ti₅O₁₂ composite anode materials for stable and ultrahigh power lithium-ion batteries, *J. Power Sources.* 236 (2013) 169–174. doi:10.1016/j.jpowsour.2013.02.055.
- [94] H. Liu, W. Li, D. Shen, D. Zhao, G. Wang, Graphitic Carbon Conformal Coating of Mesoporous TiO₂ Hollow Spheres for High-Performance Lithium Ion Battery Anodes, *J. Am. Chem. Soc.* 137 (2015) 13161–13166. doi:10.1021/jacs.5b08743.
- [95] W.-J. Zhang, A review of the electrochemical performance of alloy anodes for lithium-ion batteries, *J. Power Sources.* 196 (2011) 13–24. doi:10.1016/j.jpowsour.2010.07.020.
- [96] L.M.L. Fransson, J.T. Vaughey, R. Benedek, K. Edström, J.O. Thomas, M.M. Thackeray, Phase transitions in lithiated Cu₂Sb anodes for lithium batteries: an in situ X-ray diffraction study, *Electrochem. Commun.* 3 (2001) 317–323. doi:10.1016/S1388-2481(01)00140-0.
- [97] D.G. Kim, H. Kim, H.-J. Sohn, T. Kang, Nanosized Sn–Cu–B alloy anode prepared by chemical reduction for secondary lithium batteries, *J. Power Sources.* 104 (2002) 221–225. doi:10.1016/S0378-7753(01)00918-1.
- [98] U. Kasavajjula, C. Wang, A.J. Appleby, Nano- and bulk-silicon-based insertion anodes for lithium-ion secondary cells, *J. Power Sources.* 163 (2007) 1003–1039. doi:10.1016/j.jpowsour.2006.09.084.
- [99] X. Shen, Z. Tian, R. Fan, L. Shao, D. Zhang, G. Cao, L. Kou, Y. Bai, Research progress on silicon/carbon composite anode materials for lithium-ion battery, *J. Energy Chem.* 27 (2018) 1067–1090. doi:10.1016/j.jechem.2017.12.012.
- [100] K.C. Hewitt, L.Y. Beaulieu, J.R. Dahn, Electrochemistry of InSb as a Li Insertion Host: Problems and Prospects, *J. Electrochem. Soc.* 148 (2001) A402. doi:10.1149/1.1359194.
- [101] G.-B. Han, M.-H. Ryou, K.Y. Cho, Y.M. Lee, J.-K. Park, Effect of succinic anhydride as an electrolyte additive on electrochemical characteristics of silicon thin-film electrode, *J. Power Sources.* 195 (2010) 3709–3714. doi:10.1016/j.jpowsour.2009.11.142.
- [102] P. Poizot, S. Laruelle, S. Grugeon, L. Dupont, J.-M. Tarascon, Nano-sized transition-metal oxides as negative-electrode materials for lithium-ion batteries, *Nature.* 407 (2000) 496–499. doi:10.1038/35035045.
- [103] M. V Reddy, G.V.S. Rao, B.V.R. Chowdari, Metal Oxides and Oxysalts as Anode Materials for Li Ion Batteries, *Chem. Rev.* 113 (2013) 5364–5457. doi:10.1021/cr3001884.
- [104] C. Yuan, H. Bin Wu, Y. Xie, X.W. Lou, Mixed transition-metal oxides: Design, synthesis, and energy-related applications, *Angew. Chemie - Int. Ed.* 53 (2014) 1488–1504. doi:10.1002/anie.201303971.
- [105] F.M. Courtel, H. Duncan, Y. Abu-Lebdeh, I.J. Davidson, High capacity anode materials for Li-ion batteries based on spinel metal oxides AMn₂O₄ (A = Co, Ni, and Zn), *J. Mater. Chem.*

- 21 (2011) 10206. doi:10.1039/c0jm04465b.
- [106] Z. Liu, X.Y. Yu, U. Paik, Etching-in-a-Box: A Novel Strategy to Synthesize Unique Yolk-Shelled Fe₃O₄@Carbon with an Ultralong Cycling Life for Lithium Storage, *Adv. Energy Mater.* 6 (2016) 1502318. doi:10.1002/aenm.201502318.
- [107] Y. Ma, Y. Ma, G. Giuli, T. Diemant, R.J. Behm, D. Geiger, U. Kaiser, U. Ulissi, S. Passerini, D. Bresser, Conversion/alloying lithium-ion anodes-enhancing the energy density by transition metal doping, *Sustain. Energy Fuels.* 2 (2018) 2601–2608. doi:10.1039/c8se00424b.
- [108] Y. Ma, Y. Ma, U. Ulissi, Y. Ji, C. Streb, D. Bresser, S. Passerini, Influence of the doping ratio and the carbon coating content on the electrochemical performance of Co-doped SnO₂ for lithium-ion anodes, *Electrochim. Acta.* 277 (2018) 100–109. doi:10.1016/j.electacta.2018.04.209.
- [109] F. Mueller, D. Geiger, U. Kaiser, S. Passerini, D. Bresser, Elucidating the Impact of Cobalt Doping on the Lithium Storage Mechanism in Conversion/Alloying-Type Zinc Oxide Anodes, *ChemElectroChem.* 3 (2016) 1311–1319. doi:10.1002/celec.201600179.
- [110] F. Mueller, A. Gutsche, H. Nirschl, D. Geiger, U. Kaiser, D. Bresser, S. Passerini, Iron-Doped ZnO for lithium-ion anodes: Impact of the dopant ratio and carbon coating content, *J. Electrochem. Soc.* 164 (2017) A6123–A6130. doi:10.1149/2.0171701jes.
- [111] F. Mueller, D. Bresser, V.S.K. Chakravadhanula, S. Passerini, Fe-doped SnO₂ nanoparticles as new high capacity anode material for secondary lithium-ion batteries, *J. Power Sources.* 299 (2015) 398–402. doi:10.1016/j.jpowsour.2015.08.018.
- [112] G. Tian, Z. Zhao, A. Sarapulova, C. Das, L. Zhu, S. Liu, A. Missyul, E. Welter, J. Maibach, S. Dsoke, Understanding the Li-Ion Storage Mechanism in a Carbon Compositized Zinc Sulfide Electrode, *J. Mater. Chem. A.* (2019). doi:10.1039/C9TA01382B.
- [113] M.N. Obrovac, V.L. Chevrier, Alloy Negative Electrodes for Li-Ion Batteries, *Chem. Rev.* 114 (2014) 11444–11502. doi:10.1021/cr500207g.
- [114] C.-M. Park, J.-H. Kim, H. Kim, H.-J. Sohn, Li-alloy based anode materials for Li secondary batteries, *Chem. Soc. Rev.* 39 (2010) 3115. doi:10.1039/b919877f.
- [115] L. Corbari, G.J. Long, F. Grandjean, M. Zbinden, F. Gaill, P. Comp, Iron oxide deposits associated with the ectosymbiotic bacteria in the hydrothermal vent shrimp *Rimicaris exoculata*, *Biogeosciences.* 5 (2008) 1295–1310. doi:10.5194/bg-5-1295-2008.
- [116] S. Brunauer, P.H. Emmett, E. Teller, Adsorption of Gases in Multimolecular Layers, *J. Am. Chem. Soc.* 60 (1938) 309–319. doi:10.1021/ja01269a023.
- [117] M. Kruk, M. Jaroniec, Gas Adsorption Characterization of Ordered Organic–Inorganic Nanocomposite Materials, *Chem. Mater.* 13 (2001) 3169–3183. doi:10.1021/cm0101069.
- [118] K. Sing, The use of nitrogen adsorption for the characterisation of porous materials, *Colloids Surfaces A Physicochem. Eng. Asp.* 187–188 (2001) 3–9. doi:10.1016/S0927-7757(01)00612-4.

- [119] P. Zanello, *Inorganic electrochemistry: theory, practice and application*, Royal Society of Chemistry, 2007.
- [120] B. Ravel, M. Newville, ATHENA, ARTEMIS, HEPHAESTUS: data analysis for X-ray absorption spectroscopy using IFEFFIT, *J. Synchrotron Radiat.* 12 (2005) 537–541. doi:10.1107/S0909049505012719.
- [121] M. Herklotz, J. Weiß, E. Ahrens, M. Yavuz, L. Mereacre, N. Kiziltas-Yavuz, C. Dräger, H. Ehrenberg, J. Eckert, F. Fauth, L. Giebeler, M. Knapp, A novel high-throughput setup for in situ powder diffraction on coin cell batteries, *J. Appl. Crystallogr.* 49 (2016) 340–345. doi:10.1107/S1600576715022165.
- [122] M.-R. Gao, Y.-F. Xu, J. Jiang, S.-H. Yu, Nanostructured metal chalcogenides: synthesis, modification, and applications in energy conversion and storage devices, *Chem. Soc. Rev.* 42 (2013) 2986. doi:10.1039/c2cs35310e.
- [123] X. Bin Zhong, H.Y. Wang, Z.Z. Yang, B. Jin, Q.C. Jiang, Facile synthesis of mesoporous ZnCo_2O_4 coated with polypyrrole as an anode material for lithium-ion batteries, *J. Power Sources.* 296 (2015) 298–304. doi:10.1016/j.jpowsour.2015.07.047.
- [124] L. Hu, B. Qu, C. Li, Y. Chen, L. Mei, D. Lei, L. Chen, Q. Li, T. Wang, Facile synthesis of uniform mesoporous ZnCo_2O_4 microspheres as a high-performance anode material for Li-ion batteries, *J. Mater. Chem. A.* 1 (2013) 5596–5602. doi:10.1039/c3ta00085k.
- [125] J. Deng, X. Yu, X. Qin, D. Zhou, L. Zhang, H. Duan, F. Kang, B. Li, G. Wang, Co-B Nanoflakes as Multifunctional Bridges in ZnCo_2O_4 Micro-/Nanospheres for Superior Lithium Storage with Boosted Kinetics and Stability, *Adv. Energy Mater.* 1803612 (2019) 1803612. doi:10.1002/aenm.201803612.
- [126] G. Balachandran, D. Dixon, N. Bramnik, A. Bhaskar, M. Yavuz, L. Pfaffmann, F. Scheiba, S. Mangold, H. Ehrenberg, Elucidation of the Electrochemical Reaction Mechanism in MFe_2O_4 (M=Ni, Co) Conversion-Type Negative Electrode Systems by using In Situ X-ray Absorption Spectroscopy, *ChemElectroChem.* 2 (2015) 1510–1518. doi:10.1002/celec.201500197.
- [127] K. Wu, D. Liu, Y. Tang, In-situ single-step chemical synthesis of graphene-decorated CoFe_2O_4 composite with enhanced Li ion storage behaviors, *Electrochim. Acta.* 263 (2018) 515–523. doi:10.1016/j.electacta.2018.01.047.
- [128] L. Zhang, T. Wei, Z. Jiang, C. Liu, H. Jiang, J. Chang, L. Sheng, Q. Zhou, L. Yuan, Z. Fan, Electrostatic interaction in electrospun nanofibers: Double-layer carbon protection of CoFe_2O_4 nanosheets enabling ultralong-life and ultrahigh-rate lithium ion storage, *Nano Energy.* 48 (2018) 238–247. doi:10.1016/j.nanoen.2018.03.053.
- [129] G. Zhang, X.W. (David) Lou, Controlled Growth of NiCo_2O_4 Nanorods and Ultrathin Nanosheets on Carbon Nanofibers for High-performance Supercapacitors, *Sci. Rep.* 3 (2013) 2–7. doi:10.1038/srep01470.
- [130] Y. Luo, R. Guo, T. Li, F. Li, L. Meng, Z. Yang, Y. Wan, H. Luo, Conductive Polypyrrole Coated Hollow NiCo_2O_4 Microspheres as Anode Material with Improved Pseudocapacitive

- Contribution and Enhanced Conductivity for Lithium-Ion Batteries, *ChemElectroChem*. 6 (2019) 690–699. doi:10.1002/celec.201801513.
- [131] Y. Wang, P. Liu, K. Zhu, J. Wang, K. Yan, J. Liu, One-step fabrication of in situ carbon-coated $\text{NiCo}_2\text{O}_4@\text{C}$ bilayered hybrid nanostructural arrays as free-standing anode for high-performance lithium-ion batteries, *Electrochim. Acta*. 273 (2018) 1–9. doi:10.1016/j.electacta.2018.04.023.
- [132] B. Liu, J. Zhang, X. Wang, G. Chen, D. Chen, C. Zhou, G. Shen, Hierarchical Three-Dimensional ZnCo_2O_4 Nanowire Arrays/Carbon Cloth Anodes for a Novel Class of High-Performance Flexible Lithium-Ion Batteries, *Nano Lett.* 12 (2012) 3005–3011. doi:10.1021/nl300794f.
- [133] L. Huang, G.H. Waller, Y. Ding, D. Chen, D. Ding, P. Xi, Z.L. Wang, M. Liu, Controllable interior structure of ZnCo_2O_4 microspheres for high-performance lithium-ion batteries, *Nano Energy*. 11 (2015) 64–70. doi:10.1016/j.nanoen.2014.09.027.
- [134] Z. Wang, Q. Ru, Y. Mo, L. Guo, X. Chen, X. Hou, S. Hu, Facile synthesis of porous peanut-like - ZnCo_2O_4 decorated with rGO/CNTs toward high-performance lithium ion batteries, *J. Mater. Sci. Mater. Electron*. 28 (2017) 9081–9090. doi:10.1007/s10854-017-6641-z.
- [135] B. Liu, X. Wang, B. Liu, Q. Wang, D. Tan, W. Song, X. Hou, D. Chen, G. Shen, Advanced rechargeable lithium-ion batteries based on bendable ZnCo_2O_4 -urchins-on-carbon-fibers electrodes, *Nano Res*. 6 (2013) 525–534. doi:10.1007/s12274-013-0329-3.
- [136] J. Zhang, R. Chu, Y. Chen, H. Jiang, Y. Zhang, N.M. Huang, H. Guo, In-situ grown hierarchical ZnCo_2O_4 nanosheets on nickel foam as binder-free anode for lithium ion batteries, *Ceram. Int*. 44 (2018) 16219–16226. doi:10.1016/J.CERAMINT.2018.06.002.
- [137] W. Bai, H. Tong, Z. Gao, S. Yue, S. Xing, S. Dong, L. Shen, J. He, X. Zhang, Y. Liang, Preparation of ZnCo_2O_4 nanoflowers on a 3D carbon nanotube/nitrogen-doped graphene film and its electrochemical capacitance, *J. Mater. Chem. A*. (2015). doi:10.1039/C5TA05798A.
- [138] Y. Sharma, N. Sharma, G. V. Subba Rao, B.V.R. Chowdari, Nanophase ZnCo_2O_4 as a high performance anode material for Li-ion batteries, *Adv. Funct. Mater*. 17 (2007) 2855–2861. doi:10.1002/adfm.200600997.
- [139] Y. Ma, Y. Ma, D. Geiger, U. Kaiser, H. Zhang, G.T. Kim, T. Diemant, R.J. Behm, A. Varzi, S. Passerini, $\text{ZnO}/\text{ZnFe}_2\text{O}_4/\text{N}$ -doped C micro-polyhedrons with hierarchical hollow structure as high-performance anodes for lithium-ion batteries, *Nano Energy*. 42 (2017) 341–352. doi:10.1016/j.nanoen.2017.11.030.
- [140] M.A. Lowe, J. Gao, H.D. Abruña, In operando X-ray studies of the conversion reaction in Mn_3O_4 lithium battery anodes, *J. Mater. Chem. A*. 1 (2013) 2094–2103. doi:10.1039/C2TA01270G.
- [141] T. Yu, Y.W. Zhu, X.J. Xu, Z.X. Shen, P. Chen, C.-T. Lim, J.T.-L. Thong, C.-H. Sow, Controlled Growth and Field-Emission Properties of Cobalt Oxide Nanowalls, *Adv. Mater*. 17 (2005) 1595–1599. doi:10.1002/adma.200500322.

- [142] S. Cheng, H. Rong, Z. Jiang, Z. Zhen, G. Xie, B. Chen, B. Deng, J. Huang, Z.-J. Jiang, Parallelepipedally shaped ZnCo_2O_4 particles with a hierarchical porous structure as an anode for lithium-ion batteries, *Ionics (Kiel)*. 23 (2017) 77–85. doi:10.1007/s11581-016-1807-x.
- [143] S. Cheng, H. Rong, Z. Jiang, Z. Zhen, G. Xie, B. Chen, B. Deng, J. Huang, Z.-J. Jiang, Parallelepipedally shaped ZnCo_2O_4 particles with a hierarchical porous structure as an anode for lithium-ion batteries, *Ionics (Kiel)*. 23 (2017) 77–85. doi:10.1007/s11581-016-1807-x.
- [144] J. Bai, X. Li, G. Liu, Y. Qian, S. Xiong, Unusual formation of ZnCo_2O_4 3D hierarchical twin microspheres as a high-rate and ultralong-life lithium-ion battery anode material, *Adv. Funct. Mater.* 24 (2014) 3012–3020. doi:10.1002/adfm.201303442.
- [145] V. Šepelák, S.M. Becker, I. Bergmann, S. Indris, M. Scheuermann, A. Feldhoff, C. Kübel, M. Bruns, N. Stürzl, A.S. Ulrich, M. Ghafari, H. Hahn, C.P. Grey, K.D. Becker, P. Heitjans, Nonequilibrium structure of Zn_2SnO_4 spinel nanoparticles, *J. Mater. Chem.* 22 (2012) 3117. doi:10.1039/c2jm15427g.
- [146] R. Azmi, V. Trouillet, M. Strafela, S. Ulrich, H. Ehrenberg, M. Bruns, Surface analytical approaches to reliably characterize lithium ion battery electrodes, *Surf. Interface Anal.* 50 (2018) 43–51. doi:10.1002/sia.6330.
- [147] R. Azmi, M. Masoumi, H. Ehrenberg, V. Trouillet, M. Bruns, Surface analytical characterization of $\text{LiNi}_{0.8-y}\text{Mn}_y\text{Co}_{0.2}\text{O}_2$ ($0 \leq y \leq 0.4$) compounds for lithium-ion battery electrodes, *Surf. Interface Anal.* (2018) 1–6. doi:10.1002/sia.6415.
- [148] V. Kumar, C.R. Mariappan, R. Azmi, D. Moock, S. Indris, M. Bruns, H. Ehrenberg, G.V. Prakash, Pseudocapacitance of mesoporous spinel-type MCo_2O_4 ($\text{M} = \text{Co}, \text{Zn}$ and Ni) rods fabricated by a facile solvothermal route, *ACS Omega*. 2 (2017) 6003–6013. doi:10.1021/acsomega.7b00709.
- [149] M.C. Biesinger, B.P. Payne, A.P. Grosvenor, L.W.M. Lau, A.R. Gerson, R.S.C. Smart, Resolving surface chemical states in XPS analysis of first row transition metals, oxides and hydroxides: Cr, Mn, Fe, Co and Ni, *Appl. Surf. Sci.* 257 (2011) 2717–2730. doi:10.1016/j.apsusc.2010.10.051.
- [150] X.-B. Zhong, H.-Y. Wang, Z.-Z. Yang, B. Jin, Q.-C. Jiang, Facile synthesis of mesoporous ZnCo_2O_4 coated with polypyrrole as an anode material for lithium-ion batteries, *J. Power Sources*. 296 (2015) 298–304. doi:10.1016/j.jpowsour.2015.07.047.
- [151] C. Ai, M. Yin, C. Wang, J. Sun, Synthesis and characterization of spinel type ZnCo_2O_4 as a novel anode material for lithium ion batteries, *J. Mater. Sci.* 39 (2004) 1077–1079. doi:10.1023/B:JMSC.0000012948.27433.83.
- [152] S.-W. Lee, C.-W. Lee, S.-B. Yoon, M.-S. Kim, J.H. Jeong, K.-W. Nam, K.C. Roh, K.-B. Kim, Superior electrochemical properties of manganese dioxide/reduced graphene oxide nanocomposites as anode materials for high-performance lithium ion batteries, *J. Power Sources*. 312 (2016) 207–215. doi:10.1016/j.jpowsour.2016.02.049.
- [153] J. Maier, Nanoionics: ion transport and electrochemical storage in confined systems, *Nat. Mater.* 4 (2005) 805–815. doi:10.1038/nmat1513.

- [154] A. Ponrouch, P. Taberna, P. Simon, M.R. Palacín, On the origin of the extra capacity at low potential in materials for Li batteries reacting through conversion reaction, *Electrochim. Acta.* 61 (2012) 13–18. doi:10.1016/j.electacta.2011.11.029.
- [155] J.-M. Tarascon, P. Poizot, S. Laruelle, S. Grugeon, L. Dupont, Nano-sized transition-metal oxides as negative-electrode materials for lithium-ion batteries, *Nature.* 407 (2000) 496–499. doi:10.1038/35035045.
- [156] A.S. Aricò, P. Bruce, B. Scrosati, J. Tarascon, W. van Schalkwijk, Nanostructured materials for advanced energy conversion and storage devices, *Nat. Mater.* 4 (2005) 366–377. doi:10.1038/nmat1368.
- [157] H. Duncan, F.M. Courtel, Y. Abu-Lebdeh, A Study of the Solid-Electrolyte-Interface (SEI) of ZnMn_2O_4 : A Conversion-Type Anode Material for Li-Ion Batteries, *J. Electrochem. Soc.* 162 (2015) A7110–A7117. doi:10.1149/2.0141513jes.
- [158] Z. Zhao, G. Tian, A. Sarapulova, V. Trouillet, Q. Fu, U. Geckle, H. Ehrenberg, S. Dsoke, Elucidating the energy storage mechanism of ZnMn_2O_4 as promising anode for Li-ion batteries, *J. Mater. Chem. A.* 6 (2018) 19381–19392. doi:10.1039/C8TA06294C.
- [159] M.S. Song, Y.J. Cho, D.Y. Yoon, S. Nahm, S.H. Oh, K. Woo, J.M. Ko, W. Il Cho, Solvothermal synthesis of ZnMn_2O_4 as an anode material in lithium ion battery, *Electrochim. Acta.* 137 (2014) 266–272. doi:10.1016/j.electacta.2014.05.126.
- [160] D. Bresser, E. Paillard, R. Kloepsch, S. Krueger, M. Fiedler, R. Schmitz, D. Baither, M. Winter, S. Passerini, Carbon coated ZnFe_2O_4 nanoparticles for advanced lithium-ion anodes, *Adv. Energy Mater.* 3 (2013) 513–523. doi:10.1002/aenm.201200735.
- [161] N. Du, H. Zhang, B.D. Chen, J.B. Wu, X.Y. Ma, Z.H. Liu, Y.Q. Zhang, D.R. Yang, X.H. Huang, J.P. Tu, Porous Co_3O_4 Nanotubes Derived From $\text{Co}_4(\text{CO})_{12}$ Clusters on Carbon Nanotube Templates: A Highly Efficient Material For Li-Battery Applications, *Adv. Mater.* 19 (2007) 4505–4509. doi:10.1002/adma.200602513.
- [162] H. Hu, B. Guan, B. Xia, X.W. Lou, Designed formation of $\text{Co}_3\text{O}_4/\text{NiCo}_2\text{O}_4$ double-shelled nanocages with enhanced pseudocapacitive and electrocatalytic properties, *J. Am. Chem. Soc.* 137 (2015) 5590–5595. doi:10.1021/jacs.5b02465.
- [163] P. Yu, C. Li, X. Guo, Sodium Storage and Pseudocapacitive Charge in Textured $\text{Li}_4\text{Ti}_5\text{O}_{12}$ Thin Films, *J. Phys. Chem. C.* 118 (2014) 10616–10624. doi:10.1021/jp5010693.
- [164] A.P. Cohn, L. Oakes, R. Carter, S. Chatterjee, A.S. Westover, K. Share, C.L. Pint, Assessing the improved performance of freestanding, flexible graphene and carbon nanotube hybrid foams for lithium ion battery anodes, *Nanoscale.* 6 (2014) 4669–4675. doi:10.1039/C4NR00390J.
- [165] G.A. Muller, J.B. Cook, H.S. Kim, S.H. Tolbert, B. Dunn, High performance pseudocapacitor based on 2D layered metal chalcogenide nanocrystals, *Nano Lett.* 15 (2015) 1911–1917. doi:10.1021/nl504764m.
- [166] D.Y.W. Yu, C. Fietzek, W. Weydanz, K. Donoue, T. Inoue, H. Kurokawa, S. Fujitani, Study

- of LiFePO_4 by Cyclic Voltammetry, *J. Electrochem. Soc.* 154 (2007) A253. doi:10.1149/1.2434687.
- [167] Q. Zhang, S.-Z. Huang, J. Jin, J. Liu, Y. Li, H.-E. Wang, L.-H. Chen, B.-J. Wang, B.-L. Su, Engineering 3D bicontinuous hierarchically macro-mesoporous LiFePO_4/C nanocomposite for lithium storage with high rate capability and long cycle stability, *Sci. Rep.* 6 (2016) 25942. doi:10.1038/srep25942.
- [168] C. Yuan, L. Zhang, L. Hou, L. Zhou, G. Pang, L. Lian, Scalable Room-Temperature Synthesis of Mesoporous Nanocrystalline ZnMn_2O_4 with Enhanced Lithium Storage Properties for Lithium-Ion Batteries, *Chem. - A Eur. J.* 21 (2015) 1262–1268. doi:10.1002/chem.201404624.
- [169] L. Xiao, Y. Yang, J. Yin, Q. Li, L. Zhang, Low temperature synthesis of flower-like ZnMn_2O_4 superstructures with enhanced electrochemical lithium storage, *J. Power Sources.* 194 (2009) 1089–1093. doi:10.1016/j.jpowsour.2009.06.043.
- [170] G. Zhang, L. Yu, H. Bin Wu, H.E. Hoster, X.W.D. Lou, Formation of ZnMn_2O_4 Ball-in-Ball Hollow Microspheres as a High-Performance Anode for Lithium-Ion Batteries, *Adv. Mater.* 24 (2012) 4609–4613. doi:10.1002/adma.201201779.
- [171] Z. Zheng, Y. Cheng, X. Yan, R. Wang, P. Zhang, Enhanced electrochemical properties of graphene-wrapped ZnMn_2O_4 nanorods for lithium-ion batteries, *J. Mater. Chem. A.* 2 (2014) 149–154. doi:10.1039/C3TA13511J.
- [172] J. Jamnik, J. Maier, Nanocrystallinity effects in lithium battery materials: Aspects of nano-ionics. Part IV, *Phys. Chem. Chem. Phys.* 5 (2003) 5215–5220. doi:10.1039/b309130a.
- [173] X. Tang, Q. Feng, J. Huang, K. Liu, X. Luo, Q. Peng, Carbon-coated cobalt oxide porous spheres with improved kinetics and good structural stability for long-life lithium-ion batteries, *J. Colloid Interface Sci.* 510 (2018) 368–375. doi:10.1016/j.jcis.2017.09.086.
- [174] R.S. Kalubarme, S.M. Jadhav, B.B. Kale, S.W. Gosavi, C. Terashima, A. Fujishima, Porous Mn-doped cobalt oxide@C nanocomposite: a stable anode material for Li-ion rechargeable batteries, *Nanotechnology.* 29 (2018) 285705. doi:10.1088/1361-6528/aac034.
- [175] B. Donkova, D. Mehandjiev, Mechanism of decomposition of manganese(II) oxalate dihydrate and manganese(II) oxalate trihydrate, *Thermochim. Acta.* 421 (2004) 141–149. doi:10.1016/j.tca.2004.04.001.
- [176] Y. Deng, S. Tang, Q. Zhang, Z. Shi, L. Zhang, S. Zhan, G. Chen, Controllable synthesis of spinel nano- ZnMn_2O_4 via a single source precursor route and its high capacity retention as anode material for lithium ion batteries, *J. Mater. Chem.* 21 (2011) 11987. doi:10.1039/c1jm11575h.
- [177] K.S. Irani, A.P.B. Sinha, A.B. Biswas, Effect of temperature on the structure of manganites, *J. Phys. Chem. Solids.* 23 (1962) 711–727.
- [178] Z. Ma, H. Zhang, Z. Yang, Y. Zhang, B. Yu, Z. Liu, Highly mesoporous carbons derived from biomass feedstocks templated with eutectic salt ZnCl_2/KCl , *J. Mater. Chem. A.* 2

- (2014) 19324–19329. doi:10.1039/C4TA03829K.
- [179] M. Chen, X. Xia, M. Qi, J. Yuan, J. Yin, Q. Chen, Self-supported porous CoO semisphere arrays as binder-free electrodes for high-performance lithium ion batteries, *Mater. Res. Bull.* 73 (2016) 125–129. doi:10.1016/j.materresbull.2015.08.035.
- [180] L. Malavasi, P. Galinetto, M.C. Mozzati, C.B. Azzoni, G. Flor, Raman spectroscopy of AMn_2O_4 (A = Mn, Mg and Zn) spinels, *Phys. Chem. Chem. Phys.* 4 (2002) 3876–3880. doi:10.1039/b203520k.
- [181] J.G. Kim, S.H. Lee, Y. Kim, W.B. Kim, Fabrication of Free-Standing $ZnMn_2O_4$ Mesoscale Tubular Arrays for Lithium-Ion Anodes with Highly Reversible Lithium Storage Properties, *ACS Appl. Mater. Interfaces.* 5 (2013) 11321–11328. doi:10.1021/am403546s.
- [182] T. Zhang, H. Yue, H. Qiu, K. Zhu, L. Zhang, Y. Wei, F. Du, G. Chen, D. Zhang, Synthesis of graphene-wrapped $ZnMn_2O_4$ hollow microspheres as high performance anode materials for lithium ion batteries, *RSC Adv.* 5 (2015) 99107–99114. doi:10.1039/C5RA16667E.
- [183] Y. Han, H. Li, J. Li, H. Si, W. Zhu, X. Qiu, Hierarchical Mesoporous Iron Fluoride with Superior Rate Performance for Lithium-Ion Batteries, *ACS Appl. Mater. Interfaces.* 8 (2016) 32869–32874. doi:10.1021/acsami.6b11889.
- [184] C. Paek, A. V. McCormick, P.W. Carr, Preparation and evaluation of carbon coated alumina as a high surface area packing material for high performance liquid chromatography, *J. Chromatogr. A.* 1217 (2010) 6475–6483. doi:10.1016/j.chroma.2010.08.037.
- [185] W. Zhou, D. Wang, L. Zhao, C. Ding, X. Jia, Y. Du, G. Wen, H. Wang, Template-free fabrication of graphene-wrapped mesoporous $ZnMn_2O_4$ nanorings as anode materials for lithium-ion batteries, *Nanotechnology.* 28 (2017) 245401. doi:10.1088/1361-6528/aa6ec4.
- [186] K. Zhong, B. Zhang, S. Luo, W. Wen, H. Li, X. Huang, L. Chen, Investigation on porous MnO microsphere anode for lithium ion batteries, *J. Power Sources.* 196 (2011) 6802–6808. doi:10.1016/j.jpowsour.2010.10.031.
- [187] A. Sadezky, H. Muckenhuber, H. Grothe, R. Niessner, U. Pöschl, Raman microspectroscopy of soot and related carbonaceous materials: Spectral analysis and structural information, *Carbon N. Y.* 43 (2005) 1731–1742. doi:10.1016/j.carbon.2005.02.018.
- [188] H. Guo, X.-F. Wang, Q. Qian, F. Wang, X. Xia, A Green Approach to the Synthesis of Graphene Nanosheets, *ACS Nano.* 3 (2009) 2653–2659. doi:10.1021/nn900227d.
- [189] B. Fan, A. Hu, X. Chen, S. Zhang, Q. Tang, J. Wang, W. Deng, Z. Liu, K. Xiao, Hierarchical Porous $ZnMn_2O_4$ Microspheres as a High-Performance Anode for Lithium-Ion Batteries, *Electrochim. Acta.* 213 (2016) 37–45. doi:10.1016/j.electacta.2016.07.030.
- [190] S.J. Rezvani, F. Nobili, R. Gunnella, M. Ali, R. Tossici, S. Passerini, A. Di Cicco, SEI Dynamics in Metal Oxide Conversion Electrodes of Li-Ion Batteries, *J. Phys. Chem. C.* 121 (2017) 26379–26388. doi:10.1021/acs.jpcc.7b08259.
- [191] Y.-Y. Hu, Z. Liu, K.-W. Nam, O.J. Borkiewicz, J. Cheng, X. Hua, M.T. Dunstan, X. Yu, K.M. Wiaderek, L.-S. Du, K.W. Chapman, P.J. Chupas, X.-Q. Yang, C.P. Grey, Origin of

- additional capacities in metal oxide lithium-ion battery electrodes, *Nat. Mater.* 12 (2013) 1130–1136. doi:10.1038/nmat3784.
- [192] M.-G. Park, G.-K. Sung, N.-E. Sung, J.-H. Kim, C.-M. Park, Partially reversible Li_2O formation in ZnO: A critical finding supporting realization of highly reversible metal oxide electrodes, *J. Power Sources.* 328 (2016) 607–614. doi:10.1016/j.jpowsour.2016.08.053.
- [193] L. Cabo-Fernandez, D. Bresser, F. Braga, S. Passerini, L.J. Hardwick, In-Situ Electrochemical SHINERS Investigation of SEI Composition on Carbon-Coated $\text{Zn}_{0.9}\text{Fe}_{0.1}\text{O}$ Anode for Lithium-Ion Batteries, *Batter. Supercaps.* 2 (2019) 168–177. doi:10.1002/batt.201800063.
- [194] M. Ahmad, S. Yingying, A. Nisar, H. Sun, W. Shen, M. Wei, J. Zhu, Synthesis of hierarchical flower-like ZnO nanostructures and their functionalization by Au nanoparticles for improved photocatalytic and high performance Li-ion battery anodes, *J. Mater. Chem.* 21 (2011) 7723–7729. doi:10.1039/c1jm10720h.
- [195] S. Laruelle, S. Grugeon, P. Poizot, M. Dollé, L. Dupont, J.-M. Tarascon, On the Origin of the Extra Electrochemical Capacity Displayed by MO/Li Cells at Low Potential, *J. Electrochem. Soc.* 149 (2002) A627. doi:10.1149/1.1467947.
- [196] Y. Ma, Y. Ma, D. Geiger, U. Kaiser, H. Zhang, G.T. Kim, T. Diemant, R.J. Behm, A. Varzi, S. Passerini, ZnO/ZnFe₂O₄/N-doped C micro-polyhedrons with hierarchical hollow structure as high-performance anodes for lithium-ion batteries, *Nano Energy.* 42 (2017) 341–352. doi:10.1016/j.nanoen.2017.11.030.
- [197] P. Lavela, G.F. Ortiz, J.L. Tirado, E. Zhecheva, R. Stoyanova, S. Ivanova, High-performance transition metal mixed oxides in conversion electrodes: A combined spectroscopic and electrochemical study, *J. Phys. Chem. C.* 111 (2007) 14238–14246. doi:10.1021/jp074142s.
- [198] F. Nobili, S. Dsoke, F. Croce, R. Marassi, An ac impedance spectroscopic study of Mg-doped LiCoO_2 at different temperatures: Electronic and ionic transport properties, *Electrochim. Acta.* 50 (2005) 2307–2313. doi:10.1016/j.electacta.2004.10.044.
- [199] P. Li, K. Wu, P. Wang, X. Lin, H. Yu, M. Shui, X. Zheng, N. Long, J. Shu, Preparation, electrochemical characterization and in-situ kinetic observation of $\text{Na}_2\text{Li}_2\text{Ti}_6\text{O}_{14}$ as anode material for lithium ion batteries, *Ceram. Int.* 41 (2015) 14508–14516. doi:10.1016/j.ceramint.2015.07.095.
- [200] Y.-L. Shi, M.-F. Shen, S.-D. Xu, Q.-C. Zhuang, L. Jiang, Y.-H. Qiang, Electrochemical impedance spectroscopy investigation of the FeF_3/C cathode for lithium-ion batteries, *Solid State Ionics.* 222–223 (2012) 23–30. doi:10.1016/j.ssi.2012.06.024.
- [201] X. Luo, X. Zhang, L. Chen, L. Li, G. Zhu, G. Chen, D. Yan, H. Xu, A. Yu, Mesoporous ZnMn_2O_4 Microtubules Derived from a Biomimetic Strategy for High-Performance Lithium/Sodium Ion Batteries, *ACS Appl. Mater. Interfaces.* 10 (2018) 33170–33178. doi:10.1021/acsami.8b10111.
- [202] F. Pang, S. Hou, P. Wang, M. Liu, Y. Luo, L. Zhao, $\beta\text{-MnO}_2/\text{Metal-Organic Framework}$

- Derived Nanoporous ZnMn_2O_4 Nanorods as Lithium-Ion Battery Anodes with Superior Lithium-Storage Performance, *Chem. – A Eur. J.* 25 (2019) 5043–5050. doi:10.1002/chem.201806006.
- [203] T. Zhang, H. Yue, H. Qiu, Y. Wei, C. Wang, G. Chen, D. Zhang, Nano-particle assembled porous core-shell ZnMn_2O_4 microspheres with superb performance for lithium batteries, *Nanotechnology*. 28 (2017) 105403. doi:10.1088/1361-6528/aa5a49.
- [204] V. Augustyn, P. Simon, B. Dunn, Pseudocapacitive oxide materials for high-rate electrochemical energy storage, *Energy Environ. Sci.* 7 (2014) 1597–1614. doi:10.1039/c3ee44164d.
- [205] M. Abdollahifar, S.-S. Huang, Y.-H. Lin, Y.-C. Lin, B.-Y. Shih, H.-S. Sheu, Y.-F. Liao, N.-L. Wu, High-performance carbon-coated ZnMn_2O_4 nanocrystallite supercapacitors with tailored microstructures enabled by a novel solution combustion method, *J. Power Sources*. 378 (2018) 90–97. doi:10.1016/j.jpowsour.
- [206] Y. Meng, D. Wang, Y. Wei, K. Zhu, Y. Zhao, X. Bian, F. Du, B. Liu, Y. Gao, G. Chen, Competition between insertion of Li^+ and Mg^{2+} : An example of TiO_2 -B nanowires for Mg rechargeable batteries and $\text{Li}^+/\text{Mg}^{2+}$ hybrid-ion batteries, *J. Power Sources*. 346 (2017) 134–142. doi:10.1016/j.jpowsour.2017.02.033.
- [207] S.H. Yu, X. Feng, N. Zhang, J. Seok, H.D. Abruña, Understanding Conversion-Type Electrodes for Lithium Rechargeable Batteries, *Acc. Chem. Res.* 51 (2018) 273–281. doi:10.1021/acs.accounts.7b00487.
- [208] S.-W. Kim, H.-W. Lee, P. Muralidharan, D.-H. Seo, W.-S. Yoon, D.K. Kim, K. Kang, Electrochemical performance and ex situ analysis of ZnMn_2O_4 nanowires as anode materials for lithium rechargeable batteries, *Nano Res.* 4 (2011) 505–510. doi:10.1007/s12274-011-0106-0.
- [209] C. Schütter, T. Husch, V. Viswanathan, S. Passerini, A. Balducci, M. Korth, Rational design of new electrolyte materials for electrochemical double layer capacitors, *J. Power Sources*. 326 (2016) 541–548. doi:10.1016/j.jpowsour.2016.06.022.
- [210] C. Schütter, S. Passerini, M. Korth, A. Balducci, Cyano Ester as Solvent for High Voltage Electrochemical Double Layer Capacitors, *Electrochim. Acta*. 224 (2017) 278–284. doi:10.1016/j.electacta.2016.12.063.
- [211] S. Grugeon, P. Jankowski, D. Cailieu, C. Forestier, L. Sannier, M. Armand, P. Johansson, S. Laruelle, Towards a better understanding of vinylene carbonate derived SEI-layers by synthesis of reduction compounds, *J. Power Sources*. 427 (2019) 77–84. doi:10.1016/j.jpowsour.2019.04.061.
- [212] J.S. Lee, S.T. Kim, R. Cao, N.S. Choi, M. Liu, K.T. Lee, J. Cho, Metal-air batteries with high energy density: Li-air versus Zn-air, *Adv. Energy Mater.* 1 (2011) 34–50. doi:10.1002/aenm.201000010.
- [213] A. Guéguen, P. Novák, J. Berg, XPS Study of the Interface Evolution of Carbonaceous Electrodes for Li- O_2 Batteries during the 1st Cycle, *J. Electrochem. Soc.* 163 (2016) A2545–

- A2550. doi:10.1149/2.0351613jes.
- [214] Z. Ding, B. Yao, J. Feng, J. Zhang, Enhanced rate performance and cycling stability of a CoCO_3 -polypyrrole composite for lithium ion battery anodes, *J. Mater. Chem. A*. 1 (2013) 11200–11209. doi:10.1039/c3ta12227a.
- [215] D.C. Bock, G.H. Waller, A.N. Mansour, A.C. Marschilok, K.J. Takeuchi, E.S. Takeuchi, Investigation of Solid Electrolyte Interphase Layer Formation and Electrochemical Reversibility of Magnetite, Fe_3O_4 , Electrodes: A Combined X-ray Absorption Spectroscopy and X-ray Photoelectron Spectroscopy Study, *J. Phys. Chem. C*. 122 (2018) 14257–14271. doi:10.1021/acs.jpcc.8b01970.
- [216] S. Permien, S. Indris, A.-L. Hansen, M. Scheuermann, D. Zahn, U. Schürmann, G. Neubüser, L. Kienle, E. Yegudin, W. Bensch, Elucidation of the Conversion Reaction of CoMnFeO_4 Nanoparticles in Lithium Ion Battery Anode via Operando Studies, *ACS Appl. Mater. Interfaces*. 8 (2016) 15320–15332. doi:10.1021/acsami.6b03185.
- [217] A. Manceau, M.A. Marcus, S. Grangeon, Determination of Mn valence states in mixed-valent manganates by XANES spectroscopy, *Am. Mineral.* 97 (2012) 816–827. doi:10.2138/am.2012.3903.
- [218] S. Zhang, L. Zhu, H. Song, X. Chen, J. Zhou, Enhanced electrochemical performance of MnO nanowire/graphene composite during cycling as the anode material for lithium-ion batteries, *Nano Energy*. 10 (2014) 172–180. doi:10.1016/j.nanoen.2014.09.012.
- [219] M. Zarrabeitia, F. Nobili, M.Á. Muñoz-Márquez, T. Rojo, M. Casas-Cabanas, Direct observation of electronic conductivity transitions and solid electrolyte interphase stability of $\text{Na}_2\text{Ti}_3\text{O}_7$ electrodes for Na-ion batteries, *J. Power Sources*. 330 (2016) 78–83. doi:10.1016/j.jpowsour.2016.08.112.
- [220] J. Rodríguez-Carvajal, Recent advances in magnetic structure determination by neutron powder diffraction, *Phys. B Condens. Matter*. 192 (1993) 55–69. doi:10.1016/0921-4526(93)90108-I.
- [221] K.L. Parry, A.G. Shard, R.D. Short, R.G. White, J.D. Whittle, A. Wright, ARXPS characterisation of plasma polymerised surface chemical gradients, *Surf. Interface Anal.* 38 (2006) 1497–1504. doi:10.1002/sia.2400.
- [222] J.H. Scofield, Hartree-Slater subshell photoionization cross-sections at 1254 and 1487 eV, *J. Electron Spectros. Relat. Phenomena*. 8 (1976) 129–137. doi:10.1016/0368-2048(76)80015-1.
- [223] M. Herklotz, F. Scheiba, M. Hinterstein, K. Nikolowski, M. Knapp, A.C. Dippel, L. Giebeler, J. Eckert, H. Ehrenberg, Advances in in situ powder diffraction of battery materials: A case study of the new beamline P02.1 at DESY, Hamburg, *J. Appl. Crystallogr.* 46 (2013) 1117–1127. doi:10.1107/S0021889813013551.

9 Curriculum Vitae

Personal Data

Name: Zijian Zhao

Place of Birth: Tianjin, China

Gender: Female

Nationality: Chinese

Publications during the PhD period

- 1) Z. Zhao, G. Tian, A. Sarapulova, V. Trouillet, Q. Fu, U. Geckle, H. Ehrenberg, S. Dsoke, Elucidating the energy storage mechanism of ZnMn_2O_4 as promising anode for Li-ion batteries, *J. Mater. Chem. A*. 6 (2018) 19381–19392.
- 2) Z. Zhao, G. Tian, V. Trouillet, L. Zhu, J. Zhu, A. Missiul, E. Welter, S. Dsoke, In Operando analysis of the charge storage mechanism in a conversion ZnCo_2O_4 anode and the application in flexible Li-ion batteries, *Inorg. Chem. Front.* 6 (2019) 1861–1872.
- 3) Z. Zhao, G. Tian, A. Sarapulova, G. Melinte, J.L. Gómez-Urbano, C. Li, S. Liu, E. Welter, M. Etter, S. Dsoke, Mechanism Study of Carbon Coating Effects on Conversion-Type Anode Materials in Lithium-Ion Batteries: Case Study of ZnMn_2O_4 and ZnO–MnO Composites, *ACS Appl. Mater. Interfaces*. 11 (2019) 29888–29900.
- 4) G. Tian†, Z. Zhao†, A. Sarapulova, C. Das, L. Zhu, S. Liu, A. Missiul, E. Welter, J. Maibach, S. Dsoke, Understanding the Li-ion storage mechanism in a carbon composited zinc sulfide electrode, *J. Mater. Chem. A*. 7 (2019) 15640–15653.
- 5) D. Stępień, Z. Zhao, S. Dsoke, Shift to Post-Li-Ion Capacitors: Electrochemical Behavior of Activated Carbon Electrodes in Li-, Na- and K-Salt Containing Organic Electrolytes, *J. Electrochem. Soc.* 165 (2018) A2807–A2814.
- 6) G. Tian, Z. Zhao, T. Zinkevich, K. Elies, F. Scheiba, H. Ehrenberg, A crosslinked polyethyleneglycol solid electrolyte dissolving LiTFSI for rechargeable lithium batteries, *ChemSusChem*. (2019) cssc.201901587. doi:10.1002/cssc.201901587.
- 7) C. Li, A. Sarapulova, Z. Zhao, Q. Fu, V. Trouillet, A. Missiul, E. Welter, S. Dsoke, Understanding the Lithium Storage Mechanism in Core–Shell Fe_2O_3 @C Hollow Nanospheres Derived from Metal–Organic Frameworks: An In operando Synchrotron Radiation Diffraction and in operando X-ray Absorption Spectroscopy Study, *Chem. Mater.* 31 (2019) 5633–5645.
- 8) N. Sabi, A. Sarapulova, S. Indris, S. Dsoke, Z. Zhao, M. Dahbi, H. Ehrenberg, I. Saadoun, Evidence of a Pseudo-Capacitive Behavior Combined with an Insertion/Extraction Reaction Upon Cycling of the Positive Electrode Material $\text{P2-Na}_x\text{Co}_{0.9}\text{Ti}_{0.1}\text{O}_2$ for Sodium-ion Batteries, *ChemElectroChem*. 6 (2019) 892–903.

- 9) G. Tian, F. Scheiba, L. Pfaffmann, A. Fiedler, V.S.K. Chakravadhanula, G. Balachandran, Z. Zhao, H. Ehrenberg, Electrostatic self-assembly of LiFePO₄ cathodes on a three-dimensional substrate for lithium ion batteries, *Electrochim. Acta.* 283 (2018) 1375–1383.

Previous Publications

- 1) Z. Zhao, Y. Wang, M. Li, R. Yang, High performance N-doped porous activated carbon based on chicken feather for supercapacitors and CO₂ capture, *RSC Adv.* 5 (2015) 34803–34811.
- 2) Y. Wang, R. Yang, M. Li, Z. Zhao, Hydrothermal preparation of highly porous carbon spheres from hemp (*Cannabis sativa* L.) stem hemicellulose for use in energy-related applications, *Ind. Crops Prod.* 65 (2015) 216–226.
- 3) Y. Wang, R. Yang, Y. Wei, Z. Zhao, M. Li, Preparation of novel pigskin-derived carbon sheets and their low-temperature activation-induced high capacitive performance, *RSC Adv.* 4 (2014) 45318–45324.